WOLFF

BIOMIMETICS AND FUNCTIONAL NANO-STRUCTURES

BIELEFELD UNIVERSITY

Biomimetics and functional nanostructures

Annalena Wolff

Copyright © 2014 Wolff

BIELEFELD UNIVERSITY

Declaration

I wrote this thesis by myself and used none but the indicated resources.

Bielefeld, February, 2014

Annalena Wolff

Comitee:

Prof. Dr. A. Hütten
Prof. Dr. T. Huser

Date of submission:February, 2014

"...although we humans cut nature up in different ways, and have different courses in different departments, such compartmentalization is really artificial and we should take our intellectual pleasures where we find them."

-Richard Feynman, Feynman Lectures 1

Contents

Introduction

Richard Feynman's speech "There is plenty of room at the bottom" [1] is often regarded as the conceptual origin of nanotechnology. In his speech Feynman talked about a novel reseach field in which systems could be constructed and altered on a small scale. The developments of the electron microscope (TEM)[1], the scanning tunneling microscope (STM) [2] and the atomic force microscope (AFM)[3] were essential to establish this new field of research between the atomic and macroscopic scale, since these methods allowed the imaging and manipulation of systems down to the atomic scale. New methods, which are often based on electron microscopy, have been developed throughout the last few decades. 3D tomography, in which a dualbeam device (a device that combines an electron microscope with a focused ion beam which is used to structure samples) is used allows to cut away thin slices of a material and to image the material after the cutting process. This technique allows sample sections to be studied in situ with nanometer resolution from which a 3D tomogram, that visualizes the 3D arrangement of the sample, can be reconstructed [3]. Nanotechnology has since emerged as a highly interdisciplinary field. Scientists of many different fields, including physics, chemistry, biology, and material science often collaborate to tackle the unique issues that arise when working on such a small scale. At this scale, quantum mechanical effects dominate and thus new physical properties emerge when going from the macroscopic scale to the nanoscale. For example coulomb blockades are an effect due to charge quantization in which the charging energy of a structure is greater than the thermal energy provided, leading to sequential, non-coherent tunneling through the system [4, 5, 6]. Another size-dependent effect that

[1] The first TEM was developed in 1931 by Ernst Ruska and Max Knoll. Ernst Ruska was awarded the nobel prize in physics 1986 "for his fundamental work in electron optics, and for the design of the first electron microscope" [2]

[2] The STM was developed by Gerd Binning and Heinrich Rohrer which were awarded the nobel prize "for their design of the scanning tunneling microscope"[2].

[3] The first AFM was developed in 1986 by Gerd Binning, Calvin Quate and Christoph Gerber.

occurs at this lengthscale is superparamagnetism, in which thermal fluctuations are sufficiently large to spontaneously demagnetize a magnetized sample in the absence of a magnetic field. Using this effect, the magnetization of the material can be switched on and off by external fields [7]. These new effects not only lead to new technologies such as ferro fluids (magnetic ink for printing bar codes) and single electron transistors [4, 5, 6, 8] but also represent a problem for further miniturization of devices such as hard disc drives, in which the superparamagnetic effect leads to a memory loss due to thermal fluctuations. Magnetically anisotropic materials are of great interest for the magnetic and magneto-optic recording industry since high anisotropies allow a stable magnetic behavior even at small scales without encountering the problem with superparamagnetism [9, 10, 11] and thus allows a further device miniturization (required for higher magnetic recording densities). On the other hand the switchable magnetism leads to new technological applications, for example nanoparticular biosensors [12, 13].

The smallest building blocks of nano-systems are represented by nanoparticles, which are small solids that consist of only a few hundred to a thousand atoms. These structures, especially magnetic nanoparticles, have been studied by many scientists due to their unique properties and possibilities for applications [7, 14, 15, 16, 17, 18, 19, 20, 21]. In the medical sector these small building blocks are already used for contrast enhancement in magnetic resonant imaging [7, 22, 23, 24] and have lead to the development of new medical treatments such as hyperthermia therapy and nano-assisted drug delivery [25, 26, 27, 28]. In hyperthermia therapy nanoparticles are injected into the tumor of the patient and alternating magnetic fields are used to produce a localized tissue heating which destroys the tumor [29, 30]. In the latter treatment nanoparticles are delivered to the area of choice within the body via magnetic fields where medication, which is attached to the nanoparticle is locally released [7, 28]. For cancer patients this could allow a reduced dosage of chemotherapy and therfore less side effects [7]. Such small building blocks that have the ability to deliver drugs to specific regions within the human body have not only sparked great interest in the science and medical community but have also inspired science fiction authors. In Star Trek™[4], submicroscopic robots referred to as

[4] Stark Trek is a registered trademark of CBS Studios Inc.

"nanoprobes" are used by the Borg (a cybernetic life-form of different species within the Star Trek Universe) for assimilation, a process in which these nanoprobes move through the subjects blood stream, distributing Borg technology through the body turning subjects into new members of the Borg species [31].

In addition to nanotechnology, advances in bioengineering and stem cell research have also been used as inspirational material for science fiction authors. In the movie Alien: Resurrection (by 20th Century Fox) a clone of the late antagonist Allen Ripley is created from a blood sample taken before her death. A new alien queen is surgically removed from the body and is used to breed aliens for study and possible military purposes. How far away is science from such fictional stories, in which body parts or whole organisms are engineered? The first mamal, a sheep named Dolly, was successfully cloned in 1996 [32] using induced pluripotent stem cells (adult stem cells which have been reprogrammed to be pluripotent). The adult stem cells, which have the potential to form various constituents of the human body offer the possibility to engineer organs or tissues which are required for the medical treatments [5] of degenerative illnesses or surgery [33]. The process in which stem cells specialize into the various structures of the body is referred to as differentiation [33]. Stem cell differentiation *ex vivo* is currently triggered by so called biochemical cues, which lead to severe side effects within the human body [34] in the regenerative medical approaches. New differentiation mechanisms need to be found if stem cell differentiation is to be used as safe, future treatment.

[5] These medical treatments, referred to as regenerative medicine, aim to repair or replace damaged tissue could therefore possibly cure debilitating illnesses such as Parkinson's disease [33], which are currently deemed incurable.

Two opposite interdisciplinary projects were carried out in this work: one in which biological structures were use to influence the nanostructures and another in which nanostructures were used to influence biological entities.

The first part of this thesis provides a detailed description of the devices which were used in this work. The devices are explained prior to the two projects which were carried out in this work since

some devices were used in both projects.

In the second part, a biomimetic approach to synthesize well defined nanoparticles at room temperature is explored. Biomimetics is the use of principles found in biological structures and mechanisms for technical applications [35].

The aim of the other project in the third part of this work is to study stem cell differentiation via nanostructures in order to overcome the issues that arise with the conventional differentiation triggers (biochemical cues) in regenerative medicine/bioengineering. A detailed motivation of the research, neccessary theory to understand the work as well as a chapter overview at the end of the motivation is given separately for each part.

Part I

Devices and Methods

The Alternating Gradient Magnetometer

Alternating Gradient Magnetometry (AGM) offers the possibility to determine the magnetic properties[6] of samples. In this work a *MicroMag*^{TM}2900 from *Princeton Measurements Corporation* is used. This device allows measurements with a sensitivity of up to 10 nemu standard deviation at a maximal external magnetic field of $\pm 1114\,\mathrm{kA \cdot m^{-1}}$ at room temperature [36]. The schematic of the AGM setup can be found in Figure 1. The major components are outer coils[7], a pair of inner coils[8] and a sample holder which is connected to a piezo. The sample, magnetized by a static homogeneous magnetic field produced by the outer coils, acts as a dipole and is deflected in the alternating gradient field [9], created by the inner coils. This displacement is detected by the piezo. A change of the static homogeneous field, measured by a hall sensor, leads to a change in the magnetization of the sample. The force of the gradient field acting on the sample changes, resulting in a deflection of the sample which is then measured by the piezo. The displacement signal is transformed into a voltage signal by the piezo which is then plotted against the homogeneous field strength. The resonant operating frequency of the sampleholder and the sample needs to be determined prior to the measurements to calculate the magnetic moment since it is dependent on the mass of the sample. To achieve this, the frequency of the applied AC voltage (at the inner coils) is varied

[6] This includes whether the material is diamagnetic, paramagnetic, ferromagnetic or superparamagnetic. In case of ferromagnetic substances, the coercivity can be determined as well as the magnetization and remanence for a known sample volume.

[7] These coils create a homogeneous magnetic field.

[8] These coils create the alternating gradient field.

[9] The alternating gradient field is sinusoidal with time.

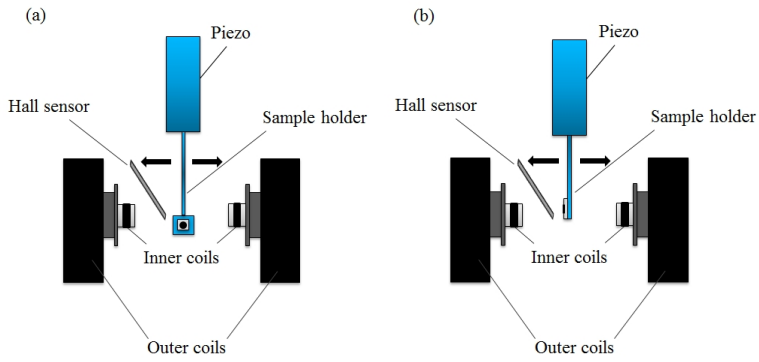

Figure 1: AGM setup for (a) parallel (in-plane) measurements and (b) perpendicular (out-of-plane) measurements. The AGM setup was drawn in analogy to [37].

until the voltage[10] determined with the piezo has reached its maximum.

The AGM measurements can be performed in-plane and out-of-plane if anisotropy is expected. The magnetic behavior along the two directions can be determined this way. The different possible measurement orientations are sketched in Figure 1.

[10] The voltage determined by the piezo is maximal for the resonant frequency.

The Transmission Electron Microscope

Transmission electron microscopes (TEM) have become one of the most common tools for structural analysis on the nanoscale since their first commercial construction in 1936 [38]. They allow the visualization of structures well below the resolution of optical microscopes, even down to single atoms (for graphene) for thin[11] samples. These devices not only offer insights about sample morphology but also about many other properties including the microstructure, crystal structure and local chemistry, if equipped with either an Electron Energy Loss Spectrometer (EELS) or Energy Dispersive X-ray (EDX) detector.

[11] The TEM can image samples with a thickness of less than 100 nm.

Setup

A TEM consists of an electron gun in which the electron beam is generated, a column in which electromagnetic lenses form the electron beam and where the specimen is inserted, as well as a detector at the end of the column which detects the transmitted electrons. A typical TEM setup is displayed in Figure 2.

Gun: Two types of electron guns are predominantly used: a thermionic emission cathode with either a tungsten needle or a LaB_6 crystal, or a Field Emission Gun (FEG). The tungsten needle, displayed in Figure 3, is heated electrically. At the tip of the needle (the hottest point when heated), electrons obtain a sufficiently high energy to overcome the work function of the material and leave the metal. A Wehnelt electrode focusses the emitted electrons. The second type of electron gun, the FEG, consists of a tungsten

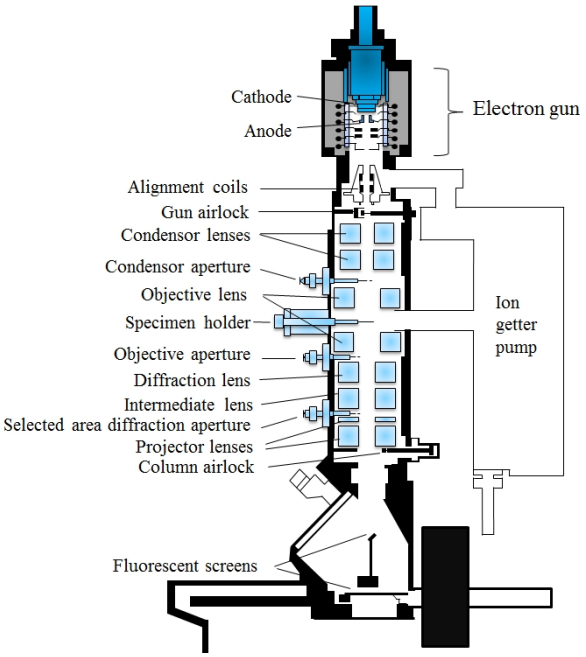

Figure 2: Schematic of a TEM setup, in analogy to [39]. The TEM consists of a gun, which is situated in the top of the device, a column (middle section) in which an electromagentic lens sytem and apertures are used to control the electron beam and where the sample is inserted, as well as a fluorescent screen and detector which are situated at the bottom of the device. The fluorescent screen visualizes the image and can be used to select the region of choice in the sample. An ion getter pump creates a high vacuum, neccessary for imaging.

needle and a pair of anodes to which a voltage is applied. The resulting potential allows for to extraction of electrons from the needle. A more detailed description is given in the DualBeam chapter.

The electrons are accelerated by the potential between the cathode and an anode. This acceleration voltage determines the wavelength of the electrons and therefore the resolution (Rayleigh criterium):

$$\delta = \frac{0,61\lambda}{N.A.} = \frac{0,61\lambda}{n \cdot \sin\alpha} \tag{1}$$

with δ as the smallest resolvable distance, λ as the electron wavelength, N.A. as the numerical aperture, n as the refractive index of the viewing medium (n=1) and α as the collection angle (of the focussing lenses). Relativistic calculations for electrons accelerated with a voltage $U \gg 80\,\mathrm{kV}$ are neccessary due to the high electron velocities ($v = 0.7 \cdot c$ at $U = 200\,\mathrm{kV}$) [38].

Column: A system of electromagnetic lenses focusses the electron beam. The condensor lenses form the electron beam. The

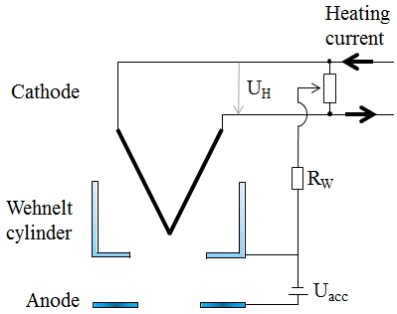

Figure 3: Illustration of an electron gun, drawn in analogy to [40]. The electrons, which are emitted from the tip of the tungsten needle are focused by the Wehnelt cylinder. The voltage which is used to accelerate the electrons is represented by U_{acc}. The heating current, used to heat the filament, is illustrated as black arrows.

objective lens, which is situated above and below the specimen,changes the image focus and creates the first intermediate image.
The intermediate and projection lenses magnify and project the image onto a fluorescent screen or a CCD camera. A high vacuum ($\approx 10^{-5}$ Pa) in the column is achieved using an ion getter pump. The electron beam cannot be transmitted far through air since the electrons would be strongly scattered by the air molecules before they reach the sample. A well-controlled and coherent electron beam, however, is essential for imaging, thus a high vacuum in the column is required.

The TEM offers a nominal resolution well below 1 Å [38]. However, abberations reduce the resolution (subnanometer resolution). The energy of the emitted electrons is statistically spread (±1 eV). Electrons with a higher energy are less bent by the lenssystem and are thus focussed behind the nominal focus point. Electrons with a lower energy are focused before the nominal focus point. This effect is referred to as chromatic abberation. The spherical abberation leads to a stronger bending of electrons farther from the optical axis than of those closer to the optical axis. As a result, a point is imaged as a disc. Apertures along the beam path block the off-axis electrons, however they lead to a reduced brightness and resolution due to the smaller collection angle. Astigmatism arises from the non-ideal cylindrical symmetry of the lenses and leads to different focussing strengths and thus a focus spread.

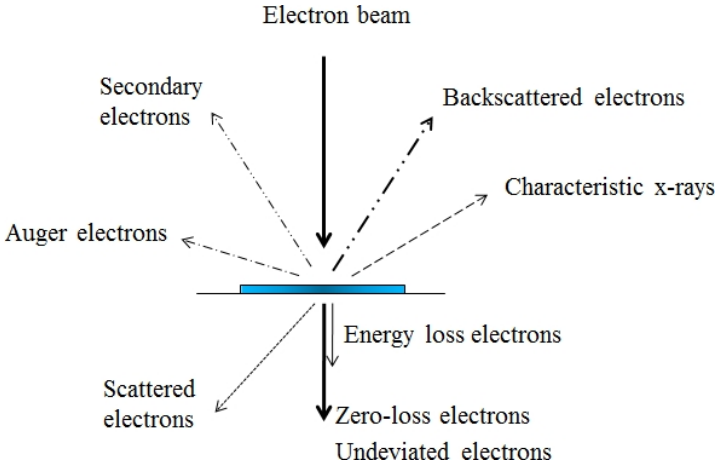

Figure 4: Interaction of the electron beam with the sample surface. Different types of interactions occur.

Electron interaction

The electrons, traversing through the specimen, interact with the sample in elastic (undeviated electrons as well as backscattered electrons and zero-loss electrons) and inelastic collisions (generating characteristic x-rays, secondary electrons, auger electrons, energy loss electrons). The different types of interactions are sketched in Figure 4.

Characteristic x-rays: Incoming energetic particles, in this case electrons, remove electrons from inner shell orbitals in the specimen atoms, leaving a vacancy in this lower atomic state. Characteristic x-rays are created by transitions of electrons from a higher to the energetically favorable, lower, vacant state within the atom. The difference in energy between these two states is characteristic for each element and released in form of a photon. A more detailed description of this process is given in the DualBeam chapter.

Secondary electrons (SE): Secondary electrons are created by ionizing an atom with a primary energetic particle. A part of the primary particle's energy is transferred to the secondary electron. This secondary electron is then emitted from the atom. Several types of secondary electrons exist such as photo electrons (if the incoming particle is a photon) and auger electrons. For auger electrons the atom is ionized by an incoming energetic particle

creating a vacancy in a lower state. This vacancy is filled with an electron from a higher state. The difference in energy between the two states is transfered to a third electron (auger electron) which is then emitted from the atom. Auger electrons often occur for lighter elements.

Backscattered electrons (BSE): Backscattered electrons are electrons that are scattered back towards the incident specimen surface. Two types of backscattered electrons exist; elastically and inelastically BSE.

Energy loss electrons: Electrons loosing energy in interactions with the sample are referred to as inelastically scattered electrons. The energy loss is equivalent to the difference in energy between two states[12] involved in the interaction process.

[12] The states can be either atomic states or conduction band states for plasmon excitation.

Zero-loss electrons: Two types of zero-loss electrons exist. Electrons that are transmitted through the sample without interaction are the first type of zero loss electrons referred to as undeviated electrons. These can be observed for thin samples. A second class of zero-loss electrons are elastically scattered electrons. Elastically scattered electrons interact with the specimen atoms' nuclei and pass through the sample without loosing energy. This can either lead to electrons that pass through the sample at an angle towards their initial incident path or on the same path if scattered several times.

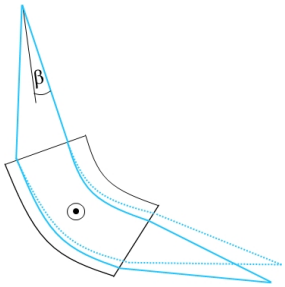

Figure 5: Basic setup of an EELS detector. The detector which is mounted below the projector lenses in the TEM, separates the electrons according to their energies.

Operation modes

In this work a Philips CM100 with an acceleration voltage $U = 80\,\mathrm{kV}$ was used. The TEM is equipped with a tungsten needle. For a more detailed structural analysis a FEI TECNAI F20 High Resolution Transmission Electron Microscope (HRTEM) with an acceleration voltage $U = 200\,\mathrm{kV}$ was used.

The TECNAI F20 is equipped with a FEG and a Gatan GIF Tridem Spectrometer EELS detector which allows single nanoparticle composition measurements. The EELS spectrometer which is mounted after the projector lenses separates the electrons by their energies with a sector magnet. A schematic of the EELS detector is given in Figure 5.

The TEM allows different analytical modes to study the morphology, the microstructure as well as the chemical properties of the specimen. The different modes are given in Figure 6.

Bright field: In bright field imaging, the transmitted electrons are detected and create the image. The objective aperture is positioned in a way that only undiffracted electrons pass to form the image, see Figure 6 (a). In this mode, objects appear dark.

Dark field: In the dark field mode, displayed in Figure 6 (b), (c) only the electrons scattered in a particular direction are used for imaging. The primary beam is blocked[13]. The objects appear bright in this mode.

[13] This can be achieved by either tilting the primary beam (axial dark field) or moving the objective aperture (dirty dark field).

HRTEM: High resolution TEM visualizes columns of atoms within the specimen. For HRTEM imaging the diffracted beams are superimposed with the primary beam resulting in an interference pattern. Special crystal orientations and defocus conditions as well as image simulations for a quantitative analysis are required to obtain information about the atomic structure of the sample.

Electron Diffraction: Evaluations of the electron diffraction pattern give information about the lattice structure of the sample. All reflexes in the diffraction pattern fulfill Bragg's law

$$\mathrm{n}\lambda = 2\mathrm{d}_{\mathrm{hkl}} \sin\theta \tag{2}$$

with the electron wavelength λ, the interplanar spacing d_{hkl}, n as an integer and the angle between electron beam and lattice plane. Braggs law is sketched in Figure 8. For a cubic lattice the relation between the interplanar spacing d_{hkl} and the lattice constant a is given by:

$$d_{hkl} = \frac{a}{\sqrt{h^2 + k^2 + l^2}} \tag{3}$$

with h,k,l as the Miller indices. The interplanar spacing d_{hkl} can be calculated from the electron diffraction pattern by measuring the distance r between the diffraction spots in the image plane:

$$r \cdot d_{hkl} = \lambda L \tag{4}$$

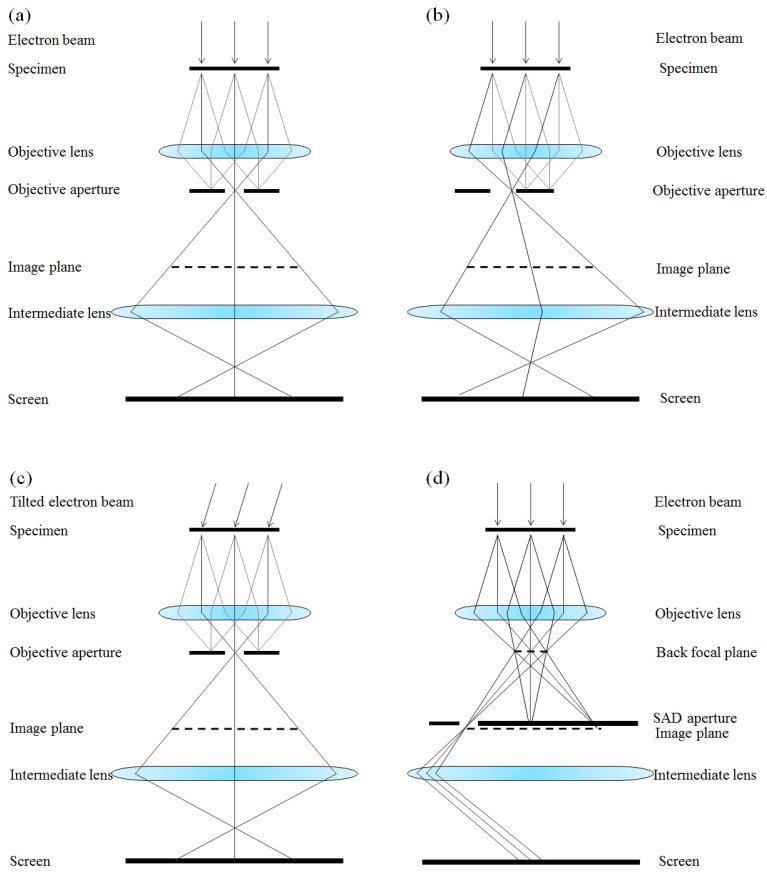

Figure 6: TEM modes, drawn in analogy to Fultz and Howe [41] (a) Bright field: Undeviated electrons are detected. (b) Dark field: In this dirty dark field mode, the diffracted electrons are detected. The objective aperture is positioned in such a way that the undeviated electrons are blocked and the deviated electrons can pass the aperture. (c) Dark field: In this axial dark field mode the primary beam is tilted and the objective aperture positioned as in bright field imaging. This way, deviated electrons (which are now parallel to the column) are detected. (d) SAD: The objective aperture is removed and the SAD aperture inserted in the image plane.

for small angles ($\sin\theta \approx \theta$). The wavelength λ of the electrons and the camera length L of the setup need to be determined prior.

Selected Area Diffraction (SAD): Diffraction patterns of selected areas (200 nm in diameter for the TECNAI F20), called selected area diffraction (SAD), can be obtained. The "selected area aperture", neccessary to limit the region which creates the diffraction pattern, is inserted and placed around the area of choice, as sketched in Figure 6 (d). For each diffraction reflex, the region within the selected area creating the reflex can be visualized by inserting the objective aperture and positioning it around the reflex. The electron beam needs to be tilted and a dark field image is obtained

after switching to imaging mode and removing the SA aperture. Areas producing the chosen reflex appear as bright regions in the dark field image.

Electron energy loss spectroscopy (EELS): EELS allows an element sensistive analysis of the specimen with a spatial resolution down to the atomic level [42]. In EELS measurements, the change in energy of the electrons after traversing the sample is measured. A difference between the initial electron energy and the traversed electron energy is caused by the interactions of the incident electrons with the specimen atoms. An EELS spectrum (see Figure 7) gives the interaction probability over the energy loss. The main features are a zero loss peak, a plasmon peak, a background and characteristic edges. The zero loss peak is caused by electrons that are practically not scattered while passing through the sample as well as elastically scattered electrons. Elastic scattering occurs when the incident electron interacts with the atomic nuclei. The mass of the electron is a lot smaller than that of the nuclear mass and thus the resulting energy exchange so minimal that it cannot be measured. Electrons that generate plasmon excitation only

Table 1: Theoretical energy values for characteristic edges of oxygen, iron and cobalt above 100 eV from "A chart of Inner Shell loss edge energies for EELS Gatan 1985".

Element	E / eV	Line
O	532	K
Fe	708	L_3
Fe	721	M_2
Co	779	L_3
Co	794	L_2

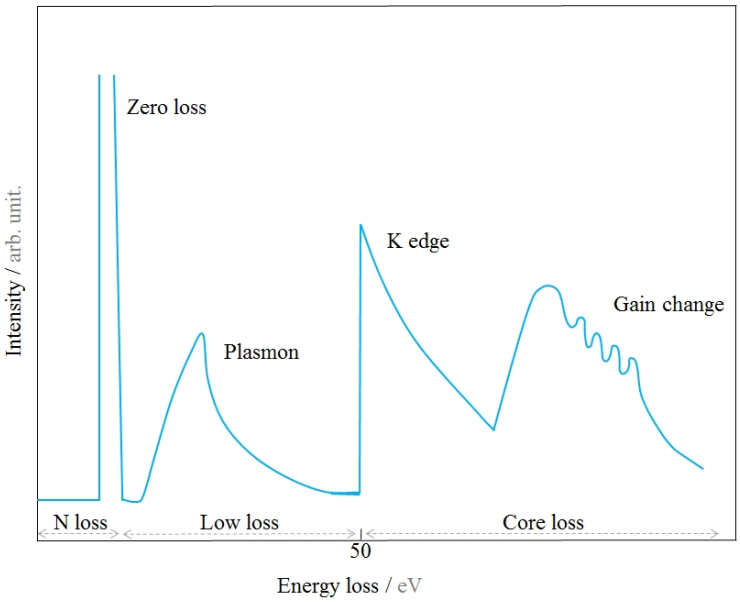

Figure 7: Illustration of a typical EELS spectrum, sketched in analogy to [43]. The EELS spectrum can be separated into a no energy loss region, a low energy loss region, and a core loss region. No energy loss occurs for either unscattered or elastically scattered electrons. A low energy loss occurs, among others for valence band electron interactions. The core loss occurs for electrons which interact with inner-shell electrons of the specimen. These core losses are used for the chemical analysis of the specimen.

loose a small amount of energy ($\approx 25\,\mathrm{eV}$). This loss is caused by interactions of electrons with electrons in the valence band. The energy losses above $\approx 50\,\mathrm{eV}$ are caused by interactions with inner atomic shells. The incident electrons and inner shell electrons are similar in mass and give rise to a measurable energy exchange (loss). The incident electrons ionize the specimen atoms by interacting with core electrons[14]. The ionization energy is element specific and thus the recorded energy loss of the traversed electrons allows an elemental analysis of a sample. Theoretical energy values for oxygen, iron and cobalt can be found in Table 1. Further information on transmission electron microscopy can be found in the following works: [38, 40, 41, 42, 43, 44].

[14] The characteristic x-rays produced in this process are used in EDX analysis.

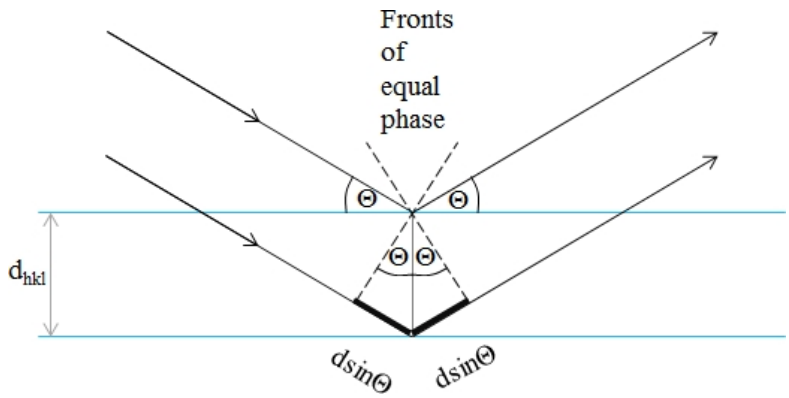

Figure 8: Illustration of Braggs law. The incident beam scatters of two different, parallel lattice planes (blue lines). The distance between the lattice planes is given as d_{hkl}. The lower beam path is increased by $2d_{hkl}\sin\theta$ which is indicated by the black lines, leading to constructive/destructive interference with the upper beam. θ represents the angle between the incident beam and the lattice plane.

The DualBeam device

DuaBeam systems such as the FEI Helios Nanolab 600i, used in this work, allow the characterization and modification of samples on the nanoscale within a single device. The basic components of such a system are an electron beam column, an ion beam column, a gas injection system (GIS), a tiltable stage, a manipulator (omniprobe) as well as several detectors. A schematic of the setup is given in Figure 9. An EDX system by Edax is included in this device to allow elemental analysis of the specimen. The electron beam is used for structural analysis of the specimen. The ion beam is mostly used for structuring but it can also be used for surface analysis. The drawback of the ion beam characterization method is the destruction of the sample surface due to the high-mass ions. A comparison of electrons and ions is given in Table 2. The GIS allows for the deposition of different materials, such as platinum, onto the sample. The sample can be positioned at different angles to the ion beam and electron beam by a tiltable stage in accordance with the application requirements. The omniprobe is used to remove sample sections and to move them to a desired spot.

Property	Electron	Ion
Charge	-1	+1
Size	0.000 01 nm	0.2 nm
Mass	9.1×10^{-31} kg	1.2×10^{-25} kg
Velocity (30 kV)	$10^{8}\,\mathrm{m \cdot s^{-1}}$	$2.8 \times 10^{5}\,\mathrm{m \cdot s^{-1}}$
Momentum (30 kV)	$9.1 \times 10^{-23}\,\mathrm{kg \cdot m \cdot s^{-1}}$	$3.4 \times 10^{-20}\,\mathrm{kg \cdot m \cdot s^{-1}}$
Penetration depth (in iron at 30 kV)	1800 nm	20 nm

Table 2: Comparison of ion and electron properties. A more detailed quantitative comparison of the particles is given in Yao's work [45].

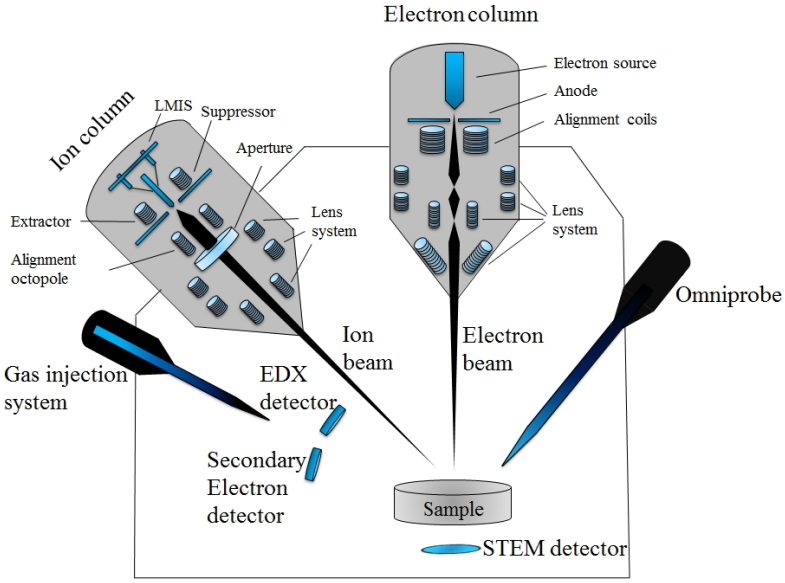

Figure 9: Schematic of a DualBeam device, showing the main components. The device consists of an electron column as well as an ion column, different detectors, a gas injection system, an omniprobe and a tiltable sample stage.

Electron Beam Column

The electron beam column consists of a Field Emission Gun (FEG), electrostatic as well as electromagnetic lenses and apertures. A schematic of the electron beam column is given in Figure 9.

Field emission gun (FEG): The main components of a FEG are a tungsten needle and a pair of anodes. A typical FEG setup is displayed in Figure 10. A voltage applied to the anodes creates a potential which allows electrons to be extracted from the tungsten needle by lowering its potential barrier. FEGs can only be operated in an ultra high vacuum, in contrast to other electron guns. However, their high current density and small energy spread gives them a superior quality. A more detailed description of FEGs can be found in Williams' and Carter's work [38, 45].

Electron beam optics: The accelerated electrons, emitted from the FEG, are focussed using a lenssystem and several apertures. Magnetic lenses are most commonly used to focus fast, low mass

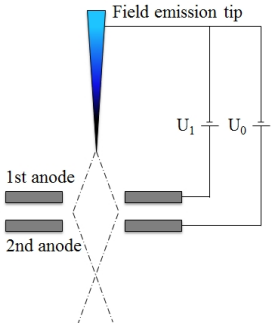

Figure 10: Illustration of a field emission gun, drawn in analogy to Yao's work[45].

particles since magnetic fields are easily produced. The magnetic fields acting on the electrons are created by washer shaped coils[15]. The Lorentz force acting on the electrons passing through the electron column is given by:

[15] The field strength is regulated by the currents through the coils.

$$\vec{F} = -e(\vec{v} \times \vec{B}) \tag{5}$$

with e as the elementary charge, $\vec{v}$ as the electron's velocity and $\vec{B}$ as the magnetic field. This force focuses the electrons. A lens system at the end of the column moves the electron beam across the sample for sample imaging. Further reading on electron beam optics can be found in Yao's work [45].

Electron interaction: Two classes of interaction processes at the surface of the sample exist, the elastic collision and the inelastic collision. The elastic collision causes surface sputtering, displacement of lattice atoms and formation of defects while the inelastic collision produces secondary electrons, x-rays, and optical photon emission by transferring some of the electron's energy. A more detailed description of the interactions is given in the TEM chapter.

Ion Beam Column

The basic parts of an ion beam column, see Figure 9, are a liquid metal ion source (LMIS), from which ions are extracted, and ion beam optics which focus the ions and move them across the specimen by electrostatic fields.

Liquid metal ion source (LMIS): A LMIS[16] is a point source which consists of a tungsten needle, a liquid metal reservoir as well as an extraction electrode at a negative potential ($U = (-5\,\mathrm{kV}) - (-15\,\mathrm{kV})$). The setup of a LMIS is sketched in Figure 11. Gallium, most commonly used in LMIS, is heated to the melting point[17] and flows towards the tip of the tungsten needle. The extractor pulls the liquid metal into a conical shape with a cusp at its end, referred to as Taylor cone. A balance of the electrostatic force and surface tension force is created at this point [45]:

[16] LMIS are usually operated in a modest vacuum of $1,33 \times 10^{-5} - 1,33 \times 10^{-7}$ mbar.

[17] The melting point of gallium is 29.8 °C.

$$\frac{1}{2}\epsilon_0 E^2 = \frac{2\gamma}{r} + p \tag{6}$$

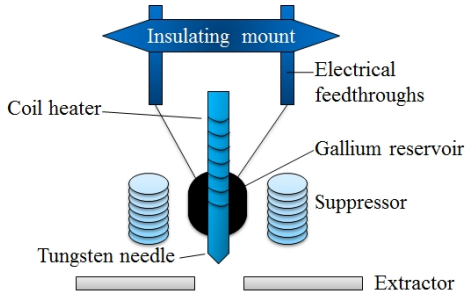

Figure 11: Typical setup of a Liquid Metal Ion Source. The coil heater is used to heat gallium to its melting point which then flows to the tip of the tungsten needle. The liquid metal forms a cone and ions are emitted from the cusp of the cone which form the ion beam. The schematic was drawn in analogy to Yao's work [45].

with ϵ_0 as the permittivity of the vacuum, E as the electrostatic field, γ as the surface tension, r as the principal radius of the cone, and p as the modification that explains the cusp at the end of the cone. The ion beam is created once the quilibrium requirements for the static taylor cone is violated (field stress $\gg$ surface tension). Ions are extracted from the electrode by a complex process involving field evaporation and field ionization of metal atoms in the vapor state. In the field evaporation process, the potential barrier preventing evaporation is lowered by the applied field E. This barrier can then be overcome by ionization of the evaporating gallium atoms. The energy required for the evaporation process can be described by

$$Q_E = Q_0 - \sqrt{n^3 \cdot e^3 \cdot E} \tag{7}$$

with Q_0 as the energy required to produce ions in free space and E as the applied field strength, lowering the potential barrier. A more detailed theoretical description is given in Yao's work [45].

A voltage ($\approx +2\,\mathrm{kV}$), applied to the suppressor, regulates the extracted current. This way the applied voltage to the extractor does not need to be altered, and thus a beamdrift can be avoided.

The lifetime of the source is proportional to the amount of material that is loaded onto the emitter substrate. Backsputtering of incompatible material as well as exposure to chemicals in the vacuum system can shorten the lifetime of the source. For high resolution performance, the source should be operated at a low current. The energy distribution broadens with increasing current [45] and temperature. Mutual repulsion of the ions leads to an increase in beam diameter and thus lowers structuring resolution.

Ion Beam Optics: The Lorentz force acting on the charged particles in magnetic lenses is directly dependent on the particle velocities. Since the velocity of the ions is much smaller than that of electrons (see Table 2), magnetic optics able to focus ions would be extremely large. Instead, electrostatic fields are used to focus ions onto a desired spot on the sample since the force acting on the ions is independent of the particle's velocity:

$$\vec{F} = -q \cdot \vec{E} \tag{8}$$

Ion interaction: Ions possess a smaller penetration depth than electrons (see Table 2) and are therefore more sensitive towards surface structures. In contrast to electrons, ions cause surface damage such as internal- and surface dislocation and rearrangements due to a momentum transfer, as well as sputtering. In addition, ion implantation occurs. The different processes are sketched in Figure 12. A more detailed description of sputtering and ion implantation can be found in Yao's work [45].

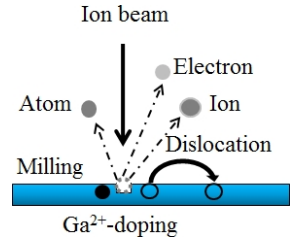

Figure 12: Interaction of ions with a sample. This illustration was drawn in accordance to Yao's work [45].

Electron Microscopy

Scanning electron microscopy (SEM) as well as scanning transmission electron microscopy (STEM) can be perfomed within the DualBeam device. In both methods the electron beam is scanned across the sample surface. Secondary electrons or backscattered electrons are detected in the SEM mode while transmitted electrons are detected in the STEM mode. Both methods are illustrated in Figure 13. An additional lens, the immersion lens, can be inserted into the beam path for both SEM and STEM imaging to allow high resolution imaging [18]. Different detection modes are available for STEM imaging. The different detector regions, which are operated in the different modes, are sketched in Figure 13.

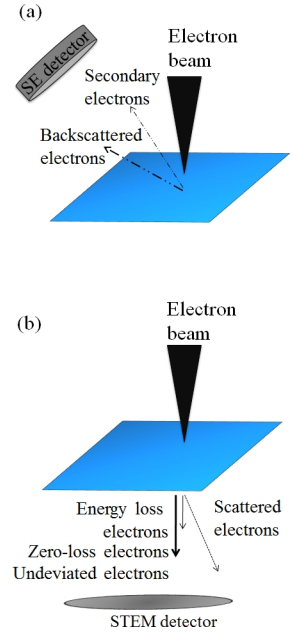

Figure 13: Illustration of the SEM (a) and STEM (b) imaging techniques.

[18] The immersion mode applies an extra magnetic field in-between the electron column and the sample to increase the resolution.

Bright Field (BF): Only undeviated electrons are detected in this mode. Areas in which electrons pass through the sample appear bright while areas in which electrons are scattered appear dark. A detailed description of bright field imaging is given in the TEM chapter.

Dark Field (DF): Scattered electrons are detected in this mode. Areas of the specimen where electrons are scattered appear bright. A detailed description of dark field imaging is given in the TEM chapter.

High Angle Annular Dark Field (HAADF): The HAADF mode offers a way to detect electrons that are scattered at high angles and allows Z-contrast imaging. HAADF is an element specific mode. Higher atomic numbers and thicker regions of the sample are represented in brighter regions in these images.

A special STEM sample holder is used for STEM imaging since the detector is inserted below the sample.

Energy Dispersive X-ray Spectroscopy (EDX)

EDX provides an elemental analysis of the specimen. In this method, characteristic X-rays produced by the interaction of high energetic particles (electrons) with the specimen are collected and their energy dispersion is evaluated. An EDX setup usually consists of a source of high energy radiation[19], a solid state detector and signal processing electronics.

[19] Electrons are used as high energy radiation in this device.

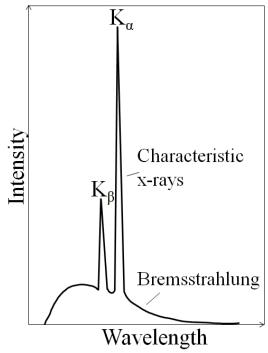

Figure 14: Illustration of a characteristic X-ray spectrum. The spectrum consists of Bremsstrahlung and characteristic X-rays. The latter are used for the elemental analysis in EDX.

High enery electrons ionize atoms in the sample leaving a vacant lower state. An outer shell electron with a higher energy fills the energetically more favorable vacancy in the inner shell. The difference in potential energy is released. A single ionization can lead to many emissions. Vacancies in lower states will be filled with electrons from outer shells. Thus, several transitions take place to return the atom to the energetically favored ground state. This process is sketched in Figure 15.

The EDX spectrum consists of a superposition of white X-rays (Bremsstrahlung) and peaks which are characteristic for a type and amount of each element in the sample. A typical EDX spectrum is given in Figure 14.

A spectrum is obtained by scanning a selected region and integrating the detected photon signal for all points. The optimal acceleration voltage U_0 and therefore the electron energy E_0 is

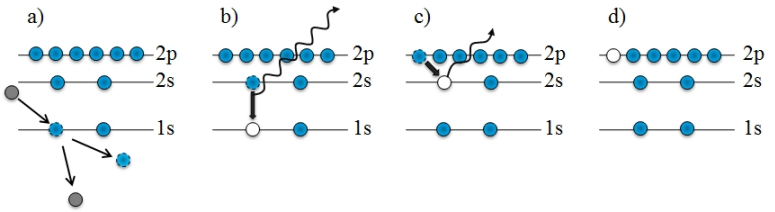

Figure 15: Illustration of the characteristic X-ray generation, used for EDX analysis. (a) Ionization of a sample atom: The incoming electron (blue) ionizes the atom and leaves a vacancy in a lower state (1s). (b) Electron transition from outer electron to the vacant lower state: An electron from a higher state (2s) fills the vacancy in the lower state (1s) which is energetically more favorable. The difference in energy between the states 2s and 1s is emitted in form of a photon. (c)-(d) Several further transitions from higher to lower states return the atom to the ground state. Photons, with energies corresponding to the differences in energy between the states, are released in the transitions.

dependent on the ionization energy of the elements and should be calculated prior to the measurement using

$$\frac{E_0}{E_c} \gg 2 \tag{9}$$

with E_c as the critical ionization energy of the elements. The ionization energies for different elements and the according acceleration voltage are given in Table 3.

For a successful measurement, the detector deadtime should be between 20 % – 40 %. This can be regulated by setting different amptimes. Elements in the spectrum can be identified automatically or manually in the progam EDAX Genesis. Peak identification can be checked using the HPD method in which a theoretical spectrum of the chosen peaks is superimposed onto the measurement. The background can be subtracted either automatically or manually. The program allows to manually add supporting points to the spectrum which are considered in the background subtraction. A quantitative EDX analysis goes beyond the scope of this work. Further information about quantitative EDX analysis can be found in Eggert's work [46]. EDAX Genesis provides a feature that can display elemental maps of the sample. Elements of choice are determined by measuring a spectrum of the sample prior to mapping. During
the mapping, a spectrum is recorded for each scanned point and the elements of interest are displayed for each scanned point afterwards. An overlay of the elements represents not only the regions within the sample where the element is present but also gives a first insight into the ratio of the different elements in specific regions. A longer dwelltime is chosen for mapping, in contrast to a spectrum measurement, to obtain a high enough photon count neccessary to

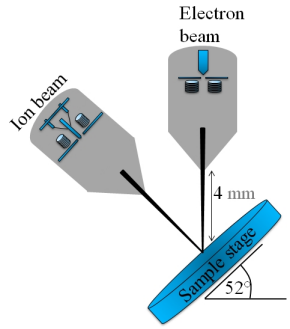

Figure 16: Geometry used for FIB structuring. The incident ion beam is perpendicular to the sample surface. The electron beam and ion beam are focussed onto the same spot which is called the point of coincidence which is located ad the eucentric height.

Table 3: Ionization energies of different elements[47] and the optimal acceleration voltage for the DualBeam device, calculated using Equation 9.

Element	E_C keV	U_0 kV
Ti	6.8	20
Fe	7.9	20
Co	7.9	20

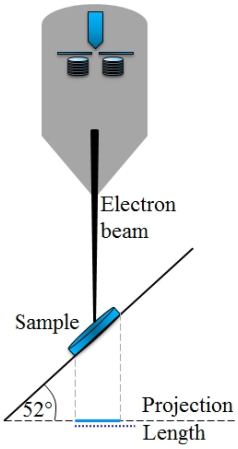

Figure 17: Projection length in comparison to the real sample length for a tilted stage position.

display the elements. During the measurements a charge of electrons can build up in the sample, creating a potential that deflects the beam while scanning the sample.

The drift control option provided by EDAX Genesis avoids this error. The area of choice is scanned with a lower magnification prior to the EDX measurement. Only a set fraction (most commonly 25%) of this scanned area is used in the measurement. The rest of the scan is used as the drift detection area for the drift control. The drift control periodically takes an electron image of the sample and compares it to the reference electron image. This allows the program to correct the mismatch caused by beam drift.

Structuring

Samples can be structured on the nanometer scale by either a milling process, where material is removed from the sample, or via deposition, where different materials are deposited onto the sample surface.

In a milling process energy and momentum are transferred from the ion beam to the surface atoms which are then removed from the surface. The ion beam remains in a spot for a specified time (dwelltime) before it moves to another spot where it remains for the set dwelltime. A beam overlap ensures the smooth milling of structures.

The FIB allows the deposition of different materials. Conductors, insulators and carbon based materials can be separately deposited onto a sample in an area of choice. In this process gaseous precursors are brought onto the sample surface with a fine capillary nozzle. The ion beam or electron beam is simultaneously used to decompose the gas molecules into volatile and nonvolatile products. The nonvolatile products remain on the surface as the deposited material. This process is sketched in Figure 18. Choosing the right aperture, and therefore current, is essential to deposit material and needs to be calculated for each pattern separately. A too high current leads to sputtering instead of deposition because the gas is consumed too quickly. An insufficient current leads to excessive gas flux and a small deposition rate. The ideal current density for deposition ranges from $6\,\mathrm{pA}\cdot\mu\mathrm{m}^{-2}$ to $10\,\mathrm{pA}\cdot\mu\mathrm{m}^{-2}$.

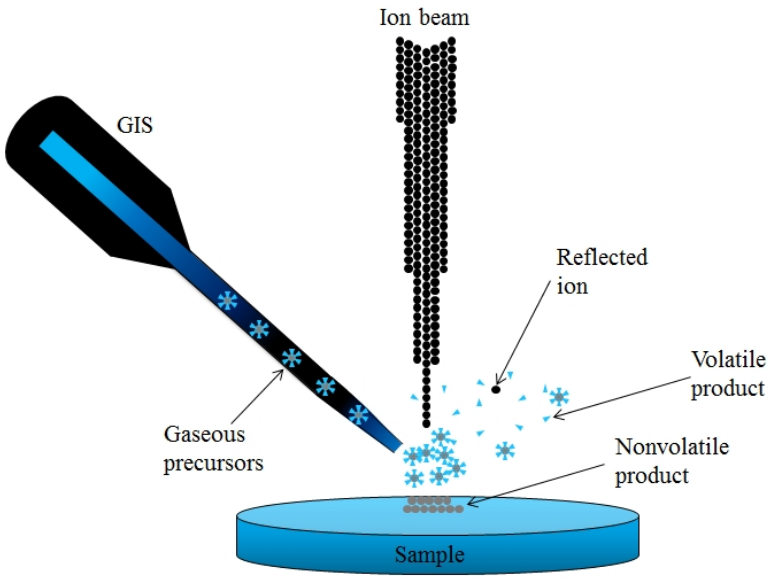

Figure 18: Schematic of a deposition process using the ion beam. Gaseous precursors are introduced onto the sample surface by the GIS. The ion beam decomposes the precursors into volatile products and nonvolatile products. The volatile products are removed by the vacuum pumps. The nonvolatile products remain on the sample surface as deposited material. This illustration was drawn in accordance to Yao's work [45].

Structuring processes are conducted with the stage tilted at 52° and in the point of coincidence at the eucentric height[20]. At this tilt the ion beam is perpendicular to the sample surface. The eucentric height is the height where the stage can be tilted with only a minimal lateral image movement. At the coincidence point the ion beam and electron beam are focused on the same spot. This is illustrated in Figure 16. When the electron beam is used for imaging during the structuring process, the tilt correction option needs to be applied to correct the mismatch in scale in y-direction in the SEM image caused by measuring the length in the projection instead of the actual length. This is illustrated in Figure 17.

The Helios Nanolab 600 is able to structure simple geometries, including lines, rectangles and circles, from which complex geometrical structures can be milled (and also deposited). In addition, the device can cut cross-sections, illustrated in Figure 19, which are used for lift-out processes.

[20] The ion beam and the electron beam are at an angle of 52° to each other.

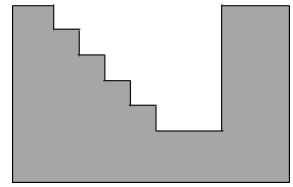

Figure 19: Illustration of a cross-section which is used for lift-out processes.

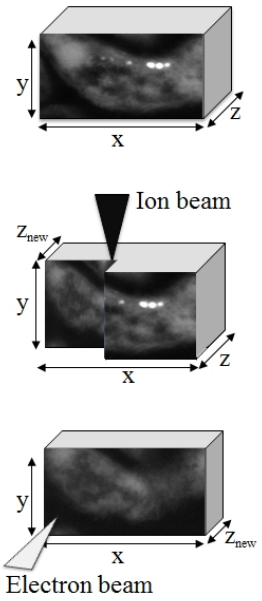

Figure 20: Principle of 3D tomography: The front face (x- y-direction) of the sample is imaged using the electron beam (grey triangle). The ion beam (black triangle) is then used to remove a thin slice (the slice thickness can be adjusted by the yshift parameter in the advanced milling options) of the sample which is represented by z and z_{new} with $z \gg z_{new}$. The new front face is imaged again using the electron beam. This process is repeated until the sample is completely sectioned.

[21] To achieve a higher surface sensitivity, low acceleration voltages between 3 kV to 5 kV are used for this technique.

[22] The stepsize in z is set by the y-pitch parameter in the advanced milling options for a cleaning cross section pattern.

3D Tomographie

The full range of DualBeam capabilities are required for 3D tomography in which a 3D image of a sample is obtained. In this *slice and view* technique the front face of the sample is imaged using the electron beam and then removed by the ion beam, exposing the next underlying layer which is then subsequently imaged using the electron beam. This process is illustrated in Figure 20. The sample stage is tilted to 52° so that the sample surface is perpendicular to the ion beam, to allow a precise straight cut of the sample. At this angle the front face of the sample can be simultaneously imaged with the electron beam. A tilt correction needs to be applied to obtain a correct sample height (see Section Structuring).

The image set of the different sample layers is then used to reconstruct a 3D image of the sample using the program Avizo 7. This technique therefore gives information of the 3D (internal structure) arrangement of the sample. The x-resolution and y-resolution of the 3D reconstruction are given by the electron beam (which is used to image the front layer of the sample). The z-resolution of the 3D tomogram is given by the ion beam (which defines the step size of the cut) and the electron beam surface sensitivity[21]. A low ion beam current and carefully chosen step size in z-direction are therefore neccessary for a succesful 3D tomogram. The step size in z-direction can be set in the advanced options of the cleaning cross section pattern (y-pitch parameter). Several image slides of a structure are required for a useful 3D reconstruction. The sectioning stepsize (in z-direction) therefore needs to be adjusted to the sample. A larger stepsize for larger and coarser samples is useful to allow a full sample sectioning within a reasonable timeframe. A small stepsize is required for more delicate structures and smaller samples[22].

Sample conductivity is of great importance for 3D tomography. In a non-conductive sample the beam charges build up, leading to a deflection of the beam and thus preventing a precise sectioning and imaging. Non-conductive samples can be coated with a gold layer through which the charges can flow and thus the problem can be circumvented. Further information on 3D tomography is given in Akemeier's and Midgley's work [3, 48].

The Fluorescence Correlation Spectrometer (FCS)

FCS, developed in the 1970s by Magde *et al.* [49], can be used to determine diffusion coefficients, association constants, concentrations, as well as the molecule or particle sizes. In FCS, time dependent intensity fluctuations are studied. These intensity fluctuations are caused by particles labelled with a fluorescent dye that diffuse through a small excitation volume, typically 1 fL, which is created by a focused laser and a confocal aperture. The fluorescent dye, attached to the particle, is excited within the excitation volume and emits photons which are then detected. The excitation and emission processes are illustrated in the Jablonski diagram, shown in Figure 21. The excited state has a specific lifetime of a few nanoseconds. The time between 2 photons emitted from the same molecule, diffusing through the excitation volume, is hence correlated. A photon burst of uncorrelated processes form the background noise.

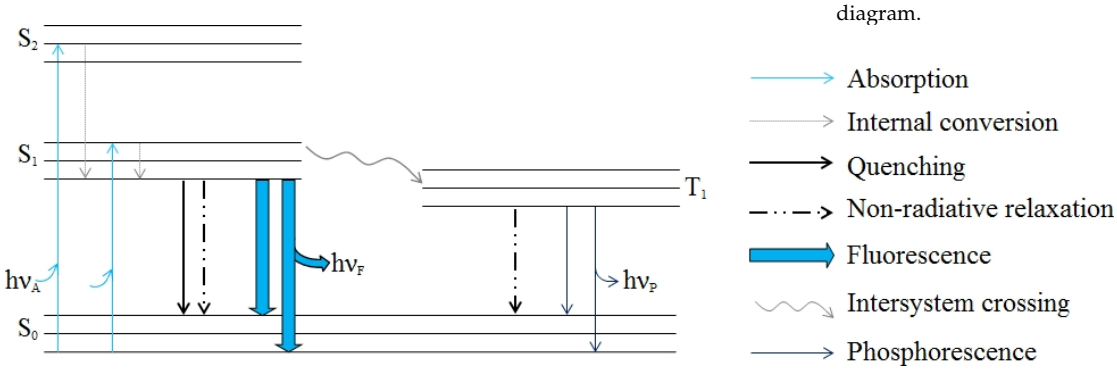

Figure 21: The Jablonski diagram is sketched in analogy to [50]. It illustrates the absorption and emission processes. Here the singlet ground state S_0 as well as the first S_1 and second S_2 singlet electronic states with the vibrational levels are sketched. These states are split into vibrational levels. T_1 represents an excited triplet state which is also split into the vibrational levels. The different types of excitation, energy transfer and emission are given in the right part of the diagram.

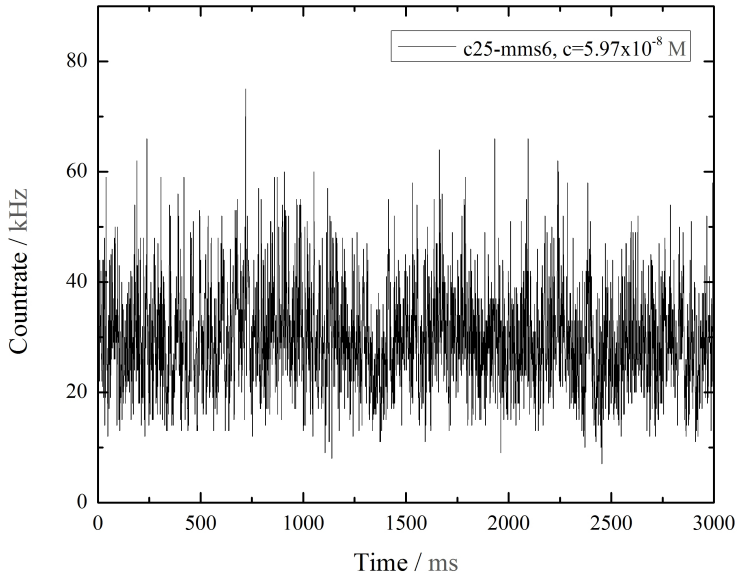

Figure 22: Countrate detected in the measurements. The count rate of c25-mms6 with the concentration $c = 5.97 \times 10^{-8}$ M is displayed here.

A typical photon count rate is displayed in Figure 22. This measured fluorescence signal is checked for self-similarity which increases for correlated photons. The best measurement performance is obtained for a nanomolar concentration of fluorophores in the detection volume. A higher concentration of molecules within the detection volume results in too many excited molecules from which the emitted photons cannot be differentiated.

A typical FCS setup is sketched in Figure 23. A frequency doubled Nd:Yag laser with a wavelength $\lambda = 532$ nm was used in this work to create the excitation volume. The intensity of the laser can be reduced using the intensity control wheel. The molecules in the excitation volume emit photons, redshifted[23] in comparison to the excitation signal, which can pass the dicroidic mirror. The signal is then focused and filtered. The pinhole along the beam path blocks the stray light from unfocussed planes, leading to an increased resolution along the optical axis. The filtersystem filters the remaining laserlight. The remaining signal is split into two beams and detected by two avalanche photo diodes (APDs). This way, the limitation of the deadtime of the detectors, typically 35 ns[24], can be overcome. A cross correlation is done since two detectors

[23] This effect, where the emitted photons are less energetic than the incident photons and thus have larger wavelengths is referred to as Stokes shift.

[24] The lifetime of fluorescent signals is typically a few nanoseconds only.

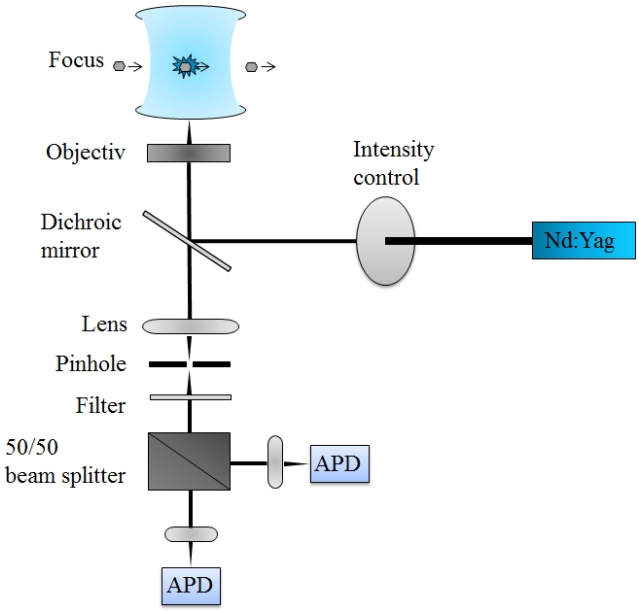

Figure 23: FCS setup. A frequency doubled Nd:Yag laser creates an excitation volume through which molecules diffuse. The molecules are labelled with a fluorescent dye which is excited by the laser and emits a photon. The photon passes an optical system and is detected by one of two APDs. The dye of the molecule is excited several times while travelling through the excitation volume.

are used and two time dependent signals are independently recorded. The detected time dependent signal of both detectors is then correlated leading to a higher accuracy due to a reduction of detector specific artefacts.

Diffusion coefficients and particle sizes can be obtained from the correlated fluorescent signal for a known focal radius[25]. The focal radius is different for each setup and needs to be identified if the size of the diffusing molecules and the diffusion coefficient is to be calculated from the data. The focal radius of this setup was determined to $\omega_0 = 568.4\,\text{nm}$ by measuring the diffusion time of the fluorescent dye Atto565[26] with a known diffusion constant of $D_{Atto565} = 2.59 \times 10^{-6}\,\text{cm}^2 \cdot \text{s}^{-1}$ [51] and a measured diffusion time of $\tau_{\text{D,Atto565}} = 311.8\,\mu\text{s}$ by [52]:

$$D_{Atto565} = \frac{\omega_0^2}{4\tau_{Atto565}} \,. \tag{10}$$

FCS measurements also allow binding studies, for exampe between peptides and nanoparticles, from which the association constant can be determined. This constant describes the situation

[25] This focal radius is different for each setup and needs to be determined for each setup separately.

[26] Atto 565 was purchased from Attotec, Siegen, Germany.

where 50 % of all possible binding sites are occupied:

$$K_D = \frac{[Nanoparticle] * [Peptide]}{[Nanoparticle - Peptide - complex]} \tag{11}$$

with the nanoparticle, peptide, and nanoparticle-peptide concentrations. Peptides binding onto nanoparticles lead to an increase in the hydrodynamic radius, see Figure 24, and therefore an increase in diffusion time. A sharp increase in diffusion time for a sufficient peptide concentration occurs. This change saturates once more than 50 % of all possible binding sites are occupied. The hydrodynamic radius and thus the diffusion time remain constant once the nanoparticle is fully saturated by peptides. The association constant can be obtained by plotting the concentration versus the diffusion time and fitting the data with a sigmoidal function such as the Hill function [52]:

$$\tau_D = \tau_0 + \frac{(\tau_1 - \tau_0) \cdot c^n}{K_D^n + c^n} \tag{12}$$

where τ_0 is the initial diffusion time, τ_1 the final diffusion time, c^n the concentration of peptides and K_D^n the association constant. Further information on this technique can be found in these works: [50, 53].

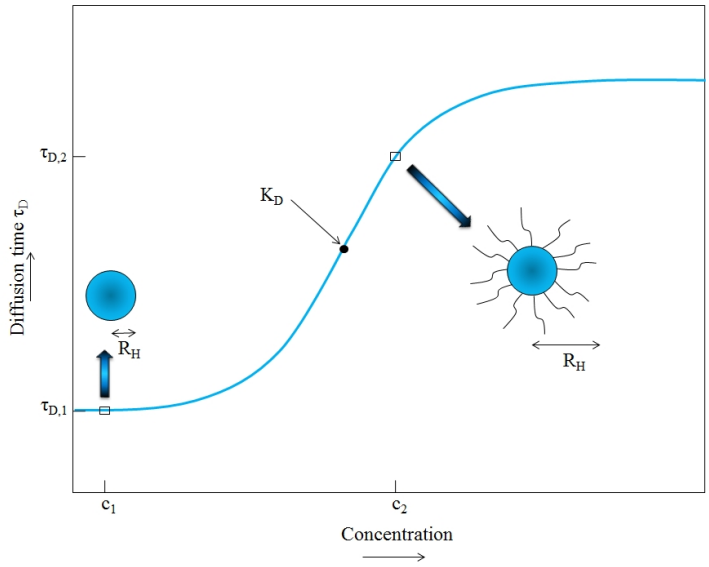

Figure 24: This sketch illustrates the change in diffusion time with increase in peptide concentration. The increase in diffusion time is caused by an increase in the hydrodynamic radius of the peptide-nanoparticle complex. The association constant gives the peptide concentration at which 50 % of the binding sites are occupied.

The X-Ray Diffractometer

"We have new means of investigating the structure of crystals. Instead of guessing the internal arrangement of the atoms from the outward form assumed by the crystal, we find ourselves able to measure the actual distance from atom to atom." -Bragg [54]

Bragg's[27] and Laue's[28] early and important contributions concerning diffraction of X-rays of crystals not only verified that crystals are built of periodically arranged atoms but also lead to the development of new spectroscopic methods. Since then X-Ray Diffractometry (XRD) has developed into a common tool to study the internal structure and atomic arrangement within crystalline materials. The advances in computing power today allow the evaluation of powder patterns, as sketched in Figure 25, which has since evolved to be one of the most important methods to identify materials and characterize their intrinsic structure.

The crystal structure can be derrived from the spectrum using the diffraction angle and intensities as well as the peak shape. This

[27] Sir William Henry Bragg and William Lawrence Bragg were awarded the Nobel Prize in Physics 1915 "for their services in the analysis of crystal structure by means of X-rays"[2]

[28] Max von Laue was awarded the Nobel Prize in Physics 1914 for his discovery of the diffraction of X-rays by crystals"[2].

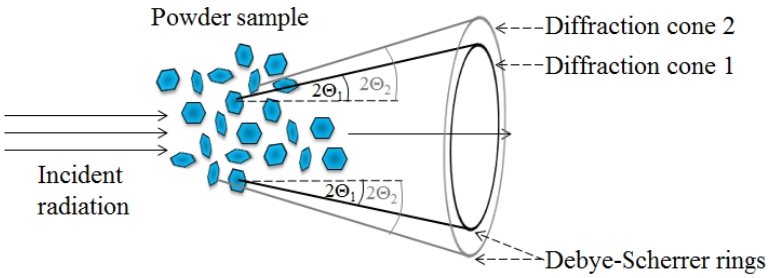

Figure 25: Illustration of a XRD powder sample, sketched in analogy to [55]. The radom orientation of the crystallites leads to diffraction cones instead of specific reflexes obtained for single crystals.

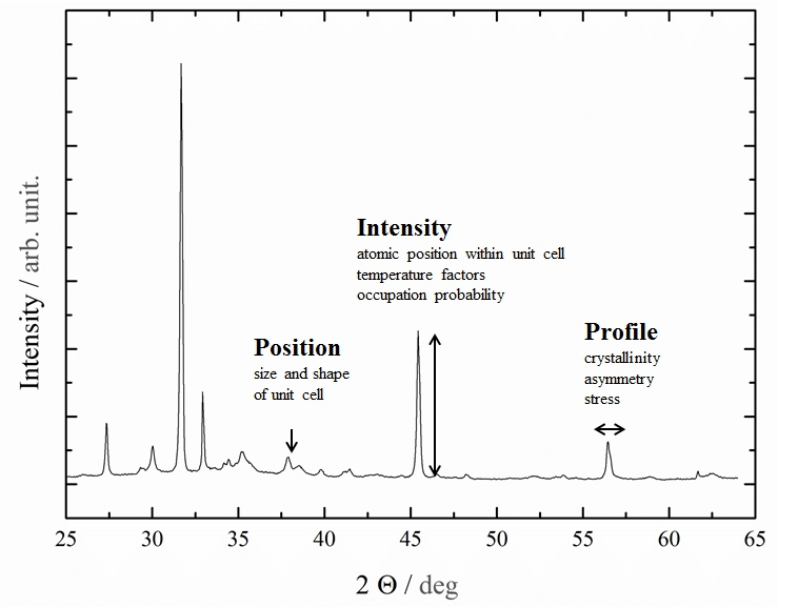

Figure 26: XRD pattern of biosynthesized cobalt ferrite nanoparticles after 28 days. The size and shape of the unit cell can be derived from the peak position. The peak intensity gives information about the atomic position within the unit cell. The peak profile is influenced by the crystallinity as well as stress within the solid structure.

is illustrated in the powder spectrum given in Figure 26. According to Bragg's law the diffraction angle depends on the wavelength λ, used in the experiments as well as the unit cell size. The size and symmetry of the unit cell can be calculated with the interplanar spacing d_{hkl} after the peakes are indexed.

$$n\lambda = 2d_{hkl} \sin\theta,\ n \in \mathrm{N}\,. \tag{13}$$

Bragg's law and the relation between the interplanar spacing and the lattice constant for a cubic crystal symmetry are given in the TEM section. The peak intensity depends on the atom type and arrangement within the unit cell. The 3D atomic structure of the crystal can be obtained from the intensity. The peak shape depends on the crystallite size as well as the crystallinity of the sample and stress.

Several systematic deviations from an ideal spectrum can occur which are most commonly caused by preferred orientation, size and strain effects.

Preferred orientation: Preferred orientation occurs when the crystallites are not statistically oriented. Common examples are

disc-like nanoparticles that preferentially lie flat on the wafer surface. The preferred orientation influences the reflex intensities, leading to an overproportional intensity for specific peaks. Thus, the intensities are unreliable, making it difficult to obtain information about the atomic arrangement within the unit cell.

Strain and size effects: The peak shape as well as the peak position can deviate due to strains within the crystal. A crystal with an increased lattice constant leads to a shift in peak position towards smaller angles if the strain is equivalent in all directions. In polycrystalline materials strains can effect the crystallites differently: some crystallites have an increased lattice parameter while other crystallites display a reduced lattice parameter. These deviations lead to either symmetric or asymmetric peak broadening, both of which can be observed in the XRD spectrum in Figure 26 at $2\theta = 32°$ (symmetric) and at $2\theta = 36°$ (asymmetric). The crystallinity of the sample determines the reflex profile. Poor crystallinity leads to peak broadening. The given XRD spectrum shows that solids of different crystallinity are present in the sample thereby leading to different peak shapes.

For a single or a limited amount of substances present in the sample, the XRD spectrum can be compared to literature spectra using several databases, such as the Inorganic Crystal Structure Database (ICSD), to determine the phase. If several substances or phases are present, their peaks overlap which makes it difficult to identify the substances. Further information on XRD can be found in the following works: [56, 57, 58, 59, 60, 61, 62].

In this work, a Philips X'Pert Pro MPD equipped with a CuK_α

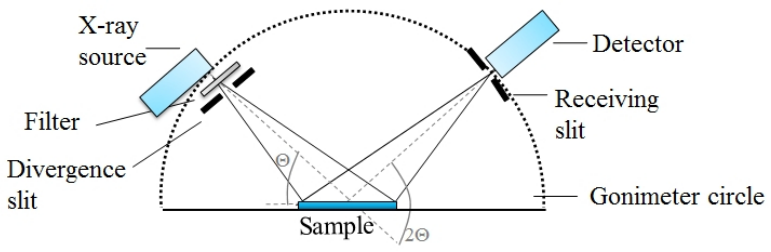

Figure 27: Illustration of the Bragg Brentano setup, drawn in analogy to [63]. X-rays from the anode are diffracted by the powder sample. The detector moves along the gonimeter circle and detects the diffracted X-rays dependending on the diffraction angle.

radiation source of a wavelength $\lambda = 1.5418\,\text{Å}$ is used. The Bragg-Brentano setup is sketched in Figure 27. The X-rays produced in the X-ray source are diffracted by the powder sample. A detector counts the diffracted X-rays against the diffraction angle. Both the X-ray source and the detector move along the gonimeter circle during the measurement. The staytimes and the stepsize between the measurement positions of the detector are set prior to the measurement.

DC Magnetron Sputtering

In a sputtering process the surface of a solid target is removed by high energetic particles (nobel gas ions) and deposited as a coating layer onto a desired substrate.

Electrons are accelerated in an externally applied potential. They gain enough energy to ionize the nobel gas atoms which are introduced into the sputter chamber thereby creating a plasma. The nobel gas ions are accelerated towards the target, which lies at a negative potential, and remove the target material which is then deposited onto the substrate located above the target.

In the magnetron sputtering process, a permanent magnet behind the target controls the motion of the electrons. The magnetic field confines the electrons[29] to a circular path at the surface of the target disk due to Lorentz force:

$$\vec{F} = -e(\vec{E} + \vec{v} \times \vec{B}) \tag{14}$$

[29] The deflection of the high mass ions by the magnetic field can be neglected.

with e as the elementary charge, $\vec{E}$ as the electric field, $\vec{v}$ as the particle velocity, and $\vec{B}$ as the magnetic field. This results in an extended path, creating a greater nobel gas ionization rate. The increased ionization rate leads to a greater sputter rate close to the spiral path.

Two sputter machines were used in this work: a home-built sputtering device, referred to as HBSD, in which tantalum and gold are sputtered and a commercially available sputtering machine Leybold L560 in which titanium is sputtered. Argon is used as a nobel gas in both devices. The home-built machine is described in more detail only since both machines work similarly. A detailed description of the commercially available device Leybold L560 is given in Hempel's PhD thesis [64].

"HBSD"-Setup

A schematic of this sputtering machine is displayed in Figure 28. The HBSD is separated into a prechamber and a main chamber where the sputtering takes place. The sample is inserted into the prechamber which is pumped using a prevacuum pump until a pressure of 0.3 Pa is reached. The sample is inserted into the main chamber using the transferbars and the manipulator afterwads. This way the vacuum in the main chamber is maintained while inserting the sample. Once the pressure in the main chamber has reached 3×10^{-5} Pa, the argon plasma can be started. The sputtering itself is done in a so called windy vacuum due (0.3 Pa) to a constant flow of argon gas into the chamber. The sample is moved directly over the sputter source by pushing and rotating the transferbar 2. The sputter process starts instantaneously once the sample is moved directly over the sputter source.

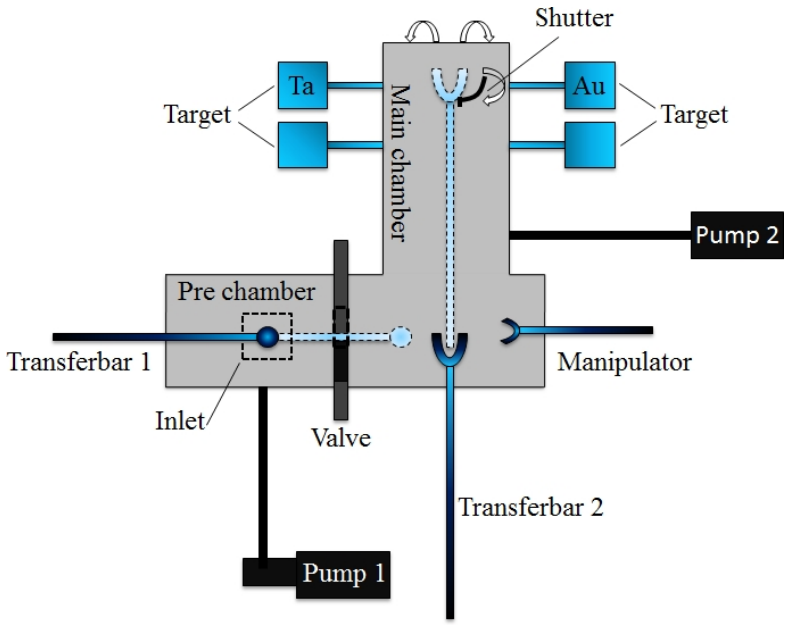

Figure 28: Setup of the HBSD. Samples are inserted into a prechamber, which is pumped prior to inserting the specimen into the main chamber to prevent a loss of vacuum. The sputtering process is started and the sample is moved directly over the target.

Part II

Biomimetic nanoparticlesynthesis

Motivation

Nanotechnology has led to dramatic advances in the biomedical sector and the magnetic recording industry, and it continues to generate novel applications in a variety of fields today [12, 13, 26, 65, 66, 67, 68, 69]. One of the current scientific challenges lies within synthesizing complex systems and nanoparticles with specific physical properties from molecular to macroscopic scale for a variety of applications. In diagnostics, iron oxide nanoparticles are used to enhance the magnetic resonance imaging (MRI) contrast and could, in future, also be used to deliver drugs to specific regions within the body (drug delivery) [26, 65, 66]. Other applications include data storage, nanomotors, ferrofluids, magnetic inks, shock absorbers, or sensors [12, 13, 67, 68, 69].

A nanoparticle, the primary building block in nanotechnological applications, is defined as a particle with a size $d \ll 100\,\text{nm}$ in at least one dimension. Magnetic, electrical, and optical properties of bulk materials change at this scale due to an increasing ratio of surface to volume atoms[30] as well as quantum mechanical effects (f.e. the coulomb blockade) which occur at this lengthscale. In addition to the size effect, the physical properties of nanoparticles are also influenced by the particle morphology. For spherical nanoparticles all distances and directions are equivalent. Disc shaped nanoparticles, however, have different sizes in different directions and thus an additional source of anisotropy, called shape anisotropy, arises. This property is of great interest for the magnetic recording industry since anisotropic materials could allow further miniturization of data storage devices which is currently limited due to the superparamagnetic effect [70]. Since the physical properties depend on the morphology, microstructure, and composition of the

[30] The surface to volume ratio increases for a reduced particle radius R with $\frac{1}{R}$ for spherical nanoparticles.

particles, a high degree of control over those properties is essential if they are to be used for practical applications.

Nanoparticles can be created using either top-down methods[31] or bottom-up methods[32]. In conventional chemical bottom up syntheses, precursor molecules are used to synthesize nanoparticles. Different solvents, temperatures, and injection methods are used to tailor the nanoparticle properties. The drawback of these costly, conventional approaches is the lack of control over size, shape, and phase of the nanoparticles. These chemical syntheses are furthermore very sensitive to the synthesis conditions, hence reproducibility is a further issue.

[31] Nanoparticles are created from a bulk material through fragmentation. Common top-down methods include lithography and molecular beam epitaxy. Nanoparticle size and shape are difficult to control using this approach.

[32] Common bottom-up methods are reduction of metallic salts and decomposition of organometallic compounds in a solution.

Recent studies showed that biomineralized nanoparticles, occuring in natural systems such as magnetotactic bacteria (MTB) or migratory birds [71, 72], out-perform conventionally synthesized nanoparticles. Biological systems regulate the synthesis of biominerals under mild conditions and can control chemical and therefore physical properties of these nanosized crystals. Magnetotactic bacteria are a simple biological system which produces highly oriented magnetic nanoparticles. This system has been studied intensively to understand biomineralization processes [73, 74, 75]. Recent studies revealed that the protein MMS6 is involved in nanoparticle formation while several other proteins regulate the alignment within the magnetotactic bacteria [66, 74, 75, 76, 77, 78, 79, 80, 81, 82, 83].

The influence of proteins on inorganic crystal formation, as observed for MTB, has since lead to the development of biomimetic approaches for better controlled nanoparticle bottom-up syntheses [84, 85, 86, 87, 88, 89, 90, 91, 92, 93, 94, 95, 96, 97, 98, 99, 100, 101]. This approach is illustrated in Figure 29. These biomimetic approaches[33] aim to specifically tailor particle properties under mild conditions which cannot be achieved with conventional chemical bottom up syntheses under similar conditions [89, 90, 91, 92, 93, 95, 96, 97, 98, 100, 102, 103, 104, 105]. Today, different polypeptides are used in bioinspired syntheses to control microstructure, morphology and composition of nanoparticles [106]. The polypeptides, used in the biosyntheses, are material specific and can either be selected through combinatorial peptide libraries [106] or via biomimicking natural systems that produce inorganic crystals, such as magnetotactic bacteria [102]. The advantage of biomineralization

[33] Even though our technical instruments these days outperform nature in terms of speed and precision, natural systems are not only more flexible and adaptable but also more resistant to pertubations.

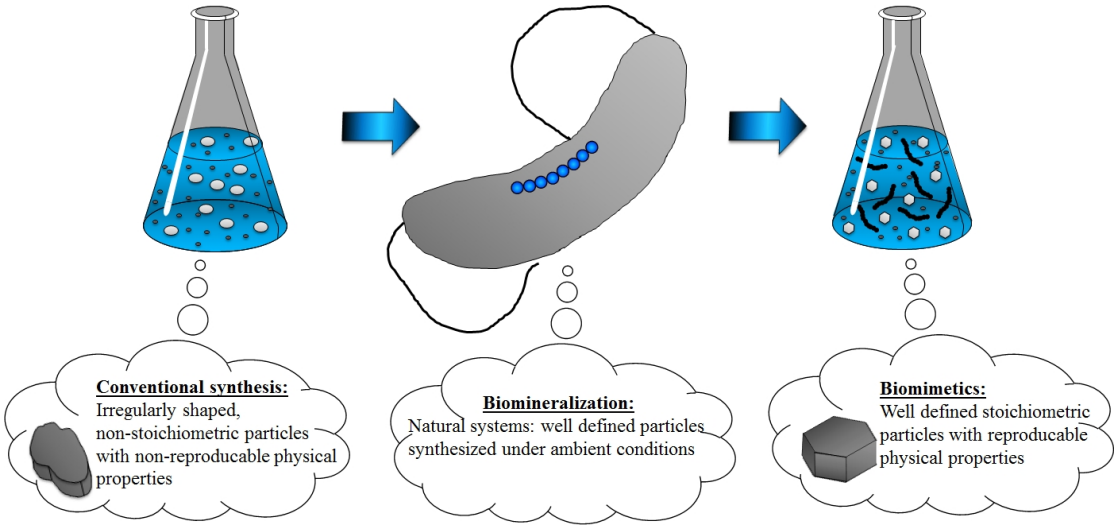

Figure 29: Representation of the basic idea behind this chapter. Nanoparticles with well defined physical properties which meet the demands for applications, cannot be synthesized by conventional chemical approaches. Mimicking the biomineralization process, occuring in magnetotactic bacteria, could allow to synthesize well defined nanoparticles in a reproducable manner.

over combinatorial peptide libraries is that only one peptide is required, which has previously been optimized by nature, instead of some 10^6 random peptide sequences from which the strongest binding peptide is selected [106]. However, the limited amount of inorganic compositions found within these natural systems was considered to be the drawback of biomineralization.

It was previously shown that biomimetic approaches can be used to synthesize inorganic crystals which do not occur in the natural systems [103, 107] and that the associated drawback with biomineralization can thus be overcome. Prozorov *et al.* used a polypeptide called c25-mms6 [107], a short synthetic version of the protein MMS6, found within magnetotactic bacteria to synthesize cobalt ferrite nanoparticles. Cobalt ferrite nanoparticles have attracted great interest in the biomedical and high density storage fields due to their unique properties such as high coercivity, chemical and physical stability, large magnetocrystalline anisotropy and moderate saturation magnetizations [9, 28, 108, 109, 110, 111]. Previous work [112] showed that c25-mms6 alters the morphology, microstructure, and composition of the cobalt ferrite nanoparticles and therefore the resulting physical properties. The engineering

process, however, remained elusive.

Since the influence of the polypeptide c25-mms6 on cobalt ferrite crystal growth is not yet understood, this work focusses on the interaction mechanism between the inorganic nanoparticles and the polypeptide, as well as on the effect of the c25-mms6 on cobalt ferrite nanoparticle formation, growth, and physical properties. The work aims to provide a better understanding of the underlying mechanisms in biomimetic approaches which are required if such approaches are to be succsesfully used in future.

This part is divided into 7 chapters. The theory neccessary to understand this work is discussed in chapter 1. Chapter 2 follows by looking at the natural system on which the biomimetic approach is based, using 3D tomography. This chapter is not neccesary to understand the nanoparticle synthesis, however, it was included for a more comprehensive work. The third chapter introduces the bioinspired synthesis. The fourth chapter deals with the peptide-inorganic crystal interaction occuring in the bioinspired synthesis and discusses the active center as well as possible function of the synthetic polypeptide. This chapter is discussed prior to the effect of c25-mms6 on nanoparticle growth to allow a complete crystal growth description (which includes the interaction) in the following chapter. Comparisons to the biosynthesis and a control experiment (nanoparticle synthesis without the polypeptide) are given where neccesary. The fifth chapter aims to describe the underlying nanoparticle growth process in the bioinspired synthesis and compares the results to a conventional chemical approach, which was conducted under equivalent conditions. The implications on the physical properties are discussed at the end of this chapter. The results are compared to those obtained in the initial study by Prozorov *et al.*[107]. Chapter six describes further initial studies of the bioinspired synthesis as well as the conventional approach with varried reaction parameters. In the first study, the synthetic polypeptide is added at a later stage of the nanoparticle growth and the obtained nanoparticles are analyzed and compared to a control experiment. A conventional synthesis at an increased temperature is carried out and the influence of temperature on particle formation is compared to the effect of the synthetic polypeptide in the bioinspired

approach. In a final study the influence of the starting composition is studied by changing the cobalt to iron ratio in the synthesis. Chapter seven and chapter eight give a summary and outlook.

Theory

This chapter provides the neccessary theoretical background for this work. The crystallographic description of cobalt ferrites (spinels) is followed by the description of classical and non-classical crystal formation theories, which are used to describe the nanoparticle formation. The biomineralization processes are discussed afterwards. The last part of this chapter gives an introduction into magnetism.

Spinels

The first written record of spinels dates back to the 16th century [113, 114]. Since then, spinels have been studied by many scientists due to their unique properties such as a high chemical and physical stability [9, 109, 111]. The crystallographic structure can be described by three sublattices: an anion sublattice, a tetrahedral cation sublattice and an octahedral cation sublattice. Spinels exist in a normal and inverse form. The unit cell of a normal spinel consists of eight $A^{2+}B_2^{3+}O_4^{2-}$ units. 56 atoms are included in this unit cell, 32 anions and 24 cations. 64 tetrahedral interstitial sites A (of which 8 are occupied by cations) and 32 octrahedral sites B (of which 16 are occupied by cations) exist in the unit cell.The normal spinel structure is based on an fcc packing of oxygen. It is a cubic densly packed structure of anions and cations, which occupy interstitial sites. In normal spinels, the A atoms occupy half of the available tetrahedral sites and the B atoms occupy half of the available octahedral sites [115]. In the inverse spinel structure, the cations A and B occupy octahedral sites while only B occupies tetrahedral sites. The inverse spinels can be described with the formula $B^{tet}(AB)_2^{oct}O_4$. Besides the normal and inverse structure, spinels can also display a mixed structure. These

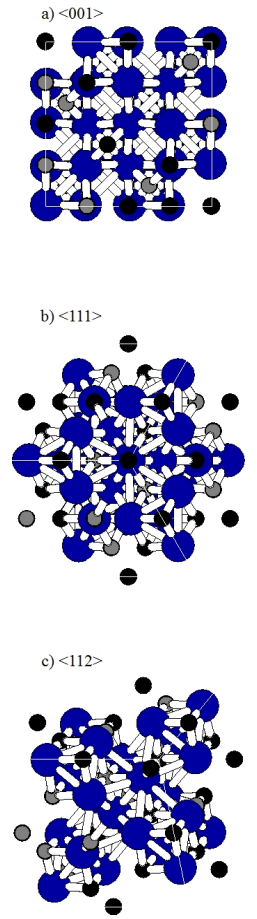

Figure 30: Co_2FeO_4 crystal structure simulated with the program FindIt. Oxygen is displayed in blue, cobalt in black and iron in grey. The crystal structure is given in different directions: (a) ⟨001⟩, (b) ⟨111⟩, (c) ⟨112⟩.

mixed spinels can be described by $(A_{1-x}B_x)_{tet}[A_xB_{2-x}]_{oct}O_4$ with x as the degree of inversion[34] [116].

[34] The space group $Fd\bar{3}m$ describes the majority of spinels.

Cobalt ferrites are one spinel type among the known 1000 types [117] which have been studied intensively for their potential use in magnetic recording applications and drug delivery systems, among many other possible applications [9, 28, 108, 109, 110, 111, 115, 118, 119, 120, 121, 122, 123, 124, 125, 126, 127, 128, 129, 130, 131, 132]. Here, cobalt and iron are the cations while oxygen is the anion. The most commonly described cobalt ferrite phase is $CoFe_2O_4$. However, a Co_2FeO_4 phase as well as several intermediate, non-stoichiometric phases such as $Co_{1.1}Fe_{1.9}O_4$ have been reported [133, 134]. The crystal structure along different directions for the Co_2FeO_4 phase, simulated using the program FindIt, is given in Figure 30.

More information on ferrites and spinel structures can be found in these works [135, 136, 137, 138].

Crystal formation

[35] In this work, crystal formation denotes the nucleation and growth process.

Crystal formation[35] has been studied throughout human history. Reports about applied crystal growth date back as early as 1500 BC, where salt and sugar crystallization was practiced [139]. A deeper understanding of this process only formed in the last decades of the 19th century with Gibb's phase equilibrium concept [139]. Today crystal formation is regarded as a process in which atoms or molecules organize into 3D oriented structures over time. It can be separated into two main categories:

Nucleation: Nucleation describes the process in which the initial nuclei form due to local non-equilibrium conditions. From these nuclei, the crystals grow.

Crystal growth: During this stage, the nuclei grow. Today, two theories try to explain crystal growth: the classical growth theory which has been used to explain crystal growth for the past century and the new oriented attachment theory. In the classical theory, growth occurs via atom by atom or monomer by monomer[36] adsorption as well as via Ostwald ripening[37]. For the past 100 years,

[36] A monomer represents the smallest building block from which the crystal is built.

[37] In this later stage of crystal growth smaller particles dissolve in favor of bigger particles.

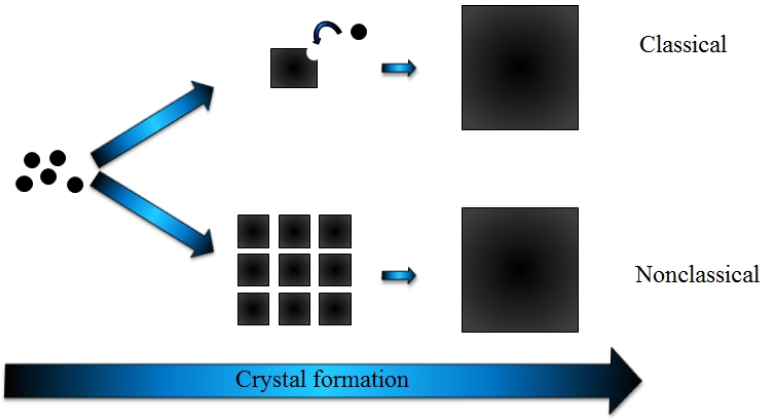

Figure 31: Classical vs. non-classical crystal formation processes. According to the classical theory, crystal growth occurs via epitactic monomer addition to the crystal. In the non-classical growth theory, crystal formation is a multistep process in which small intermediate structures form which aggregate into a mesocrystal, then fuse to form the secondary crystal.

crystal growth has been explained by classical growth theories. Lately, non-classical growth theories, such as oriented aggregation/attachment, have emerged, trying to explain experimental results that cannot be satisfactorily explained by the classical theory [140, 141, 142, 143, 144]. A sketch of both the classical process and the non-classical process is given in Figure 31.

Classical nucleation and crystal growth theory: LaMer Model

The classical nucleation theory was invented by Volmer, Weber, Becker, and Doring between 1926 and 1935 [145]. The theory assumes that crystal growth occurs via epitactic addition of monomers[38]. This idea is displayed in Figure 31. LaMer and Dinegar created the LaMer model in the 1950s which is based on the classical nucleation theory. The model is sketched in Figure 32. According to the LaMer-Model chemical reactions lead to the formation of monomers. The amount of monomers increases due to chemical reactions that release the monomers until a supersaturation is reached. The first nuclei, referred to as fluctuating nuclei, are formed in stage I. These initial nuclei are unstable and dissolve faster than free monomers can adsorb onto the flucuating nuclei surface. The kinetics are described by the length of the arrow. The rate of monomer adsorption onto

[38] Monomers are the the smallest building blocks of which a crystal is composed.

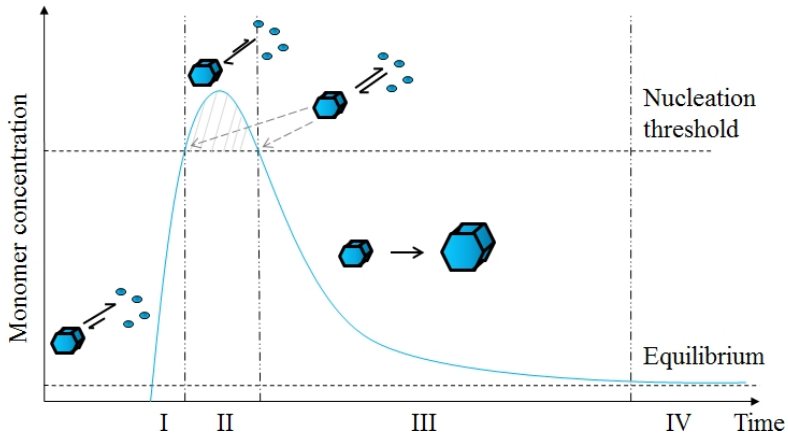

Figure 32: LaMer model. In stage I the monomer concentration increases until a supersaturation is reached. At the nucleation threshold, stable nuclei are formed. The rate for monomer adsorption and dissociation is equivalent at the threshold. In stage II stable nuclei are formed. The rate of adsorbing monomers is greater than that of dissolving nuclei. In stage III the nuclei start to grow through epitactic monomer adsorption. The amount of monomers decreases and the nucleation of new nuclei stops after the monomer concentration falls below the nucleation threshold. In Stage IV the monomer concentration has reached its equilibrium.

the flucuating nuclei is increased with the increase in monomer concentration, and reaches a threshold where the rate of adsorbing and desorbing monomers is equivalent. At this point (stage II), stable nuclei are formed. The amount of monomers now decreases because they were used to form the stable nuclei. The nucleation of nuclei stops once the saturation falls below the nucleation threshold (stage III). Growth of the nuclei to larger crystals occurs now through epitactic monomer adsorption until the supersaturation is diminished. In addition, a coarsening often occurs at the later stages of crystal growth in which larger particles grow at the expense of smaller particles. This growth mechanism occurs once the reactants in the solution in which the particles grow are depleted [141].

The LaMer model is based on four assumptions[145]:

Nuclei structure: The inner structure of the critical nuclei is equivalent to the inner structure of single crystals. The physical properties, including the entropy, are equivalent.

Surface: The nuclei are spheres with a well defined surface

$$A = 4 \cdot \pi \cdot r^2 \tag{15}$$

and the surface energy is homogeneous. Different crystallographic faces with different energy contributions are thus not incorporated into the model.

Nuclei formation: The nucleation rate remains constant and the chemical and physical conditions of the medium unchanged during the nucleation process.

Growth: Growth of the nuclei into crystals occurs via epitactic monomer addition and replication of the crystal unit cell.

Recent studies showed that the assumptions on which the LaMer model is based disagree with the experiments. In 1995 Frenkel and ten Wolde modelled the structure of crystal nuclei and the crystal nucleation barrier and found sequential nuclei formation in their computer simulations [145, 146]. The simulation result was experimentally verified by Ras *et al.* in 2011 [145, 147]. Further molecular dynamic simulations showed that attractive interaction between the nuclei are likely to lead to a growth process via aggregation, which is excluded in the LaMer model. Yau and Venkilo found that the nuclei surfaces are rather polyhedrons than spheres [145, 148]. Presently, a general description of crystal formation is being developed in which important classical concepts are incorporated, for example the important concept of free energy which remains valid according to Baumgartner *et al.* [149].

Gibbs free energy concept

For nucleation to occur, the dynamic equilibrium with the surrounding medium needs to be disturbed. In an equilibrium, the free energy is minimal. The neccessary disturbance can be created by a change in temperature, pressure, pH, or chemical potential, among others. The nucleation is a thermodynamically driven process. Equilibrium is described by the lowest state of Gibbs free energy G, defined as

$$G = H - TS \,. \tag{16}$$

The second law of thermodynamics states that a reaction can only take place for

$$\Delta G \ll 0 \,. \tag{17}$$

A supersaturation is required for the reaction. A more detailed description for this reason can be found in Ennen's work [37].

The Gibbs free energy can be used to describe the formation and growth of the nuclei. The volume energy which is given by

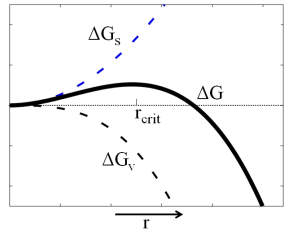

Figure 33: Total Gibbs free energy as well as the surface and volume contribution for spherical crystal formation. Nuclei with a size below the critical value are unstable and dissolve while larger nuclei with $r_{nuclei} \gg r_{crit}$ are stable and grow.

ΔG_V is decreased with the formation of small nuclei. However, an increase in surface energy arises due to the nuclei surface. The total Gibbs free energy is the superposition of the volume and the surface contributions:

$$\Delta G = -\Delta G_V \cdot V + \Delta G_S \cdot S \tag{18}$$

where ΔG_V is the Gibbs free energy for the volume, V is the volume of the nucleus, ΔG_S is the surface free energy, and S is the nucleus surface. The total Gibbs free energy as well as the two contributions are displayed in Figure 33. According to this diagram, nuclei with diameters below a critical threshold dissolve while nuclei with larger diameters start to grow. This critical radius can be calculated by the maximum of the Gibbs free energy:

$$\frac{\partial \Delta G}{\partial r} = 0 \tag{19}$$

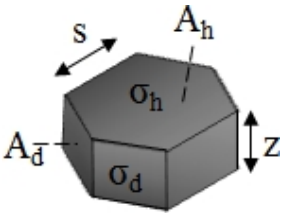

Figure 34: Geometry used to calculate the Gibbs free energy for hexagonally-shaped discs.

The Gibbs free energy for nanoparticle formation is often given for a spherical shape only [150]. According to Muthukumar *et al.* [151] the Gibbs free energy of hexagonal disc formation can be calculated using the hexagonal geometry, displayed in Figure 34. Considering the different surface energy contributions, the Gibbs free energy can be written as

$$\Delta G = -\Delta G_V \cdot \frac{3}{2} \cdot \sqrt{3} s^2 \cdot z + \sigma_h \cdot 3\sqrt{3} \cdot s^2 + 6 \cdot \sigma_d \cdot z \cdot s \tag{20}$$

with $A_h = \frac{3}{2} \cdot \sqrt{3} s^2$, $A_d = z \cdot s$, and the volume $V = \frac{3}{2} \cdot \sqrt{3} s^2 \cdot z$ and σ_h, σ_d as the surface energies of the corresponding crystal faces. For a hexagonal disc, the critical diameters neccessary to form stable nuclei can be calculated by extremizing the Gibbs Free Energy:

$$\frac{\partial \Delta G}{\partial z} = 0 \rightarrow s_{\text{crit,hexa}} = \frac{4}{\sqrt{3}} \cdot \frac{\sigma_d}{\Delta G_V} \tag{21}$$

$$\frac{\partial \Delta G}{\partial s} = 0 \rightarrow z_{\text{crit,hexa}} = \frac{4\sigma_h}{\Delta G_V} \,. \tag{22}$$

The critical Gibbs free energy is obtained by inserting the critical values into Equation 20

$$\Delta G_{\text{crit,hexa}} = \frac{48}{\sqrt{3}} \frac{\sigma_d^2 \sigma_h}{\Delta G_V} \,. \tag{23}$$

Non-classical crystal formation: Oriented attachment

In 1998, Penn and Banfield introduced a new crystal growth model to explain experimental findings of agglomeration based crystal growth processes that cannot be accounted for by classical theory [141, 152, 153, 154, 155]. This oriented attachment process is dominated by kinetics and describes the intermediate stage between nucleation and Ostwald ripening[156]. In this non-classical theory, the nuclei form and grow into primary particles (referred to as primary building blocks) which then self-assemble into metastable, intermediate phases such as mesocrystals [157, 158, 159]. Several mesocrystal formation mechanism have been proposed and are summarized in Cölfens work [144, 159]. They possess a colloidal composition and have similar size and shape as the oriented aggregates which can either be iso-oriented crystals or single crystals [157, 159, 160]. Here, the primary particles reorient along a specific crystallographic direction and adjacent particles can fuse at similar crystallographic faces to form the final "secondary nanoparticle". These secondary particles often display unusual morphologies.
The conversion from the mesocrystal to an oriented aggregate reduces the surface energy by removing surfaces. A phase transformation prior to the aggregation can often be observed as well [161]. This multistep growth process is sketched in Figure 35. Further information on the ongoing discourse as well as classical and non-classical crystal formation can be found in these articles and books: [140, 144, 157, 159, 160, 162, 163, 164, 165, 166, 167, 168, 169, 170, 171, 172]

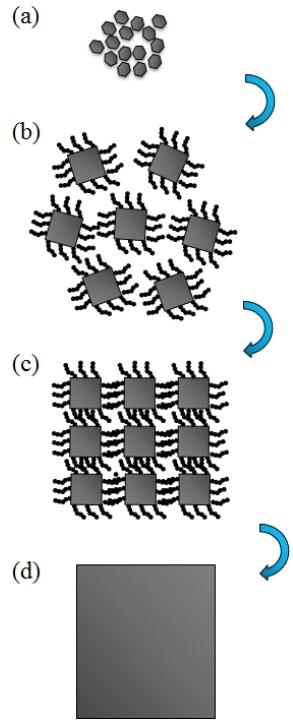

Figure 35: Proposed steps in an oriented attachment process in the presence of organic additives: (a) crystallites are formed, (b) the crystallites grow into substructures called primary building blocks, (c) the primary building blocks orient along a common crystallographic axis, (d) the oriented primary building blocks fuse and form the final, secondary nanoparticle.

Biomineralization

Biomineralization is an over 500 million year old natural process within organisms which use inorganic materials from their enviroments to form inorganic structures, e.g. nanoparticles, for various purposes[72, 157]. Today over 60 minerals within such organisms have been identified, with magnetite and ferrihydrite as the most common [20]. These inorganic crystals, created at ambient temperatures (below 100 °C) in the biomineralization process [20], display a well-controlled composition, microstructure, and morphology,

out-performing those crystals obtained in conventional bottom up approaches. Biomineralization can be separated into two categories [173]:

Biologically induced mineralization: In this process nanoparticle properties depend on enviromental conditions such as temperature and pH. The minerals tend to be poorly crystalline and lack specific morphologies. A broad size distribution is often observed in this process [173].

Biologically controlled mineralization: Minerals with well defined microstructure and morphology are created in this mineralization process. This high degree of control is achieved by a sealed cell wall or cytoplasm, creating an independent reaction chamber. Ions are transported into the chamber until supersaturation is reached and mineralization induced [173]. This process, which is illustrated in Figure 36, can be found in magnetotactic bacteria.

[39] Their name is derrived from their ability to migrate along the local geomagnetic field.

Magnetotactic bacteria (MTB)[39], first reported in 1975 by R. Blakemore [75], have been studied intensively due to their ability to synthesize magnetic nanoparticles under mild conditions with a high degree of control over the mineralization process. The nanoparticles in MTBs are permanent magnets which act as compasses. This allows the bacteria to migrate along earth's magnetic field. The magnetic particles are aligned in chains parallel to the major axis of the bacteria leading to a maximal net magnetic moment[40].

[40] The net magnetic moment is the sum of all particle magnetic moments.

MTB are known to synthesize magnetite Fe_3O_4, greigite Fe_3S_4, combinations of greigite and iron pyrite FeS_2 with sizes between 25 nm and 120 nm and a narrow size distribution [73, 92]. The inorganic crystals are surrounded by a thin organic membrane consisting of proteins and phospholipids [73, 92].

MTB represent the simplest system in which biomineralization occurs [72]. However, the biomineralization process of MTB is not yet well understood due to its complexity. Understanding this mechanism would not only give insights into more complex biomineralization processes but could also allow a synthesis of complex materials at ambient temperature with a high degree of control, a process which cannot be achieved to such an extent by conventional chemical approaches today [72]. Studies showed that the biomineralization process within the bacteria is encoded in the

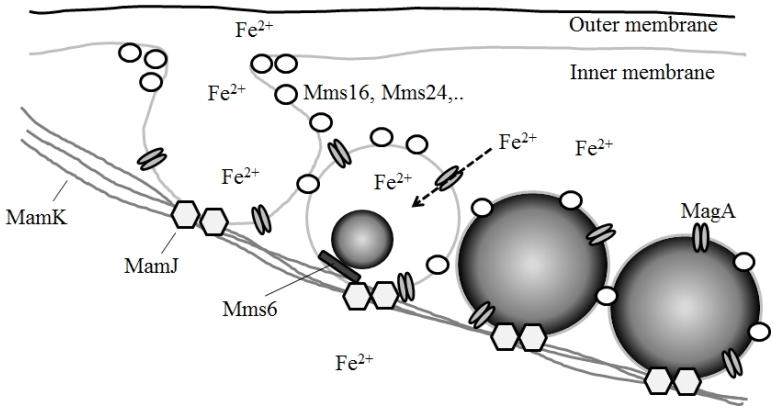

Figure 36: Proposed biomineralization process within magnetotactic bacteria. The cytoplasmic membrane invaginates to form a vesicle. Ferrous iron is transported into the geochemically independent reaction compartment by a protein called magA. Several further proteins control the particle growth and their alignment into a chain. This sketch was drawn in analogy to [74].

genetic blue print [174]. More than 20 proteins are involved in the controlled biomineralization process. These proteins are responsible for the reaction chamber formation, the mineral transport into the chamber, contolled crystal growth as well as the arrangement of the nanoparticles into chains [74, 174]. A schematic of this process can be found in Figure 36. For more information on magnetotactic bacteria, please refer to the following articles: [173, 175, 176, 177, 178, 179, 180, 181, 182, 183, 184, 185, 186, 187, 188].

Proteins and Peptides

Proteins are macromolecules formed by a chain of amino acids which are linked via peptide bonds. An amino acid, displayed in Figure 37, consists of a carboxyl group, a carbon atom, a hydrogen atom, an amino group, and a variant side chain[41]. The side chain distinguishes the different amino acids from each other. It can be either polar, unpolar, acidic, or alkaline. Amino acids form a chain which is referred to as either peptide, polypeptide or protein, depending on the length of the amino acid chain. A chain of amino acids consisting of up to 100 amino acids is called either peptide or polypeptide while a chain with more than 100 amino acids is referred to as protein. A peptide bond is drawn in Figure 38. In this work the names peptide and polypeptide are used synonymously.

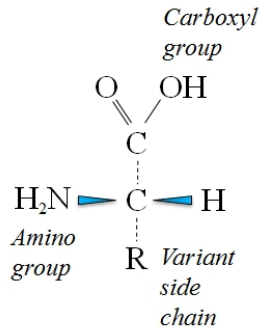

Figure 37: An amino acid consists of an amino group, a carboxy group, a carbon and a hydrogen atom, as well as a side chain.

[41] Two different amino acid types exist. The amino group H_2N can be found on either the left hand side of the carbon atom C (L-AA) or on the right hand side of C (D-AA) (enantiomer). The (L-AA) can be found in proteins only.

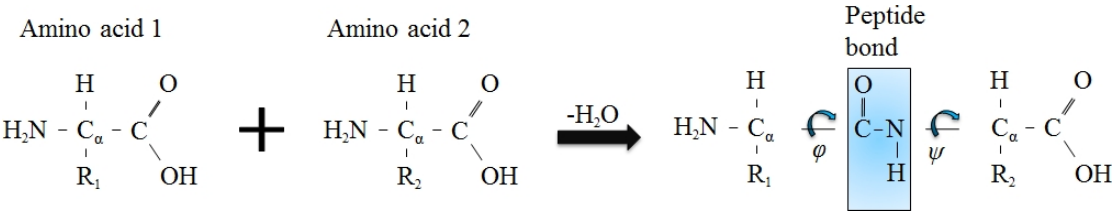

Figure 38: Two amino acids combine by forming a peptide bond. During bond formation, the carboxyl group COOH interacts with the amino group H_2N of the second amino acid and forms a peptide bond. During bond formation, H_2O is released.

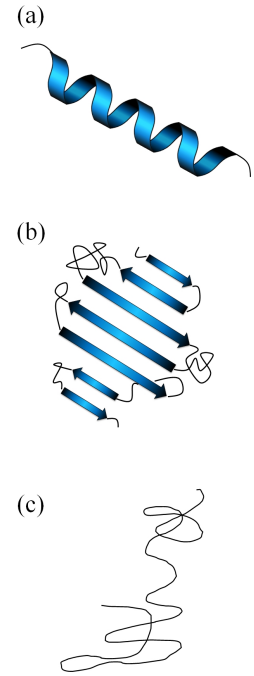

Figure 39: Different secondary structures of peptides. (a) The α-helix is a uniform twist in the polypeptide chain. (b) A β-sheet consists of antiparallel strands. (c) A random coil displays no specific secondary structure.

The carboxy group COOH of the first amino acid combines with the amino group H_2N of the second amino acid. H_2O is released during bond formation. The peptide bond is planar and has a partial double bond character. Two degrees of freedom, the angles φ and ψ, exist per peptide, their values are restricted by the side chains. The peptide configuration can be described with a theoretical model called "worm like chain model". A description of this model can be found in [189]. The structure of a protein is separated into primary structure, secondary structure, tertiary structure and quarternary structure [190]:

Primary structure: The primary structure is determined by the sequence of the amino acids which form the peptide through peptide bonds.

Secondary structure: The secondary structure is a locally energetically favored conformation. It is created by hydrogen bonds between CO and NH. The most common structure, the α-helix, is a uniform twist of the polypeptide chain with the side chains pointing outwards. The α-helix is sketched in Figure 39 (a). A β-sheet, created by an interaction of neighbouring parts of the primary structure or several polypeptide chains consists of interacting strands aligned either parallel or antiparallel. An antiparallel aligned β-sheet is sketched in Figure 39 (b). Proteins which lack a specific secondary structure are referred to as random coils, an example of which is sketched in Figure 39 (c).

Tertiary structure: The tertiary structure describes the 3D structure created by interactions of the amino acids initially far away from each other in the primary structure. The thermodynamic

process in which the tertiary structure of a protein is formed is called protein folding[42]. The tertiary structure is the energetically favored state. The unique 3D structure of a protein is mostly determined by the primary structure and length of the peptide chain. This correlation is known as the dogma of biochemistry.

Quarternary structure: The quarternary structure describes the agglomeration of folded polypeptides by disulfide bonds.

[42] This process is driven by a decrease in enthalpy.

Proteins/polypeptides have a variety of specific functions which include but are not limited to the formation of structural components for cells (f.e. actin filaments), serving as antibodies to protect the body from viruses and bacteria (f.e. immunoglobulinB), transmitting signals between cells for biological processes (hormones such as insulin[43]), and catalyzing specific reactions (enzymes[44]). In the latter case, proteins/polypeptides lower the activation energy for a specific chemical reaction which increases the reaction rate. This is illustrated in Figure 40. Catalysts do not alter the thermodynamics but the kinetics of chemical reactions [191, 192]. Further information on the variety of proteins/polypeptide functions as well as on catalysts can be found in several works [191, 192, 193, 194, 195, 196, 197, 198].

[43] Frederick Grant Banting and John James Rickard Macleod were awarded the Nobel Prize for "the discovery of insulin" in 1923 [2].

[44] A.H.T. Theorel was awarded the Nobel Prize "for his discoveries concerning the nature and mode of action of oxidation enzymes" [2].

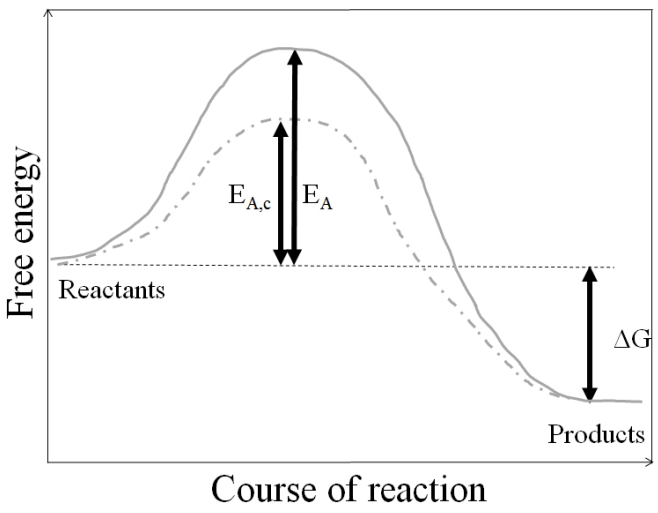

Figure 40: A catalyst offers an alternative reaction path (dashed line) with a lower activation energy $E_{A,c}$ in comparison to a non-catalyzed reaction path (solid line) with a higher activation energy E_A.

Magnetism

This section gives a short introduction into magnetism by describing the most important concepts. This section does not aim to provide a full quantum mechanical description of magnetism. A more detailed description can be found in these works: [26, 37, 199, 200, 201].

Physical Origin of Magnetism

[45] The magnetic moment arising from the proton is 2000 times weaker than that of the electron due to their difference in mass. The magnetic moment of the atom is thus dominated by the electron contribution.

The magnetic properties of a material are caused by the electron[45] orbital motion and spin [26]. A magnetic moment is associated with each. The overall magnetic moment of an atom is made up of the single parts:

$$m_{\text{atom}} = g_J \cdot \mu_B \cdot \sqrt{J(J+1)} \tag{24}$$

$$g_J = 1 + \frac{J(J+1) - L(L+1) + S(S+1)}{2J(J+1)} \tag{25}$$

with J as the atom total angular momentum, the g-factor g_J, L as the total orbital quantum number, and the many-electron-quantum number S. The g-factor describes which magnetization is dominant. For $g_J = 1$ the magnetization is caused by the orbital motion of the electrons. For $g_J = 2$ the magnetization is caused by the electron spin [202]. Different magnetic properties arise depending on the electron motion causing the magnetization[127].

Different types of magnetism

Electron spin, orbital motion and change in orbital motion in an externally applied field are the origins of the magnetic moments. The moments can be either oriented in such a way that they cancel each other, leading to a zero net magnetic moment (diamagnetism), or they are oriented in such a way that a non-vanishing magnetic moment exists (paramagnetism, collective magnetism). The magnetization describes the orientation of magnetic moments per unit volume in magnetic fields [202]:

$$\vec{M} = \frac{1}{V} \sum_i \vec{m}_i \tag{26}$$

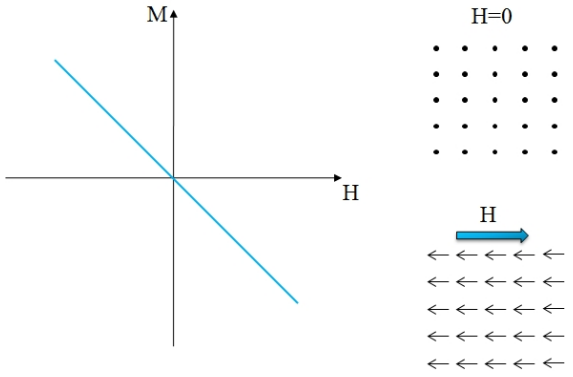

Figure 41: H/M curve of a diamagnetic substance. The sketch on the right hand of the image shows that no magnetic moments exist in the absence of a magnetic field. Once an external magnetic field is applied the moments align. This illustration is drawn in analogy to Tilley's work [199].

with V as the magnetic volume, $\vec{m}_i$ as the i^{th} magnetic moment and $\vec{M}$ as the magnetization.

Diamagnetism: Diamagnetic materials do not possess an intrinsic magnetic moment. Atoms with closed shells are usually diamagnetic since the spins and orbit movements cancel out in occupied shells[46]. If an external field is applied to a diamagnetic substance, a change in orbital motion is caused, resulting in an induced magnetic moment opposing the field (weak effect). This is illustrated in Figure 41.

[46] Au, Ag and Cu are examples for diamagnetic substances.

Paramagnetism: Paramagnetic materials possess intrinsic moments. Atoms with incomplete shells possess orbital angular momentum as well as spin. The resulting moments, which do not interact with each other, are oriented randomly in the abscence of an external field and thus cancel out statistically. This leads to a zero net magnetic moment. If an external field is applied the majority of moments orient along the field lines[47], leading to a net magnetic moment greater than zero. This is illustrated in Figure 42.

[47] Thermal effects, among others, prevent the full alignment.

Collective magnetism: The collective magnetism describes all materials with interacting moments. The interaction leads to an alignment of the moments which can be either parallel (ferromagnetism) or antiparallel (antiferromagnetism) for equal contributions, or antiparallel with unequal contributions (ferrimagnetism). The alignment in ferromagnetic, antiferromagnetic, and ferrimagnetic materials is sketched in Figure 44. A general

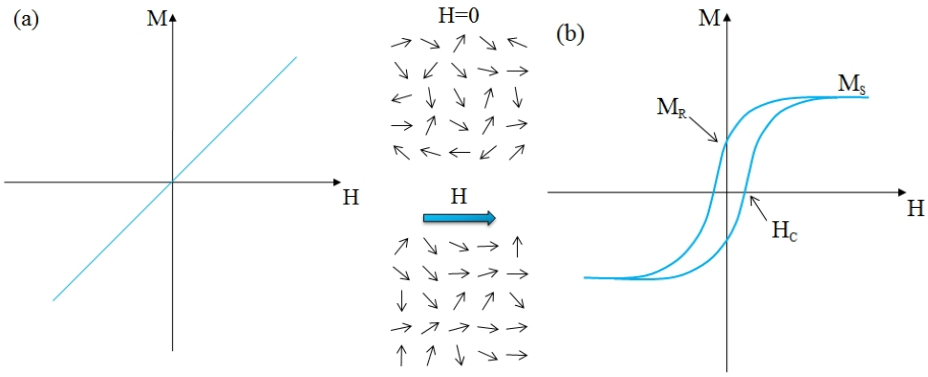

Figure 42: (a) H/M curve for a paramagnetic substance. This sketch is drawn in analogy to Tilley's work [199]. (b)Ferromagnetic magnetization curve. The magnetization increases in an externally applied field until the saturation magnetization M_S is reached. The remanence M_R represents the remaining magnetization after removing the externally applied field. The opposing field at which a zero net magnetization is obained is referred to as coercivity H_c.

description is given for ferromagnetic materials only to avoid repetition.

Ferromagnetic materials have parallel aligned moments over large distances which are caused by interacting moments. Ferromagnetic (bulk) materials are divided into domains by domain walls. Domains are local regions with parallel aligned moments that display saturation magnetization.

The domains within the ferromagnetic material are randomly oriented leaving a zero net magnetization. The magnetization process occuring in the presence of an externally applied field is sketched in Figure 43. If a field is applied, the domain wall moves in the direction of the field, resulting in a non-zero net magnetic moment. After the domain wall has moved, the moment is at an angle θ to the externally applied field direction which rotates to align parallel to the applied field in a final step. Saturation is reached when all moments are aligned. The magnitude of the saturation magnetization does not change in this process. It is displayed by the length of the arrow in Figure 43. An increase in magnetization is caused by the increase in orientation of the magnetic moments. Reducing the applied field leads to a reduction in the magnetization until it has reached a value called remanence M_R. This is the magnitude of the magnetization in a ferromagnetic material that remains after the applied field is reduced to zero. The opposite field needed to reduce the magnetization to zero is called coercivity H_c. The behavior of

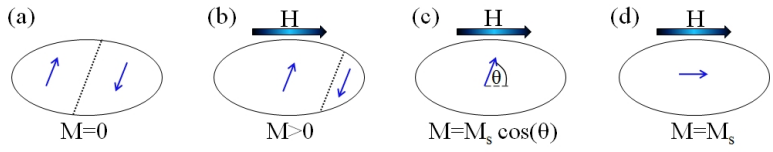

Figure 43: Magnetization process in ferromagnets: (a) Initially, in the absence of a field, the domains are oriented in such a way that a zero net moment is obtained. (b) When an external magnetic field is applied the domain wall moves in direction of the field leading to a non-zero net magnetic moment. (c) The domain wall moves until a single domain particle is obtained, which can be at an angle to the external field direction. (d) A torque acts on the moment and aligns it parallel to the applied field.

ferromagnetic materials in an externally applied field is sketched in Figure 42.

Only the elements iron, cobalt and nickel and their combinations are ferromagnetic. A detailed reasoning for this is given in Ennen's work [37].

Anisoptropy

In magnetic anisotropic materials the magnetic properties depend on the direction. Several kinds of magnetic anisotropies exist, the most common are:

Crystal anisotropy: Easy axes and hard axes exist in anisotropic materials. The easy axis is the axis where saturation magnetization is achieved at low fields. Anisotropy is mainly caused by spin-orbit coupling. In an externally applied field, the field tries to reorientate the electron spins. Due to the spin-orbit-coupling the orbit tries to reorientate as well. Because the orbit is strongly coupled to the lattice the energy, neccessary to rotate spin from the easy axis, is the energy which is required to overcome the spin-orbit coupling and is called anisotropy energy. The interactions are sketched in Figure 45.

Shape anisotropy: Shape can also be a source of anisotropy for non-spherical samples. It is easier to magnetize along a long axis rather than a short axis in a crystal. The short axis and long axis of a disc-like nanoparticle are displayed in Figure 46.

Stress anisotropy: Magnetic anisotropy can be induced by plastic deformation and is referred to as stress anisotropy.

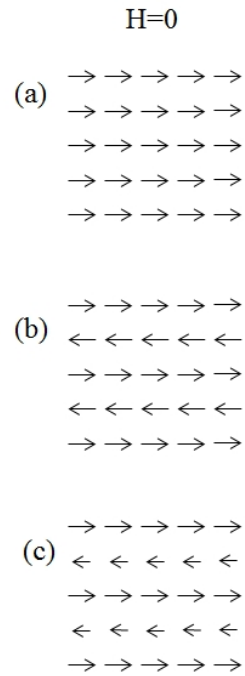

Figure 44: Collective magnetism: The moments can either align (a) parallel (ferromagnetism) or (b) antiparallel (antiferromagnetism) for equal contributions. (c) Ferrimagnetic materials display antiparallel alignment with unequal contributions.

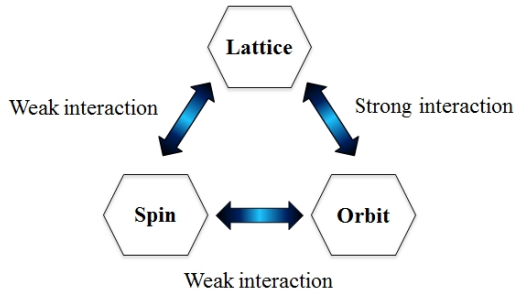

Figure 45: Illustration of the spin-orbit-lattice interaction.

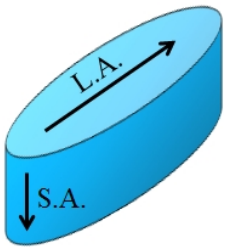

Figure 46: A non-spherical object gives rise to a shape anisotropy. Magnetization along the long axis is easier than along the short axis.

Magnetism in nanostructures

The theoretical study of nanoparticles dates back to the 1930s where Frenkel and Dorfman studied the unusual effects of sufficiently small particles. They found that below a critical diameter, nanoparticles should be single domain [20]. Unusual effects, such as superparamagnetism, increased magnetic anisotropy in comparison to bulk, and changes in Curie temperatures for nanoscale systems created great interest among many researchers.

The size of the nanostructures influences the magnetic properties of the material. Larger, ferromagnetic particles become single domain particles once their diameter subceedes the single domain limit. A further reduction of particle size leads to a phenomenon called superparamagnetism. The relation between size and coercivity (and magnetic properties) is displayed in Figure 47.

Single domain particles: Ferromagnetic particles with a size below a critical threshold D_{SD} are single domain particles. These single domain particles display maximal coercivity. The magnetization of a single domain particle can be described via macro spin models where a single magnetic moment is used to describe the magnetic properties instead of several parallel aligned magnetic moments existing in the structure. The strength of the macro magnetic moment corresponds to the magnetic moment of the ensemble of parallel aligned magnetic moments.

Superparamagnetism: Superparamagnetic behavior can be observed for small ferromagnetic particles with sizes below D_{SPM}. The energy needed to reverse the magnetization of the particle is

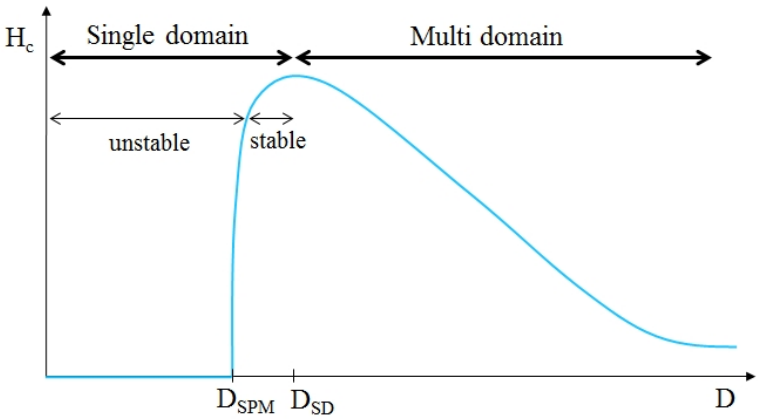

Figure 47: Dependence of the coercivity on the particle size. Above a critical size D_{SD} the particles are multidomain particles (bulk behavior). Particles with sizes below this limit are single domain. The single domain particles are separated into 2 categories: stable and unstable. Particles with sizes between D_{SD} and D_{SPM} are stable while particles with sizes below D_{SPM} are unstable. The magnetization can flip at room temperature.

proportional to the anisotropy constant[48] K_{eff} and the particle volume V [26]. For small particles or particles with a low anisotropy constant, the energy needed to reverse the magnetization can be overcome by the thermal energy:

$$k_B T > k_{eff} V \ . \tag{27}$$

These particles are thus classed as unstable since their magnetization can flip at room temperature. The H-M curve of such a superparamagnetic sample is sketched in Figure 48.
This effect is used in several biomedical applications such as hyperthermia therapy. The magnetization curve does not show coercivity or remanence, but does reach saturation. Superparamagnetism can still be described with the macro spin model since the ferromagnetic coupling between the single atomic moments remains.

[48] Anisotropy describes the preferred orientation of magnetization along a specific crystal axis.

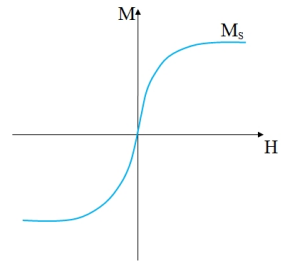

Figure 48: H-M curve of a superparamagnetic substance. Superparamagnetic particles display a saturation magnetization but no coercivity.

3D Tomography on magnetotactic bacteria

This chapter outlines how 3D tomography was performed on magnetotactic bacteria to introduce the natural system on which the biomimetic approach is based, as well as to test the maximal resolution that can be achieved with the Helios Nanolab600. Previous 3D tomography studies by Akemeier [48] concerned larger structures in which 20 nm small parts within biological tissue (single lipid bilayers) could be resolved. However, many biological systems, such as cells, have internal structures below 20 nm [190]. Magnetotactic bacteria, with sizes around 2 µm to 5 µm and with structures like magnetosome membranes below 20 nm, represent a great sample to test the possible resolution of this *slice and view* technique.

Sample preparation

This section describes the sample preparation of the magnetotactic bacteria for the 3D tomography. The bacteria were provided by Dr. Damien Faivre (Max Planck Institute of Colloids and Interfaces, Potsdam) and were stained and prepared for the 3D tomography by Stephanie Hoehn (Faculty of Biology, Bielefeld University) and Christoph Wigge (Buchmann Institute for Molecular Life Science, Goethe University Frankfurt).

Staining

The bacteria were pre-fixed in a mixture of 500 µL aldehyde (GA) [49] (2.5 %) and 500 µL sodium phosphate buffer (0.05 M) for 1 h at

[49] This chemical crosslinks the proteins in the samples.

room temperature. The sample was washed three times afterwards in sodium phosphate buffer (0.05 M, pH=7) and centrifuged for 3 min at 16000 g. In the following step the buffer was exchanged with 1 mL sodium cacodylate buffer (0.1 M, pH=7.4) and the sample stored at 4 °C overnight. The sample was afterwards washed three times using 200 µL sodium cacodylate buffer (0.1 M). The sample was post-stained with an osmium tetroxide (OsO_4)[50] - sodium cacodylate buffer solution (1 mL osmium tetroxide (1 %) and 3 mL of the sodium cacodylate buffer (0.1 M)) for 1 h at room temperature. The sample was afterwards washed three times (3× 10 min) using the sodium cacodylate buffer (0.1 M) and incubated in tannic acid (1 %) for 1 h at room temperature. In a further step the sample was washed with MilliQ 3× and afterwards stained using 1 mL uranyl acetate (1 %) for 1 h at room temperature. The sample was afterwards washed 3× using MilliQ and dehydrated using ETOH in an increased series using 1 mL ETOH (50 %) for 1 h at room temperature which is then exchanged for 1 mL ETOH (70 %) in which the sample is incubated at 4° over night. The dehydration is completed by two further steps in which the ETOH is exchanged for 1 mL ETOH (90 %) and the sample incubated for 1 h at room temperature and afterwards in 1 mL ETOH (100 %) for 1 h at room temperature. In a final four-step process the sample is embedded in epon resin[51]: first the ETOH is replaced by a 2:1 ETOH resin mixture (3 mL ETOH (100 %) and 1.5 mL epon) and the sample slowly rotated for 1 h. In the second step, the 2:1 ETOH resin mixture is replaced by an 1:1 ETOH resin mixture (3 mL ETOH (100 %) and 3 mL epon) and the sample incubated for 1 h while being slowly rotated; the ETOH resin mixture is afterwards replaced by a 1:2 ETOH resin mixture (2 mL ETOH (100 %) and 4 mL epon) and the sample slowly rotated for 1 h. In the final step, the ETOH resin mixture is replaced by 1 mL epon, the sample centrifuged for 20 s to move the bacterial pellet to the bottom of the eppendorf vial, and placed on a shaker for 2 h. The sample is cured for 12 h at 60° (the eppendorf vial is open) to evaporate the remaining ETOH.

[50] Osmium crosslinks the lipids in the bacteria.

[51] The epon is heated to 60° for 15 min to liquify it.

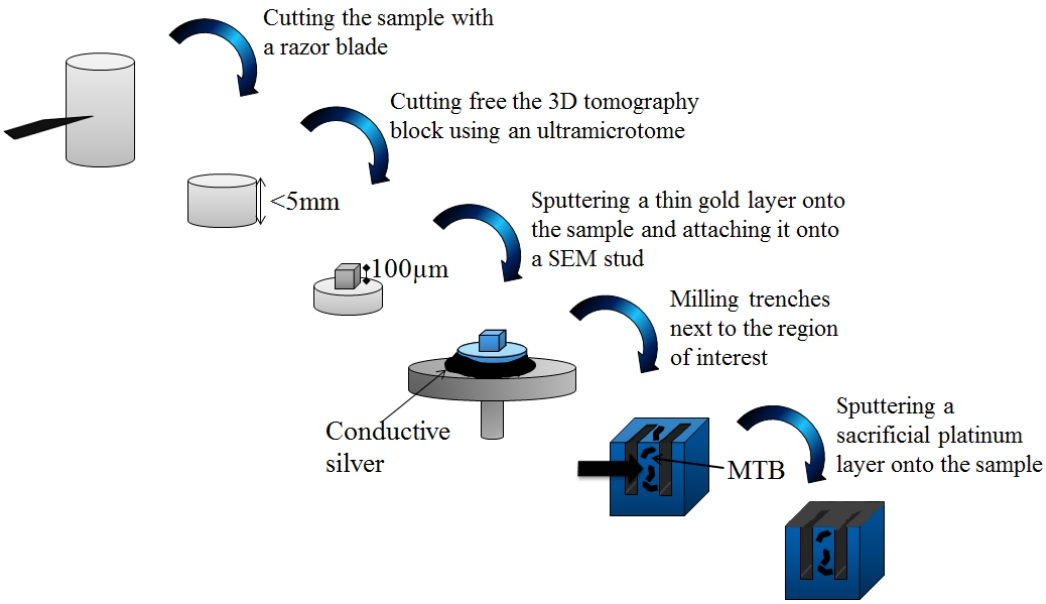

Figure 49: Multi-step preparation process for 3D tomography: in a first step the sample is cut using a razor blade to a height which is below the maximal sample height for the DualBeam device; a 100 µm sized block (area which is to be sectioned) is cut using an ultramicrotome; after attaching the sample to a SEM stud a thin gold layer is sputtered onto the sample; in a last step trenches around the area of choice are milled (to prevent redeposition during the sample sectioning) and a sacrificial platinum layer is deposited on top of the sample to ensure smooth milling.

Preparation for the 3D tomography

The embedded sample needs to be cut to an appropriate size that can be handled using a DualBeam device before the 3D tomography can be performed. After removing the eppendorf vial the sample was cut into a block $\ll 5$ mm in height using a razor blade. An EM UC 7 ultramicrotome (Leica AG, Wetzlar, Germany) was afterwards used to create a 100 µm × 100 µm × 100 µm large block on top of the sample (which contains the magnetotactic bacteria) that is used for the 3D tomography. The sample was then attached to a conventional scanning electron microscope stud using carbon tape and conductive silver. Afterwards, a thin gold layer (≈ 30 nm) was sputtered onto the sample to improve conductivity, an essential step for good image quality. Trenches around the area of choice were milled using a DualBeam device to prevent problems caused by redepositing material during the *slice and view* process. All preparations, illustrated in Figure 49, were carried out by Christoph Wigge at Frankfurt University.

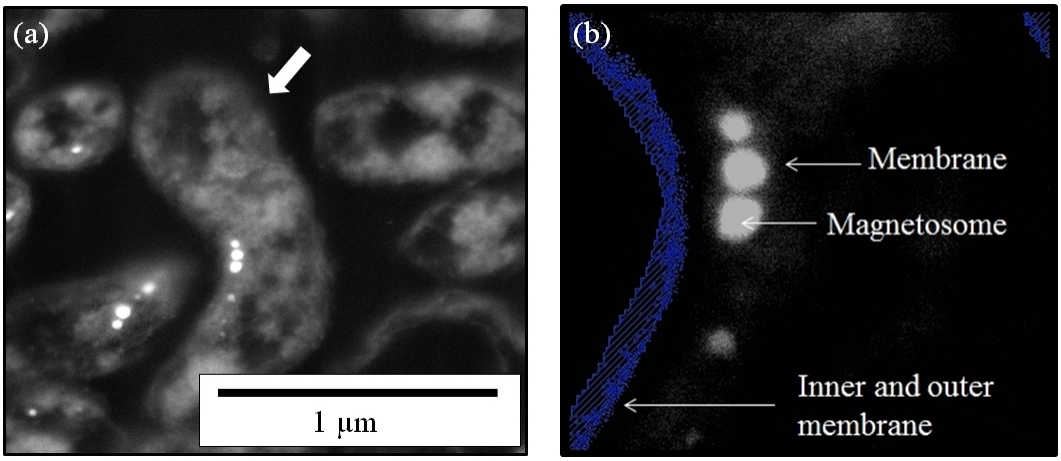

Figure 50: (a) SEM image of the first 3D tomogram layer used for the 3D reconstruction of a single MTB which is marked by the white arrow. (b) The enhanced contrast SEM image displaying part of the MTB shows that the mangetosome membrane around the nanoparticles is clearly visible. The dark purple lines represent the inner and outer membrane of the bacterium. The length of this image correpsonds to 500 nm.

3D tomography and image processing

An area containing several bacteria (see Figure 50) was sectioned using the ion beam with an acceleration voltage of 30 kV and an ion beam current of 6.5 nA. The different slices were imaged using the electron beam with an acceleration voltage of 3 kV and a current of 0.69 nA in the back scattered electron (BSE) detection mode. The BSE detection mode was found to yield the best imaging results which is due to the sample staining. The low acceleration voltage allows a surface sensitive imaging which is essential for a succsesful 3D tomography. The inter-slice distance was chosen as 12 nm for which the milling pitch in z-direction (distance between the imaged slices) was set to 3 nm, with every fourth layer being imaged. This sectioning method was chosen since it allows to section areas of interest (such as magnetosomes) in more detail with more slices without having to change the *slice and view* process.

The front layer of the image stack (which contains 48 slices) is given in Figure 50. This SEM image of the MTB, which are all oriented in different directions, shows that the internal structures such as magnetosomes and empty vesicles are clearly visible. The sub 10 nm thin magnetosome membranes around the magnetite nanoparticles (magnetosomes) can also be resolved (contrast en-

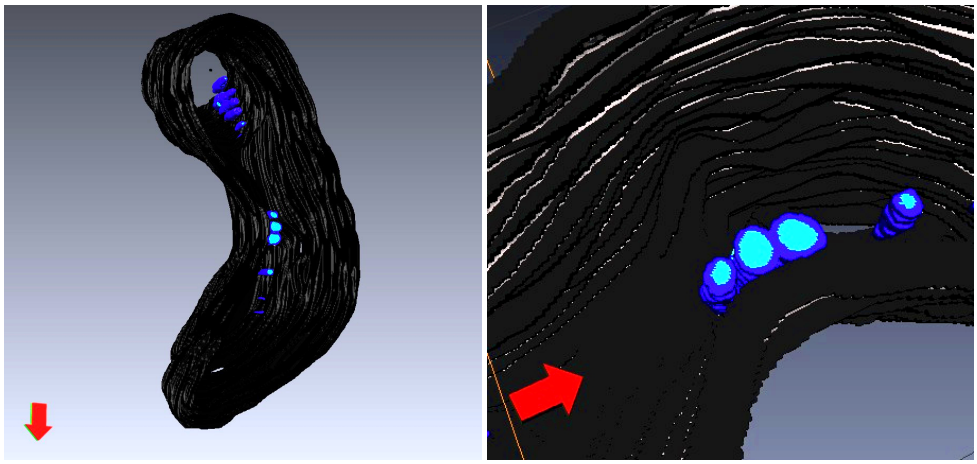

Figure 51: Left: 3D tomogram of a single magnetotactic bacterium. The inner and outer membrane of the bacterium is displayed in black, the magnetosomes are displayed in a light blue and the magnetosome membrane is displayed in a dark blue. Right: Enlarged area within the single magnetotactic bacteria which shows the encapsulated magnetosomes. The magnetosome membranes are displayed in a dark blue, the magnetosomes are displayed in a light blue and the inner and outer membrane of the bacterium is displayed in black.

hanced SEM image in Figure 50) using this technique. The 3D reconstruction of a single chosen bacterium is given in Figure 51. All magnetosomes (light blue), their surrounding membranes (dark blue), several empty vesicles (dark blue), as well as the the inner and outer MTB membrane (black) were reconstructed manually for each slice and combined afterwards to form the 3D tomogram. The slices were aligned manually using a reference point on the images to counteract the small image shifts that occur during the *slice and view* due to image drifts and larger thermal drifts of the electron beam.

Conclusion

The 3D tomography, conducted on the MTB, shows that this *slice and view* technique can be used to resolve sub 10 nm structures within biological samples, which are below the previously suggested resolution of 20 nm proposed by Akemeiner [48]. The advantage of this high resolution *slice and view* technique over conventional TEM sectioning is that the sample can be sectioned and imaged within a single device without loosing sections in between two slices. It therefore allows a complete sample imaging and 3D reconstruction which cannot be achieved by conventional TEM sections[52].

[52] The preparation process of conventional TEM sections (100 nm thin slices) leads to "missing slices" between two TEM sections which prevents a complete imaging of the sample.

Synthesis of cobalt ferrite nanoparticles

The synthesis of the cobalt ferrite nanoparticles for the biomimetic approach consists of two parts:

- the synthesis of the synthetic polypeptide c25-mms6[53]
- the synthesis of the cobalt ferrite nanoparticles in which the synthetic polypeptide is used

The synthesis of the synthetic polypeptide c25-mms6[54] was carried out analogously to Prozorov *et al.* [107] by Marco Wissbrock from the Chemistry Faculty of University Bielefeld. The amino acid sequence of c25-mms6 is given in Figure 53. The properties of c25-mms6 are given in Table 4.

The basic, bioinspired synthesis of the cobalt ferrite nanoparticles was carried out in analogy to Prozorov *et al.*, but without pluronic gel. 50 µL $CoCl_2$-solution (0.66 M) and 200 µL $FeCl_2$-solution (0.33 M) were added to 750 µL c25-mms6-solution (6.92×10^{-9} M) while stirring. 10 µL Hydrochloric acid (HCl, 37 %) (0.0016 M) was added and the obtained mixture incubated for 30 min at 4 °C. The mixture was afterwards brought back to room temperature. 11 µL hydrogen

[53] c25-mms6 is a shorter synthetic version of the full length protein MMS6 found in magnetotactic bacteria.

[54] Peptides are less complex than proteins due to their reduced amount of amino acids. However, they often still display material specific affinities [203]. Prozorov *et al.* previously showed that 25 amino acids (c25-mms6) from the c-terminal region of the full length protein MMS6, responsible for inorganic crystal formation within magnetotactic bacteria, has the same effect on inorganic crystal growth [107] allowing for a faster and easier polypeptide synthesis.

Property	Value
Molecular weight	$2890\,\mathrm{g \cdot mol^{-1}}$
Netcharge at pH 7	-4
Acidic amino acids	7
Alcaline amino acids	3
Hydrophilic amino acids	6
Hydrophobic amino acids	9

Table 4: Properties of c25-mms6, taken form the "Peptide Property Calculator" [204].

peroxide (H_2O_2, 33 %) and 70 µL aqueous NaOH (1 M) were then added to the mixture. 700 µL NaOH (1 M) was added to complete the reaction. The suspension obtained was kept at room temperature to allow crystal growth up to 28 d.

A control experiment without the synthetic polypeptide was synthesized under equivalent conditions to the biosynthesis. The effect of c25-mms6 on particle growth was studied by comparing the results of the biosynthesis (with c25-mms6) to those of the control experiment (without c25-mms6). 750 µL distilled water was used instead of the 750 µL c25-mms6 solution (6.92×10^{-9} M) in the control experiment. The parallel performed syntheses are sketched in Figure 52.

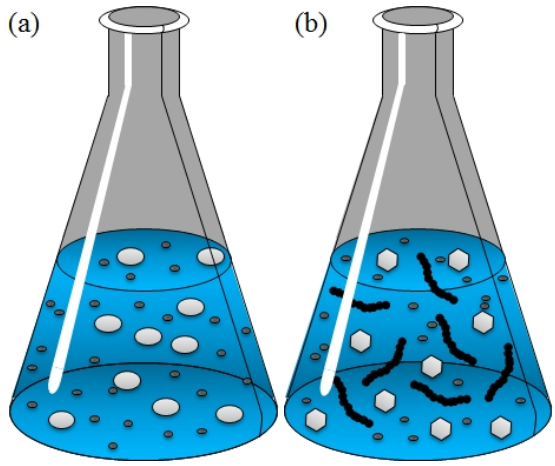

Figure 52: Flasks representing the control experiment synthesis (a) and the biosynthesis (b).

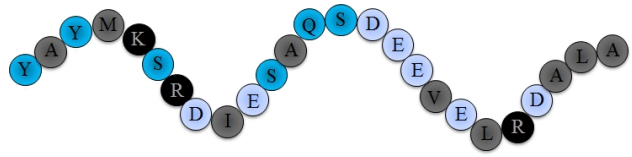

Figure 53: Primary structure of c25-mms6: The different latters represent the different amino acids (see Appendix A). The light blue color represents acidic amino acids, blue represents hydrophilic amino acids, grey represents hydrophobe amino acids and black represents alkaline amino acids.

Polypeptide-inorganic crystal interaction

Todays knowledge of peptide-inorganic crystal interaction is still limited. This interaction is difficult to generalize since it is influenced by many peptide parameters, such as peptide length, amino acid sequence and secondary structure [106]. The inorganic crystal size as well as lattice structure and surface chemistry also affect the interaction [106, 205, 206, 207]. Several reports found that peptides inhibit pathological mineralization, kinetics and can alter impurity signatures [207]. The complex interaction makes it neccessary to study the inorganic crystal-peptide interaction for each system separately. The influence of c25-mms6 on cobalt ferrite nanoparticles was studied previously [112] showing that the synthetic polypeptide allows the formation of stoichiometric $Co_xFe_{3-x}O_4$ nanoparticles with a specific shape all of which could not be achieved by conventional chemical syntheses. The basic results of the previous study are summarized in Figure 54. The interaction of polypeptides and inorganic crystals, however, remained elusive.

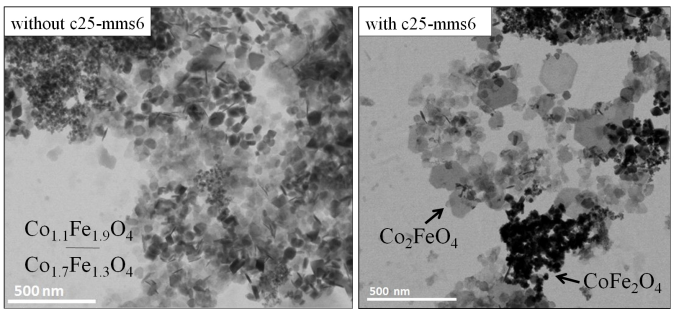

Figure 54: STEM images of the cobalt ferrite nanoparticles synthesized with (right) and without (left) the synthetic polypeptide. The STEM images were taken from the previous work [112].

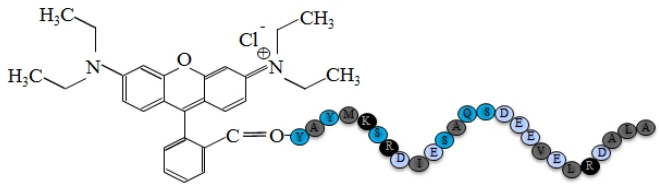

Figure 55: Schematic of the labelled polypeptide c25-mms6. The N-terminal was labelled using the fluorescent dye RhodaminB.

Prozorov *et al.* previously proposed for this system, that c25-mms6 forms micelle-like structures (see Figure 57) onto which the nanoparticles grow. To verify this theory, fluorescence correlation spectroscopy (FCS) was conducted in which a possible micelle formation as well as the type of interaction between peptide and inorganic crystal was studied. The N-terminal of c25-mms6 was labelled with the fluorescent dye RhodaminB [55] for the FCS measurements. In a second experiment, the function of c25-mms6 was investigated using TEM, EDX and XRD. The effect of different regions of the peptide on cobalt ferrite growth as well as the role of the primary structure of the polypeptide, using a randomized sequence of c25-mms6, was studied. The results are compared to the biosynthesis with the unaltered c25-mms6 and to a control experiment without any peptide.

[55] RhodaminB was purchased from Alfa Aeser.

Polypeptide labelling and syntheses with different c25-mms6 concentrations

The polypeptide synthesis was carried out analogously to Prozorov *et al.* [107]. However, the N-terminal of the polypeptide was labelled with the fluorescent dye RhodaminB[56]. The amino acid sequence of c25-mms6 and the labelling are sketched in Figure 55. High performance liquid chromatography (HPLC) measurements[57] were conducted to verify that the fluorescent dye RhodaminB was succesfully attached to c25-mms6. The HPLC spectrum is given in the Appendix B in Figure 152.

Three c25-mms6 solutions with the concentrations c=5.97×10^{-8} M, c=5.97×10^{-9} M, and c=5.97×10^{-10} M were prepared for the FCS measurements to study the proposed micelle formation. The different solutions were obtained by a dilution series of a highly con-

[56] RhodaminB has an absorption maximum of 542 nm-554 nm

[57] These measurements were conducted by Marco Wissbrock.

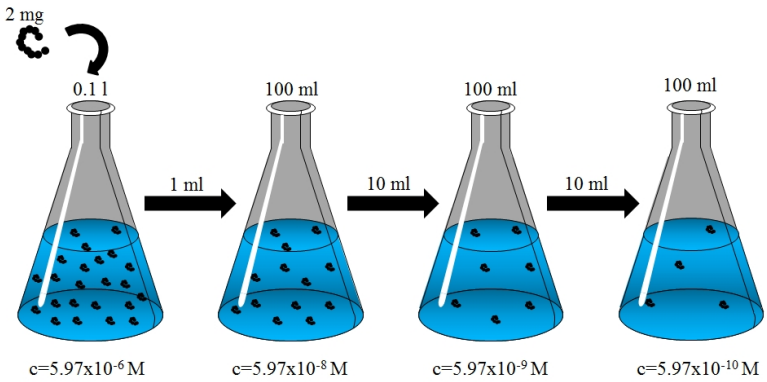

Figure 56: Flasks representing the production of the different peptide concentrations by diluting the original peptide solution.

centrated c25-mms6 solution (5.97×10^{-6} M). The highly concentrated c25-mms6 solution was obtained by adding 2 mg c25-mms6 to 0.1 L distilled water. The dilution series is illustrated in Figure 56. The different solutions obtained in the dilution series were used for the experiments.

Four basic syntheses of the cobalt ferrite particles, using the labelled polypeptide and the different polypeptide concentrations obtained in the dilution series, were carried out to study the interaction strength of the synthetic polypeptides with the inorganic crystals. The obtained suspension was kept at room temperature to allow crystal growth for one day.

Micelle formation

Prozorov *et al.*[107] previously suggested for the c25-mms6 - cobalt ferrite system that the peptides aggregate and form micelles onto which the inorganic crystals grow. This process is sketched in Figure 57. According to their suggestion, the polypeptides must aggregate and the micelles must display the same size and shape as the particles. To verify this hypothesis, peptides in solution (as used for the synthesis) with different peptide concentrations were measured at room temperature. For micelle formation a concentration dependent aggregation is expected as well as a hydrodynamical radius of approximately the nanoparticle size. The hydrodynamic radius is the radius of a hypothetical sphere which possesses the same

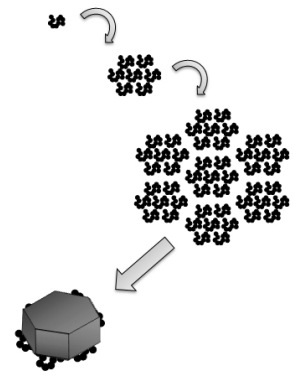

Figure 57: Interaction mechanism between c25-mms6 and $Co_xFe_{3-x}O$ nanoparticle, proposed by Prozorov *et al.* The peptides form micelle-like strucutres onto which the cobalt ferrite nanoparticles grow. This sketch is drawn in analogy to Prozorov *et al.* [107].

diffusion properties as the actual structure.

The correlated time dependent fluorescence signals for the different concentrations obtained in the measurements are given in Figure 58 (a)-(c). The diffusion time is obtained by fitting the time dependent fluorescence signal with the simple diffusion model

$$G(\tau) = \frac{1}{\langle N \rangle}(1 + \frac{t}{\langle \tau_D \rangle})^{-1} \tag{28}$$

with $G(\tau)$ as the correlation function, $\langle N \rangle$ as the mean number of particles diffusing through the excitation volume, t as the time and $\langle \tau_D \rangle$ as the diffusion time. The diffusion time in relation to the concentration is given in Table 5.

Table 5: Diffusion times for different peptide concentrations, obtained by fitting the diffusion model to the correlated fluorescence signal of the measurements.

conc. M	diffusion time μs
5.97×10^{-8}	342 ± 2
5.97×10^{-9}	328 ± 9
5.97×10^{-10}	308 ± 15

The measured diffusion times for the different peptide concentrations only vary within the measurement errors. A concentration based aggregation, which would result in a significant increase in diffusion time was expected for micelle formation, but could not be observed.

The diffusion coefficient of the polypeptide was determined to

$$D_{\text{c25-mms6}} = \frac{\omega_0^2}{4 \cdot \tau_{\text{D,c25-mms6}}} = 2.43 \times 10^{-10}\,\text{m}^2 \cdot \text{s}^{-1} \tag{29}$$

using the average diffusion time $\tau_{\text{D,c25-mms6}} = 330\,\mu\text{s}$ and the focal radius of the setup $\omega_0 = 568.4\,\text{nm}$. The average diffusion time is the mean diffusion time of the three concentration based measured diffusion times. The focal radius of the setup was determined in the device section in the FCS chapter.

The hydrodynamic radius can be calculated using the Stokes-Einstein equation

$$D_{\text{c25-mms6}} = \frac{k_B T}{6 \cdot \pi \cdot \eta(T) \cdot R_H} \tag{30}$$

with D as the diffusion coefficient, the Boltzmann constant $k_B = 1.38 \times 10^{-23}\,\text{J} \cdot \text{K}^{-1}$, T as the temperature in Kelvin, $\eta(T)$ as the viscosity and R_H as the hydrodynamical radius. For room temperature T=298 K, $\eta(T) = 0.0009\,\text{N} \cdot \text{s} \cdot \text{m}^{-2}$ [50], the hydrodynamic radius was calculated to $R_H = 1.1\,\text{nm}$. These measurements show neither a concentration based aggregation nor the required hydrodynamic

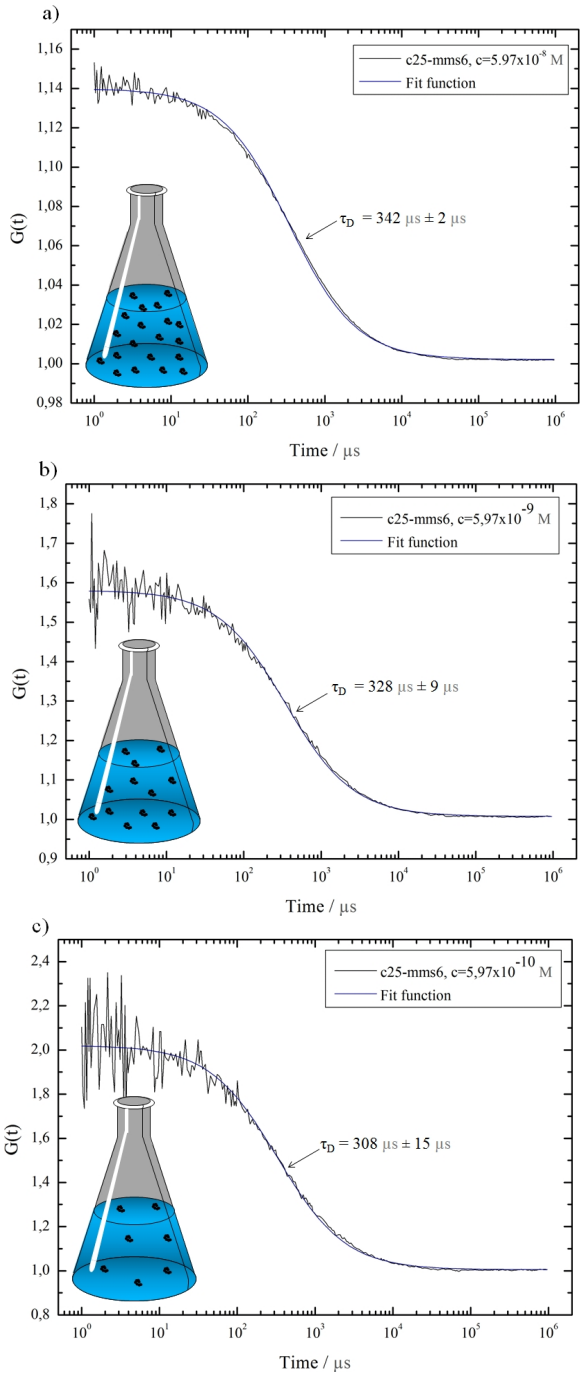

Figure 58: Correlation functions of the different peptide concentrations. The time dependent fluorescence signal was fitted using the simple diffusion model. (a) Data for an increased peptide concentration. (b) Data for the original concentration, used in the biosynthesis. (c) Data for a decreased peptide concentration. The flasks in the left corner illustrate the different peptide concentrations.

radius close to the nanoparticle diameter of around 50 nm. Prozorov's hypothesis of micelle formation is thus unlikely. Another interaction mechanism, in which single polypeptides adsorb or bind onto the nanoparticles, is more likely.

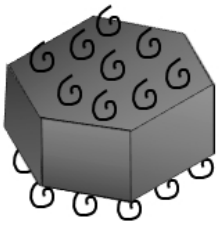

Figure 59: Adsorption mechanism, in which the polypeptides bind onto the nanoparticle. A face specific interaction is sketched here.

Peptide-nanoparticle interaction

The first set of measurements showed that micelle formation does not occur. Instead a single peptide-nanoparticle interaction, as sketched in Figure 59, is more likely.

To determine the type and strength of the interaction between peptide and nanoparticle, the bioinspired particles were synthesized using four different peptide concentrations. The strength of the interaction can be extrapolated from the concentration based change in results. Binding molecules change the hydrodynamic radius of the sample and hence lead to a change in diffusion time, which can be measured.

TEM evaluations of the nanoparticles, given in Figure 60, show that the labelling did not affect particle growth. The microstructure and morphology of the particles synthesized with the labelled polypeptide were investigated with the TEM after 1 day. The TEM image with an EDX spectrum, verifying the cobalt, iron and oxygen within the nanoparticles[58] is given in Figure 60. The average diameter was determined to $D_{av} = 40\,\text{nm} \pm 29\,\text{nm}$ for 420 particles. 52 % of these particles are hexagonally-shaped, which is in good agreement with the biosynthesis.

[58] All other elements are either side products within the nanoparticle suspension or elements in the DualBeam device used for the EDX measurements.

Figure 63 shows the obtained curves with respect to the different peptide concentrations. The FCS signal of the bioinspired nanoparticles with the normal, slightly increased and lowered peptide concentration (Figure 63 (a)-(c)) do not correlate, indicating that a quenching process occurs.

To verify the quenching, the solution with the original synthesis concentration $c = 6.92 \times 10^{-9}$M was diluted to 1:100 as well as 1:1000. The measured count rates of the free peptide with an equivalent concentration to the original biosynthesis as well as the different dilutions of the complex were compared to each other. The count rates can be found in Table 6. A comparison of the count rate for the nanoparticle-peptide complex to the free peptides shows that

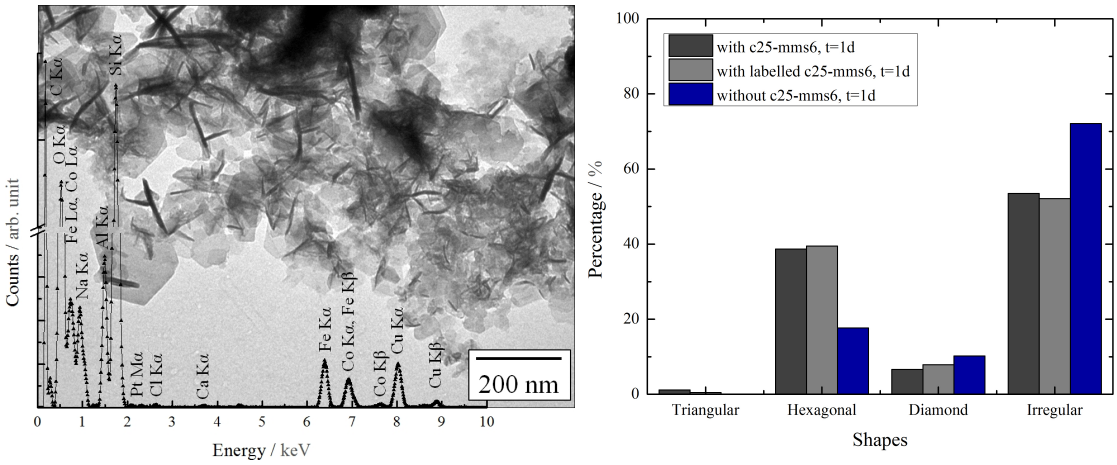

Figure 60: Left: TEM image with an EDX spectrum of the nanoparticles, synthesized with the labelled polypeptide. Platinum and aluminium do not belong to the sample. The platinum contaminations within the DualBeam chamber and aluminium are always recorded when measuring an EDX spectrum of a TEM grid since elements below the TEM grid (on the sample holder) are also detected. Right: Percentage of shapes observed for the Rhodamin labelled c25-mms6 synthesized particles in comparison to the original biosynthesis and the control experiment.

the count rate for the complex is significantly reduced in comparison to the count rate of the free peptide with equivalent concentration. This effect can be explained by a quenching process. The quenching process is sketched in Figure 62. Furthermore, the first dilution (1:100) increases the count rate. The dilution disturbs the equilibrium and removes peptides from the nanoparticle surface. Quenching does not occur anymore and therefore leads to an increased count rate despite the lower concentration. A lower concentration normally leads to a reduced count rate for non-quenched systems. A further dilution of the disturbed system reduces the amount of peptides and thus leads to a reduced count rate.

Particles with the highest peptide concentration (see Figure 63 (d)) display a correlated intensity signal. The diffusion time

Complex	Count rate kHz
Peptide	3.36 ± 0.65
Peptide-NP	0.54 ± 0.04
Peptide-NP diluted 1:100	1.2 ± 0.03
Peptide-NP diluted 1:1000	0.9 ± 0.003

Table 6: Count rates for the free peptide, the peptide-nanoparticle complex with an equivalent peptide concentration as well as two diluted peptide-nanoparticle complexes.

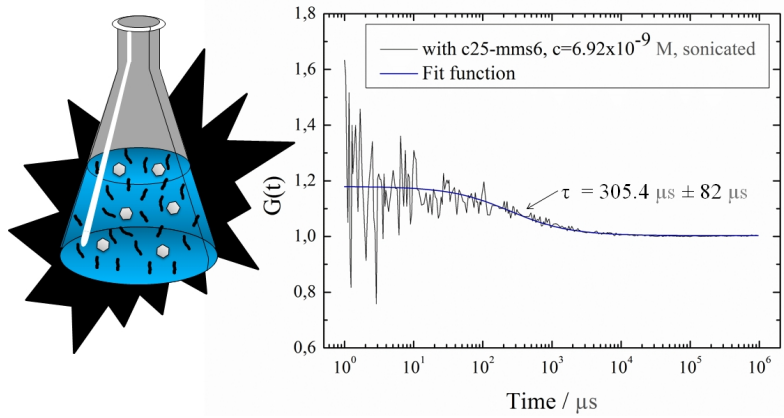

Figure 61: Time dependent fluorescence signal for the sonicated c25-mms6 - nanoparticle complex. The flask on the left hand side illustrates that the peptides are removed from the nanoparticle surface by sonication.

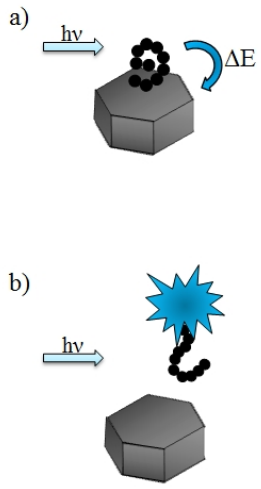

Figure 62: Schematic of the quenching and fluorescence process. (a) For an attached peptide, an energy transfer from the excited fluorphore on the peptide to the nanoparticle occurs. (b) A free peptide emits a photon when excited, since no energy transfer to the nanoparticle occurs.

$\tau_D = 465\,\mu s \pm 179\,\mu s$, however, corresponds to that of the peptides in solution within the measurement error. The measurements indicate that at this high concentration all binding sites on the nanoparticle are saturated and that some proteins are left in solution which are not quenched and give a signal. More white noise in comparison to the peptide-only-solution leads to a larger error.

The quenching interferes with the binding strength evaluation since no correlated signals are obtained. To obtain some information about the binding strength despite the quenching process, the sample with the original synthesis concentration $c = 6.92 \times 10^{-9}$M was sonicated and then measured. The obtained FCS spectrum is given in Figure 61. The mean diffusion time of the sonicated sample was determined to $\tau_D = 305.4\,\mu s \pm 82\,\mu s$. The diffusion time corresponds to the free peptide, indicating that sonication removes the peptide from the nanoparticle surface. A chemical binding type is thus unlikely. Adsorption is the most likely mechanism. Adsorption is advantegeous for applications since the peptides can easily be removed after the synthesis.

Discussion

The measurements show that the peptides adsorb onto the nanoparticle surface. To estimate how many nanoparticles adsorb, the

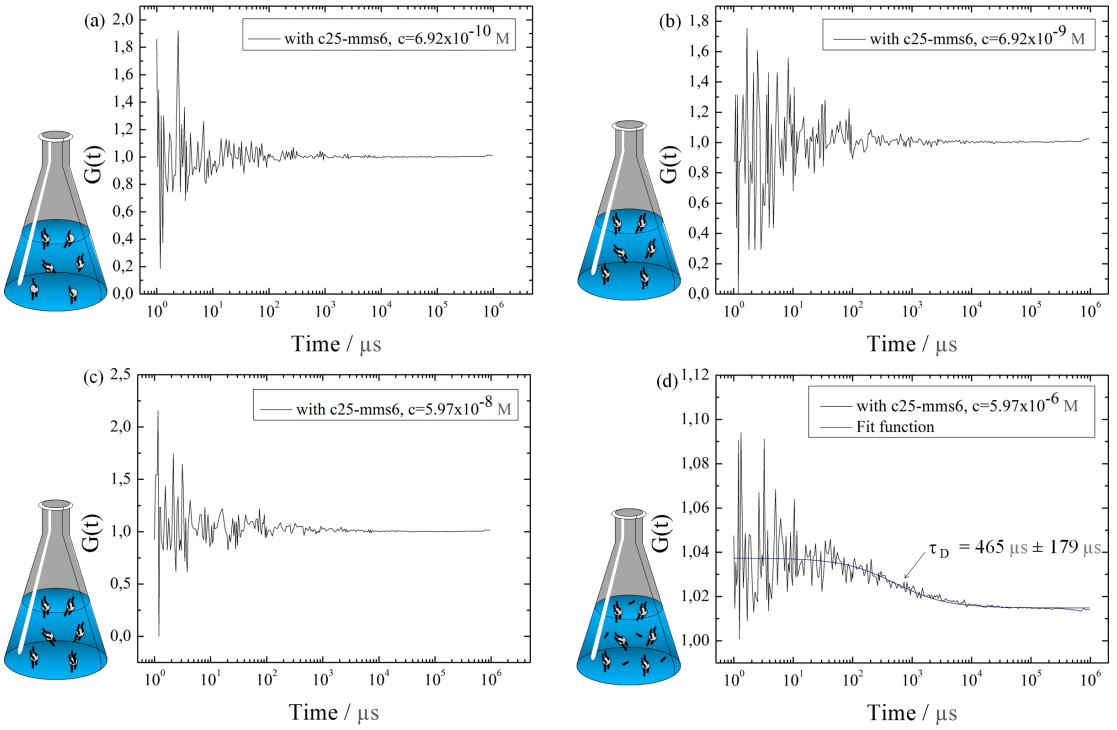

Figure 63: FCS measurements of the c25-mms6 - nanoparticle complex for different peptide concentrations: (a) reduced concentration (b) original concentration, (c) slightly increased concentration, (d) highly increased concentration. The flasks on the left hand side of the data illustrate the peptide-nanoparticle ratio. The interaction of the peptide and nanoparticles is displayed inaccurately in the flasks. The peptide does not stretch out and interact with one end. This incorrect drawing was chosen for a better visualization.

average area of the different nanoparticle faces as well as the average area of the peptide is calculated. The number of adsorbed peptides can be calculated from the comparison:

$$A_{NP} = N_{Peptid} \cdot A_{Peptid} \tag{31}$$

where A_{NP} is the nanoparticle surface, N_{Peptid} is the number of peptides, and A_{Peptid} is the area of a single peptide required for an adsorption process. The area that a single peptide occupies on a nanoparticle can be calculated using:

$$A_{Peptid} = \pi \cdot r^2 = 3.8\,\mathrm{nm}^2 \tag{32}$$

with the hydrodynamic radius $r = R_H = 1.1$ nm determined in the FCS measurements.

The surface area of a single hexagonally-shaped nanoparticle, sketched in Figure 64, can be calculated by

$$A_{NP} = 2 \cdot A_h + 6 \cdot A_d \tag{33}$$

with

$$A_h = \frac{3\sqrt{3}}{2} \cdot s^2 = 1167\,\mathrm{nm}^2 \tag{34}$$

$$A_d = z \cdot s = 212\,\mathrm{nm}^2 \tag{35}$$

for $z = 10\,\mathrm{nm}$, and $s = 21\,\mathrm{nm}$ which are the dimensions of a final nanoparticle[59]. $N_{Peptide} = 949$ peptides can bind on a single nanoparticle, $N_{Peptide} = 614$ peptides bind on the A_h surfaces and $N_{Peptide} = 335$ peptides bind on the side faces A_d. Whether a face specific interaction occurs cannot be determined from these measurements since the amount of particles obtained in a synthesis is unknown and cannot be measured.

[59] These dimensions were determined in EELS and TEM measurements. s was determined from the TEM images with the relation 2s=d with d as the particle diameter.

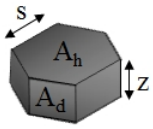

Figure 64: Geometry of a hexagonally-shaped nanoparticle. The size $s = \frac{d}{2}$ with d as the nanoparticle diameter and z as the nanoparticle thickness. A_h are the top/bottom surfaces. A_d represents the side surfaces.

However, electron diffraction measurements of the biosynthesized particles after 28 days allow the interpretation of a face specific adsorption. Figure 65 shows an electron diffraction pattern of a truncated hexagonal disc. This disc displays the (111) top/bottom crystal face as well as the (-211) top/bottom crystal face. The crystal faces were determined by indexing the zone axis (ZA) of the electron diffraction pattern. The circled reflexes belong to the [111] ZA while the reflexes marked with rectangles belong to the [-211] ZA. The non indexed reflexes belong to the [111] ZA of a tilted electron diffraction pattern. The (222), (333), reflexes of the [-211] ZA are closer to the primary beam than literature, indicating a distorted crystal structure along the body diagonal. The crystal structure is stretched along this diagonal by 3%. The lattice parameter is similar to that of magnetite which is synthesized within MTB. An increase in the body diagonal can also be observed in the magnetite nanoparticles with magnetotactic bacteria [72], indicating that the interaction mechanism of c25-mms6 and the inorganic crystal is face specific. Face specific peptide-inorganic crystal interaction has previously been reported [157]. Despite this interpretation, a face specific adsorption is not verified and requires further studies.

Simulation

Peptide simulations were carried out to further study the interaction between the polypeptide and the nanoparticle. The simulations,

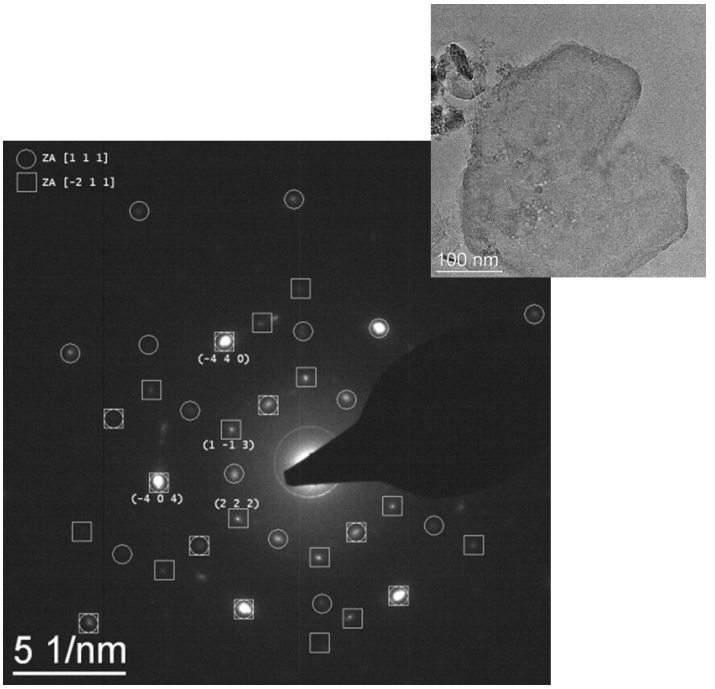

Figure 65: Electron diffraction pattern of a truncated hexagonally-shaped disc, obtained in the biosynthesis. The reflexes are labelled in accordance with their ZA.

carried out by Cemil Yigit at the Helmholtz-Zentrum Berlin für Materialien und Energie GmbH, show the peptide conformation within the peptide solution. The conformation gives information about possible interaction mechanisms between the peptide and the inorganic crystal. An equilibration, neccessary to get the starting structure in a local energy minimum prior to the molecular dynamic (MD) simulation, was done for 5 ns. The peptide was afterwards simulated for 1 µs using the SPC/E model with H_2O as explicit solvent molecules. Sodium ions were added to obtain a charge neutralized system (sodium was found in the EDX spectra of all samples studied in this work (see Figure 60)). The simulated c25-mms6 conformation is displayed in Figure 66. An equal mass of all non-hydrogen atoms is assumed in this model [208]. The gyration radius of the peptide was determined to $r_g = 0.9$ nm using

$$R_g^2 = \sum_{i=1}^{N} \frac{(r_i - R_c)^2}{N} \tag{36}$$

with R_c as the center of mass, r_i as the i^{th} coordinate radius and N

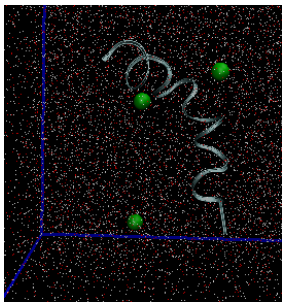

Figure 66: Result of the MD simulation: the synthetic polypeptide shows a helical conformation. The sodium ions are represented by the green spheres. The solvent molecules are represented by the blue dots. The blue lines represent the x-, y- and z-axis.

as the number of non-hydrogen atoms which is in good agreement with the measured hydrodynamic radius $r_H = 1.1\,nm$ in the FCS measurements, considering that the fluorescent label rhodaminB contributes to the hydrodynamic radius. The simulation shows that c25-mms6 forms an α-helix. A dipole moment is associated with the helical structure which was determined to be $5.71 \times 10^{-28}\,C \cdot m$ from the simulation. The simulation indicates that the interaction between the polypeptide and the inorganic crystal could be caused by electrostatic interaction with a monopole-dipole interaction between the peptide and the iron or cobalt ions in the lattice of the cobalt ferrite crystal. This interaction however cannot be simulated at present due to a lack of reliable literature values (f.e. Lenard-Jones parameters) for the iron and cobalt ions Fe^{3+}, Co^{2+} and Co^{3+}. Whether conformational changes occur in the presence of the cobalt and iron ions cannot be predicted by this simulation.

Circular dichroism (CD) spectroscopy was performed by Marco Wissbrock to verify the simulated secondary structure obtained in the simulation. The wavelength was scanned between 190 nm to 300 nm with interval steps of 0.1 nm. The CD spectra, given in Figure 67 do not show a helicity of the polypeptide but a random coil. A possible cause for the discrepancy could be the different conditions (sodium concentrations) in the simulation and the experiment. A high concentration of sodium ions was present in the simulation and absent in the CD spectroscopy measurements since the high sodium concentration does not allow CD spectroscopy measurements. Instead a lower sodium concentration (in comparison to the simulation) was chosen for the CD measurments which did not increase the helicity. However, the difference in sodium concentration in the measurement and the simulation is still significantly large and therefore does not allow a direct comparison. Helicity could only be observed by adding 20 % trifluoroethanol (TFE), however, almost all peptides form α-helices at this TFE concentration [209]. Due to the discrepancy in conditions between the simulation and the CD spectroscopy it is not possible to experimentally verify the simulated peptide conformation and thus possible interaction mechanisms. Whether or not α-helices form, which would point to a possible monopole-dipole interaction, cannot satisfactorally be determined. If the sodium ions cause the discrepancy, the cobalt and iron ions

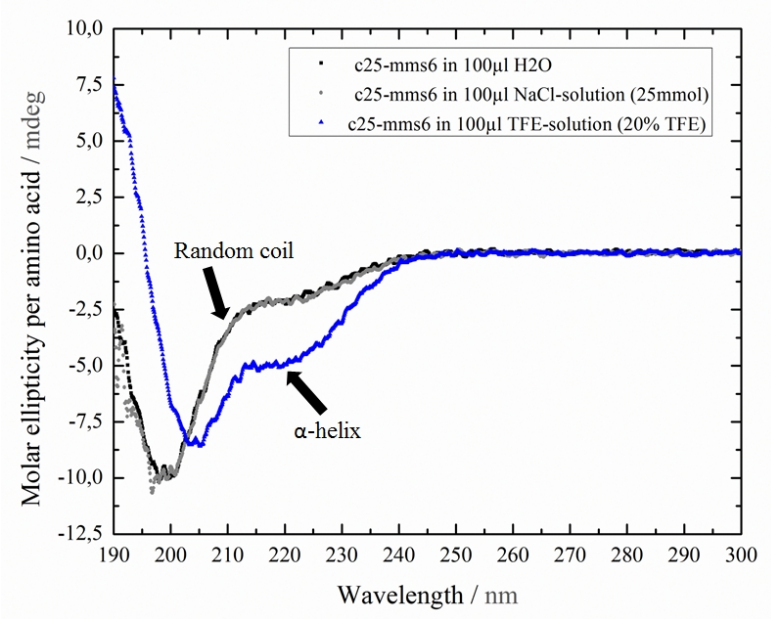

Figure 67: CD spectra of c25-mms6. The black spectrum corresponds to c25-mms6 in distilled water, the grey spectrum to c25-mms6 in NaCl-solution (25 mM) and the blue spectrum corresponds to c25-mms6 in TFE solution (20 % TFE). A random coil can be observed for the distilled water and NaCl solution. The polypeptide forms an α-helix in the TFE solution.

could also possibly influence the peptide conformation and this cannot be studied until useful literature values for cobalt and iron, as well as a method in which the peptide conformation in the presence of the different ions can be measured are available.

Active Center

To better understand the function of c25-mms6 in the peptide-nanoparticle interaction, different sections of the peptide as well as a randomized sequence of the peptide were used to synthesize the cobalt ferrite nanoparticles. The obtained nanoparticles are compared to the original biosynthesis and a control experiment without any peptide after 5 days. The different sections were used to determine whether c25-mms6 can be further reduced and to evaluate the active areas of the peptide. The randomized sequence was used to determine the influence of the primary structure of the peptide and therefore whether the peptide has a specific function or if it can be replaced by similar peptides or ligands of similar size.

Synthesis

The syntheses were carried out analogously to the previous ones. However in these four syntheses, c25-mms6 was replaced by the different peptides. The characteristics of the different peptides are given in Table 7. Figure 68 shows the different peptides used in the experiments. The N-terminal peptide consists of the first 8 amino acids of c25-mms6. The C-terminal peptide consists of the last 9 amino acids of c25-mms6. The remaining 8 amino acids, located in the middle section of c25-mms6, form the middle section peptide. The randomized sequence peptide has the same length, molecular weight, and amounts of acidic, alkaline, hydrophilic, and hydrophobic amino acids as c25-mms6. However, the sequence of the amino acids is altered.

Results

TEM images of the nanoparticles obtained after 5 days in the original synthesis with c25-mms6, in the control experiment without any peptide, in the experiments with the different sections, as well as in the randomized sequence are displayed in Figure 70. Nanoparticles could not be obtained for the N-terminal and middle section of the polypeptide. Only small crystallites were obtained. These measurements show that the N-terminal and middle section of c25-mms6 prevent nanoparticle growth. Nanoparticles were only obtained for the C-terminal and the randomized sequence. The C-terminal particles, with a diameter of $D = 24\,\text{nm} \pm 13\,\text{nm}$ are smaller in comparison to the bioysnthesis. The majority of particles (74 %) are irregularly-shaped, as shown in Figure 73. The size distribution of the particles synthesized with the C-terminal of c25

Table 7: Properties of the peptides, used in this experiment. The properties of the randomized sequence (Random) are equivalent to those of the original c25-mms6. The difference between these peptides is their amino acid sequence. The values were obtained from [204].

Properties	N terminal	Middle section	C terminal	Random
Net charge at pH7	1	-3	-2	-4
acidic AA	1	3	3	7
alkaline AA	2	0	1	3
hydrophilic AA	3	3	0	6
hydrophobic AA	2	2	5	9

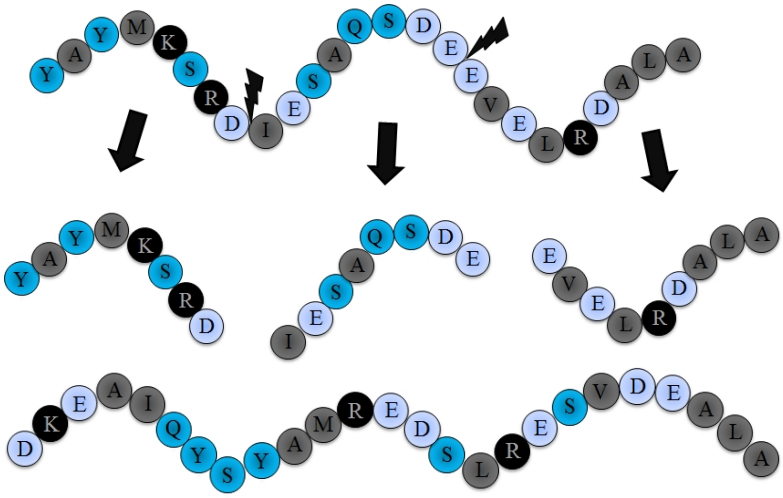

Figure 68: Different peptides used in the syntheses to determine the active center as well as the influence of the primary structure of the peptide on nanoparticle growth. Top: c25-mms6, middle: different areas of the peptide c25-mms6, Bottom: randomized sequence.

-mms6, given in Figure 70 is lognormally distributed, indicating that Ostwald ripening already occurs at this stage of the growth process. HRTEM measurements show that these particles are unstable. They disintegrate during the HRTEM measurements, as shown in Figure 71. This effect was also observed for the control experiment particles, which were synthesized without a polypepide. In contrast, stable nanoparticles were obtained in the c25-mms6 synthesis. The measurements show that the C-terminal nanoparticles are similar to the control experiment particles. The presence of the elements cobalt and iron within the nanoparticles was verified using STEM and EDX measurements (see Figure 73). The corresponding mapping in Figure 74 shows that the discs are richer in cobalt while the spheres are richer in iron which is in good agreement with previous studies [134]. The XRD spectrum of these particles, displayed in Figure 71, shows features of both the control experiment (blue arrows) as well as the original biosynthesis (black arrows). It indicates that the C-terminal has an effect on the particle composition since several peaks for the stoichiometric cobalt-rich phase can be indexed in the spectrum, but cannot form the biosynthesized nanoparticles completely.

The random sequence particles, with a diameter of $D = 29\,\text{nm} \pm 17\,\text{nm}$ are smaller in comparison to the original biosynthesis. Their

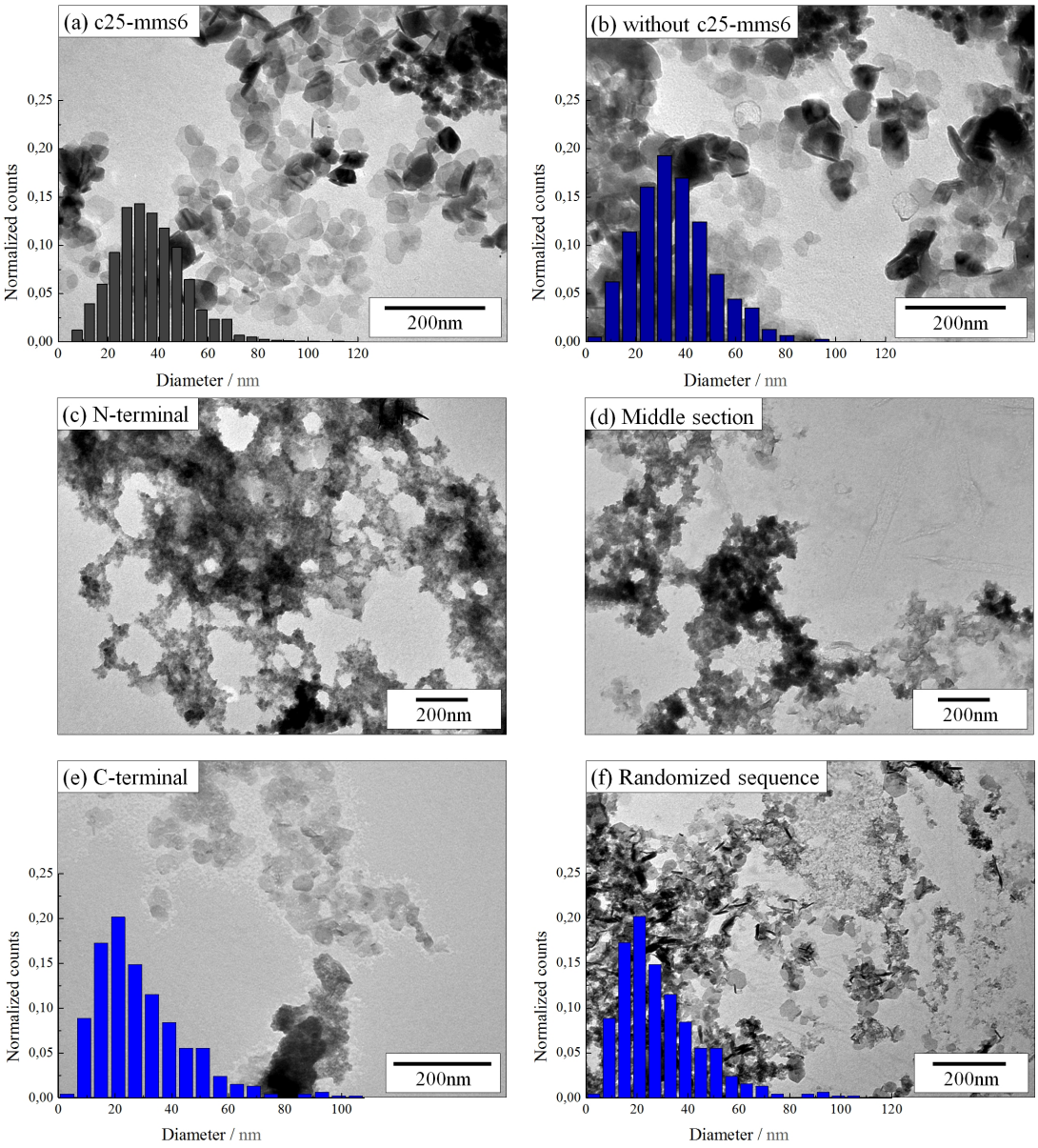

Figure 69: TEM images of the nanoparticles after 5 days obained in the original synthesis, the control experiment, the N-terminal, the middle section, and the C-terminal synthesis as well as for the randomized sequence. The size distributions were normalized with respect to the number of nanoparticles used in the evaluation. For the c25-mms6 synthesis, 1568 particles were evaluated. 772 particles were used in the evaluation of the control experiment, 415 nanoparticles were evaluated in the C-terminal synthesis, and 451 particles synthesized with the randomized sequence were evaluated. Size distributions for the N-terminal and middle section are not given since no particles were obtained in these approaches.

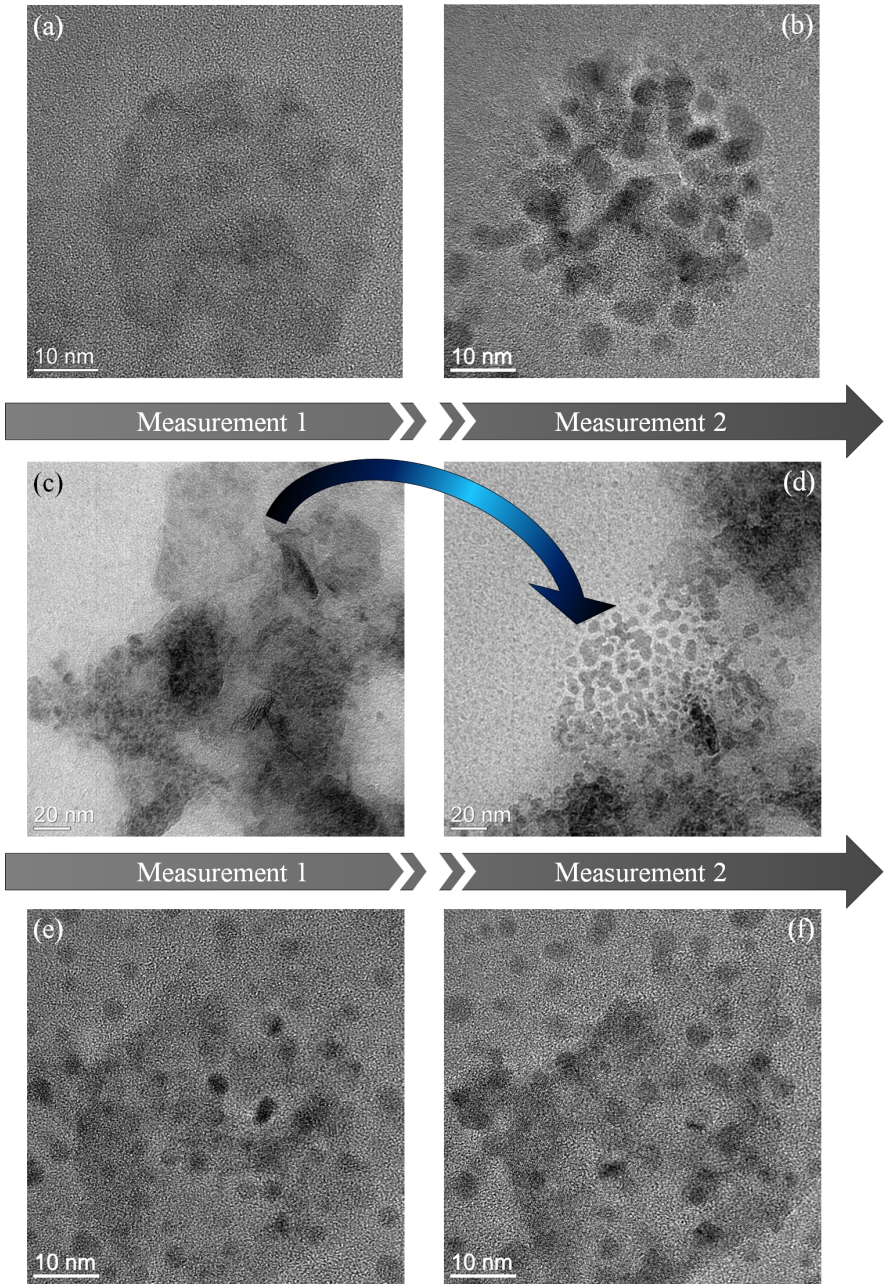

Figure 70: HRTEM images of the control experiment particles (a)-(b), the particles synthesized with the C-terminal of c25-mms6 (c)-(d) and the original biosynthesis (e)-(f). The HRTEM images were taken in succession and show that the control experiment nanoparticles as well as the C-terminal particles disintegrate during the measurements and are hence unstable. The nanoparticles, obtained in the original biosythesis, are stable.

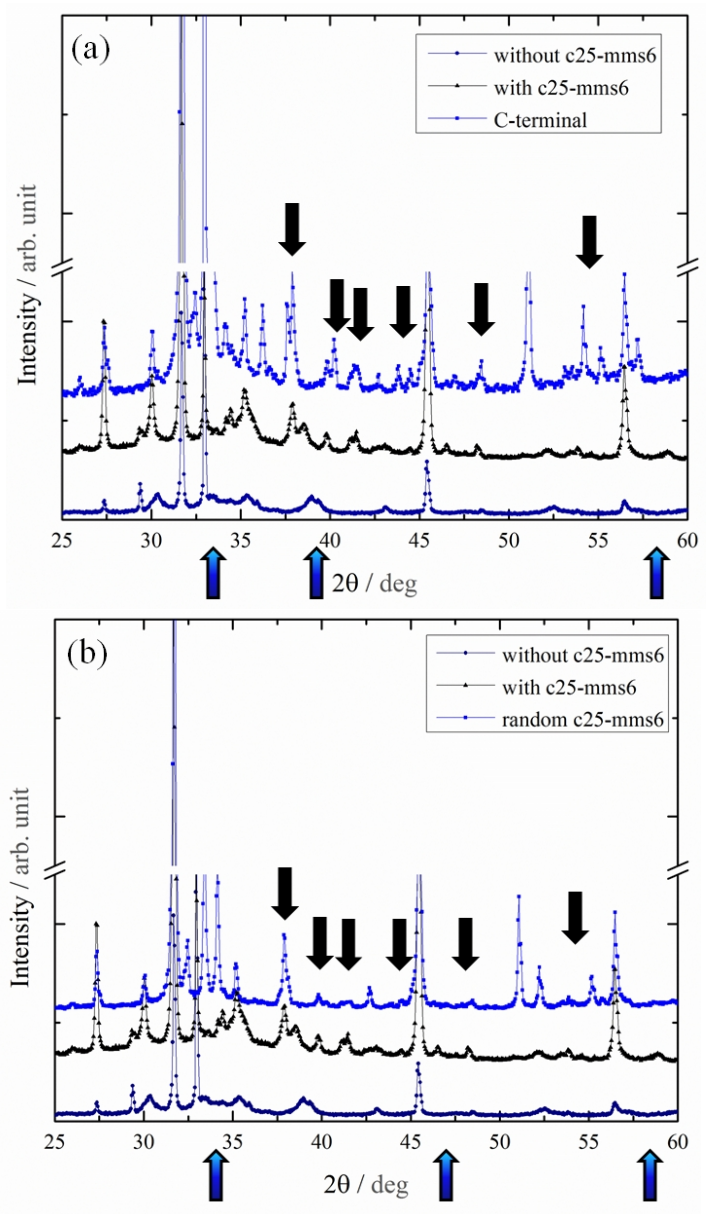

Figure 71: XRD measurements of the control experiment particles (dark blue spheres), and the biosynthesis (black triangles) in comparison to (a) the C-terminal synthesis (blue rectangles) and (b) the randomized sequence (blue rectangles). The black arrows indicate the similarities to the biosynthesis, the blue arrows mark the control experiment features. An offset between the measurements was inserted to allow for a better visualization and comparison of the spectra.

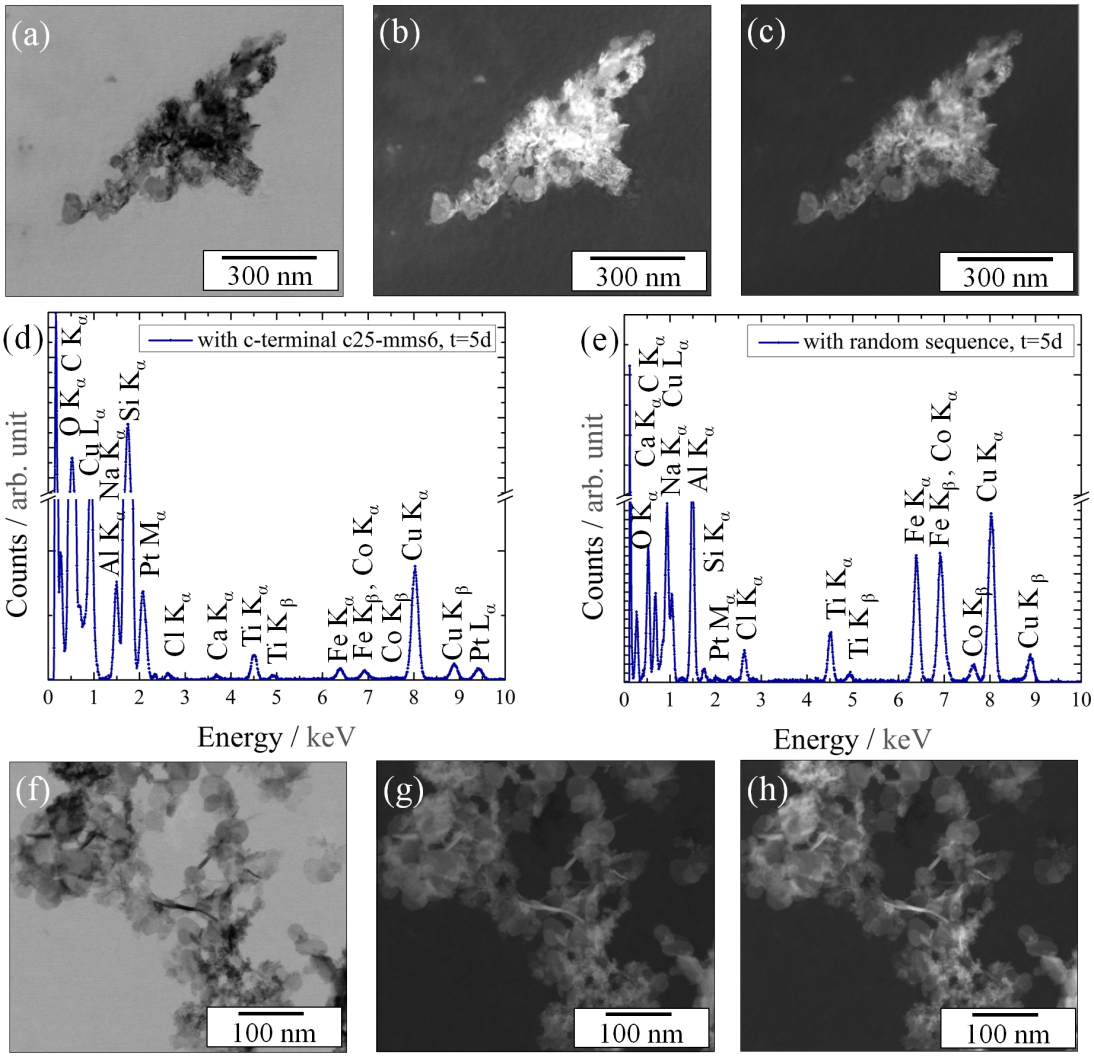

Figure 72: STEM, EDX and XRD measurements of the particles obtained in the C-terminal and randomized sequence syntheses. The STEM images were recorded using a voltage of 20 kV and a current of 86 pA. The EDX measurements, corresponding to the STEM images, were recorded using a dwelltime of 900 ms to allow a mapping using a voltage of 20 kV and a current of 1.4 nA. The platinum, aluminium and titanium peaks do not belong to the sample. When measuring a thin TEM grid, the sample holder and contaminations within the DualBeam device are also recorded.

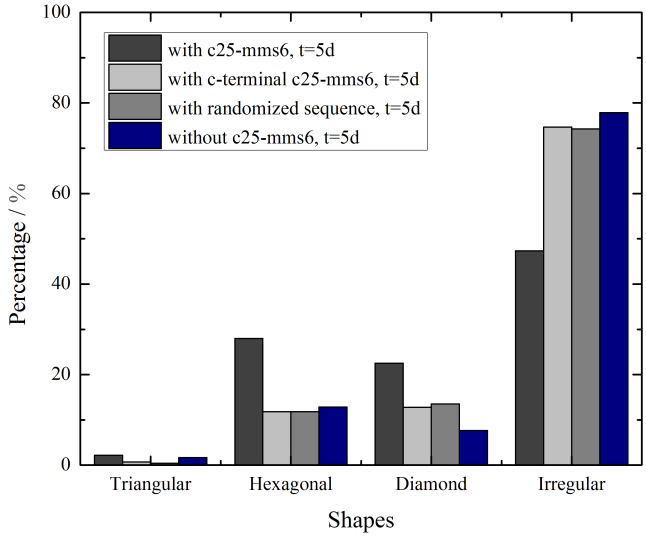

Figure 73: Percentage of different shapes, obtained with c25-mms6, with the C-terminal of c25-mms6, with the randomized sequence of c25-mms6 as well as the control experiment after 5 days of the particle growth.

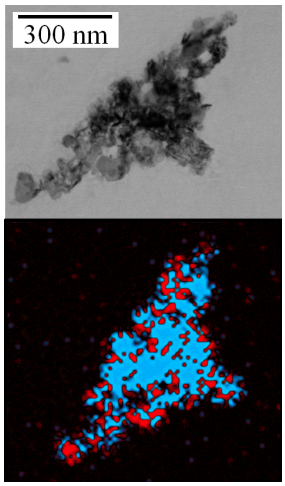

Figure 74: Mapping of the nanoparticles synthesized with the C-terminal. Cobalt is displayed in red and iron is displayed in blue. The mapping of the nanoparticles, given in the STEM image in Figure II shows that regions in which the discs are prominent are rich in cobalt while the regions with predominantly smaller spheres are iron-rich. This mapping shows the phase separation of smaller, iron-rich spheres and cobalt-rich discs.

size distribution is also lognormally distributed (Figure 70). These particles are also mostly irregularly-shaped, as shown in Figure 73, and thus display the same morphology as the control experiment particles. The STEM and EDX measurements in Figure 73 verify the presence of cobalt and iron within the nanoparticles. The XRD spectrum of these particles is more similar to the control experiment spectrum (see Figure 71).

Discussion

A comparison of the particles synthesized with the C-terminal and the randomized sequence to the biosynthesis and control experiment shows that the microstructure and morphology matches the description of the control experiment particles. The bioinspired nanoparticles obtained in the biosynthesis employing c25-mms6 could not be obtained by using sections of the peptide or a randomized sequence of the amino acids. These measurements show that the polypeptide cannot be further reduced and that c25-mms6 cannot be replaced by a randomized peptide sequence. The N-terminal and middle section of c25-mms6 are likely involved in the peptide-inorganic crystal interaction while the C-terminal has a specific function.

The results show that neither single parts of the peptide nor

a randomized sequence of the peptide can be used to obtain the bioinspired nanoparticles. Particles could not be obtained for the N-terminal and middle section of c25-mms6. The net charge of the peptides cannot be linked to nanoparticle formation since particle formation was prevented by the positively charged N-terminal as well as the negatively charged middle section. A possible explaination is that those peptide sections interact with the nanoparticles and without the rest of the peptide neccessary for the function of the peptide, block particle growth. Discs were only obtained for the C-terminal and the randomized sequence. The evaluation of these particles, however, shows that these are more similar to the control experiment particles. The morphology of the particles corresponds to that of the control experiment nanoparticles. The particles obtained in the C-terminal synthesis are unstable. This was also found for the control experiment particles and stands in contrast to the biosynthesis. Even though the XRD spectrum of the C-terminal particles (Figure 71) indicates the existence of the Co_2FeO_4 phase, which should be verified in further EELS measurements, it cannot be used instead of c25-mms6 since control experiment features are still present in the XRD spectrum and the morphology of the particles only matches the control experiment particles. The emerging biosynthesis features in the XRD spectrum for the randomized sequence, indicated by the black arrows, can be explained by the similarity between the C-terminal of c25-mms6 and the C-terminal of the randomized sequence. All but one amino acid are the same with only a slightly deviating sequence between the original C-terminal and the randomized C-terminal.

The results show that c25-mms6 cannot be further shortened into oligopeptides and suggest that the N-terminal and middle section of c25-mms6 are involved in the peptide-nanoparticle interaction while the C-terminal has a specific function which is involved in the phase transformation towards the stoichiometric cobalt-rich phase. The randomized sequence shows that the primary structure, which determines the secondary structure of the protein and thus its function, is of vital importance for the function. It can hence be assumed that c25-mms6 has a function rather than acting as a ligand type molecule only. The function of the peptide, however, could not be determined from these experiments and requires further

investigation.

Summary

This chapter shows that the previously hypothesized interaction mechanism for c25-mms6 and cobalt ferrites is inaccurate. The peptides adsorb onto the nanoparticle surface like ligands. The diffusion constant of c25-mms6 was determined to $D_{c25-mms6} = 2.43 \times 10^{-10}\,\mathrm{m}^2 \cdot \mathrm{s}^{-1}$ in the FCS measurements. The measurements furthermore show that the polypeptide can easily be removed from the nanoparticle surface by sonication which is of great advantage for applications.

Synthesizing the nanoparticles with different sections of c25-mms6 as well as a randomized sequence shows that the polypeptide not only adsorbs onto the nanoparticles but that it has a function that is dependent on the primary structure. The polypeptide therefore cannot be replaced by similar polypeptides, randomized sequences of c25-mms6 or ligands with the same length. The evaluation further showed that c25-mms6 cannot be shortened to oligopeptides without loosing its function.

Influence of c25-mms6 on particle growth and physical properties

The influence of the synthetic polypeptide c25-mms6 on nanoparticle growth is discussed in this chapter. Understanding the growth process in the bioinspired synthesis not only gives information about the effect of c25-mms6 on cobalt ferrite nanoparticles but also reveals the mechanism with which the nanoparticles form. This knowledge is of vital importance if the particle properties are to be tailored for applications since the physical properties depend on the microstructure, morphology, and composition of the particles. The influence of c25-mms6 on the magnetic properties is discussed later in the chapter and related to possible influences in the growth process.

Analytical methods

The composition, morphology and microstructure of bioinspired synthesized nanoparticles and control experiment nanoparticles (synthesized without c25-mms6) were studied at different stages of the growth process using transmission electron microscopy (TEM), high resolution transmission electron microscopy (HRTEM), electron energy loss spectroscopy (EELS), electron diffraction, and X-ray diffraction (XRD) measurements. Only a combination of these techniques allows a useful determination of the nanoparticle properties due to the complexity of the inorganic crystal. Previous studies of this system [134] showed a lattice distortion of 3 % in comparison to the literature value as well as the existence of several intermediate phases, making it difficult to evaluate the particle properties solely

by EDX or XRD which measure an ensemble of particles and their phases only.

Dynamic light scattering, conventionally the method of choice to analyze reaction kinetics and nanoparticle growth, was found to be unsuitable in this study due to nanoparticle agglomeration and sedimentation. To study crystal growth, TEM samples were prepared at different stages of the growth process and the diameter evaluated manually for each sample. The kinetic of the growth process was obtained this way. For the TEM, HRTEM, EELS, EFTEM, and electron diffraction measurements, 2 µL of the particle suspension was dropcasted onto either carbon coated TEM-grids or silicon dioxide coated TEM grids[60] which were purchased from Plano GmbH. Excess solution was removed using filter paper.

[60] Carbon coated TEM grids are advantageous for TEM. However they lead to a significant carbon contamination in the DualBeam device. Silicon oxide coated TEM grids are the material of choice for the DualBeam analysis.

The microstructure and morphology of the particles was studied using the Philips CM100 TEM as well as the FEI TECNAI F20 HRTEM. The quantitative analysis of the size and shape was performed manually by measuring the nanoparticle sizes and counting the shapes in the TEM images using the program Scion. A statistically sufficient amount of nanoparticles was used for the quantitative analysis. The change in morphology with time was studied by evaluating the percentage of specific nanoparticle shapes at the different stages of crystal growth. Furthermore, electron diffraction measurements and selected FFTs of HRTEM images were used to determine the top/bottom crystal faces of the nanoparticles by indexing the zone axis (ZA)[61]. Electron diffraction is only useful if a single particles can be measured in an area with a 200 nm radius. For more densely packed regions of interest, the local information of a single nanoparticle can be obtained from the FFT of the HRTEM images, which also show the lattice in the reciprocal space. The electron diffraction patterns and FFTs were indexed using the Program Digital Micrograph. The theoretical diffraction pattern of $CoFe_2O_4$ was used to index the specific reflexes and ZA.

[61] Only the top/bottom crystal face can be determined this way. In the following chapters, the determined top and bottom crystal faces are often only referred to as crystal faces for ease of reading.

TEM was chosen over the STEM inside the Dualbeam since the nanoparticles were dropcasted directly from the reaction suspension and thus the reaction residue forms a coating layer on the nanoparticles which leads to a poor resolution for a lower applied voltage in the STEM. The difference between the two methods is illustrated in Figure 75. Furthermore, the TEM allowed the study of

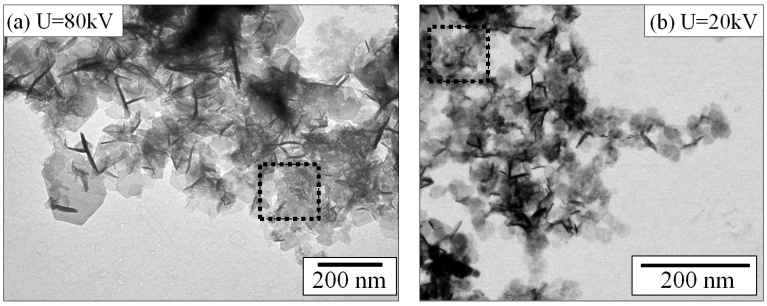

Figure 75: A comparison of a (a) TEM and (b) STEM image of the biosynthesized particles shows that smaller discs are clearly visible in denser areas in the TEM image, while these discs are hardly visible in the STEM image.

cracked windows in the grids which would have been torn during the STEM measurements. Cracked windows were obtained after drop-casting the particle suspension of the early stages of the crystal growth process onto the grid due to the unfinished chemical reaction which corrodes the TEM grids.

The composition of the particle ensemble was studied using EDX. The Helios Nanolab600 Dual Beam device was used for the EDX measurements. EELS measurements allowed single particle composition measurements as well as several measurements within a single nanoparticle with larger diameters. The TECNAI F20 HRTEM together with a Gatan GIF Tridem spectrometer were used for the EELS measurements. The local composition within single particles was measured using a spectrometer entrance aperture to select regions with a diameter of $\approx 25\,\text{nm}$ within the nanoparticle. The EELS spectra from which the composition of the single nanoparticles was determined are given in the Appendix C as supplementary data to improve readability. For the quantitative analysis, from which the particle composition was determined, the pre-edge background was subtracted from the recorded EELS spectra, leaving only the element specific absorption edges. For this, a power-law fit was performed which is indicated by the dashed curve in Figure 76. The peak intensities were then quantified using the Hatree-Slater model and the signals shown as gray areas in the spectrum (see Figure 76). The quantified EELS measurements of the elements cobalt and iron, with an accuracy of 10 %, were used to determine the composition of the cobalt ferrites $Co_xFe_{3-x}O_4$. All HRTEM, EELS and electron

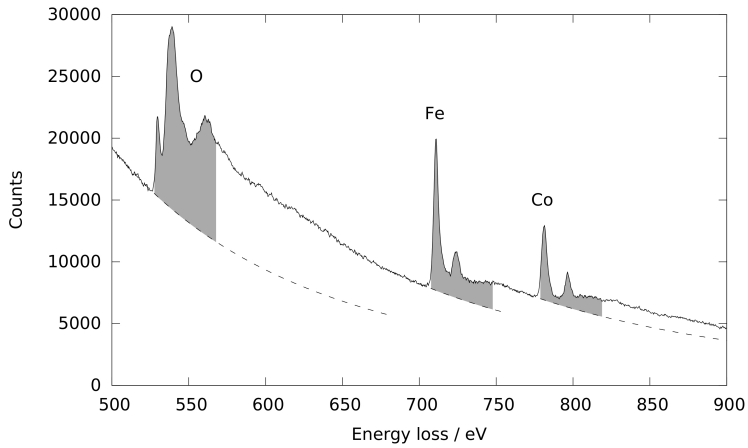

Figure 76: Exemplary EELS spectrum of a biosynthesized particle after 1 day which was used to determine the nanoparticle composition. An exposure time of 10 s was used to record the spectrum. The recorded spectrum is displayed by the solid line. The signals which were used for the quantitative analysis are given as gray areas. For convenience, the EELS edges are labelled with the corresponding elemental abbreviations. The power-law fit, performed to subtract the pre-edge background is displayed by the dashed line.

diffraction measurements were performed by Walid Hetaba at the USTEM Facility at TU Wien unless otherwise indicated. The evaluation of the measurements, obtaining the FFTs from the HRTEM images, indexing the electron diffraction images as well as FFTs was done together with Walid Hetaba and Stefan Löffler. The measurements were conducted at the USTEM facility of the Vienna University of Technology.

The crystal structure and compositions were verified and further studied using XRD. Staytimes between 27 s and 30 s were used in the experiments. These measurements were performed by Patrick Thomas and Christian Sterwerf at the Faculty of Physics at Bielefeld University. The counts were normalized by the staytimes to allow a comparison of the data. A stepsize of 0.05° was chosen as the increment. 60 µL of the particle suspension were dropcasted onto a thermal-oxidized silicon wafer for the experiments. The program FullProf and the inogranic crystal structure database (ICSD) were used in combination with EDX spectra of the samples to indentify the peaks and determine the lattice parameters. The peaks caused by the side phases such as NaCl are not indexed in the spectrum to prevent overcomplicated data.

Alternating gradient magnetometry (AGM) measurements were conducted to measure the magnetic properties of the nanoparticle ensemble at different stages of the growth process. 2 µL of the particle suspension was dropcasted onto a 4 mm × 4 mm native

oxide silicon wafer for these experiments. Parallel (in-plane) and perpendicular (out-of-plane) measurements were conducted since a shape dependent anisotropy was expected.

The influence of c25-mms6 on nanoparticle formation, growth and magnetic properties was investigated by comparing biosynthesized nanoparticles with particles synthesized without the polypeptide in a control experiment at different stages of the growth process. Samples were taken between 1 minute and 28 days after the reaction started.

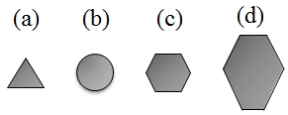

Figure 77: Different disc shapes, observed in the TEM measurements: (a) triangular shape, (b) irregular shape, (c) hexagonal shape, (d) diamond-like shape.

Control experiment

Larger discs of various non-stoichiometric $Co_xFe_{3-x}O_4$ phases as well as smaller spheres of different non-stoichiometric iron-rich $Co_xFe_{3-x}O_4$ compositions were obtained in this synthesis. The small spheres are not considered here, since they form after 1 day as a side product due to the starting composition. The phase separation of the spheres and the discs can be seen in the EFTEM image, given in Appendix B. The starting ratio of cobalt to iron was chosen to 1:2 to allow comparison to previous work [107, 134]. Since the discs are of a cobalt-rich composition, the residual iron precursor in the solution formed the side product.

Figure 78 shows the nanoparticles obtained at different stages of the growth process. The different shapes, observed in the TEM measurements are sketched in Figure 77. Crystallites as well as discs with triangular (a), irregular (b), hexagonal (c) and diamond (d) shapes, were obtained in this synthesis. The diamond shape is similar to the hexagonal shape with the exception that two sides are elongated and is therefore included in the hexagonal shape in this work. The majority of nanoparticle discs synthesized in this conventional chemical synthesis are irregularly-shaped (75 %) after 1 minute. EELS measurements of the discs at the early stage of nanoparticle growth (5 minutes) show that the discs are of an iron-rich composition $Co_{1.4}Fe_{1.6}O_4$. The initial nanoparticle diameter was determined to $D_{av} = 27\,\text{nm} \pm 13\,\text{nm}$. The size distribution of the particles, given in Figure 78, is lognormally distributed indicating that Ostwald ripening occurs at this stage of the nanoparticle growth.

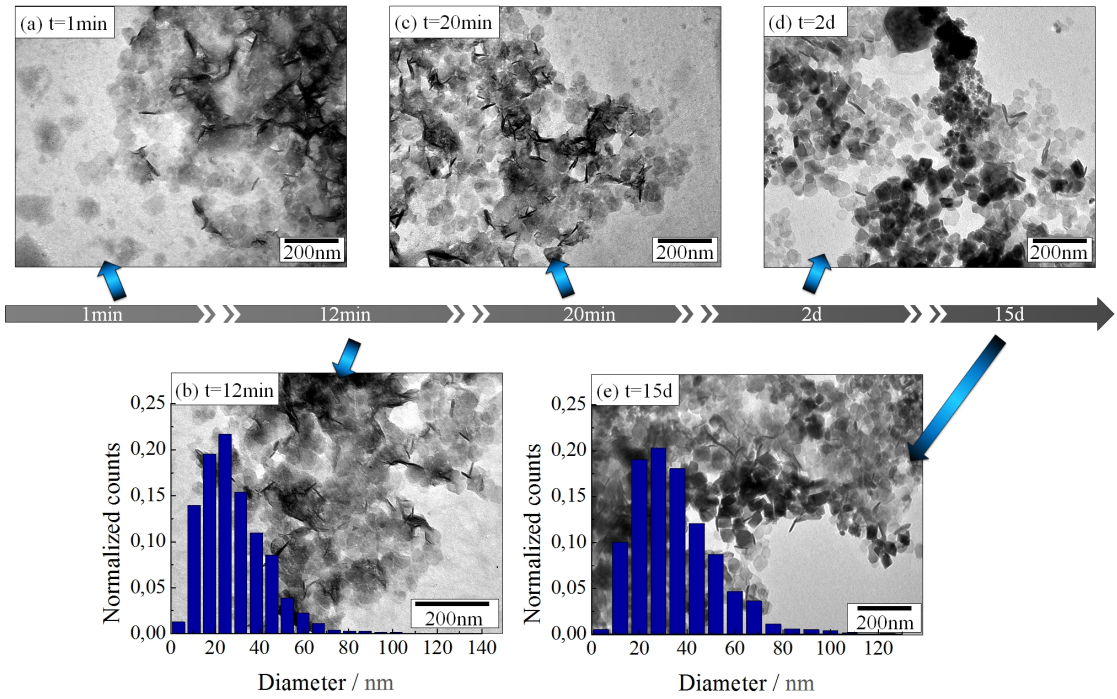

Figure 78: TEM images of particles synthesized without c25-mms6 at different times of the growth process. (a) 1 minute, (b) 12 minutes, (c) 20 minutes, (d) 2 days, (e) 15 days. The counts of both distributions (12 minutes and 15 days) are normalized by the amount of particles used for the statistic to allow a better comparison. 701 particles were evaluated for the 12 minute sample. 986 particles were used in the evaluation for the 15 day sample.

A more detailed structural analysis of the particles after 5 minutes shows that the discs disintegrate during HRTEM and EELS measurements (Figure 79). These measurements indicate that the discs are unstable at this stage of the particle growth and thus in an intermediate stage.

The final nanoparticles after 15 days are still predominantly irregularly-shaped (75 %). Their diameter was determined to $D_{av} = 35\,\text{nm} \pm 17\,\text{nm}$. The size distribution (see Figure 78) is lognormally distributed. The size range of the particles remains unchanged in comparison to the size distribution after 20 min. However the maximum is shifted towards larger diameters with time, indicating that midsize particles grow and smaller particles, with diameters less than 10 nm, dissolve in favor of bigger ones. This indicates that Ostwald-ripening (OR) occurs during crystal growth.

A more detailed analysis of previous EELS measurements [112]

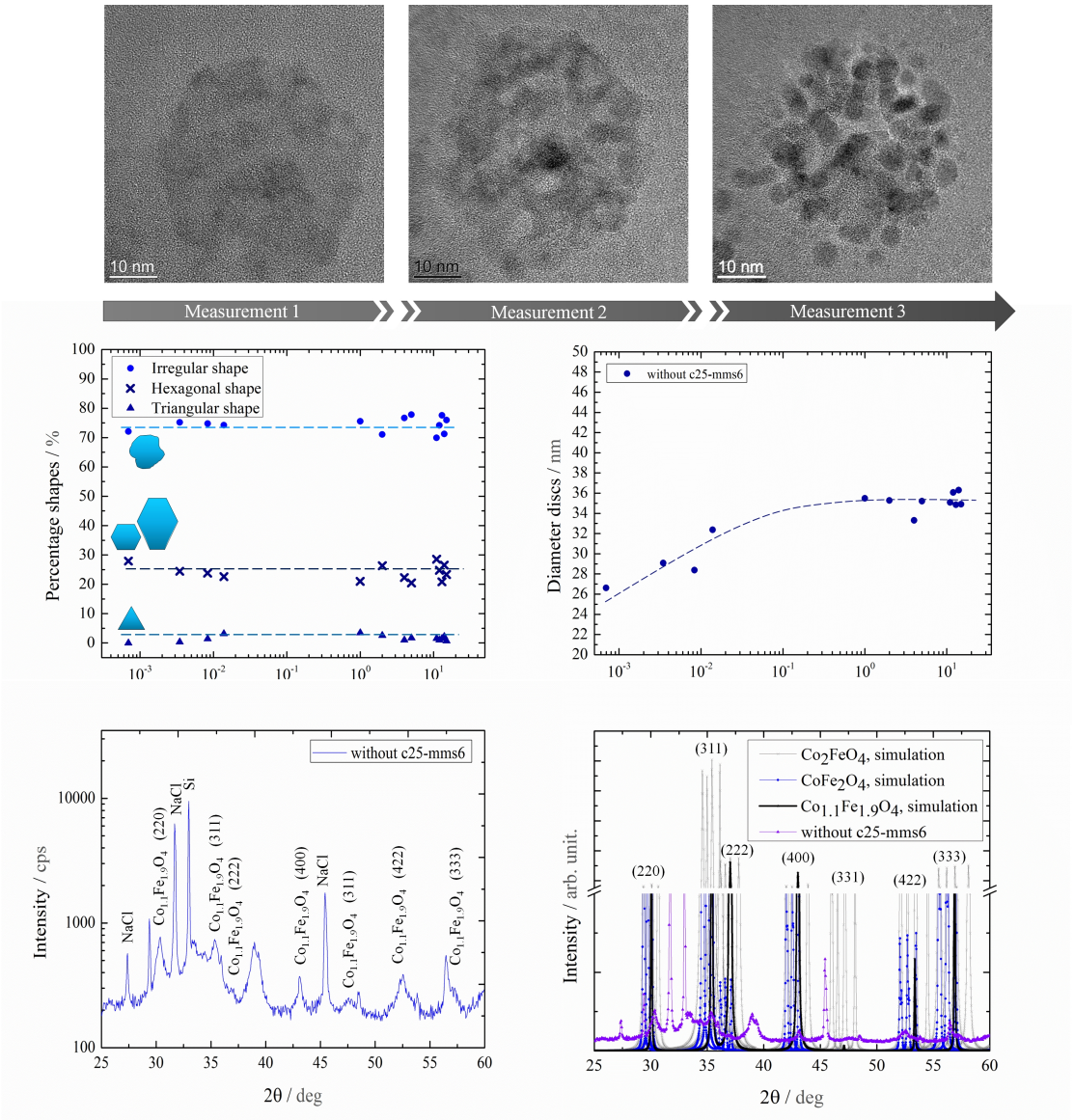

Figure 79: Top: HRTEM images of a control experiment particle after 5 minutes. The images from left to right were take in succession during the measurements and show that the particle disintegrates in the electron beam. Middle: Percentage of shapes observed in the TEM measurements (left), for which a change in shape with time could not be observed and change in disc diameter with time for the control experiment particles (right). The line serves only to better illustrate the increase in diameter which occurs during the first day of the growth process (right). Bottom: XRD measurements of the control experiment nanoparticle and biosynthesized particles after 28 days (left). Simulation of the stoichiometric cobalt-rich phase and non-stoichiometric $Co_{1.1}Fe_{1.9}O_4$ phase for different lattice parameters as well as the measured XRD spectrum of the control experiment particles (right).

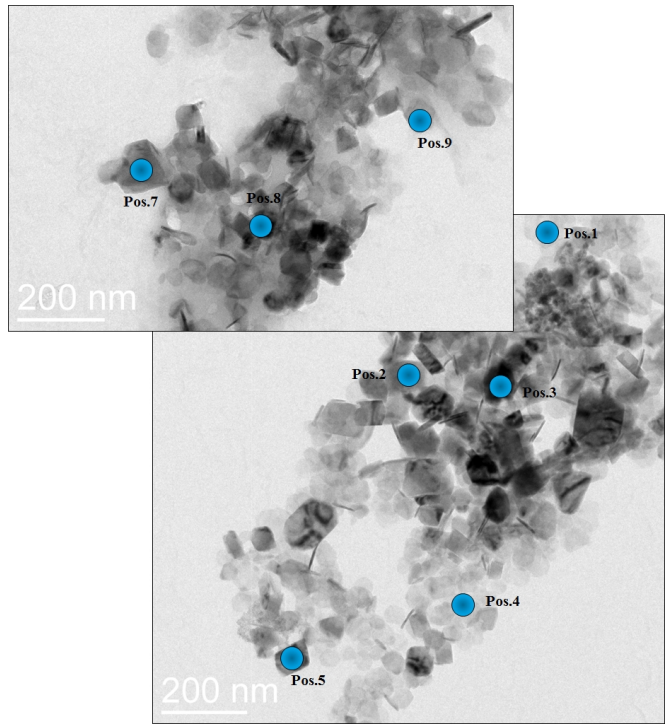

Figure 80: TEM images of the control experiment particles. The regions in which EELS measurements were conducted are circled. These measurements were performed by Inga Ennen at USTEM at TU Wien.

Table 8: Composition of different particles obtained in the control experiment after 15 days. The different positions correspond to measurements of single nanoparticles which are marked in Figure 80.

Pos.	Phase
1	$Co_{1.7}Fe_{1.3}O_4$
2	$Co_{1.5}Fe_{1.5}O_4$
3	$Co_{1.5}Fe_{1.5}O_4$
4	$Co_{1.7}Fe_{1.3}O_4$
5	$Co_{1.5}Fe_{1.5}O_4$
7	$Co_{1.5}Fe_{1.5}O_4$
8	$Co_{1.3}Fe_{1.7}O_4$
9	$Co_{1.5}Fe_{1.5}O_4$

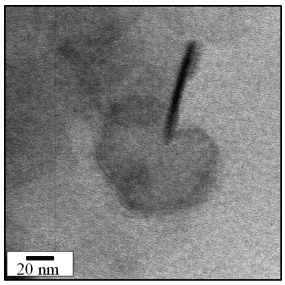

Figure 81: TEM image of a hexagonally-shaped control experiment particles.

showed a shape dependent composition of the nanoparticles after 28 days. The TEM measurement, showing the EELS measurement locations, is given in Figure 80 while the corresponding nanoparticle phase is given in Table 8. Smaller, irregularly-shaped discs are of an iron-rich composition $Co_{1.3}Fe_{1.7}O_4$. An increase in cobalt content can be observed for larger irregularly-shaped particles. Their composition was determined to be $Co_{1.5}Fe_{1.5}O_4$. Truncated hexagonally-shaped discs are of a cobalt-rich composition $Co_{1.7}Fe_{1.3}O_4$. Figure 81 shows a hexagonally-shaped particle. It's phase was determined to be $Co_{1.7}Fe_{1.3}O_4$ in EELS measurements. Stoichiometric Co_2FeO_4 dics could not be observed. The final top/bottom crystal face was previously determined to (112) [112]. The peaks for stoichiometric $Co_2Fe_1O_4$ also cannot be observed in XRD measurements (see Figure 79). Instead, the $Co_{1.1}Fe_{1.9}O_4$ phase can be indexed. At present, no crystal structure values such as the lattice parameters, for the other non-stoichiometric cobalt ferrite phases exist in the literature. However, the remaining unidentified peaks are likely

to belong to the $Co_{1.3}Fe_{1.7}O_4$ and $Co_{1.7}Fe_{1.3}O_4$ phases. Considering the XRD simulation of the stoichiometric cobalt ferrite phases and the non-stoichiometric iron-rich phase, the peaks for the other non-stoichiometric phases are likely to be in the vicinity of the simulated peaks. Considering the XRD measurement of the control experiment particles, it is likely that the extreme peak broadening is therefore not only caused by stress and strain in the sample which is often observed for nanoparticles, but also by the superposition of the non-stoichiometric cobalt ferrite phase peaks.

The percentage of irregular shapes, displayed in Figure 79, remained unchanged at 75 % throughout the entire growth process. An increase in diameter can be observed until 1 day. The change in disc diameter with time is plotted in Figure 79.

Biomimetic approach: nanoparticle growth

Nanoparticles at different stages of the biomimetic growth process are displayed in Figure 82. The measurement after 1 minute shows that the initially formed particles in the biosynthesis display the same morphology as the control experiment discs. 75 % of the initially formed discs in the biosynthesis are irregularly-shaped. The initial disc diameter was determined to $D_{av,t=1min}$ =29 nm±15 nm. The size distribution of discs after 12 minutes is displayed in Figure 82. A double peak can be observed in the size distribution at that time with a larger maximum at around D_{large} ≈40 nm as well as a smaller maximum at D_{small} ≈5 nm to 20 nm. The composition of the particles at the early stages was determined to $Co_{1.1}Fe_{1.9}O_4$ in EELS measurements and corresponds to the cobalt to iron starting ratio used in the synthesis. The top/bottom crystal face was determined to (112) in electron diffraction measurements (see Figure 83). This crystal face was also found as the final top/bottom crystal face of the control experiment nanoparticles in earlier work [134].

To gain a better insight into the change in morphology and composition at the early stages of the growth process, hexagonally-shaped nanoparticles were studied after 5 minutes, 1 day, and 2 days, and were compared to each other. These nanoparticles with their corresponding inverted electron diffraction pattern at different stages of the growth process are displayed in Figure 83. The inverted

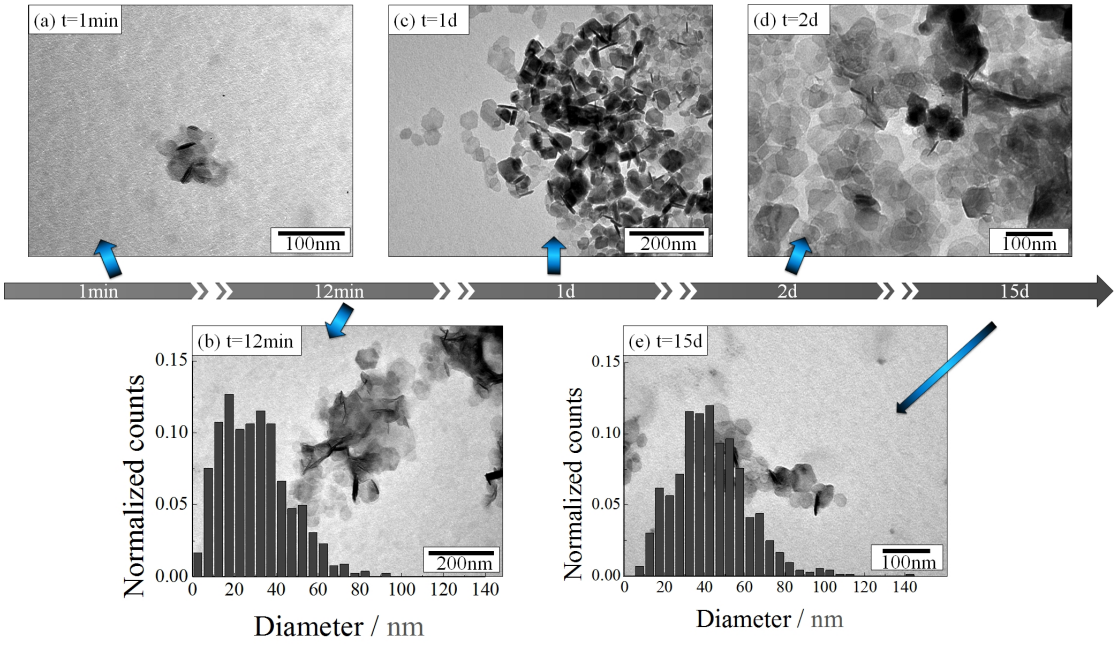

Figure 82: TEM images of particles synthesized with c25-mms6 at different stages of the bioinspired crystal growth: (a) 1 minute, (b) 12 minutes, (c) 1 day, (d) 2 days, (e) 15 days. Size distribution of the bioinspired discs after (a) 12 minutes and (b) 15 days. The counts were normalized with respect to the amount of particles used for the evaluation. N=781 particles after 12 minutes and N=726 particles after 15 days were used for the evaluation.

intensity display of the electron diffraction pattern was chosen for a better visualization of the diffraction spots. The electron diffraction patterns are direct representations of the nanoparticles' reciprocal lattices. A sharp ring in the diffraction pattern after 5 min shows that this material is polycrystalline and that the crystallites, that lie in the same ZA, are randomly oriented. These discs are stable, in contrast to the control experiment at the same stage of the growth process as shown by the HRTEM images taken in succession in Figure 84.

$$d_{hkl} = \frac{a}{\sqrt{h^2 + k^2 + l^2}} \tag{37}$$

d_{hkl} was measured in the first electron diffraction pattern.

A change in diffraction pattern and composition with time can be observed. The prominent ring, observed in the diffraction pattern after 5 minutes, is diminished for the $Co_{1.3}Fe_{1.7}O_4$ discs after 1 d. The crystal face, determined to be (112), remains unchanged at this stage. The lattice parameter $a = 0.841$ nm was calculated from the

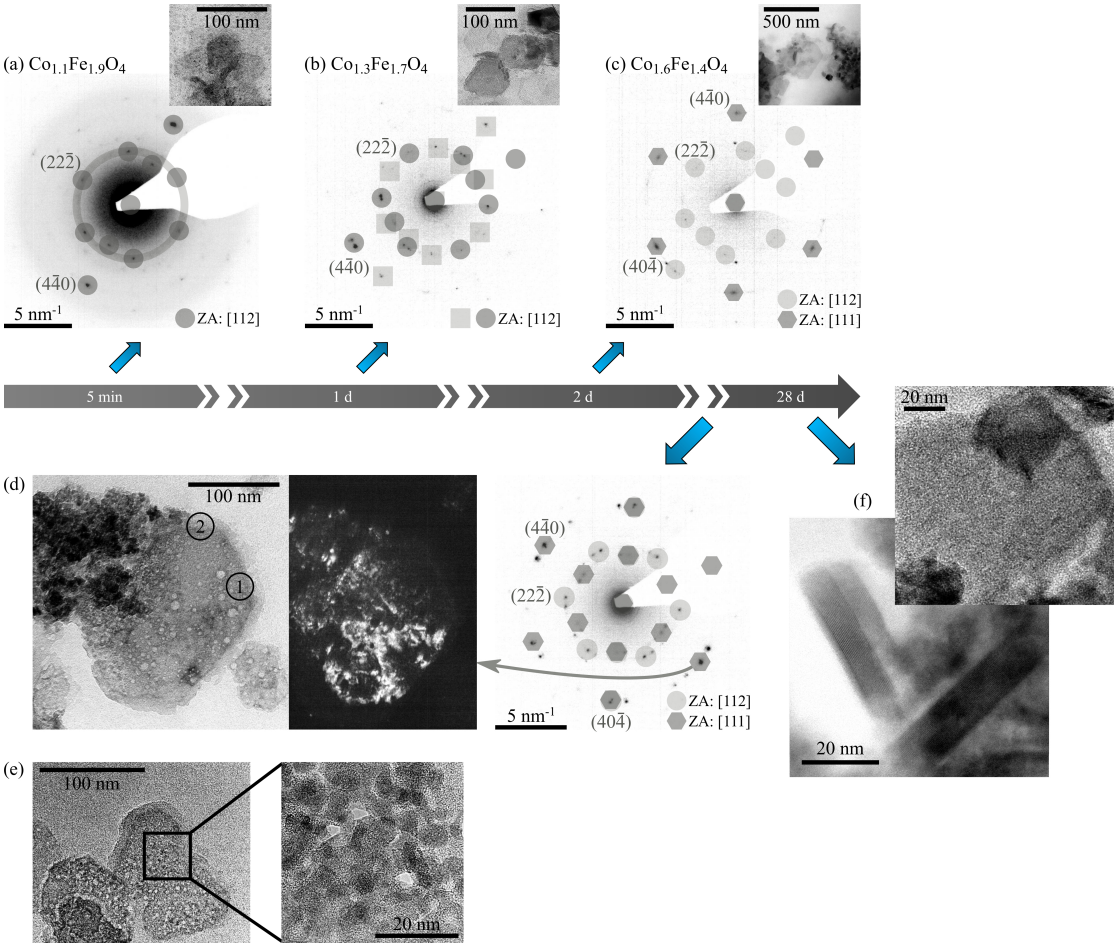

Figure 83: Top: Change in composition and electron diffraction pattern of hexagonally-shaped particles with time, obtained in the biosynthesis: hexagonal discs after (a) 5 minutes, (b) 1 day, (c) 2 days. The electron diffraction patterns are displayed with inverted intensity for better visibility. The dominating rings and reflexes are indexed. Bottom: Incomplete, intermediate structures observed throughout the growth process and the final nanoparticles: (d) Bright field image of an imcomplete diamond-shaped bio-nanoparticle and its electron diffraction pattern. The dark field image of the particle was obtained for the circled reflex in the diffraction pattern. (e) Incomplete, irregularly-shaped disc obtained as an intermediate structure in the biosynthesis. The inset shows an enlarged area of the nanoparticles. (f) Complete nanoparticle after 28 days. The lattice fringes show that these nanoparticles are monocrystalline. The inset shows that these final nanoparticles are complete.

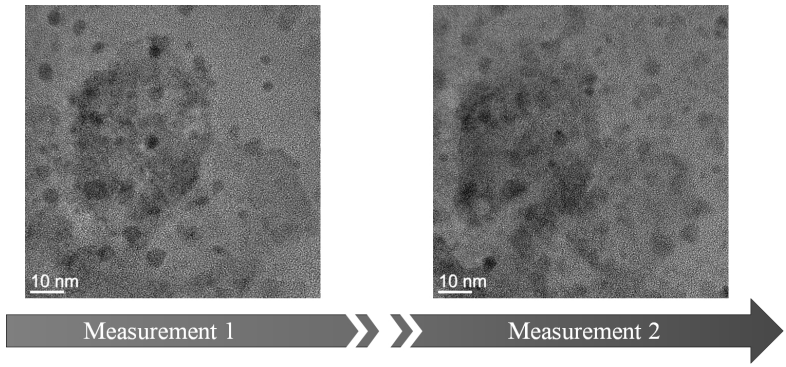

Figure 84: HRTEM images of biosynthesized diamond-shaped particles after 5 minutes. The images were taken in succession showing that the discs are stable and do not disintegrate in the electron beam.

FFT for the lattice spacing $d_{hkl} = 0.485\,\text{nm}$ in the (111) direction. It is slightly larger than the lattice parameter $a = 8.403\,\text{Å}$ for the $Co_{1.1}Fe_{1.9}O_4$ phase, given in the ICSD (ICSD 166200). An increase in the lattice parameter can be linked to atoms doping into the crystal, an effect which has previously been reported by Lagerstedt *et al.* [210]. This is in good agreement with the increase in cobalt concentration in the composition. After 2 days, the electron diffraction pattern of the cobalt-rich $Co_{1.6}Fe_{1.4}O_4$ discs shows a further increase in orientation in comparison to those after 5 minutes and 1 day. A change in crystal face can be observed. Two top/bottom crystal faces are displayed at this stage and were determined to be (112) and (111). A comparison to the electron diffraction pattern of the incomplete diamond-shaped nanoparticle shows an increase in orientation for these more completed discs. Less reflexes of a tilted diffraction pattern[62] are visible and thus show an increased orientation of the substructures.

[62] These are caused by random orientation of substructures or crystallites.

Table 9: Change in composition with time for hexagonally-shaped biosynthesized discs.

Time	Composition
5 min	$Co_{1.1}Fe_{1.9}O_4$
1d	$Co_{1.3}Fe_{1.7}O_4$
2d	$Co_{1.6}Fe_{1.4}O_4$
28d	$Co_2Fe_1O_4$

A more detailed structural analysis of the intermediate, non-stoichiometric particles shows that these incomplete discs consist of small substructures as displayed in the HRTEM measurements of an irregularly-shaped incomplete particle in Figure 83 (e). The inset of this picture shows a larger magnification of this particle. The smaller, irregularly-shaped substructures with an average diameter $D \approx 10\,\text{nm}$ are clearly visible. The size of these smaller substructures corresponds to the smaller maximum in the size distribution after 12 min. The existing lattice fringes within the substructures show that they are crystalline. TEM and EELS measurements of an incom-

plete diamond-shaped particle, displayed in Figure 83 (d), shows that this disc has densely packed regions, such as region 2, which are of a cobalt-rich composition $Co_{1.8}Fe_{1.2}O_4$. Non-aggregated areas where the substructures are still visible, such as region 1, are of an iron-rich non-stoichiometric composition $Co_{1.1}Fe_{1.9}O_4$. Compositional gradients towards a more cobalt-rich phase for denser areas can be observed for such incomplete particles, independent of their shape. The non-stoichiometric composition and incompleteness of the nanoparticle indicates that these particles are in a metastable, intermediate stage of the growth process.

The orientation of the substructures was studied by performing a dark field measurement. A reflex was selected in the electron diffraction pattern using the ojective aperture and the TEM was switched to imaging mode where a dark field image of the nanoparticle was recorded. The illuminated areas correspond to the nanoparticle areas that are aligned in such a way that they contribute to the marked reflex. The measurement shows that a substantial orientation of the substructures within the particle exists. This indicates that the substructures align during the agglomeration process. The electron diffraction pattern shows that two orientations are present, the [111] orientation and the [112] orientation.

Figure 85 shows an assembly of small discs which display a similar size as the substructures within the incomplete nanoparticles. The loose assembly of these structures indicates that this stage occurs prior to aggregating to an incomplete nanoparticle. The composition of the smaller discs was determined to be $Co_{0.8}Fe_{2.2}O_4$ using EELS. The EELS spectrum can be found in the Appendix C. FFTs of the HRTEM measurements, given in Figure 85, show that these discs are randomly oriented. The lattice parameters of the different discs were calculated by measuring the distance from the zero peak to a reflex. The lattice parameter was calculated from the measured distance with

$$d_{hkl} = \frac{a_0}{\sqrt{h^2 + k^2 + l^2}} \tag{38}$$

for the fcc lattice with d_{hkl} as the interplanar spacing, a_0 as the lattice constant, and hkl as the Miller indices. The measured d_{hkl}, reflexes and calculated lattice parameters for the different positions, labelled in the HRTEM image in Figure 85 can be found in Table 10.

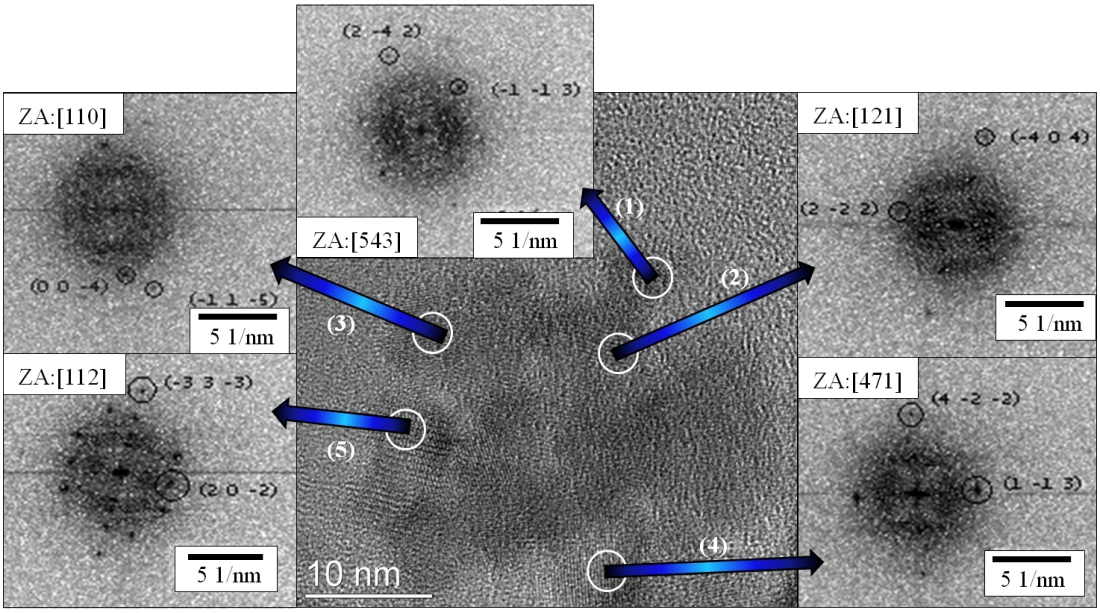

Figure 85: HRTEM image of smaller biosynthesized discs. The number at the arrows represents areas of measurements. The corresponding intensity inverted FFT show the different ZA and therefore crystal faces of the nanoparticles.

Table 10: d_{hkl} for specific reflexes used to calculate the lattice parameter of the biosynthesized discs. The positions correspond to those marked in Figure 85.

Pos.	d_{hkl} [nm]	hkl	a [nm]
1	0.258	-1-13	0.856
2	0.153	-404	0.865
3	0.215	00-4	0.860
4	0.255	1-13	0.846
5	0.164	-33-3	0.857

The measurements show that these iron-rich, small, slightly aggregated discs display different crystal faces. Their lattice parameters are increased by at least 5 % in comparison to the literature value of $CoFe_2O_4$ (ICSD 166200) which is most likely caused by doping. These measurements show that initially iron-rich particles form which possess random crystal faces and orientations. These structures then start to aggregate to form a mesocrystal-like structure as observed in the HRTEM images of the incomplete, irregularly-shaped dics.

TEM images show that the nanoparticles synthesized in the bioinspired approach change their shape during 28 days of the growth process. This change from irregularly-shaped particles to hexagonally-shaped particles was quantified and is displayed in the graph in Figure 86 and compared to the control experiment. The majority of the stoichiometric Co_2FeO_4 discs, as displayed in Figure 83 (f), are hexagonally-shaped after 28 days. The HRTEM image in Figure 83 shows that these final discs are complete and monocrystalline. The disc diameter was determined to be $D_{av,t=15d} = 43\,\text{nm} \pm 18\,\text{nm}$. Tailing can now be observed in the size distribution, indicating

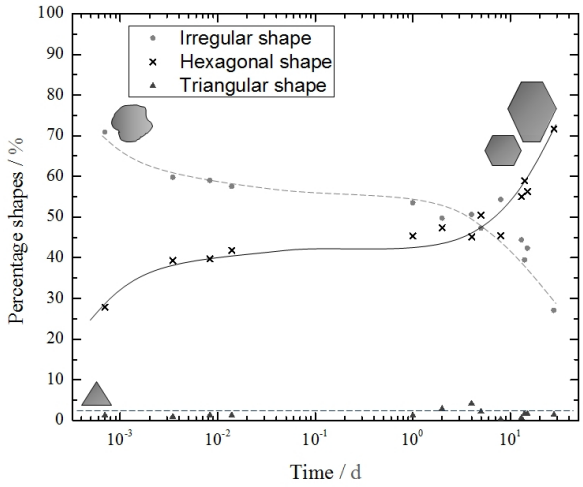

Figure 86: The percentage of irregularly-shaped particles is plotted against the time during the growth process for the bioinspired synthesis. The lines act as a guide to the eye only.

that Ostwald ripening occurs at the later stages of crystal growth. The diminishing amount of smaller particles and the increasing amount of larger particles leads to a non-symmetric size distribution (tailing). In addition, the smaller maximum is diminished in the size distribution, leading to a more narrow size distribution and therefore a smaller variance and is displayed in Figure 88. This behavior indicates that aggregation takes place for these particles where the smaller nanoparticles aggregate to the final, larger nanoparticles. This effect was observed in the HRTEM images where small discs agglomerate and form substructures which then fuse to form the final, secondary nanoparticle.

In addition, incomplete discs can be observed throughout the entire growth process. Compositional gradients within these incomplete crystals can be found with a tendency towards a more cobalt-rich phase for more complete and denser regions of the nanoparticle.

Since several cobalt ferrite phases with different lattice parameters each were found in HRTEM and EELS measuremts, an XRD spectrum with the corresponding values was simulated using the Program FindIt. The stoichiometric iron-rich phase $CoFe_2O_4$ (ICSD 166200) with the different lattice parameters $a = 8.387$ Å, $a = 8.500$ Å, $a = 8.6$ Å as well as the stoichiometric cobalt-rich phase Co_2FeO_4 (ICSD 98551) with the lattice parameters $a = 8.242$ Å,

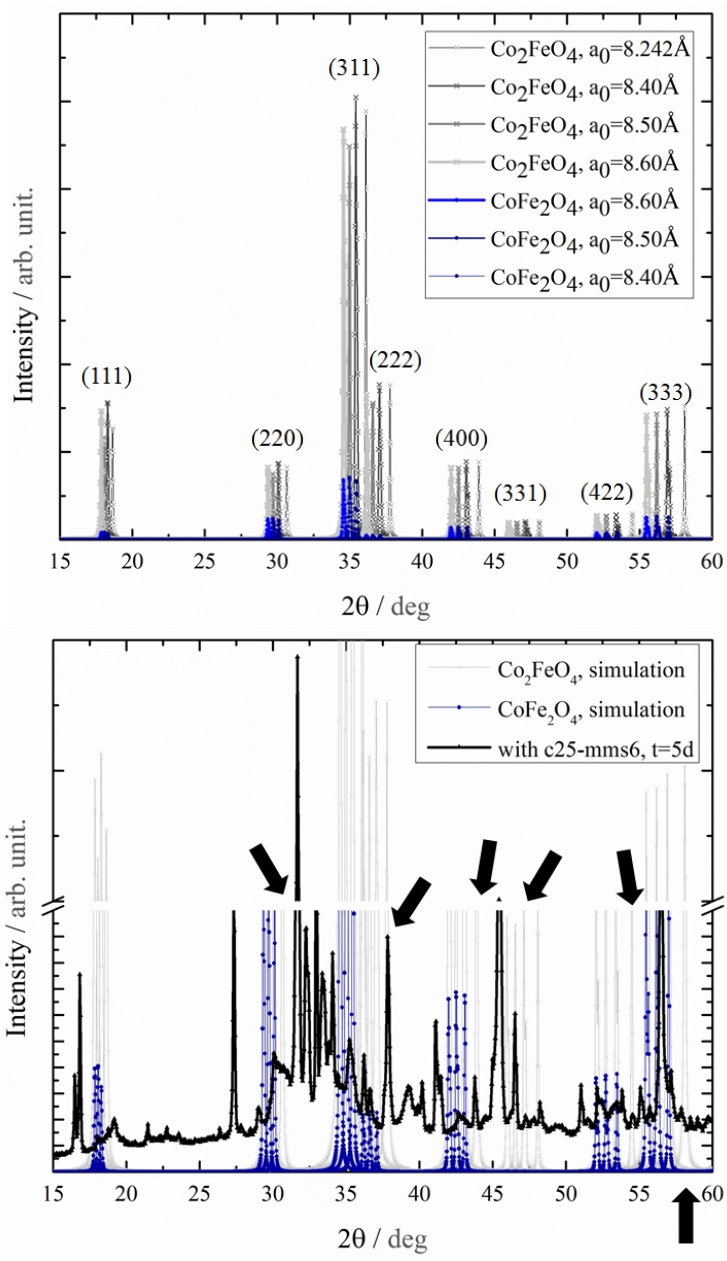

Figure 87: Simulation of an XRD spectrum for Co_2FeO_4 (ICSD 98551) and $CoFe_2O_4$ (ICSD 166200) phases with different lattice parameters. The iron-rich phase is dislpayed in blue, the cobalt-rich phase in grey. The simulation was carried out with the program FindIt. Superposition of the simulated XRD spectrum (grey) and (blue) and the measured XRD spectrum of the biosynthesized cobalt ferrite nanoparticles after 5 days (black). The arrows indicate the peaks where the cobalt-rich phase can be determined from the iron-rich phase.

$a = 8.500$ Å, $a = 8.600$ Å were used to simulate the XRD pattern of the particle ensemble. The simulated spectrum is given in Figure 87. The simulation shows that several peaks of the cobalt and iron-rich phases are present and that they overlap for different lattice parameters. It is thus difficult to differentiate between the two phases. However, whether a cobalt-rich phase is present can be seen between $2\theta = 45°$ and $2\theta = 50°$ since only a cobalt-rich phase contribution is present. This, however, still represents a very simplified version since the non-stoichiometric phases with their different lattice parameters were not taken into account due to a lack of literature values for the lattice parameters of these phases. Figure 87 shows the superposition of the simulated spectrum and the XRD measurement after 5 days. The superposition shows that the peak positions of the measured spectrum correspond to the simulated spectrum with a few additional peaks in the XRD measurement. The peaks that can only be linked to the cobalt-rich phase are indexed with an arrow. These peaks clearly show the presence of the cobalt-rich phase. However, several artifacts make it difficult to fully evaluate the obtained XRD spectrum. Preferred orientation of the nanoparticles, with the (111) face parallel to the wafer, caused by the disc shape leads to unrealiable reflex intensities and is the biggest error in this spectrum. Furthermore, the particles do not cover the wafer homogeneoulsy but form clusters. These clusters form a type of step on the wafer surface and hence increase the surface roughness. Such surface roughness causes additional absorption effects and can create distorted reflection profiles as well as shifted ghost peaks. Anisotropic size broadening, determined from the electron diffraction experiments is common for plates and can be observed as well as non-gaussian reflex profiles. Using the observed increase in lattice parameter and determined composition, it was, however, possible to index the peaks of the stoichiometric phases accordingly. Whether the peaks that could not be indexed are ghost peaks or belong to the non-stoichiometric intermediate phases cannot be determined since literature values for the lattice parameters are not available. However, the peaks are more likely to belong to the non-stoichiometric intermediate phases. This assumption is based on the fact that these reflexes occur for both the biomimetic synthesis and the control experiment. Furthermore,

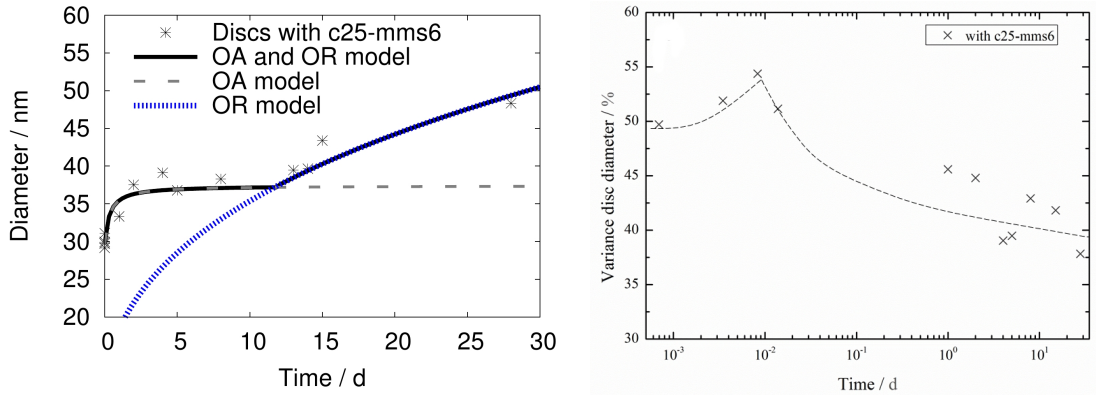

Figure 88: Left: Change in diameter with time of the biosynthesized nanoparticles. The data is fitted with the kinetic model, proposed for the oriented attachment process. Right: Change in variance with time. The line in acts as a guide to the eye only.

these reflexes vanish with time in the biosynthesis which is another indication that they could belong to the intermediate phases.

The overall growth of the discs alters from that of the control experiment. In this bioinspired synthesis, the particles do not instantaneouly grow and then reach equilibrium size, but have an incubation time of 20 minutes. Their growth starts afterwards (see Figure 88). The growth rate of these particles is reduced in comparison to the control experiment. The change in diameter with time agrees with the kinetic model previously proposed by Zhang *et al.* [211] for oriented attachment (OA) processes with Ostwald ripening (OR) dominating the later stages of crystal growth:

$$d = \frac{d_0 \cdot (\sqrt[3]{2} \cdot k_1 \cdot t + 1)}{k_1 \cdot t + 1} \ , \ t \leq 12d \tag{39}$$

$$(\frac{d}{2})^3 - (\frac{d_{OR}}{2})^3 = k_2 \cdot t \ , \ t \gg 12d \tag{40}$$

with d = disc diameter with time, d_0= initial particle size, $k_1 = 3.4 \times 10^{-5} \frac{1}{s}$ as an oriented attachment kinetic reaction constant between two particles, t= time, d_{OR} =particle diameter at which Ostwald ripening starts, and $k_2 = 6.1 \frac{\text{Å}^3}{s}$. The fitted data is displayed in Figure 88. The kinetic reaction constant for the oriented attachment process indicates that the growth process is slow. However, it cannot be compared to literature due to a lack of published values.

Comparison and evaluation

A comparison of the results obtained for the control experiment and the biosynthesis shows that c25-mms6 influences and alters the nanoparticle growth. In the control experiment non-stoichiometric $Co_xFe_{3-x}O_4$ discs of mostly irregular shape were obtained. The final top/bottom crystal face of these discs was determined to be (112). HRTEM measurements show that these particles are unstable in the early stages of crystal growth since they disintegrate during HRTEM measurements. Particle growth was found to only occur within the first day. A change in morphology, microstructure, and composition with time could not be observed.

A different behavior was observed for the biosynthesized cobalt ferrite particles. At the early stages of particle growth, the biosynthesized particles display a similar microstructure, morphology, and composition as the control experiment particles. The (112) top/bottom crystal face was found as well as an iron-rich non-stoichiometric $Co_{1.1}Fe_{1.9}O_4$ composition. The majority of discs are initially irregularly-shaped (75 %). These particles, however, do not disintegrate during HRTEM measurements in contrast to the control experiment particles, and must therefore be more stable. Furthermore, a change in shape in favor of an hexagonal shape can be observed. The final discs are mostly hexagonal shaped, display the (111) top/bottom crystal face and are of a stoichiometric Co_2FeO_4 phase. The growth behavior was also found to be influenced by the polypeptide c25-mms6. Particle growth occurs after an initial incubation time of 20 minutes. A second maximum was found in the size distribution in addition to a maximum at larger diameters at the early stages of nanoparticle growth in the biosynthesis. The maximum, located at the smaller diameter, vanishes with time. This behavior could not be observed for the control experiment.

A comparison of the XRD spectra of the bioinspired nanoparticles and the control experiment particles after 5 days, given in Figure 89, shows that the stoichiometric $Co_2Fe_1O_4$ phase is only obtained in the biosynthesis. The particles discussed in previous work appear larger. The reduced diameter found in this work can be explained by the smaller discs observed with the TEM and HRTEM measurements. This effect occured in both the bioinspired synthesis and the control

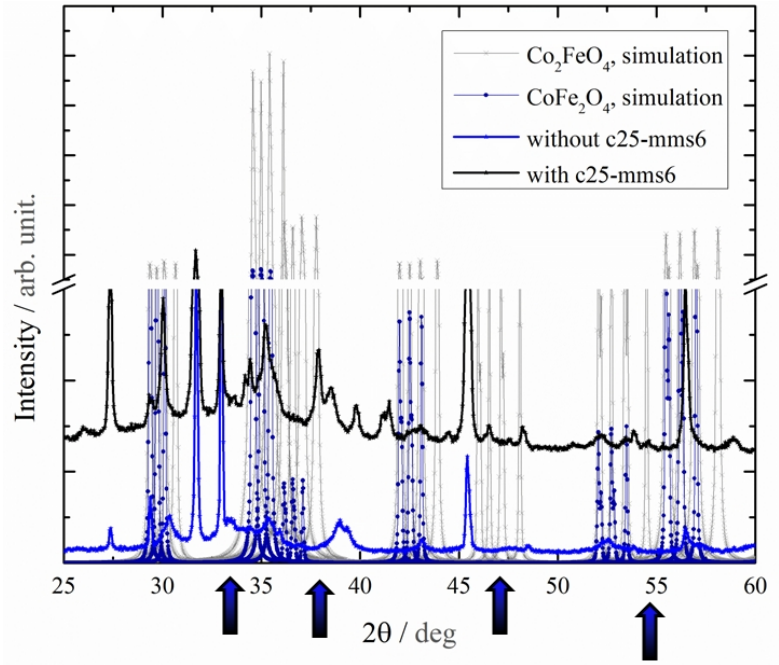

Figure 89: Comparison of the XRD spectra of the biosynthesized particles as well as the control experiment particles after 5 days to the XRD simulation for cobalt ferrites of different lattice parameters. An offset between the measurements was inserted to allow for better comparison of the measured XRD spectra.

experiment. The smaller particles accounted for in this work can hardly be observed in the STEM images and were thus mostly missed.

Phase changes

In both syntheses non-stoichiometric intermediate phases ($Co_{1.1}Fe_{1.9}O_4$ to $Co_{1.7}Fe_{1.3}O_4$) were found, indicating that several phase transformations towards a cobalt-rich phase occur. Crystallites and initially formed smaller discs possess the starting composition $Co_{1.1}Fe_{1.9}O_4$ which corresponds to the added cobalt to iron ratio in the syntheses. The larger the nanoparticles grow, and the more hexagonally-shaped[63] they are the richer in cobalt they become. The different phases observed in the experiments are indexed in the ternary CoFeO phase diagram[64], given in Figure 90. The phase diagram shows that the intermediate, non stoichiometric phases lie inbetween the stoichiometric iron-rich and cobalt-rich phases. Under the assumption of a uniform oxidation during crystal for-

[63] 25 % of the discs are hexagonally-shaped in the control experiment.

[64] This phase diagram was constructed by Prof. Andreas Hütten from the Faculty of Physics at Bielefeld University.

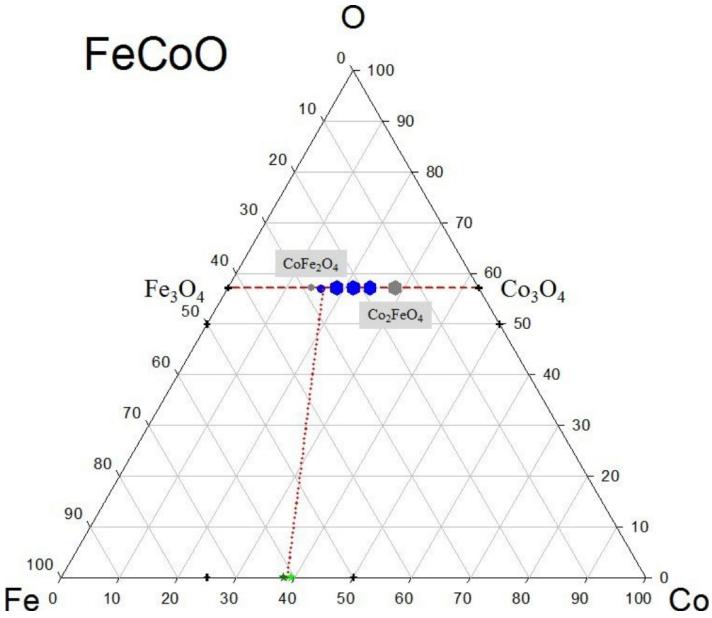

Figure 90: Ternary phase diagram of the system Fe-Co-O at room temperature. The star represents the nominal starting composition $Fe_{64}Co_{36}$. The particles synthesized with c25-mms6 are represented by grey shapes. The iron-rich phase $CoFe_2O_4$ is illustrated by a sphere, and the cobalt-rich discs Co_2FeO_4 are represented by the hexagon. The blue shapes stand for the non-stoichiometric intermediate phases. The small spherical $Co_{1.1}Fe_{1.9}O_4$ nanoparticles are depicted by the blue sphere and the non-stoichiometric discs are represented by the blue hexagonal shapes: $Co_{1.3}Fe_{1.7}O_4$ (left), $Co_{1.7}Fe_{1.3}O_4$ (right). The blue hexagon inbetween corresponds to the phase $Co_{1.5}Fe_{1.5}O_4$.

mation, the equilibrium point on the conode is the point where the dashed line ends. Several phase transformations need to occur before the final stoichiometric phases $CoFe_2O_4$ and Co_2FeO_4 can be formed in the biosynthesis (or the non-stoichiometric "final" $Co_{1,7}Fe_{1,3}O_4$ phase in the control experiment.) For each change in phase, an energy barrier needs to be overcome. This is sketched in Figure 91. In both syntheses, crystallites form the initial non-stoichiometric iron-rich phase $Co_{1.1}Fe_{1.9}O_4$. These crystallites grow and form non-stoichiometric intermediate phases. This stage is divided into substates in which compositional changes towards a more cobalt-rich non-stoichiometric phase occur during crystal growth. The control experiment particles do not possess enough energy to overcome the activation energy E_{A2} to form the stoichiometric phases. Only particles synthesized with c25-mms6 can overcome this barrier, indicating that c25-mms6 could act as a catalyst. Catalytic properties of proteins have previously been suggested for several other systems [103]. Such phase transformations are often observed in multistep biomineralization processes.

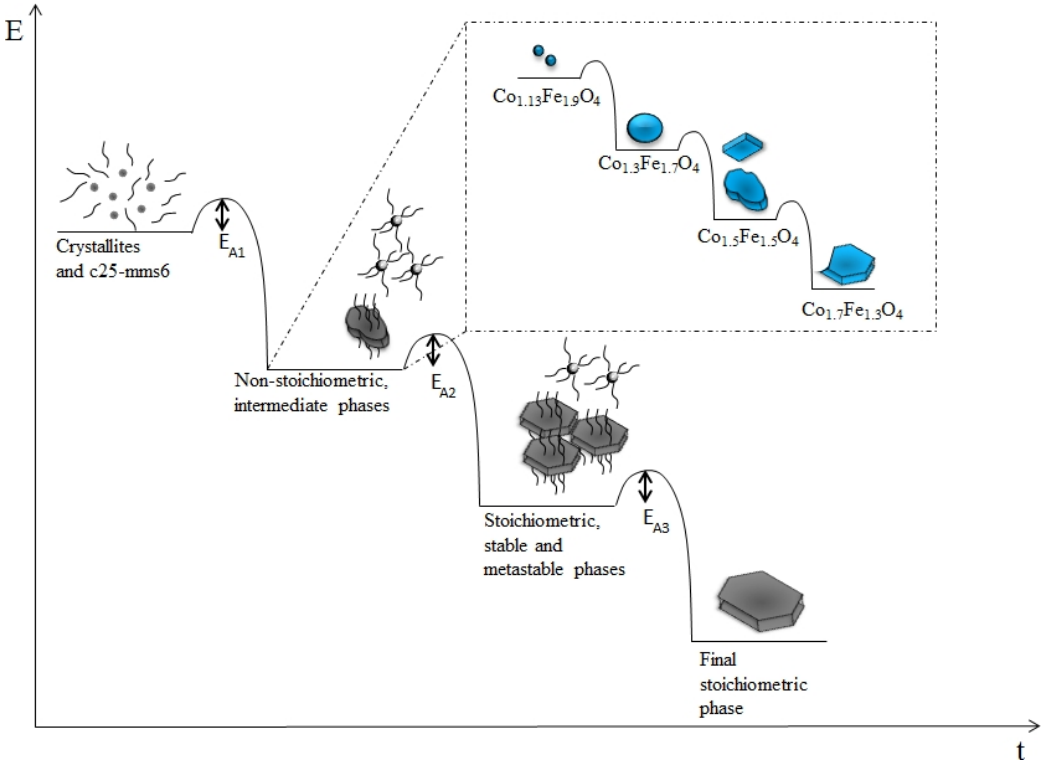

Figure 91: Illustration of the phase changes, occuring during crystal growth for the control experiment as well as the bioinspired synthesized particles.

Hypothesis: Growth process in bioinspired synthesis

The experiments indicate that the nanoparticle formation in the bioinspired synthesis is a multistep process. Such multistep processes are commonly found in natual systems and cannot be described with classical theories. The crystal formation in the bioinspired synthesis can be separated into four steps which are illustrated in Figure 92.

- Nucleation
- Polypeptide-nanoparticle interaction and growth of primary building blocks (Pbb)
- Aggregation and orientation of primary building blocks into mesocrystals
- Formation of secondary nanoparticle

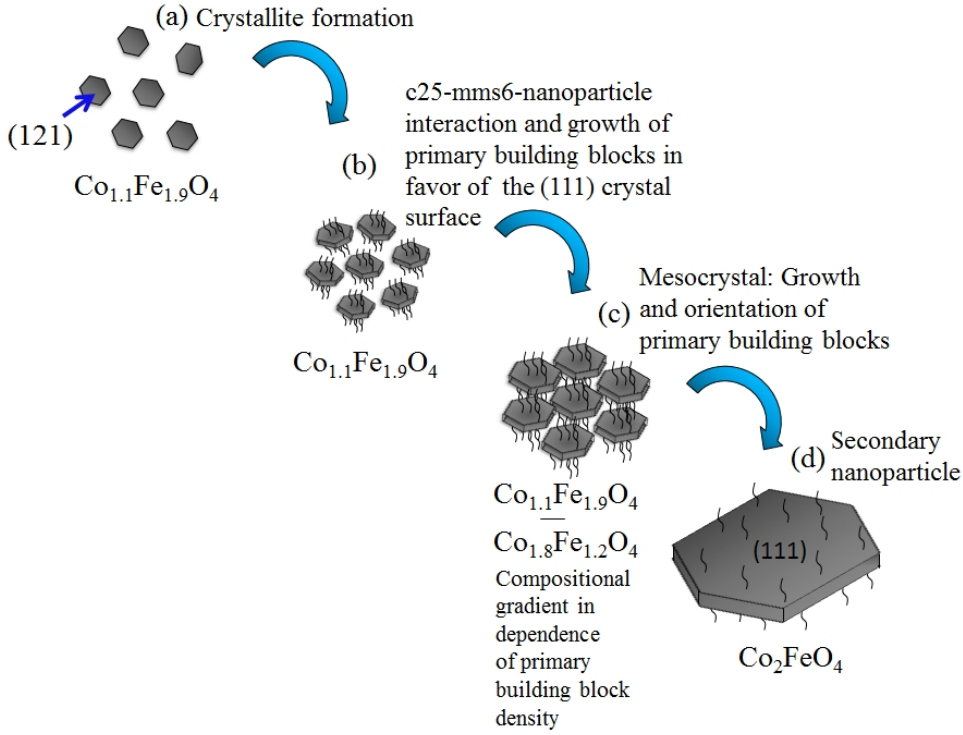

Figure 92: Schematic of the nanoparticle formation in the biomimetic growth process. (a) Crystallites are formed, (b) c25-mms6 adsorbs onto the Pbb and thermodynamically stabilizes them. (c) Growth of primary building blocks to minimize the ratio of surface to volume. These substructures then aggregate and orient along a common crystallographic axis. (d) The primary building blocks fuse and form the secondary nanoparticle. A face specific peptide-nanoparticle interaction was chosen to avoid an over-crowded illustration.

Nucleation: The nanoparticle growth was studied only. Nevertheless, a theoretical consideration of the nucleation process is discussed here to understand the formation of irregularly-shaped nanoparticles in the early stage of nanoparticle growth in both syntheses and to allow a complete nanoparticle formation evaluation. Studies by Baumgartner *et al.* show that the classical nucleation concept of the Gibbs free energy remains valid in non-classical nucleation processes [149]. The Gibbs free energy concept is used here to describe the nucleation process of the nanoparticles. The nuclei formed are not assumed to be spherical, but disc-like. The hexagonal disc-like nuclei formation is described in the theory section. The nucleation of irregularly disc-like nuclei can be modelled using the Gibbs free energy

$$\Delta G = -\Delta G_V \cdot V + \Delta G_O \cdot O \tag{41}$$

analogously to the hexagonal disc-like nuclei in the theory section.

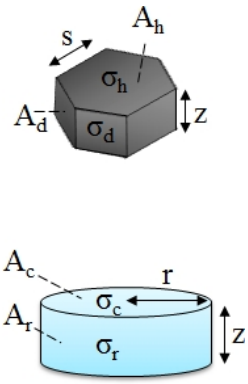

Figure 93: Geometries used to calculate the Gibbs free energy of hexagonal (top) and irregular (bottom) nuclei formation.

The irregularly-shaped nuclei are modelled using a cylindrical prism, depicted in Figure 93, which best describes the irregular morphology considering the different surface energies of the particle in different directions.

Taking the volume of a cylinder $V = \pi \cdot r^2 \cdot z$ into account, the Gibbs free energy can be written as

$$\Delta G = -\Delta G_V \cdot \pi \cdot r^2 \cdot z + 2 \cdot \sigma_c \cdot A_c + \sigma_r \cdot A_r \tag{42}$$

with $A_c = \pi \cdot r^2$ and $A_r = 2 \cdot \pi \cdot r \cdot z$, σ_c as the end surface energy and σ_r as the side surface energy. In this approach, the side face is approximated by one surface energy in analogy to the Gibbs free energy calculation of a sphere. In the latter a single surface energy is used to describe the spherical shape [150]. The critical values $r_{irreg,crit}$ and $t_{irreg,crit}$, neccessary for stable nuclei formation, can be calculated by extremizing the Gibbs free energy with respect to the radius r and height z:

$$\frac{\partial \Delta G}{\partial z} = 0 \;\rightarrow\; r_{crit,irreg} = \frac{2 \cdot \sigma_r}{\Delta G_V} \tag{43}$$

$$\frac{\partial \Delta G}{\partial r} = 0 \;\rightarrow\; z_{crit,irreg} = \frac{2 \cdot \sigma_c}{\sigma r} \tag{44}$$

The energy barrier for irregular nuclei formation is obtained for inserting the critical radii into the Gibbs free energy:

$$\Delta G_{\mathrm{irreg,crit}} = \frac{8 \cdot \pi \cdot \sigma_{\mathrm{c}} \cdot \sigma_{\mathrm{r}}^2}{\Delta G_{\mathrm{V}}} \,. \tag{45}$$

A comparison of the required Gibbs free energies for both geometries (hexagonal and irregular) yields:

$$\Delta G_{\mathrm{crit,hexa}} = \frac{48}{\sqrt{3}} \frac{\sigma_{\mathrm{d}}^2 \sigma_{\mathrm{h}}}{\Delta G_{\mathrm{V}}} \tag{46}$$

$$\Delta G_{\mathrm{irreg,crit}} = \frac{8\pi\sigma_{\mathrm{c}}\sigma_{\mathrm{r}}^2}{\Delta G_{\mathrm{V}}} \tag{47}$$

$$\frac{\Delta G_{\mathrm{crit,irreg}}}{\Delta G_{\mathrm{crit,hexa}}} = \frac{8\pi}{\frac{48}{\sqrt{3}}} = 0.91 \tag{48}$$

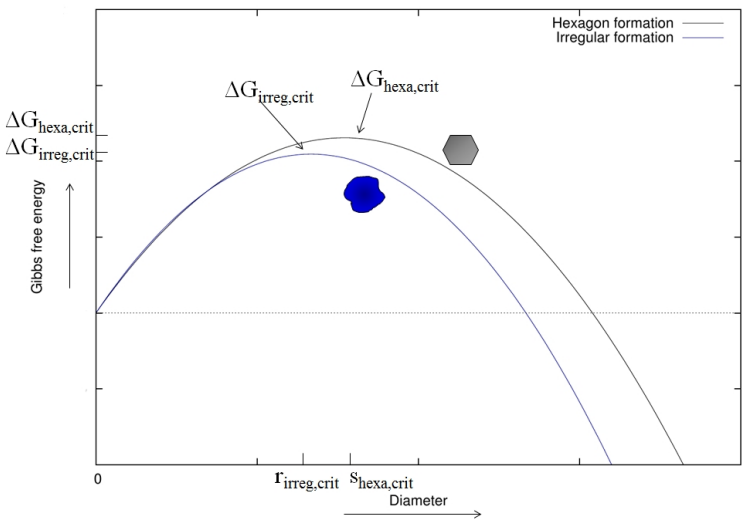

Figure 94: Plot of the Gibbs free energy for hexagonal and irregular nuclei formation. The required Gibbs free energy for the irregular nuclei $\Delta G_{\text{irreg,crit}}$ is smaller than that for the hexagonal nuclei $\Delta G_{\text{hexa,crit}}$ and therefore preferred. The corresponding critical values $r_{\text{irreg,crit}}$ and $r_{\text{hexa,crit}}$ neccessary for stable nucli formation are marked at the x-axis.

under the assumption that the initially formed crystal faces are identical, thus $\sigma_c = \sigma_h$ and $\sigma_d = \sigma_r$, see Figure 93. Both energies are plotted in Figure 94.

The required Gibbs free energy is slightly smaller for the irregular shape, thus this geometry is thermodynamically preferred. However, small fluctuations in energy allow the formation of hexagonally-shaped nuclei due to the small difference between the Gibbs free energies of the different geometries. Such small energy fluctuations occur naturally due to the natural energy distribution of the atoms[65]. A minority of atoms possess a sufficient amount of energy to form the hexagonal discs. The experiments showed that 75 % of the discs are initially irregularly shaped while 25 % are hexagonally-shaped. These calculations explain why mostly irregularly-shaped particles are obtained in both approaches after 1 min.

[65] The energy of the atoms in solution is Boltzman distributed.

Polypeptide-nanoparticle interaction and growth of Pbb: The reduction of surface energy is the driving force of crystal growth. The final morphology of the particles is linked to the surface energy. Faces with higher energies have increased growth rates and vanish in the final morphology, leaving the low energy surfaces as the final crystal faces. The final top/bottom crystal face of the cobalt ferrite

Figure 95: Different possibilities of peptide adsorption. Top: c25-mms6 only adsorbs onto the (111) crystal face. Bottom: The synthetic polypeptide adsorbs onto all crystal faces.

particles synthesized without the polypeptide was determined to be (112). The same crystal face was also found for the initially formed cobalt ferrite particles in the biosynthesis. The change in top/bottom crystal face from (112) to (111), observed in the electron diffraction measurements, indicate that the (111) surface energy must be lowered during the growth process. This effect was only observed in the biosynthesis and can therefore be linked to the reduction of surface energy by the polypeptide which adsorbs onto the inorganic crystal. The peptide adsorption was found in the FCS measurements. Growth modification by peptide adsorption has previously been reported for other systems as well [103, 151, 203]. The peptide adsorbs onto the Pbb, displaying the (112) top/bottom crystal face and interact with the inorganic crystal in such a way that growth of the Pbb, in which the (111) top/bottom crystal face forms is favored.

This adsorption process is displayed in Figure 95. The change in surface energy can qualitatively be discussed using the aspect ratio of the height and size for the Gibbs free energy (see Equation 20):

$$\frac{z}{s} = \sqrt{3}\frac{\sigma_\mathrm{h}}{\sigma_\mathrm{d}} \tag{49}$$

with σ_h as the end surface energy and σ_d as the side surface energy. Since z and s=$\frac{d}{2}$ are known from the TEM and EELS measurements the aspect ratio is used to calculate σ_h which is dependent on σ_d:

$$\sigma_\mathrm{h} = 0.27\sigma_\mathrm{d} \tag{50}$$

for the height $z = 10\,\mathrm{nm}$ and the length $s = \frac{D_{av}}{2} = 21\,\mathrm{nm}$.

The peptide therefore reduces the surface energy of this specific crystal face since $\sigma_\mathrm{h} \ll \sigma_\mathrm{d}$. σ_h was determined to the (111) crystal face in electron diffraction measurements. The (112) face was found in the control experiment as well as in the initial stages of the biomimetic approach. This indicates that the (112) face is the naturally lower surface energy for this system. The change to the (111) face shows that this surface energy must be reduced in comparison to the (112) face. Prozorov *et al.* came to a similar conclusion in their work [107]. Whether the peptide adsorbs only onto the (111) face or onto all crystal faces with predominant adsorption on the (111) face due to the larger

area of this face cannot be determined from this calculation. Surface energies for different crystal faces would be required to fully answer this question. In the Chapter "Polypeptide-inorganic crystal interaction", the amount of peptides adsorbing onto the nanoparticles was calculated to $N_{Peptide} = 949$ peptides per nanoparticle under the assumption that the peptides do not interact face-specifically. Considering the geometry, $N_{Peptide} = 614$ peptides would adsorb onto the (111) face A_{h} and $N_{Peptide} = 335$ peptides adsorb onto the side surfaces A_{d}. That means that 1.8 times as many peptides could adsorb onto the (111) face as on the (112) face. The asymmetric increase in lattice parameter along the body diagonal, however, indicates that the polypeptide-inorganic crystal interaction might be face specific and dependent on the lattice parameter. Such an interaction mechanism has been suggested previously for other systems [106].

Aggregation and orientation of primary building blocks: The polypeptide stabilized Pbb start to grow and aggregate into mesocrystal-like structures, as displayed in Figure 92. The assembly mechanism, which leads to the formation of mesocrystals is ongoing discourse and several mechanism have been proposed [144, 159]. The interparticle forces, including van-der-Waals attraction [157] and repulsive forces due to c25-mms6 or hydration layers are most likely the dominating factors in this assembly since the small substructures are below the SPM limit of cobalt ferrites [157, 159]. The initially observed loosly-assembled structures are not oriented, as shown in the HRTEM measurements of the small discs. The small discs display random top/bottom crystal faces. During the assembly into mesocrystal-like structures, the primary building blocks form the nanoparticle's substructures as observed in the HRTEM measurements. After reaching their final size, regions with the primary building blocks reorganize and align along a common crystallographic axes. This was also observed in dark field images of a diamond-shaped mesocrystal. The primary building blocks align so that the (111) face forms the the top/bottom crystal face. Such crystallographic reorientation within mesocrystals has been suggested previously [160].

Formation of secondary nanoparticles: Prior to aggregation several

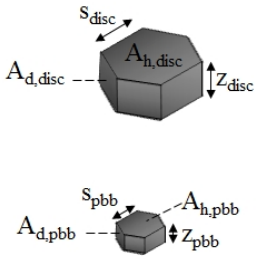

Figure 96: Geometries used to calculate the Pbb fusion.

phase transformations from an iron-rich non-stoichiometric to a cobalt-rich stoichiometric phase take place. Regions of larger substructures as well as denser regions were found to be richer in cobalt in the conducted EELS measurements of different spots within a single mesocrystal. The final phase-transformation to a stoichiometric composition is completed when neighbouring primary building blocks join at specific crystallographic faces leading to a reduced variance in disc diameter as observed in Figure 88. This fusion is driven by reduction of surface energy. Surfaces are energetically unfavorable and the mesocrystal consists of a large amount of inner surfaces due to the non-aggregated Pbb. The reduction of the inner surfaces by Pbb fusion can be calculated by estimating the number of Pbb within a mesocrystal and by then calculating the surface area of all Pbb and comparing this area to the surface area of a secondary nanoparticle. The number of Pbb N was estimated using

$$V_{\text{disc}} = N \cdot V_{\text{Pbb}} \tag{51}$$

with the disc volume $V_{\text{disc}} = \frac{3}{2}\sqrt{3}s_{\text{disc}}^2 \cdot z_{\text{disc}}$, N as the number of Pbb and $V_{\text{Pbb}} = \frac{3}{2}\sqrt{3}s_{\text{Pbb}}^2 \cdot z_{\text{Pbb}}$. The hexagonal geometries used in the calculation are displayed in Figure 96. The number of Pbb within a single mesocrystal was calculated to N=417 for $z_{\text{Disc}} = 10\,\text{nm}$, $s_{\text{disc}} = 22\,\text{nm}$, $z_{\text{Pbb}} = 1.7\,\text{nm}$, and $s_{\text{Pbb}} = 2.5\,\text{nm}$. These values were determined from TEM and EELS measurements. The surface area of a single Pbb can be calculated with

$$A_{\text{Pbb}} = 6 \cdot A_{\text{d,Pbb}} + 2 \cdot A_{\text{h,Pbb}} = 58\,\text{nm}^2 \tag{52}$$

with $A_{d,Pbb} = z_{Pbb} \cdot s_{Pbb}$ and $A_{h,Pbb} = \frac{3}{2} \cdot \sqrt{3} \cdot s_{Pbb}^2$. The surface area of a 417 Pbb calculates to $\text{A}_{\text{total,Pbb}} = 24\,176\,\text{nm}^2$. The surface area of the disc can be calculated to

$$A_{\text{disc}} = 6 \cdot A_{\text{d,disc}} + 2 \cdot A_{\text{h,disc}} = 3835\,\text{nm}^2 \tag{53}$$

with $A_{d,disc} = z_{disc} \cdot s_{disc}$ and $A_{h,Pbb} = \frac{3}{2} \cdot \sqrt{3} \cdot s_{disc}^2$. The comparison of the disc surface area to the surface area of 417 Pbb can be described by

$$\frac{A_{\text{disc}}}{N \cdot A_{\text{Pbb}}} = 0.15 \tag{54}$$

These calculations show that through the joining of the primary building blocks, the surface of the crystal is reduced by 85 %. The final phase transformation to the stoichiometric Co_2FeO_4 phase occurs at this stage.

The fact that some non-stoichiometric mesocrystals remain after 28 days can be explained the choice of the starting composition. During the Pbb fusion, a phase transformation towards a cobalt-rich phase occurs. The initial starting composition, however, is richer in iron. After 12 minutes, the cobalt precursor is substantially reduced and the iron-rich spheres form as a side product. Some particles cannot form the stoichiometric cobalt-rich phase (Co_2FeO_4) and remain in the metastable state. Similar phase transformations in multistep biomineralization processes have been discussed previously [160]. However, further studies are required to understand the principle of these transformations and to determine whether a catalytic nature of the polypeptide is responsible or if the energy released in the Pbb fusion is sufficiently large to overcome the activation energy E_{12}. Why this phase transformation is neccessary to obtain the final secondary nanoparticle should be studied to fully understand the crystal growth process.

The observed growth process contradicts the classical nanoparticle formation theory. Epitactic monomer adsorption on which the classical theory is based could not be observed. Instead an aggregation-based mechanism was found which is ruled out in the classical theory. In addition, a homogeneous nuclei surface is assumed in the classical theory. The nuclei surfaces cannot be directly observed, however the calculations and measurements indicate that the nuclei have different surfaces and different surface contributions which lead to non-spherical crystal growth. On the basis of these experimental results, it can be concluded that the classical theory does not explain the bioinspired crystal growth and that the assumptions on which the theory is based are partly invalid.

The observed multistep growth process matches the oriented attachment theory proposed by Penn and Banfield [155]. The recently proposed kinetic model agrees with the change in disc diameter where Ostwald ripening dominates the later stages of crystal growth [154, 155, 212].

Magnetic Properties

The magnetic properties of nanoparticles are influenced by the composition, microstructure, morphology, defects and the crystal lattice. The interaction of the nanoparticles with the environment is of further importance. Ferromagnetic particles tend to agglomerate due to diplole-dipole coupling. Understanding the growth process and the particle-particle interaction could allow for specific tayloring of the magnetic properties of the nanoparticles and particle systems.

This chapter discusses the magnetic properties of the particles obtained in the control experiment as well as the biosynthesis. The influence of c25-mms6, which was found to alter the crystal growth and should therefore influence the physical properties, is discussed by comparing the results for the bioinspired syntheses to the control experiment results. Here, the nanoparticle ensemble is measured instead of single nanoparticles. The AGM measurements can therefore only give first insights into the magnetic behavior, the influence of the polypeptide on the magnetic properties, and the dependence on changes in composition, crystal face, and particle size. The measurements were conducted at different stages of the nanoparticle growth processes between 5 minutes and 28 days to study the change in magnetic properties with time. Measurements in parallel (in-plane) and perpendicular (out-of-plane) orientation to the external field were carried out since a magnetic anisotropy was expected due to the disc-like nanoparticles, which preferentially lie flat on the wafer. $2\,\mu L$ of the particle suspension was dropcasted onto a $4\,mm \times 4\,mm$ large native oxide silicon wafer. The particle suspension was stewed prior to dropcasting to obtain a more homogeneous suspension fot the AGM measurements. An external field of $398\,kA \cdot m^{-1}$ was applied to obtain an overview of the magnetic properties. A stepsize of $2\,kA \cdot m^{-1}$ was chosen for these measurements. More detailed measurements were conducted with a decreased stepsize of $0.4\,kA \cdot m^{-1}$ and an externally applied field of $79.6\,kA \cdot m^{-1}$. The curves are normalized by their saturation moment to allow a comparison between the measurements and curve shapes. The magnetic volume V_{mag} for the nanoparticle ensemble is unknown. Therefore the saturation magnetization cannot be determined directly from the measurement. Calculating

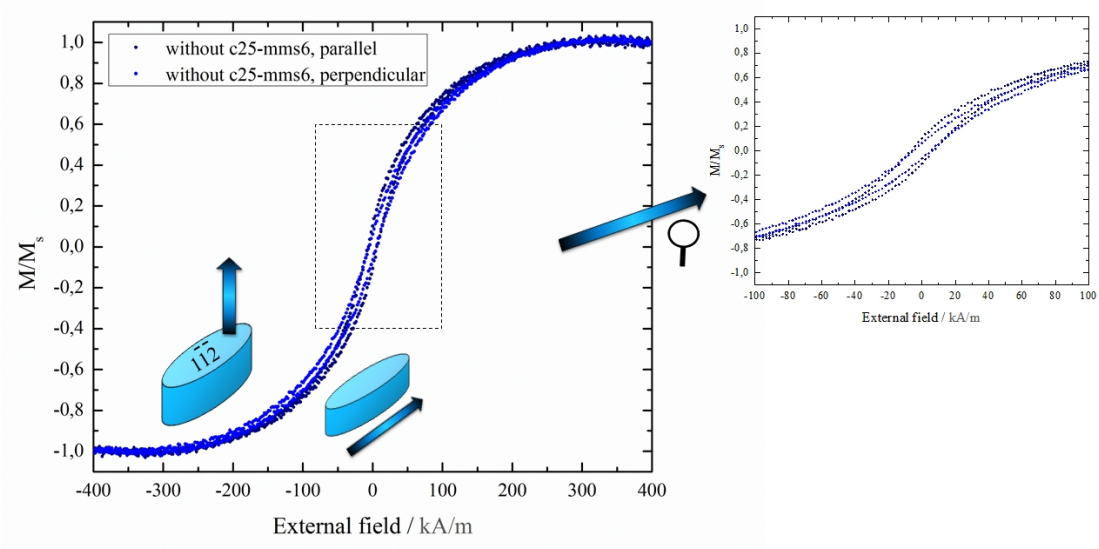

Figure 97: AGM measurements in parallel (in-plane) and perpendicular (out-of-plane) direction of the control experiment nanoparticles after 1 day. The out-of-plane direction along the $[1\bar{1}\bar{2}]$ direction is displayed in a lighter blue. The in-plane measurement is represented by the dark blue spheres. The inset shows an enlarged area of the marked H-M curve. The H-M curves are normalized with respect to to their saturation moment to allow a better comparison.

the saturation magnetization from the measurements is generally possible using

$$M_s = \frac{m_s}{V_{mag}} = \frac{m_s \rho_p}{c_p V_{sus}}, \left[\frac{\text{emu} \cdot \frac{\text{g}}{\text{cm}^3}}{\frac{\text{g}}{\mu\text{l}} \cdot \mu\text{l}} \right] \tag{55}$$

if the particle volume V_{mag} can be estimated [37]. However, different cobalt ferrite phases as well as side products such as NaCl are present, all with unknown ratios with respect to each other. This lack of information does not allow the calculation[66].

Magnetic properties of the control experiment particles

The AGM measurements of the control experiment particle ensemble after 1 day, given in Figure 97, show a hysteresis, as expected for a ferrimagnetic substance. The inset shows a more detailed measurement of the marked area in the hysteresis. The coercivity $H_{c,(in-plane)} = 6.2\,\text{kA} \cdot \text{m}^{-1} \pm 0.4\,\text{kA} \cdot \text{m}^{-1}$ appears larger in the in-plane direction than in the out-of-plane direction $H_{c,(out-of-plane)} = 4.6\,\text{kA} \cdot \text{m}^{-1} \pm 0.9\,\text{kA} \cdot \text{m}^{-1}$. However, a conclusive result cannot be obtained considering the statistical fluctuations for these measurements.

[66] The ratio of the different phases could theoretically be determined from the intensities of the XRD measurements. The preferred orientation of the discs, however, leads to unreliable reflex intensities and thus prevents the determination of the ratio.

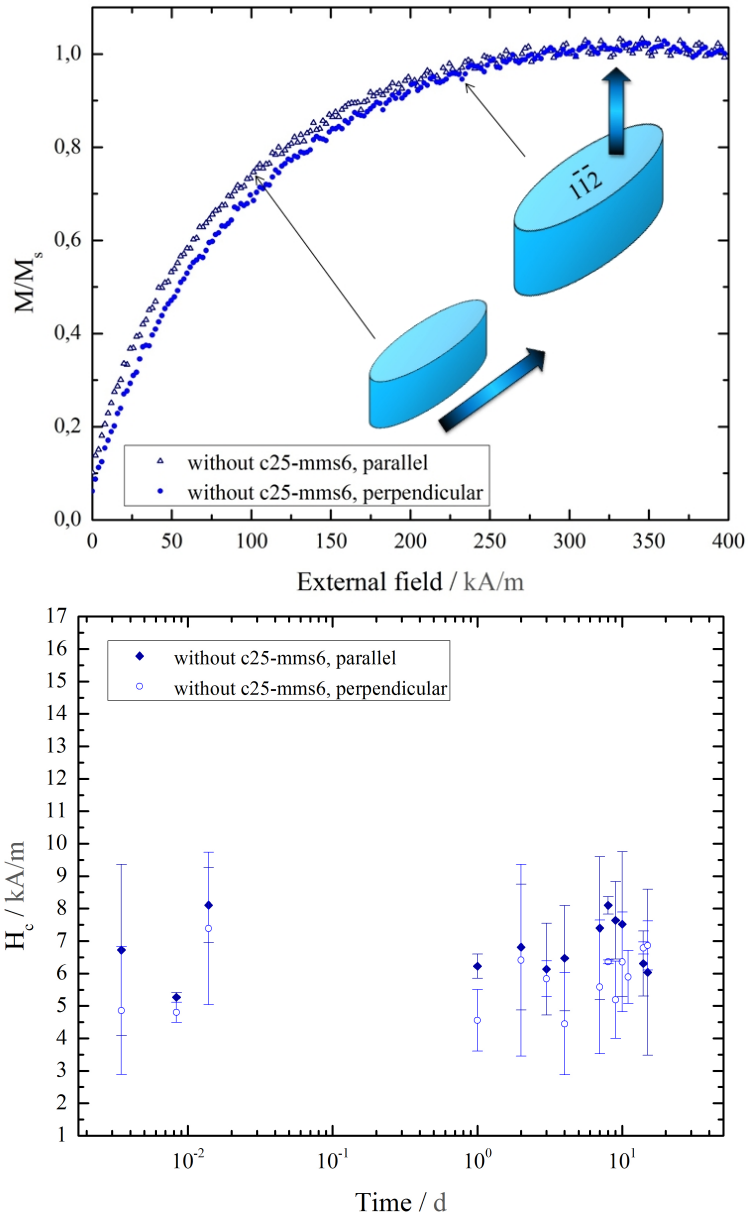

Figure 98: Top: Magnification of the control experiment magnetization measurements. The dark spheres represent the in-plane measurement, the out-of-plane measurement is repesented by the bright blue triangles. Bottom:Coercivity of the control experiment particles with time. The in-plane measurements are represented by dark blue diamonds, the out-of-plane measurements are represented by light blue spheres.

The expected anisotropic behavior and therefore the differences in field strength neccessary to completely align the magnetic moments could not be observed in these measurements. The saturation is reached at the same external field for both the in-plane and out-of-plane direction (see Figure 98). A magnetically harder axis, leading to a shifted saturation field, was expected out-of-plane due to the disc-like shape. The out-of-plane direction corresponds to the $[1\bar{1}\bar{2}]$ crystal direction which is a magnetically easier axis in cobalt ferrites [123]. Whether the magnetocrystalline anisotropy is linked to the missing anisotropy cannot be determined from the measurement.

The coercivities, measured at different stages of the nanoparticle growth process, are given in Figure 98. A change in coercivity cannot not be observed. The coercivity appears larger in the in-plane direction for all measurements, except the last two measurement points. However, the large statistical fluctuations in the coercivity, caused by the lack of control over the growth process of the control experiment particles and the resulting deviating physical properties, do not allow a more detailed evaluation of the measurements. A comparison to earlier work shows that the magnetic properties are not reproducable in this conventional approach. A coercivity, $H_c = 32\,\mathrm{kA \cdot m^{-1}}$ was obtained for the same synthesis previously [112]. The non-reproducability of the magnetic properties is most likely caused by the irregularity of the nanoparticles and is also evident in the large statistical fluctuations within the measurements of a single synthesis. Since the irregular shape is not well defined, differences in broken edges in combination with different compositions lead to uncontrollable microstructure, composition, and morphology and, therefore, physical properties.

Magnetic properties of the biomimetic particles

The bioinspired nanoparticles display a different magnetic behavior than the control experiment particles. AGM measurements, given in Figure 99, show a higher coercivity in the out-of-plane direction $\mathrm{H}_{c,(out-of-plane)} = 11\,\mathrm{kA \cdot m^{-1}} \pm 0.3\,\mathrm{kA \cdot m^{-1}}$ in comparison to the in-plane direction $\mathrm{H}_{c,(in-plane)} = 8\,\mathrm{kA \cdot m^{-1}} \pm 1.7\,\mathrm{kA \cdot m^{-1}}$. This behavior, contrary to the indicated behavior of the control experi-

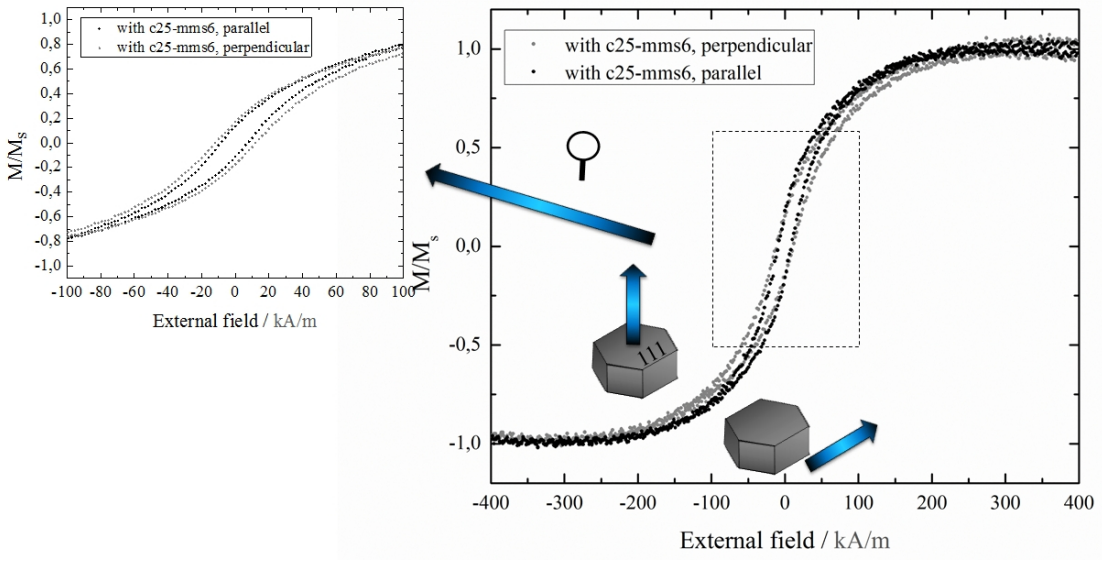

Figure 99: Hysteresis curves obtained for parallel (in-plane) and perpendicular (out-of-plane) measurement of the biosynthesized particles after 1 day. Each curve is normalized with repect to its saturation moment to allow a better comparison of the hysteresis shape. The in-plane measurement is represented by black spheres, the out-of-plane measurement along the [111] crystal direction is represented by grey spheres. The inset shows a more detailed measurement of the marked area in the hysteresis curve.

ment particles, can be observed throughtout the entire growth process, as displayed in Figure 102.

A small anisotropy can be observed for these particles. The H/M curve, given in Figure 100, shows that the saturation magnetization is achieved at slightly higher fields in the out-of-plane measurements. The out-of-plane direction corresponds to the shorter axis in the bioinspired nanoparticles as well as the [111] crystal direction which is a magnetically harder direction in cobalt ferrites [200]. If the relation between the out-of-plane direction (shape) and the crystal direction explains the small anisotropy (in comparison to the control experiment) cannot be determined from the ensemble measurement, however, it is the most plausible explaination for the observed behavior.

A change in magnetic behavior with time occurs for the biosynthesized nanoparticles. An increase in coercivity in-plane and out-of-plane with time can be observed in contrast to the control experiment particles. The increase in coercivity and change in the hysteresis shape is displayed in the H/M curves in Figure 101 for the bioinspired particles between 12 minutes and 1 day. This change

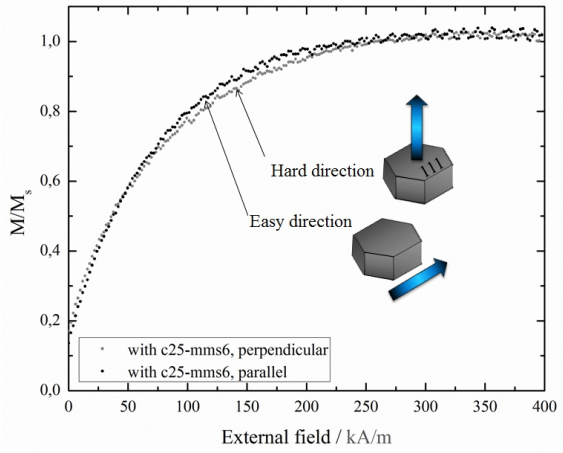

Figure 100: Magetic behavior of the biosynthesized nanoparticles in out-of-plane and in-plane direction. The in-plane direction is represented by the black spheres, the out-of-plane direction is represented by the gray spheres.

cannot be correlated to the nanoparticle size. The nanoparticle diameter remained unchanged throughout the first 20 min of crystal growth. This change in magnetic behavior is more likely linked to the change in phase. The overall increase in coercivity for both measurement directions throughout the entire crystal growth is plotted in Figure 102. The increase in coercivity out-of-plane appears steeper than for the in-plane direction.

Less statistical fluctuations, caused by a higher degree of control over the physical properties and thus microstructure, morphology and composition, allow a more detailed evaluation of these particles. According to literature, an increase in coercivity can be achieved by increasing the cobalt content in cobalt ferrites [122] which was observed in the TEM and EELS measurements and is therefore in good agreement. The AGM measurements show that the coercivity increases with time for both the in-plane and out-of-plane direction in this biomimetic approach and is thus in good agreement with the literature. The obtained values for the coercivity after 15 days were identical in several syntheses (see Table 11), showing that the biomimetic approach provides more reliable results. A size dependent change in coercivity with increase in diameter, as suspected earlier [134], could not be confirmed since an increase in coercivity can be denoted throughout the first 20 minutes of particle growth in which the nanoparticle diameter remains unchanged. A composition dependent change in coercivity occurs instead.

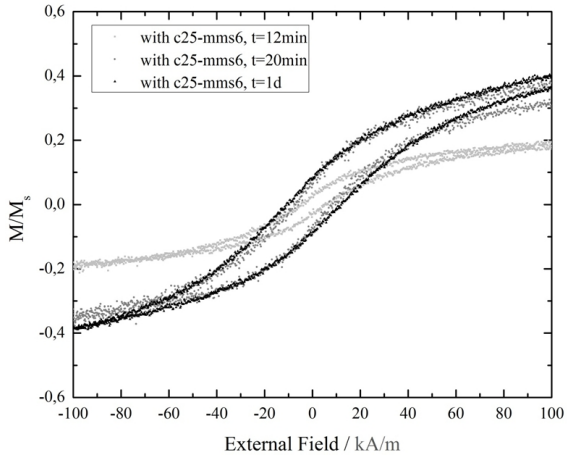

Figure 101: Hysteresis curves for the bioinspired nanoparticles between 12 minutes and 1 day in out-of-plane direction. The measurements are normalized with respect to the saturation moment after 1 day. The increase in time is represented by the change towards a darker color.

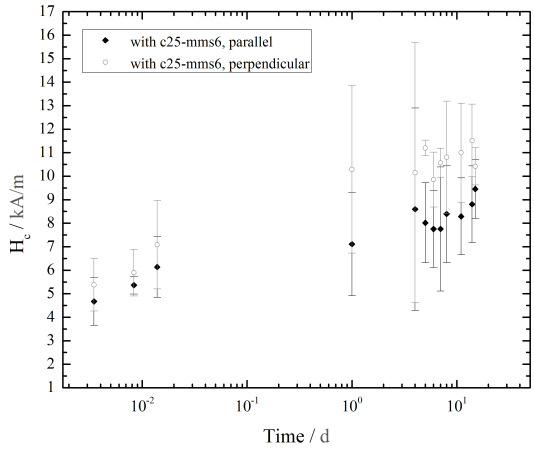

Figure 102: Change in coercivity with time for the biosynthesized nanoparticles. The in-plane measurements are represented by black diamonds and the out-of-plane measurements are represented by circles.

Evaluation and Comparison

The lack of control over the composition and shape leads to large statistical variations in the physical properties of the control experiment particles. Reproducable magnetic properties could only be obtained in the bioinspired synthesis. Well defined nanoparticles are obtained in the latter approach, leading to a higher degree of control over the magnetic properties. This is illustrated in Table 11 which summarizes the main results of several syntheses of both the control experiment and the biomimetic approach.

The anisotropy constant for the biosynthesized particles can be calculated[67] to $K_{ani} = 3.01 \times 10^3\,\mathrm{J \cdot m^{-3}}$ using the Stoner-Wohlfarth model

$$H_c = \frac{2 \cdot K_{ani}}{M_s} \,. \tag{56}$$

This value is lower than the literature value for the $CoFe_2O_4$ bulk phase $K_{ani} = 2.5 \times 10^5\,\mathrm{J \cdot m^{-3}}$ reported by Blaskov *et al.*[128]. The lower anisotropy constant results in an increased superparamagnetic limit $D_{SPM} = 46\,\mathrm{nm}$ for the iron-rich cobalt ferrite phase. The superparamagnetic limit was previously calculated to $D_{SPM} = 10\,\mathrm{nm}$ by Chinnasamy *et al.* [110].

An overall reduction of coercivity in comparison to the literature for the control experiment as well as the biosynthesis can be observed. The literature values are given in Table 11. This reduction is caused by several factors. Demagnetization fields at the sharp edges of the nanoparticles and the broken edges of the crystal reduce the coercivity. Superparamagnetism further contributes to the reduction in coercivity. A particle ensemble of larger discs as well as small spheres is studied in these measurements. The diameter of the small spheres, formed as a side product, as well as the smaller disc[68] diameters are below the superparamagnetic limit, initially calculated by Chinnasamy. Considering the calculated increased superparamagnetic limit, the majority of particles in both syntheses should display superparamagentic properties. The fact that a hysteresis can be observed in both cases can be understood when considering the size range of the particles. Several particles in both approaches display diameters above 46 nm. A superposition of ferrimagnetic particles as well as superparamagnetic spheres is studied here. The ratio of superparamagnetic to ferrimagnetic particles, dependent on the superparamagnetic limit, strongly influences the displayed coercivity. The influence of the particle agglomeration is also likely to influence the results. How strong this counteracting effect is cannot be estimated.

The expected anisotropy arising from the intrinsic magnetocrystalline anisotropy and the particle shape could only be observed for the biosynthesis. Both anisotropies are likely to cancel each other in the control experiment due to the different top/bottom crystal face.

The AGM measurements only provide a small insight into the

[67] This calculation was performed by Prof. Andreas Hütten.

Table 11: Coercivity of the bioinspired syntheses (c25-mms6) and the control experiments (w/o c25-mms6), obtained in different syntheses.

Synthesis	$H_c\,[\frac{kA}{m}]$
c25-mms6 (2009)	10.2 (15 days)
c25-mms6 (2013)	9.5 (15 days)
w/o c25-mms6 (2009)	32 (28 days)
w/o c25-mms6 (2013)	6.2 (28 days)
$CoFe_2O_4$ [134]	107.7
Co_2FeO_4 [134]	54.9

[68] The smaller discs were observed in the HRTEM measurements (see Figure 85.)

magnetic properties of the nanoparticles, since only the ensemble can be measured. Side phases such as NaCl, found in the EDX and XRD measurements, are present and reduce the total magnetic volume of the sample. Since the ratio between the side phases and the magnetic phases is unknown, it is difficult to obtain reliable information about the saturation magnetization. Furthermore, information about the magnetic properties of the single cobalt ferrite phases cannot be determined. To fully understand the magnetic properties of the different cobalt ferrite phases and shapes, further EMCD measurements in combination with EELS and HRTEM measurements are required.

Comparison to Prozorovs results

$CoFe_2O_4$ nanoparticles were previously synthesized in vitro by Prozorov *et al.* [107]. In their work, they obtained hexagonal-like discs with diameters ranging from 50 nm to 80 nm. The phase of the discs was determined by XRD measurements solely. Whether the discs are really $CoFe_2O_4$ or two phases $CoFe_2O_4$ and Co_2FeO_4 are present cannot be distinguished in the XRD spectrum. Their determined lattice parameter a= 8.373 Å could also be caused by a distorted Co_2FeO_4 crystal structure with an increased lattice parameter, as observed in these experiments. This would lead to a false identification of the phases in the XRD spectrum. It is possible that the cobalt-rich phase was missed in their evaluation. A comparison of the spectrum given by Prozorov *et al.* and the simulated spectrum is given in Figure 103. It shows that the $CoFe_2O_4$ phases with the different lattice parameters cannot be distinguished from the cobalt-rich phase Co_2FeO_4 with different lattice parameters. Their peak positions correspond to the areas where the peaks of the cobalt and iron-rich phases overlap. An overproportional (111) peak would be expected for their discs which would also predominantly have their top/bottom crystal face parallel to the substrate, thus, the reflex intensities would be unreliable and would not allow distinction between the two cobalt ferrite phases. Furthermore, the white noise in their measurements makes it difficult to determine further, smaller peaks. The strong fluctuations between $2\theta = 45°$ and $2\theta = 50°$ indicate that the smaller peaks of the cobalt-rich

phase could be present but were missed. This region is boxed with a rectangle in the spectrum. The comparison shows that it is likely that the iron-rich phase was indexed incorrectly and that the cobalt-rich phase as well as the increase in lattice parameter was missed.

Prozorov *et al.* also found the (111) top/bottom crystal face and concluded that a micelle based c25-mms6 cobalt ferrite interaction was most likely. In this work, however, the micelle based interaction could not be verified. Instead, single peptide adsorption is the most likely interaction mechanism.

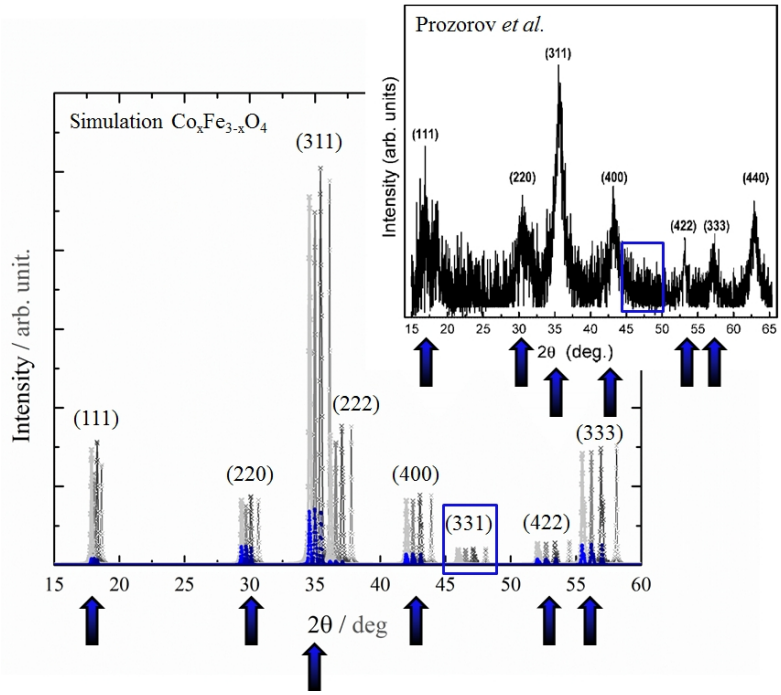

Figure 103: Comparison of Prozorov's XRD spectrum for the cobalt ferrite nanoparticles and the simulated spectrum for Co_2FeO_4 and $CoFe_2O_4$ with different lattice parameters. The peaks by which the two phases could be distinguished are highlighted with a rectangle. Prozorov's XRD spectrum was reprinted with permission from *T. Prozorov, P. Palo, L. Wang, M. Nilsen-Hamilton, D. Jones, D. Orr, S. Mallapragada, B. Narasimhan, P. Canfield, R. Prozorov*, "Cobalt Ferrite Nanocrystals: Out-Performing Magnetotactic Bacteria", **ACSNano**, 1, 2007. Copyright (2007) American Chemical Society.

Further experiments

This chapter discusses different experiments which were conducted to further study the effect and influence of c25-mms6 on the inorganic crystal formation.

Later addition of c25-mms6

The concentration dependent study suggested that c25-mms6 is likely to act as a catalyst. In this case, adding c25-mms6 to the non-stoichiometric nanoparticles obtained in the control experiment should allow the formation of hexgonal, Co_2FeO_4 nanoparticles. In this study 750 µL of the c25-mms6 solution was added to the control experiment particles after the crystal growth was completed (1 day). The microstructure and morphology of the particles was studied after 2 days (1 day after peptide addition) and 15 days.

TEM images of the particles before and after c25-mms6 addition are given in Figure 104. The TEM images show that the particles disintegrate after adding c25-mms6 (see Figure 104, 1 minute). New particles are formed afterwards. Adding the polypeptide after completed crystal growth induces a shape changing effect, not observed for the control experiment without c25-mms6. The nanoparticles change shape in favor of the hexagonal shape in an equivalent rate to the original biosynthesis. The change in shape is displayed in Figure 106. The average particle diameter was determined to $D_{av} = 35\,\text{nm} \pm 16\,\text{nm}$ after 2 days. The corresponding size distribution of these particles displays a double maximum which vanishes with time, as can be seen in the size distribution of the particles after 15 days. This behaviour can also be observed in the original biosynthesis. The size distributions of the particles

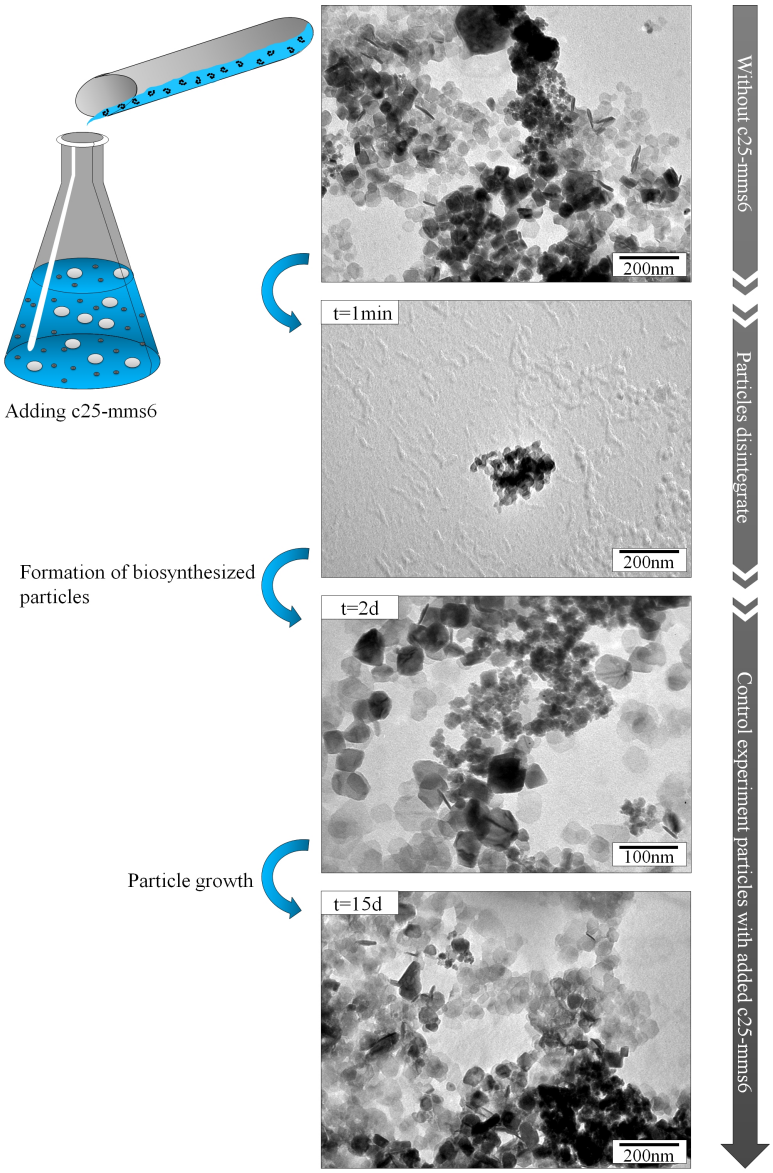

Figure 104: TEM images of the particles before and after adding c25-mms6. Top: image of the control experiment particles after 1 day. The synthetic polypeptide is added to these particles. Below: Nanoparticles at different times after the polypeptide addition. The particles disintegrate directly after adding c25-mms6 (1 minute). New nanoparticles form afterwards. The bottom images display these newly formed particles after 2 days and 15 days.

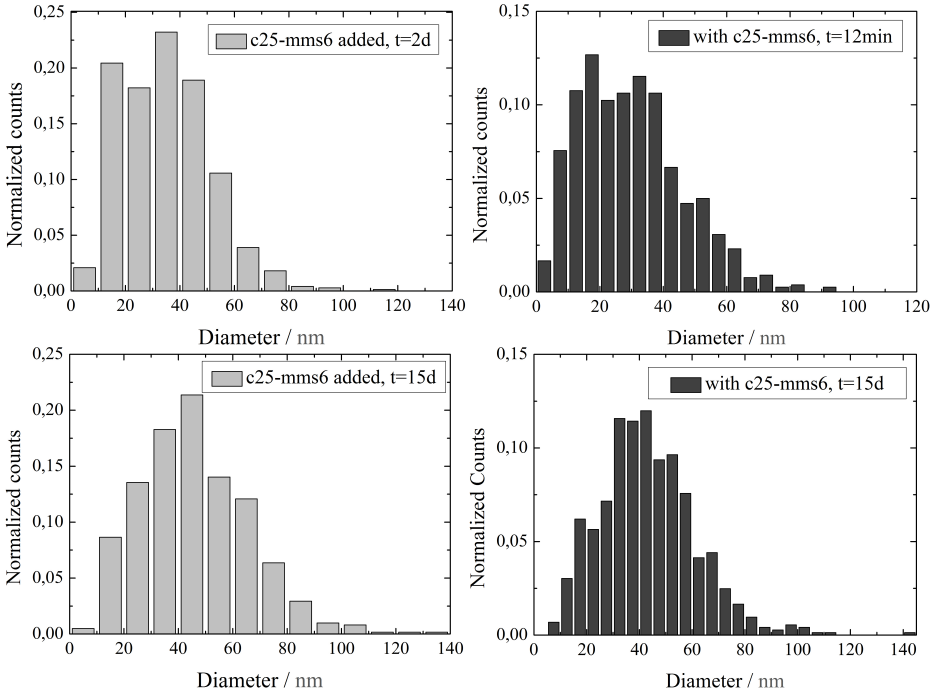

Figure 105: Comparison of the size distributions of the control experiment particles after adding c25-mms6 and the original biosynthesized particles. Left: Size distribution of the c25-mms6 added particles after 2 days and 15 days. The counts are normalized with respect to 719 particles (2 days) and 613 particles (15 days) used for the evaluation. Right: Size distributions of the biosynthesized particles.

with the added c25-mms6 and the original biosynthesis are given in Figure 105. The diameter of the particles after 15 days was determined to $D_{av} = 46\,\text{nm} \pm 20\,\text{nm}$ which is in good agreement with the biosynthesis. A comparison of the microstructure and morphology to the original bioinspired synthesis as well as the control experiment indicates that the control experiment particles, after adding c25-mms6, transform into the bioparticles. XRD measurements were conducted after 5 days as an initial compositional study. The obtained XRD spectrum is displayed in Figure 106 and compared to the control experiment spectrum and biosynthesized spectrum. The measurements show that these particles represent an intermediate stage between the biosynthesized particles and the control experiment particles, as would be expected at this stage (due to the disintegration prior and therefore delayed particle growth). Distinct XRD peaks of both approaches can be found for these particles. Whether or not the final stoichiometric phase and the lattice distortion are obtained after 15 days can only be determined

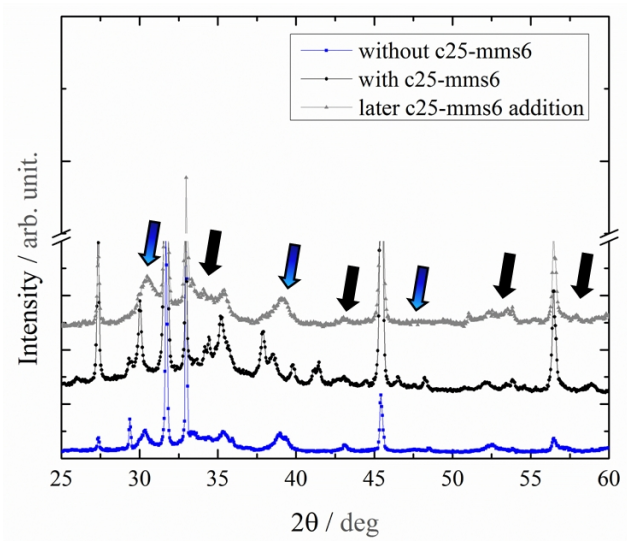

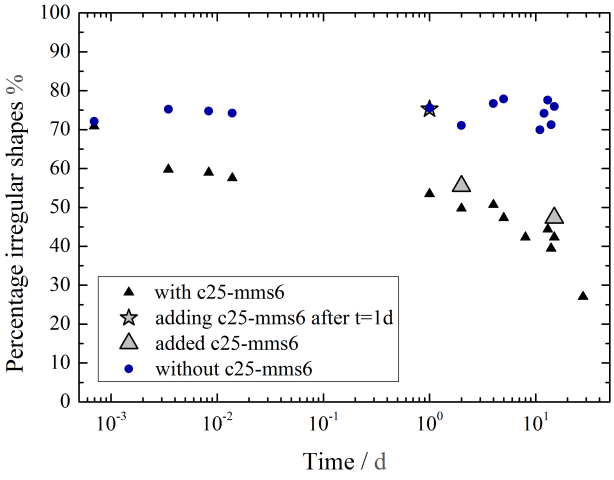

Figure 106: Top: XRD spectra of the control experiment particles (blue spheres), the biosynthesized particles (grey triangles) and of the later peptide addition particles (black stars) after 5 days. The arrows mark the distinct reflexes belonging to both the control experiment spectrum and biosynthesized spectrum, illustrating the intermediate stage of the later peptide addition particles. An offset was added for better visibility. Bottom: Change in shape with time for the c25-mms6 added particles after 2 days and 15 days (large triangles) in comparison to the control experiment (blue spheres) and the original biosynthesis (small, grey triangles).

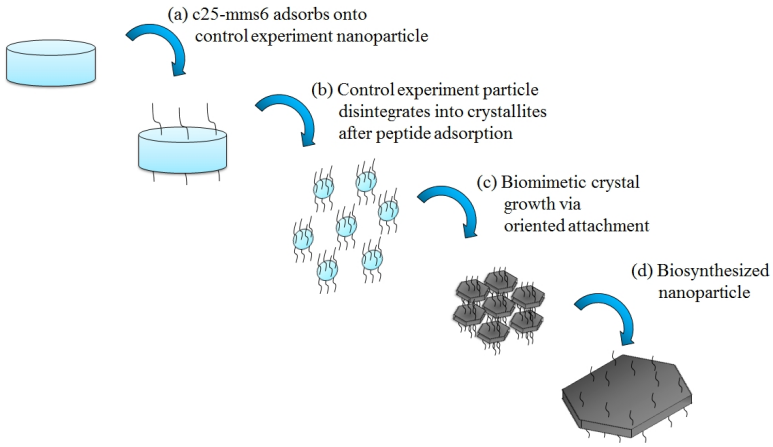

Figure 107: Schematic of the process occuring after adding c25-mms6 to the control experiment nanoparticles. c25-mms6 interacts with the control experiment nanoparticles leading to particle disintegration. The synthetic polypeptide adsorbs onto the disintegrated fragments from which the biosynthesized particles form.

Table 12: FCS Countrates, obtained for the free peptide solution, the original biosynthesis and the synthesis with the added c25-mms6 (after 20 minutes).

sample	Countrate /*kHz*
free peptide	3.36 ±0.65
biosynthesis	0.54 ± 0.04
added peptide	0.94 ± 0.13

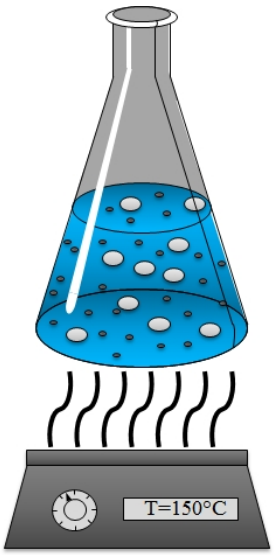

Figure 108: Illustration of the synthesis process in this high temperature study.

in further EELS and HRTEM measurements.

The later addition of c25-mms6 was also studied using FCS. In these experiments 750 µL of the RhodamineB labelled peptide (6.92×10^{-9} M) was added to the control experiment solution. An incubation time of 20 minutes was chosen before FCS measuremens were conducted. The count rates for the free peptides, the peptide addition, and the original biosynthesis after 1 day are given in Table 12. The values indicate that peptide adsorption is still occuring after 20 min, since the measured value is smaller than the free peptide value. However, this value is still twice as large as the biosynthesis value. If the peptide is added at a later stage of the particle growth, it disintegrates the particles and new particles equivalent to the original bioinspired synthesized particles form. This process is sketched in Figure 107. This initial study indicates that the synthetic polypeptide can be added at a later stage of crystal growth. However, EELS studies are neccessary to verify the existence of the stoichiometric Co_2FeO_4 phase.

High Temperature

Cobalt ferrites are conventionally synthesized at increased reaction temperatures between T=200 °C to 1000 °C [124, 125, 126, 127, 129, 213]. The original synthesis in this work was carried out at room

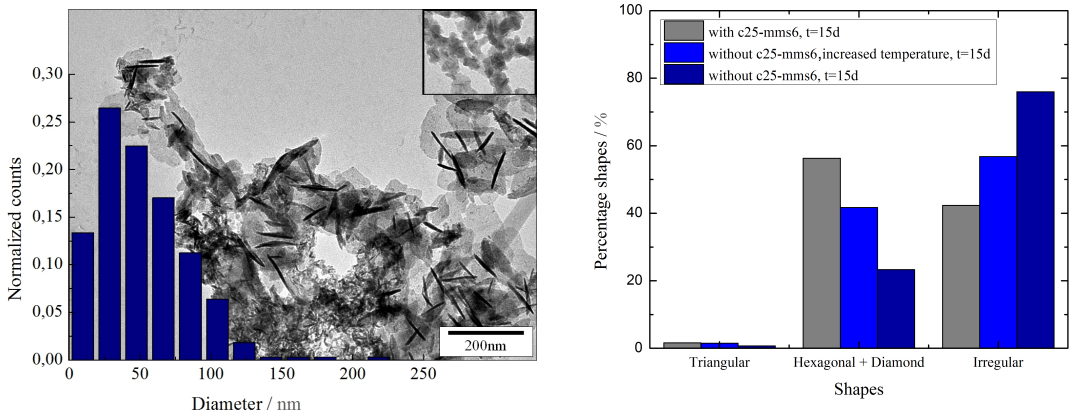

Figure 109: Left: TEM image of control experiment cobalt ferrite particles after 15 days, synthesized at a higher temperature $T = 150\,°C$. The inset shows the second type of particle obtained as a side product in this synthesis. The length of the inset rectangle is 200 nm. The counts of the particle's size distribution were normalized with respect to 329 particles used in the evaluation. Right: Comparison of the shape percentage for the control experiment (dark blue), the high temperature synthesis (blue), and the biosynthesis (gray).

temperature. In the control experiment, non-stoichiometric nanoparticles were obtained which was expected for low temperatures. In the biosynthesis, stoichiometric phases were obtained, which are commonly only achieved at high temperatures, indicating that the polypeptide helps to overcome the activation energy to form the stoichiometric phase, as sketched in Figure 91. In this approach, the control experiment particles were synthesized and heated to T=150 °C[69] for 1 hour to determine whether a higher temperature helps to overcome the activation energy E_{A2}. The effect of the raised temperature on nanoparticle formation and the phase was studied in TEM and XRD measurements and compared to the control experiment and biosynthesis, carried out at room temperature.

The TEM image, given in Figure 109, shows the particles after 15 days. Discs as well as ellipsoid agglomerated particles, displayed in the inset, were obtained in this approach. The disc diameter was determined to $D_{av} = 51\,\text{nm} \pm 32\,\text{nm}$ which is slightly larger than that of the biosynthesis. The size distribution, given in Figure 109, shows a tailing, indicating an Ostwald ripening process. A comparison of the hexagonal shape percentage to the control experiment and biosynthesis, given in Figure 109, shows that these particles represent an intermediate state between the original two approaches. 42 % of the particles are hexagonally-shaped. This increase in hexagonal shape in comparison to the control experiment

[69] This temperature was chosen due to the synthesis setup. Higher temperatures (600 °C) cannot be used for the synthesis in the chemistry lab. In addition, the lower temperature (150 °C) can be maintained throughout the synthesis for the given setup. This is illustrated in Figure 108.

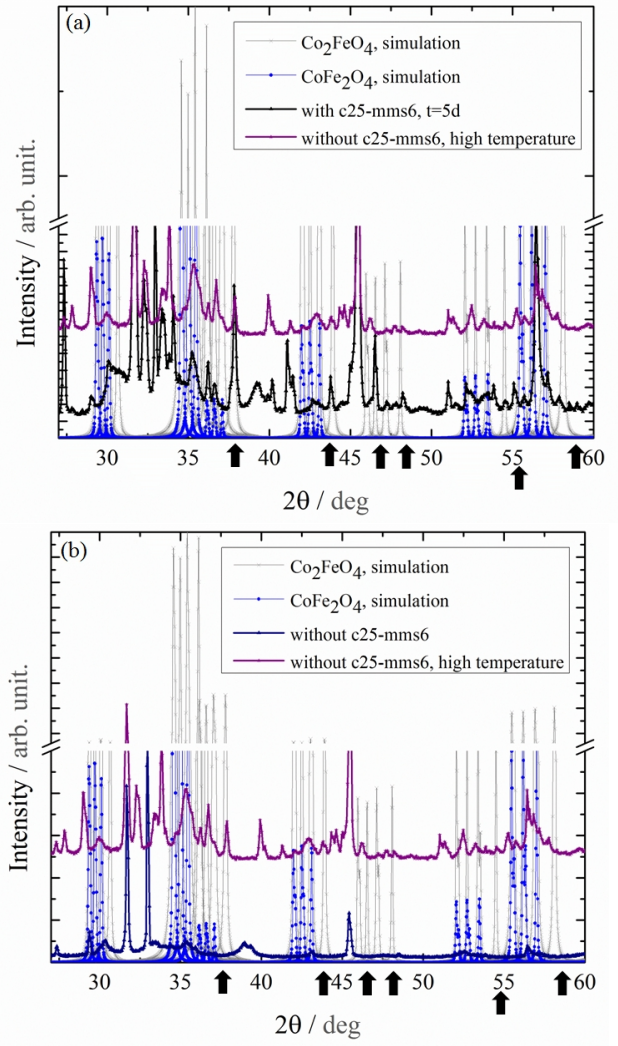

Figure 110: Comparison of the XRD spectra for the nanoparticles at 150 °C to the simulated cobalt ferrite spectra as well as the the biosynthesis (a) and the control experiment (b) after 5 days. The control experiment XRD spectrum is displayed in blue, the original biosynthesis XRD spectrum is displayed in black. The XRD spectrum of the high temperature control experiment synthesis is displayed in purple. The arrows in (a) mark the forming reflexes which belong to the Co_2FeO_4 phase. These peaks are absent in the control experiment and present in the original biosynthesis. An offset was used to allow for a better comparison of the measured XRD spectra.

indicates that a raised reaction temperature has a similar effect as c25-mms6.

The XRD spectrum is given in Figure 110 and is compared to the control experiment spectrum in (a) and to the biosynthesis in (b). The measurements show that peaks for the cobalt-rich phase start to evolve. These peaks are absent in the control experiment but present in the biosynthesis. The comparison shows that the XRD spectrum of the high temperature synthesis is in the transition from

the control experiment to the biosynthesis. To verify the presence of the Co_2FeO_4 phase, EELS measurements should be conducted.

The measurements indicate that the activation energy for the transition to a stoichiometric cobalt-rich phase can be overcome by using either a higher synthesis temperature or by adding c25-mms6. The reaction temperature of 150 °C, however, is not sufficient, as can be seen by the intermediate state of the particles between the control experiment particles and the biosynthesized particles. The results, however, show a clear trend towards the formation of more well defined and stoichiometric particles, especially considering that stoichiometric cobalt ferrites are conventionally synthesized at much higher temperatures and not at the used lower temperature. This preliminary result indirectly suggests that c25-mms6 acts as a catalyst since it has the same effect as a raised temperature.

Starting Composition

Small spherical nanoparticles of an iron-rich side phase were obtained in the original biosynthesis due to the choice of an iron-rich starting composition. In the following synthesis, a Co:Fe ratio of 2:1 was chosen to determine whether only discs would form without the side product and if c25-mms6 has the same influence on the particles obtained for the different starting composition.

Spheres could not be observed in this approach, instead only discs and a few smaller crystallites were found. The disc diameter was determined to $D_{av} = 58\,\text{nm} \pm 40\,\text{nm}$ after 15 days. These particles are larger than those in the original approach. A comparison of the particle size distribution, given in Figure 112, with the corresponding size distribution of the original approach (see Figure 105), shows that the particles synthesized with a cobalt-rich starting composition do not display a shifted maximum (as would be expected for larger particles) but display a more dominant tailing, leading to a higher average diameter. The tailing indicates that more Ostwald ripening occurs in this synthesis than in the original biosynthesis. A possible explaination for this result would be that instead of forming two separate phases (smaller $CoFe_2O_4$ and larger Co_2FeO_4), only smaller and larger cobalt-rich particles form. The smaller cobalt-rich particles dissolve in favor of the already larger cobalt-rich

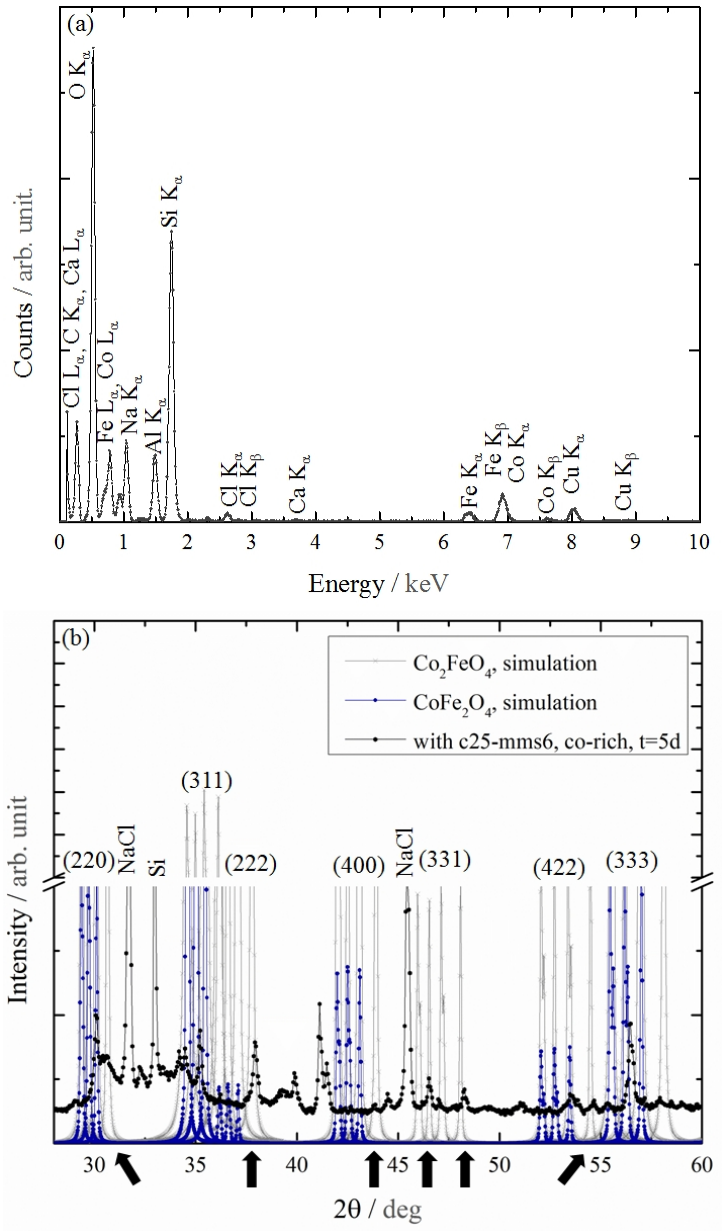

Figure 111: EDX and XRD measurements of biosynthesized particles with a cobalt-rich starting composition. (a) The EDX measurement shows the presence of the cobalt and iron within the sample as well as several side phases that exist either as side products in the particle suspension (such as NaCl) or belong to the DualBeam setup (such as Al). (b) The XRD spectrum of the particles indicates the presence of the Co_2FeO_4 phase. The distinct peaks for this phase can be found in the spectrum and are marked with the arrows.

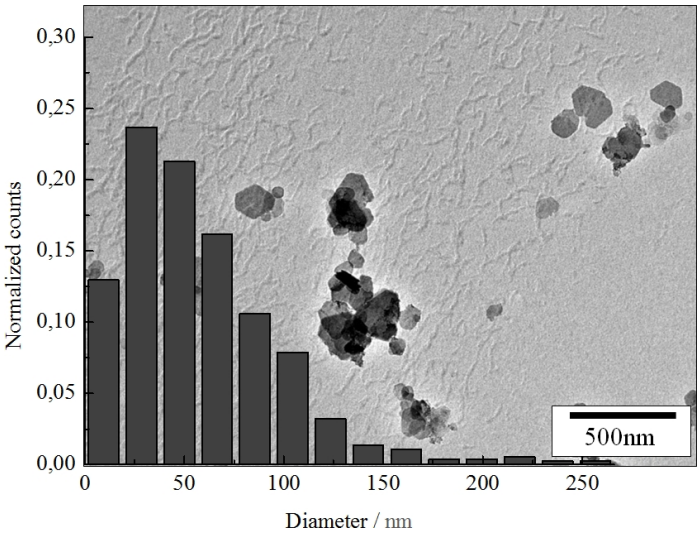

Figure 112: TEM image of particles obtained for a cobalt-rich starting ratio after 15 days. The size distribution of the particles was obtained by evaluating 748 discs and normalizing the counts with respect to this amount.

particles, leading to the observed tailing in the size distribution. 48 % of these particles are hexagonally-shaped which corresponds to the result of the biosynthesis after 15 days.

A combination of EDX and XRD measurements, given in Figure 111, allows a first compositional study. The cobalt and iron present in the cobalt ferrites, as well as side phases, such as NaCl, could be identified in the EDX spectrum and indexed accordingly in the XRD spectrum. The XRD spectrum suggests the presence of the Co_2FeO_4 phase. The distinct peaks for this phase are marked with the arrows in the spectrum. Whether the other peaks belong to the cobalt-rich phase with a distorted lattice or the iron-rich phase cannot be determined from these measurements. The presence of the marked peaks suggests that the other peaks belong to the Co_2FeO_4 phase with an increased lattice parameter. However, EELS measurements need to be conducted to distinguish the Co_2FeO_4 phase and the $CoFe_2O_4$ phase.

Conclusion

The polypeptide-nanoparticle interaction was studied using FCS. The micelle based interaction, proposed by Prozorov *et al.* could not be verified. Neither a concentration based aggregation nor a sufficiently large hydrodynamic radius, which was calculated to $R_H = 1.1\,\mathrm{nm}$ using the Stokes-Einstein equation were found. The diffusion coefficient of the synthetic polypeptides was determined to $D_{c25-mms6} = 2.43 \times 10^{-20}\,\mathrm{m^2 \cdot s^{-1}}$. The measurements showed that single peptide-inorganic crystal interactions occur in which c25-mms6 adsorbs onto the nanoparticles and can easily be removed via sonication, a characteristic that is advantageous for applications. Whether a face specific adsorption occurs could not be confirmed by the measurements. It was previously suggested that the interplanar spacings of nanoparticles are important parameters for the peptide-inorganic crystal interactions [106]. A stretched crystal structure along the [111] direction, observed in the electron diffraction measurements can also be found for the magnetite particles within the magnetotactic bacteria [72]. This distortion in both cases indicates that a face specific interaction is likely. This comparison furthermore shows that the same peptide-inorganic crystal interaction occurs in the biomimetic approach and the natural system.

The influences of different sections of the peptide on cobalt ferrite nanoparticle formation were studied along with a randomized sequence to determine a possible function of the peptide. The same effect on nanoparticle growth as c25-mms6 could neither be achieved by the different shorter sections of c25-mms6 nor by the randomized sequence. The latter shows that the amino acid sequence is of vital importance in the interaction and that the peptide therefore has a function and cannot be replaced by similar peptides or ligands of a

similar size.

The growth process of cobalt ferrite nanoparticles was studied in the presence and absence of the synthetic polypeptide c25-mms6. c25-mms6 influences the microstructure, morphology and composition of the nanoparticles by changing the growth process. The majority of the non-stoichiometric particles obtained in the control experiment display an irregular shape. Their morphology remains unchanged during the growth process and only the diameter increases throughout the first day of nanoparticle growth. The growth of the particles synthesized with c25-mms6 displays a different behavior and is therefore influenced by the synthetic polypeptide. The nanoparticle growth matches the description of an oriented attachment process. The subunits, referred to as primary building blocks in literature, could be observed in HRTEM measurements. EELS and electron diffraction experiments show that a reorientation of the primary building blocks as well as a phase transformation occurs prior to secondary nanoparticle formation. The energetically unfavorable crystal face (111) forms the final particle face, indicating that c25-mms6 adsorbs onto the initial small structures displaying the (112) crystal face in such a way that a growth in which the (111) final face is favored results. A change in shape from irregular morphology to a hexagonal shape occurs at the same time. The change in diameter matches the kinetic model recently proposed for the oriented attachment process. The final particles are stoichiometric. Stoichiometric nanoparticles could not be obtained in the control experiment. How this observed process is induced by the peptide cannot be concluded from the data. Further experiments, that give information about the peptide adsorption and show whether face specific adsorption occurs, are required to explain the observed process. The fate of the polypeptide during the primary building block fusion cannot be deduced from the experiments. Whether c25-mms6 is released during the fusion can only be answered once the peptide-nanoparticle interaction process has completely been determined.

The study of the magnetic properties showed that c25-mms6 has an effect on the physical properties (by altering the growth process). The increase in coercivity was linked to the change towards a more cobalt-rich phase which is in good agreement with the literature. In

addition, anisotropic behavior of the biosynthesized particles could be observed. Since the bioinspired synthesis offers a higher degree of control over the nanoparticle microstructure, morphology and composition, the physical properties are better controlled and were reproducable in several syntheses. Such reproducable results could not be obtained in the control experiment.

Additional experiments were carried out to further study the effect and properties of c25-mms6. In one experiment, c25-mms6 was added to fully grown control experiment particles. The evaluation of those particles at different stages of the growth process showed that the control discs disintegrate and new particles form which appear to have the biosynthesized particle properties. The result of this study suggests that c25-mms6 can also be added at a later stage as well. A similar result was obtained in a control experiment synthesis that was performed at an increased temperature (150 °C). The resulting particles represent an intermediate stage between the control experiment particles and the biosynthesized particles. Considering that cobalt ferrites are conventionally synthesized at even higher temperatures, this study indirectly shows that stoichiometric cobalt ferrites can either be obtained by an increased temperature or the synthetic polypeptide: the required activation energy can be overcome in both cases. A further study showed that the unwanted iron-rich side phase can be prevented by choosing a cobalt-rich starting composition. Further compositional studies are required in all approaches to verify that the stoichiometric phases are present in the sample. The XRD measurements can only serve as a first study.

These first principle studies show that biomimetic approaches can be applied to materials not occuring in the mimicked natural systems and that the drawback of a limited amount of materials associated with biomimetic approaches can be overcome. The work furthermore shows that oriented attachment explains the growth process and allows a well-controlled nanoparticle formation with reproducable properties which could not be achieved by a conventional chemical approach under equivalent conditions.

Outlook

The work raises several further questions which require additional studies to be fully answered. The EELS spectra of the biosynthesized nanoparticles and the control experiment particles both show differences in the oxygen finestructure. Whether these differences are linked to the particle composition, morphology or microstructure should be determined. If differences in the finestructure can be linked to the particle stability (the control experiment particles disintegrated while the biosynthesized nanoparticles were stable after allowing 5 minutes of crystal growth, see Appendix D) should be investigated.

The compositional changes in the multistep process are not yet understood and should be studied further. A ternary phase diagram for the system Co-Fe-O for room temperature[70], which is not available in literature [214, 215, 216], could be constructed using the calphad method and would help to interpret the occuring phase transitions. Studying the effect of the synthetic peptide c25-mms6 on Fe_3O_4 and Co_3O_4 could give information about the interaction process as well as the phase transformations. A corresponding ternary phase diagram[71], which also includes the stoichiometric iron-rich spinel phase $CoFe_2O_4$ is given in the literature [217]. These experiments could show whether c25-mms6 interacts with iron only or with cobalt as well.

The peptide-nanoparticle interaction should be further studied. Whether this interaction is face specific, or dependent on the lattice parameter should be determined. The results could potentially give insights into the fate of the polypeptide during the primary building block fusion.

The AGM measurements provided a first principle study since

[70] Thernary phase diagrams for this system are only given for elevated temperatures $T \gg 900\,°C$ to $1200\,°C$

[71] This ternary phase diagram does not include the cobalt-rich stoichiometric spinel phase Co_2FeO_4 and therefore does not allow a direct evaluation.

they allowed an ensemble measurement only. To understand the influence of the composition, morphology, and microstructure on the magnetic properties, EMCD measurements should be conducted. This method offers the possibility to measure the magnetic properties of single nanoparticles.

The function of c25-mms6 however is not yet determined. Whether it acts as a catalyst or simply stabilizes or destabilizes the intermediate substates and alters the surface energies of specific crystal faces needs further clarification. The phase transformation from the cobalt-rich non-stoichiometric $Co_{1.7}Fe_{1.3}O_4$ phase to the stoichiometric cobalt-rich phase Co_2FeO_4, observed only in the bioinspired synthesis, suggests that the peptide lowers the potential barrier E_{A2} (see Figure 91) and therefore acts as a catalyst. The effect of catalysts is concentration dependent. The higher the catalyst concentration the faster the reaction. An increase in the final product with increasing catalyst concentration occurs. An initial concentration based study was already performed to determine whether c25-mms6 displays a concentration dependent behavior. The bioinspired synthesis was carried out with different polypeptide concentrations, ranging from 6.92×10^{-10} M to 5.97×10^{-6} M. The results are compared to those obtained in the control experiment (0 M) and the original biosynthesis (6.92×10^{-9} M). TEM images of the particles obtained in the increased and reduced peptide concentration syntheses are given in Figure 153 in the Appendix E. An evaluation of the particles shows a c25-mms6 concentration dependent behavior. The percentage of hexagonal shapes and diameters after 15 days are given in Table 18. The amount of the hexagonally-shaped discs is reduced for the lower peptide concentration in comparison to the original biosynthesis. The obtained discs are furthermore smaller than those obtained in the biosynthesis. The discs obtained for the higher peptide concentration are larger. In addition the tailing in the size distribution is larger for these particles, showing that more particles with diameters exceeding 100 nm are formed. The amount of hexagonal shaped particles is increased for the higher peptide concentration in comparison to the original biosynthesis and the decreased peptide concentration. These results indicate that c25-mms6 may act as a catalyst. However, the growth kinetics of the different particles need to be studied to verify the catalytic

nature. For this, TEM evaluations of the particles at different stages of the growth process need to be conducted for the different concentrations. A comparison of the change in diameter with time for the different concentrations would give information about the growth kinetics, which would be faster for the increased peptide concentration. In addition, the amount of the stoichiometric cobalt-rich phase present should be compared for the different concentrations. A higher amount of Co_2FeO_4 phase should be obtained for the higher peptide concentration if c25-mms6 acts as a catalyst.

The synthesis offers room for improvement. In both approaches, broad size distributions, undesirable for applications, as well as side phases and agglomerations which can be improved by optimizing the synthesis parameters were obtained. The particles were studied directly from the reaction suspension without further treatment. Filtration and ligands could reduce the observed agglomeration and improve the sample quality in future syntheses.

Part III

New approaches in tissue engineering: functional nanostructures for stem cell differentiation

Motivation

Bio engineering and stem cell research represent two of the hottest research topics in biology and medicine at the dawn of the 21^{st} century [218]. Bio engineering is an interdisciplinary field which combines engineering with the life sciences and aims to understand complex living systems, to develop new biomedical therapies for medical issues that cannot be overcome with the current available treatments and to improve currently available treatments such as tissue engineering. Today, specialized cells are used to engineer tissues[72] used for wound repair in surgery. The problem with specialized cells is that these cells often do not have a proliferation potential[73] and that the cell source is therefore limited [219].

[72] Tissue engineering referes to all approaches that either regenerate, repair or replace tissue.

[73] The proliferation potential referes to the potential increase in the amount of cells.

Stem cells, with the ability to form the various structures within the human body such as bones, muscles, nerves, or blood represent an alternative cell source. These cells have a high proliferation rate which allows for the creation of a sufficient amount of cells for tissue engineering. Understanding and developing techniques in which stem cell differentiation, i.e. the process in which unspezialized stem cells form more spezialized cells, could lead to cures for illnesses such as Parkinson's desease, Huntington's desease, Alzheimer's desease, other neurological disorders, muscle damage, spinal cord injuries and many other harmful conditions, which are currently incureable [33].

Today, stem cell differentiation into an osteogenic lineage (bone) is induced by biochemical cues such as dexamethasone (see Figure 113). This method is successfull *in vitro*. However, the biochemical cues lead to severe side effects *in vivo*[74] and therefore represent a drawback of stem cell therapies in regenerative medicine. Different mechanisms need to be developed to induce stem cell differentiation

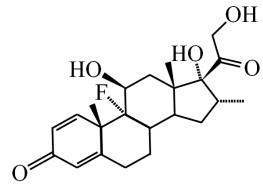

Figure 113: Chemical structure of the biochemical cue dexamethasone.

[74] Dexamethasone has an immunosuppressant effect, leading to an increased infection rate [34].

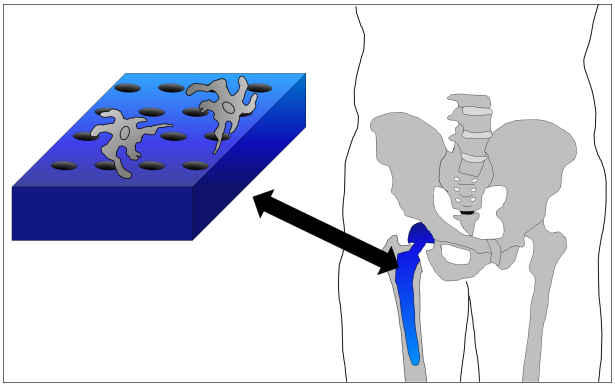

Figure 114: Possible future treatment for femoral neck fracture: A nanostructured titanium prothesis coated with stem cells could lead to a better graft adherence and improve the clinical outcome.

before it can be implemented as stem cell treatment. Recent studies by Lavenus *et al.* [34] show that differentiation of human mesenchymal stem cells[75] into an osteogenic lineage (specialization into bone) can be induced by a titanium surface with 30 nm sized pores. The mechanism, by which this stem cell differentiation is instigated, however, remains unknown. Understanding the influence of nanopores on stem cell differentiation could not only lead to new medical therapies but could also improve the clinical outcome of conventional treatments such as the treatment for femoral neck fracture. This injury is often treated by replacing the femoral neck by a titanium[76] prothesis. A nanostructured titanium prothesis[77], covered with stem cells, could not only speed up the healing process after the surgery but also lead to a better graft adherence and thus improve the clinical outcome. A sketch of this improved therapy is displayed in Figure 114.

In this work, stem cell differentiation into an osteogenic lineage was studied using a nanostructured titanium surface as a physical cue. Different nanopore sizes, 30 nm and 100 nm, were used as physical cues and their effect on differentiation studied. The first chapter aims to provide an understanding of stem cells and the differentiation process. The second chapter discusses the effect of nanopores on stem cell differentiation. In these experiments, the effect of different pore sizes in titanium coated polycarbonate membranes on stem cell differentiation is studied. The third chapter describes the engineering of nanostructured arrays using a Dual-Beam devide since well aligned arrays of 30 nm pores with different

[75] Human mesenchymal stem cells are multipotent and can form bone, cartilage, muscle, tendons, ligaments and connetive tissue [220].

[76] Titanium is conventionally used in orthopaedic surgery since it is biocompatible and has similar properties to bone.

[77] A nanostructured titanium prothesis could promote stem cell differentiation into an osteogenic lineage according to Lavenus *et al.*

inter-pore distances, which are required for further experiments, are commercially not available. A summary and outlook are given in chapters four and five.

Stem cells

Stem cells are cells which can self-renew, produce more stem cells, and differentiate into different, specific cell types. These abilities are referred to as potency. Stem cells can show different types of potency where potency describes into how many different cell types the stem cells can differentiate:

Totipotent: These stem cells, produced by the fusion of egg and sperm, can construct a whole organism with about 10^{13} cells for an adult human [221] with 200 different cell types [222]. They can differentiate into embryonic and extraembryonic stem cells.

Pluripotent: These stem cells can differentiate into almost all cell types.

Multipotent: Multipotent cells can differentiate into closely related cells.

Oligopotent: These stem cells can differentiate into a few different cell types only, for example into lymphoid or myeloid cells.

Unipotent: Unipotent stem cells can produce their own cell type only. In contrast to non stem cells, these cells can self-renew.

The different types of potency are illustrated in Figure 115. While a complete organism can be constructed from an embryonic stem cell[78], adult stem cells can only differentiate into various structures and are a vital part in the repair mechanism of different tissues within the human body [223]. Adult stem cells can be found in different tissues within the human body, for example in the bone marrow and stroma. A detailed description of all the different types of adult stem cells is beyond the scope of this work. However,

[78] These stem cells are isolated from the inner cell mass during the bastocyst stage [219].

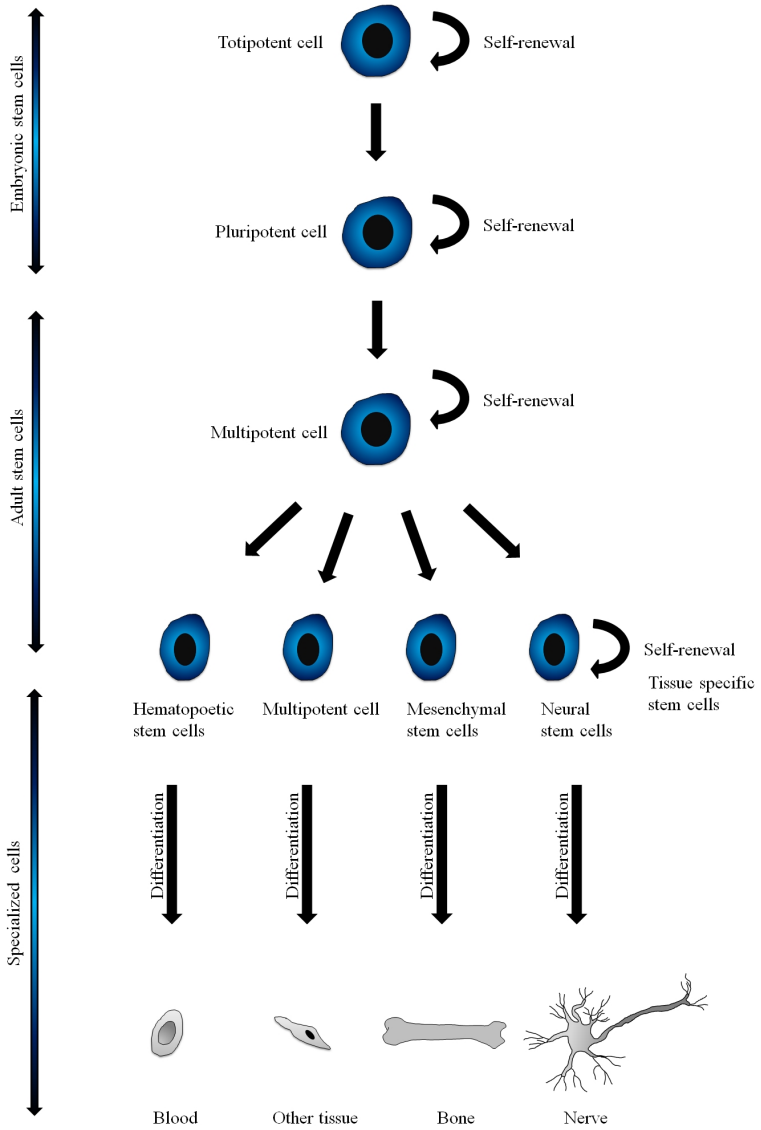

Figure 115: Overview of the different stem cell types. Totipotent stem cells form the embryonal cells. The pluripotent stem cells (embryonic) can form any kind of tissue within the organism. Multipotent stem cells (adult stem cells) can form various structures of an organism such as blood, bone, nerves, and other tissues. The process in which the stem cells specialize into the various structures is referred to as differentiation.

extensive information on stem cells is given in Li's, Lanza's, and Atala's works [33, 219, 220].

A cell consists of a membrane which separates the intracellular space from the extracellular space, a nucleus which contains the cell DNA, as well as other organells. The cytoskeleton of the cell, part of the internal structure and skeleton of the cell, influences the cell shape, division, movement, and signal transduction, among many other functions. It consists of different filament types: microfilaments such as the actin filament F-actin with a size around 7 nm; intermediate filaments with sizes around 10 nm, and microtubuli, consisting α, β tubulin with sizes around 25 nm [221] . Filopodia which are part of the cells morphology consist mainly of tightly packed F-actin bundles. They probe the enviroment around the cell and are involved in cell-cell adhesions [224]. A complete description of the organization within cells and the function of the different structures and organelles is given in Hoppe's work[190].

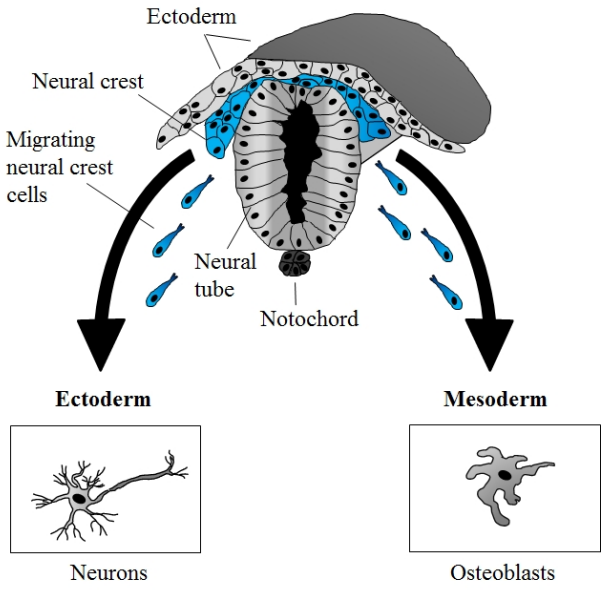

Figure 116: Schematic of the neural crest. Neural crest derived stem cells can migrate from the neural crest and differentiate into various cell types, includingneurons and osteoblasts. This schematic was drawn in analogy to Kaltschmidt *et al.* [225].

In this work, human neural crest-derived inferior turbinate stem cells (adult stem cells) were obtained from the nasal region (see Figure 117), during a routine surgery after an informed consent. The consent is in accordance with international and local (Bezirksregierung Detmold/Münster) guildelines. This type of stem cell is a promising candidate for regenerative medical treatment since it can be directly differentiated into an osteogenic lineage [226, 227, 228, 229]. A schematic of the human neural crest-derived stem cells is given in Figure 116. Neural crest cells can migrate from the neural crest and differentiate into various structures. These stem cells differentiate into either ectoderm stem cells, from which neurons can be formed, or into mesoderm stem cells which can differentiate into osteoblasts (bone).

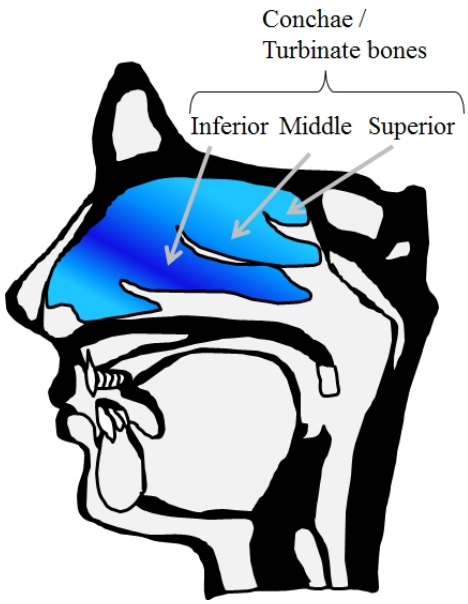

Figure 117: Schematic of the nasal region from which the stem cells were obtained. The turbinate bones are displayed in blue with the inferior turbinate bone highlighted by a darker blue.

Effect of nanopore sizes on stem cell differentiation

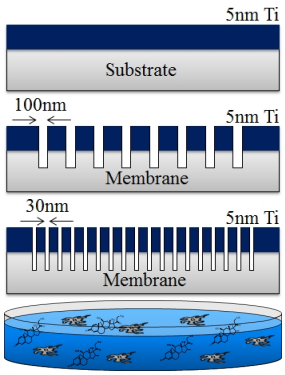

Figure 118: Illustration of the four experiments which were conducted to study the stem cell differentiation via physical cues. Top: control experiment in which a glass substrate with a 5 nm titanium layer was used. Illustrations in the middle: membranes with 100 nm and 30 nm pores, covered with a 5 nm titanium layer. Bottom: positive control experiment in which biochemical cues were used to induce differentiation into an osteogenic lineage.

Previous studies by Lavenus *et al.* [34] showed that nanoporous arrays are able to induce osteogenic differentiation of human mesenchymal stem cells. To verify whether the technique can also be applied to human neural crest-derived inferior turbinate stem cells and to better understand the differentiation process by the physical cues, four experiments, illustrated in Figure 118, were conducted:

Stem cell differentiation on unstructured titanium layers: Stem cell differentiation on an unstructured titanium layer was studied as a negative control experiment in which an unstructured glass was used as a substrate onto which a 5 nm titanium layer was sputtered using the Leybold L560. The sputtering process parameters were chosen to 120 W and 0.3 Pa.

Stem cell differentiation 100 nm *pores and* 30 nm *pores:* To study the effect of nanopore sizes on stem cell differentiation, track etched polycarbonate membranes with 30 nm pores and 100 nm pores were purchased from Watman, Maidsone, UK. A 5 nm titanium layer was sputtered onto all substrates using the Leybold L560 with the above mentioned process parameters. SEM and EDX measurements were performed to verify the intact titanium layer on the nanoporous membrane. For the SEM measurements a voltage of 20 kV and a current of 86 pA were used in the down hole visibility mode. For the EDX measurements the voltage and current were chosen to 20 kV (see Equation 9 in the DualBeam chapter) and 1.4 nA to obtain a high count rate. The EDX spectra were recorded for 5 min. The EDX spectra and SEM images of

the titanium covered, nanoporous membranes can be found in Figure 121 and Figure 122.

Stem cell differentiation via biochemical cues (positive control experiment): The positive control experiment was conducted by Matthias Schürmann. The Stem cells were cultivated in DMEM containing 10 % fetal calf serum for 48 h. Afterwards the cells were cultivated in an osteogenic induction medium which contains 100 nM dexamethasone, 10 mM β- glycerophosphae and 0.05 mM L-ascorbic adid-2-phosphate at 37 °C and 5 % CO_2 in an incubator (humidified). All chemicals were purchased from Sigma-Aldrich.

Stem cell isolation and cultivation was carried out analogously to Hauser and Grainer [229, 230] and was performed by Matthias Schürmann. A detailed description can be found in Schürmann's work [231].

Biological investigation

The most important results of the biological investigations, conducted by Matthias Schürmann, are given in Figure 119. A detailed description of the biological investigation is beyond the scope of this work, more information on the preparation and experiments can be found in Schürmann's work [231]. In this evaluation Alizarin Red S staining and von Kossa staining were used to determine the presence of calcium deposits (Ca^{2+}) which are produced by osteoblasts. Their presence is an indicator that differentiation into an osteogenic lineage occurs. The calcium deposits (visible as red areas on the micrograph) for all differentiation experiments can be seen in the columns *Alizarin Red S* and *von Kossa* in Figure 119. A further indicator for osteogenic differentiation is the alkaline phosphatase[79] (ALP) activity which is also displayed for all experiments in Figure 119. An increased ALP activity (stained cells in the micrograph) is expected for cells that are differentiating into an osteogenic lineage.

[79] Alkaline phosphatase is a hydrolase enzyme which removes phosphate groups from molecules.

The unstructured titanium layer and the 100 nm pores yield the same results. Neither an increased ALP activity (no visual stained cells in the micrograph) nor calcium deposits can be found for these stem cells, showing that stem cell differentiation does not occur in

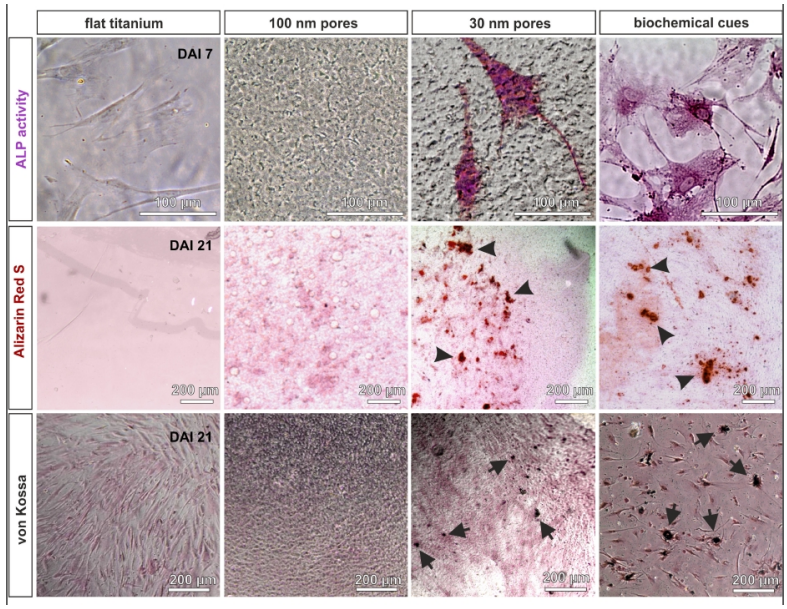

Figure 119: Biological investigation. The ALP activity (top row) for all experiments was determined at the 7^{th} day after induction (DAI) The scale bars correpsond to 100 µm. Alizarin Red S and con Kossa staining, showing calcium deposits, are given in the middle and lower row for all experiments. The scale bars for these two columns correspond to 200 µm. The experiments show that the 30 nm pores and the biochemical cues yield the same results and both promote osteogenic differentiation. The increased ALP activity (represented by the stained cells) and the calcium deposits (marked by black arrows) are clearly visible.

either case.

A different behavior can be observed for the 30 nm pores. The evaluation shows that the 30 nm pores have the same effect as the biochemical cues. In both these cases, an increased ALP activity (stained cells are clearly visible) and calcium deposits, which are marked by black arrows, could be verified, showing that osteogenic differentiation can therefore be promoted by the biochemical cue as well as the 30 nm pores.

A further biological study (qRT-PCR) showes that the 30 nm pores lead to up-regulated osteogenesis related transcripts such as the integrin subunits β_1 and α_1, osteocalcin, osterix, and BMP2. The quantitative results are given in Figure 120. In addition, an increased phosphorylation of FAK at Y397[80] was observed which is neccesary for osteogenesis via topographical cues [231].

The biological investigation shows that stem cell differentiation into an osteogenic lineage can be promoted by either biochemical cues or 30 nm pores. The mechanism behind the physical cue (30 nm pores) however remains elusive in these investigations.

[80] Y397 referes to the 397th amino acid in the protein which is tyrosin.

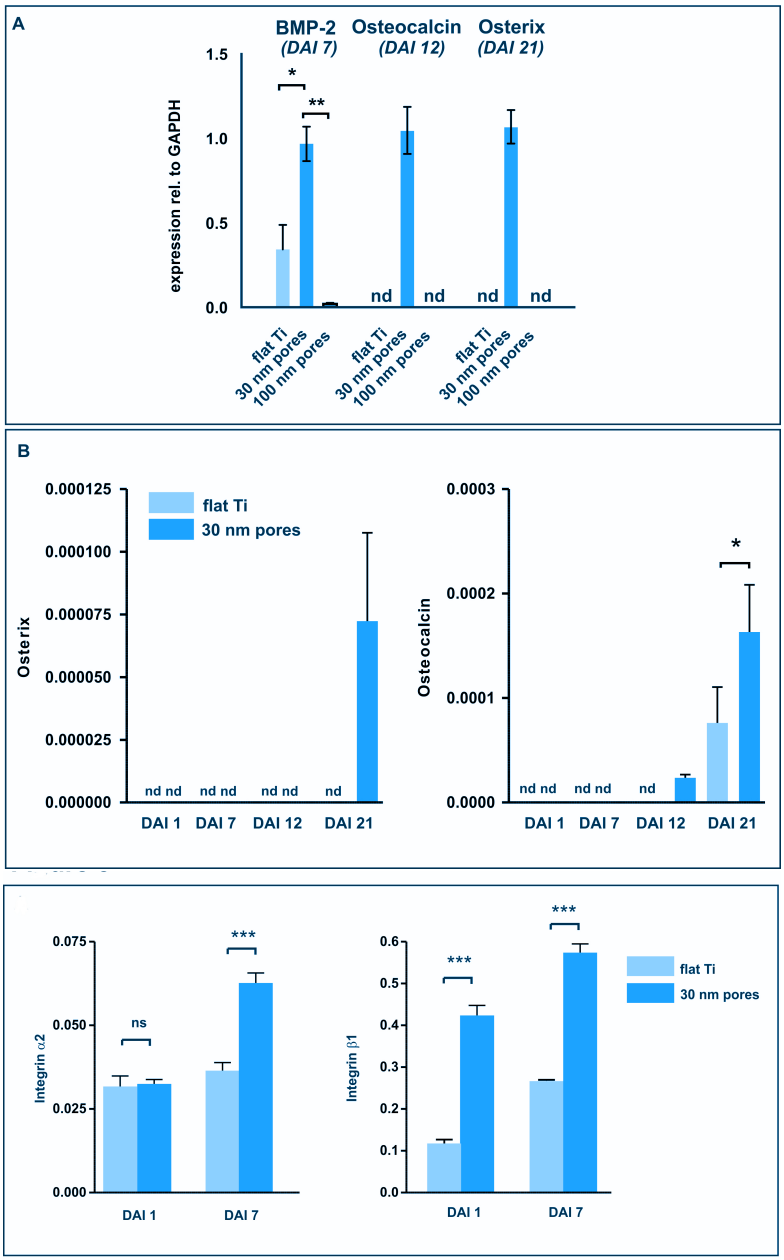

Figure 120: Quantitative analysis of the osteogenis-related transcripts: BMP2, osteocalcin and osterix for an unstructured titanium as well as for 100 nm pores and 30 nm pores (top), integrin $\alpha 2$ and integrin $\beta 1$ (bottom) for flat titanium and 30 nm pores. The graphs show elevated values for 30 nm pores for all transcripts.

Electron microscopy

To better understand the mechanism which promotes the stem cell differentiation via the 30 nm pores, the interaction of the stem cells with the nanoporous substrate was studied employing scanning electron microscopy in this work. Recent developments for low voltage imaging have opened up the path to study biological samples with a higher resolution [232]. Compared to conventional TEM-sections, this low voltage SEM method has the advantage that the entire biological sample can be studied instead of the 100 nm thin sample sections used in TEM imaging. SEM therefore offers a more complete sample analysis. In addition, a less complex sample preparation is needed since the sample can be imaged in its entirety and does not need to be cut and thinned. Furthermore, 3D tomography was performed on the stem cells on the 30 nm pores. For these experiments, the stem cells were fixed by aldehydes, post-fixed in 1.5 % OsO_4, shock frozen in propane at −185 °C, and afterwards freeze dried at 10×10^{-3} Pa prior to the electron microscopy measurements. The preparations were carried out by Matthias Schürmann and Peter Heimann from the Faculty of Biology, Bielefeld University. The DualBeam device, presented in the device chapter, was used for the SEM measurements. A low acceleration voltage (5 kV) and a low current (43 pA) were used to image the biological samples after 3 days.

100 nm *membranes*

SEM images of the 100 nm pore membranes with and without the stem cells are given in Figure 121. The corresponding EDX spectrum, verifying the presence of the titanium layer, is given at the top of Figure 121. The stem cells display a roundish shape on the asymmetrically arranged nanopores (Figure 121 (a)). A higher magnification (Figure 121 (b)) shows that the stem cell's filopodial protrusions, consisting of bundled actin filaments [233], either grow over the pores or fall into the pores but do not directly interact with the pores (inset Figure 121(b)). The filopodia protrusion thickness was determined to be 40 nm to 60 nm in the SEM images. Nanoscaled filopodia protrusions have been reported previously by

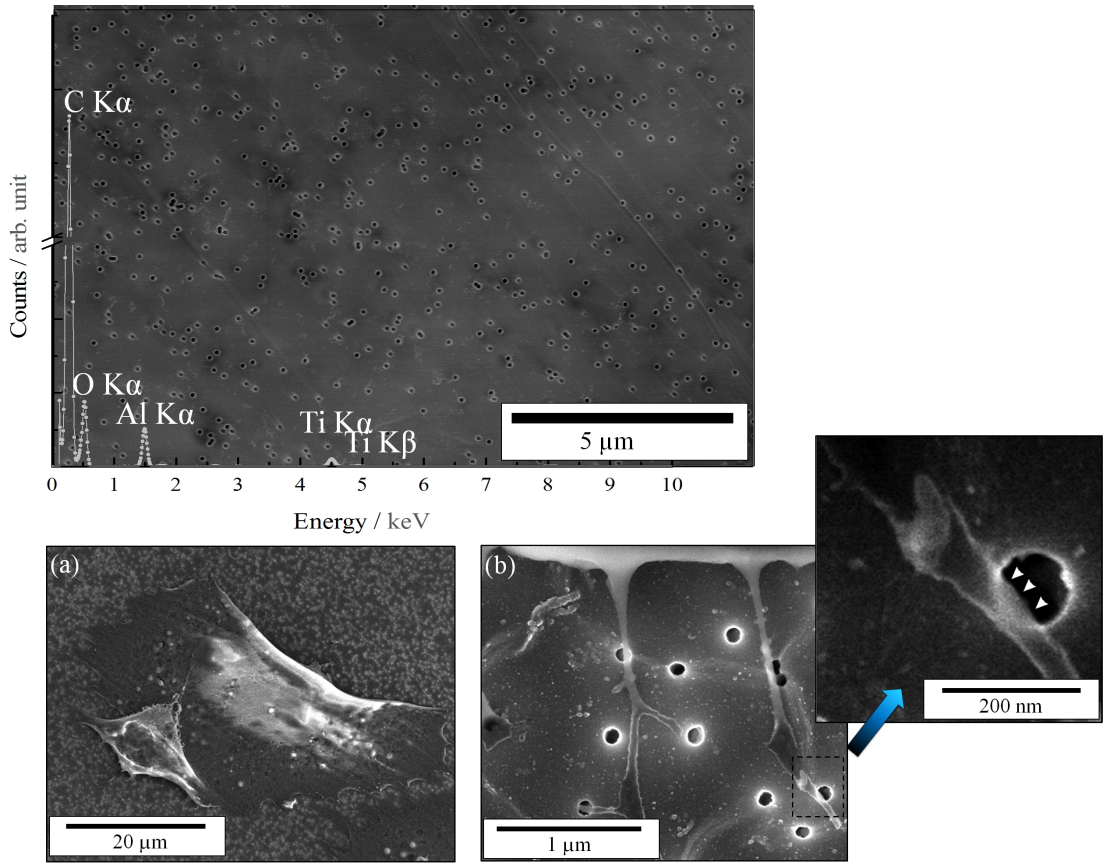

Figure 121: SEM images of the 100 nm porous membrane without (top) and with (bottom) ITSCs. (a) Lower magnification, showing a single stem cell. (b) Higher magnification showing the interaction of the stem cell with the substrate via filopodia. The EDX spectrum, verifying the presence of the titanium layer is included in the SEM image at the top.

Svitkina *et al.* [233] and Lee *et al.* [234].

30 nm *membranes*

The SEM images (Figure 122 (b)) show that the ITSC are spindly shaped, which is common for osteogenic cells. High magnification SEM images, given in Figure 122 (c)-(e), show that the stem cells directly interact with the pores via cellular protrusions (filopodia protrusions and tethers) in contrast to the stem cells cultivated on the 100 nm pores. The 40 nm to 60 nm thick filopodia protrusions, observed for the 100 nm pores, (Figure 122 (c)) are too large to directly interact with the nanopores. Instead, 10 nm thick tethers can be found between the cell membrane and the substrate (Figure

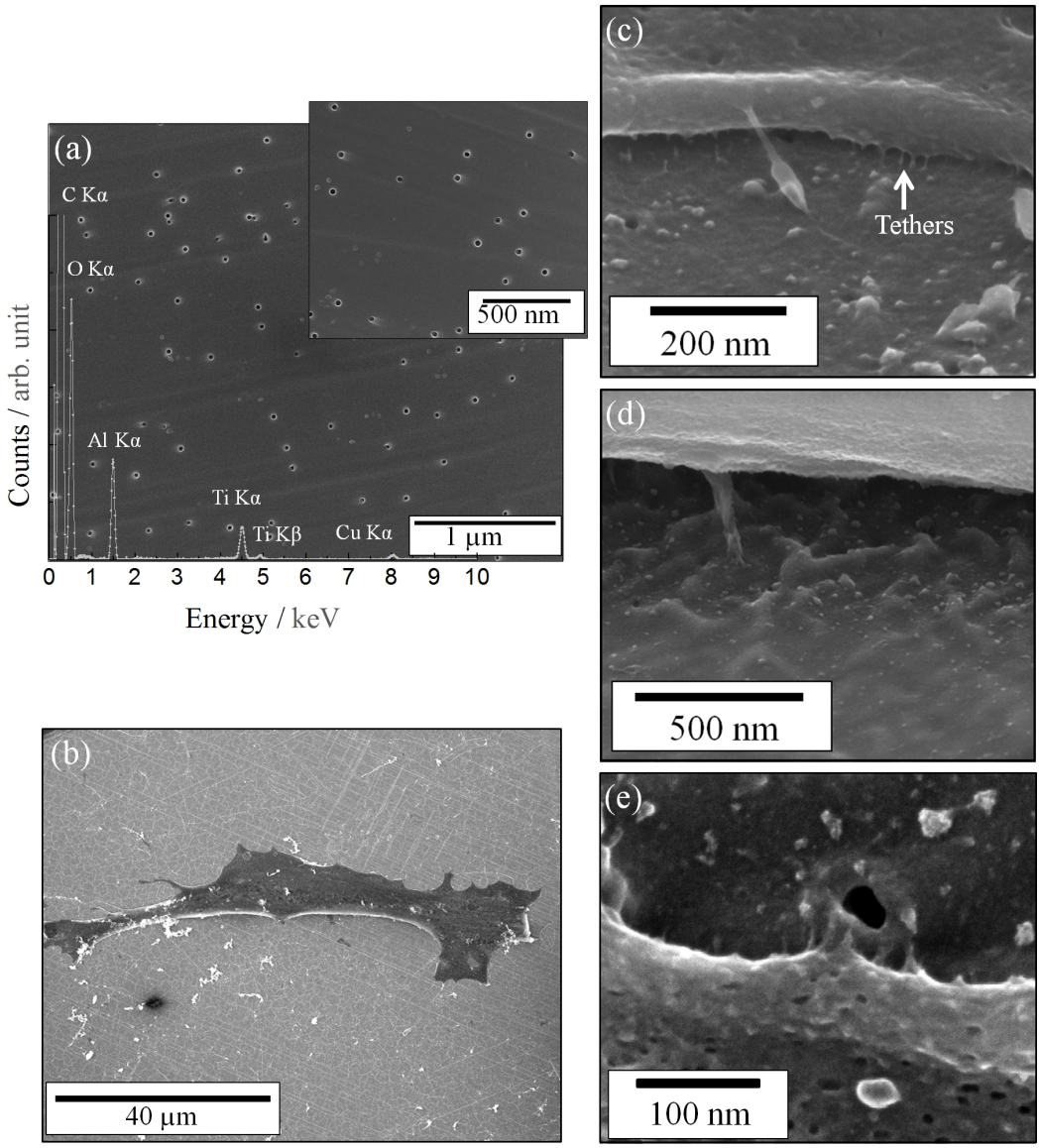

Figure 122: 30 nm pore membranes with and without stem cells. (a) SEM image showing the asymmetric pore arrangement of the nanopores. The corresponding EDX spectrum shows the presence of the titanium layer on top of the membrane. (b) Low magnified SEM image, showing a single, spindly shaped ITSC on the nanoporous membrane. (c) High resolution SEM image of the stem cell and the membrane, showing the two types of stem cell-nanoporous membrane interaction: filopodia and tethers. (d) SEM image, recorded after tilting the stage to 52°, showing single tethers below the stem cells which feel the substrate. (e) SEM image showing the interaction of the tethers with the nanopores. A higher tether density can be observed around the 30 nm small nanopores.

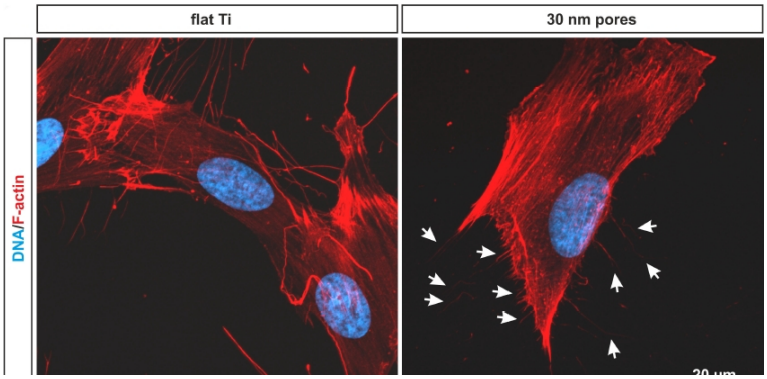

Figure 123: Confocal laser scanning microscopy analysis by Matthias Schürmann. F-actin was stained using Rhodamine-coupled phalloidin and is displayed in red while the DNA in the nucleus is displayed in blue. The actin fibers are diffusivly ordered on flat titanium (left) and highly ordered on the 30 nm pores (marked by white arrows).

122 (c)-(e)), which directly interact with the titanium surface. A higher tether density can be observed around the 30 nm pores indicating that the stem cells directly interact with the nanopore substrate. The sample stage was tilted to 52° to allow a visualization of the intersection between the cell bottom and the membrane surface (Figure 122 (d)).

3D tomography of the stem cell - nanopore system[81] was performed to further study the interaction mechanism and allow a cross-sectional view of the cells as well as a 3D visualization. An illustration of the sample setup is given in Figure 124. The ion beam parameters were set at 30 kV and 9.3 nA for the milling process with a step size in z-direction of 10 nm. All SEM imaging was performed using an acceleration voltage of 3 kV, a current of 0.34 nA, and the BSE detection mode. Each slice was recorded at different magnifications to allow for a more complete analysis of the stem cell (12000x magnification) as well as a detailed analysis for the stem cell-nanopore interaction (65000x magnification). The SEM images, as well as the inverted images, to allow a better visualization of structures and a comparison to conventional TEM sections, are given in Figure 125 and Figure 126. The different structures within the cell are labelled in the SEM image. Figure 126 shows a cross section of the stem cell, the titanium covered membrane and the nanopore with a sufficiently high resolution to resolve ribosomes which are around 15 nm as well as membranes which are around 5 nm thick [190]. A cross section of a direct interaction mechanism of the cell with a nanopore is shown in Figure 125. The images

[81] The preparation was carried out in a similar fashion to the preparation of the MTB in the second Chapter of Part two. A detailed sample preparation is given in Appendix F.

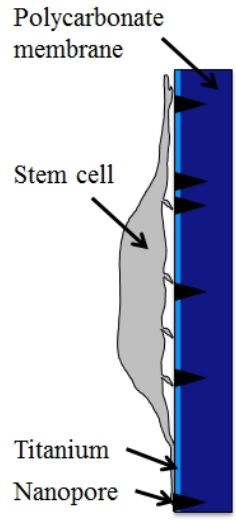

Figure 124: Illustration of the stem cell on the polycarbonate membrane (30 nm pores) and their orientation used for the 3D tomography. The polycarbonate membrane is displayed in a dark blue, the titanium layer in a bright blue, the nanopores are displayed in black, and the stem cell is displayed in gray.

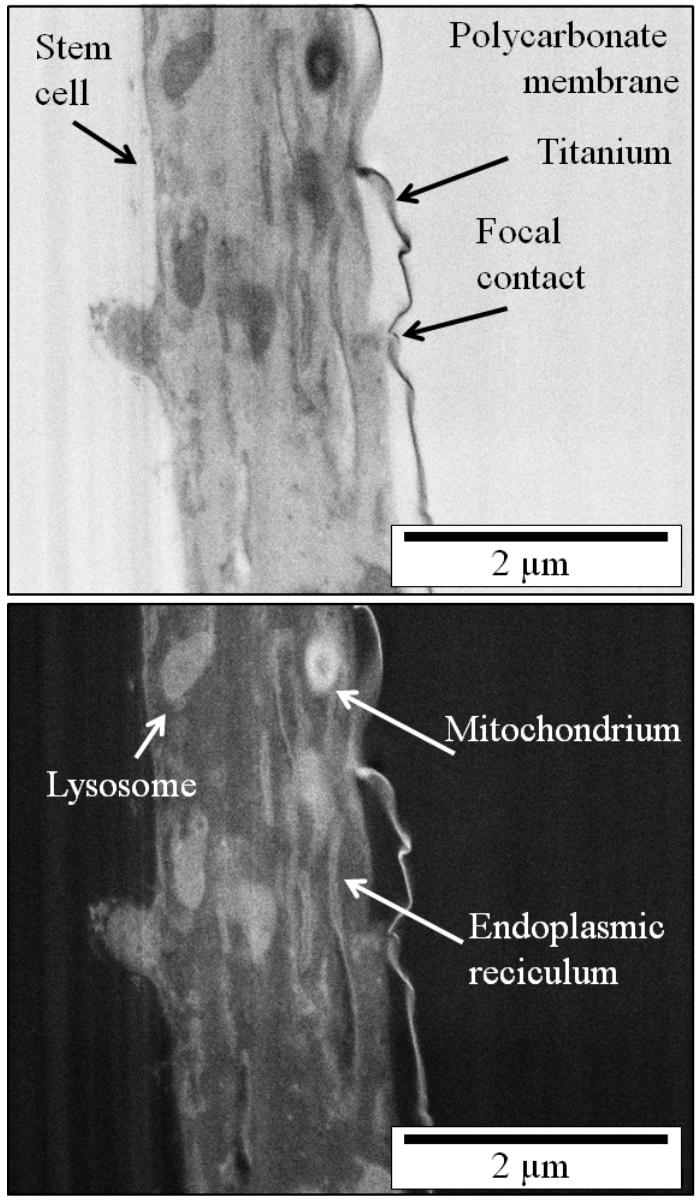

Figure 125: SEM image (bottom) and inverted SEM image (top) of cross section of the stem cell - nanopore substrate system with a lower magnification (25000x) showing the focal contact of the stem cell with a nanopore. Different cell structures (endoplasmic reticulum, lysosome, mitochondrium) are labelled.

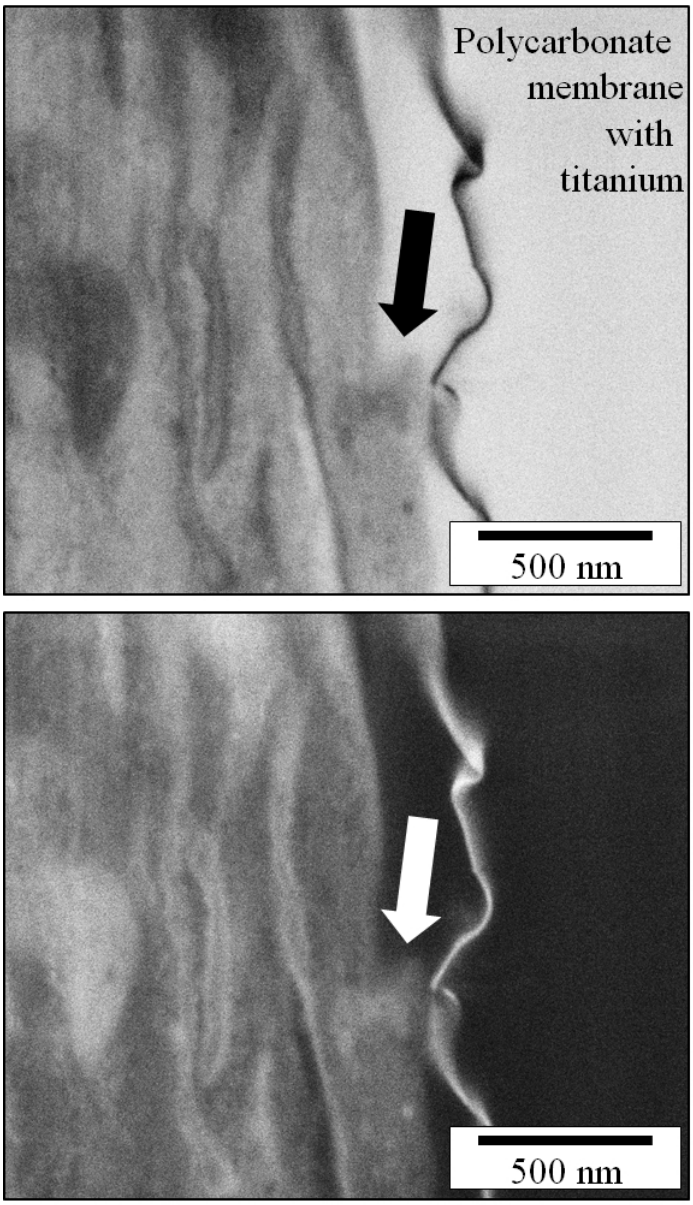

Figure 126: SEM image (bottom) and inverted SEM image (top) of the cross section of the stem cell - nanopore substrate system, displayed in Figure 125 with a higher magnification (65000x) to allow a better visualization of the focal contact.

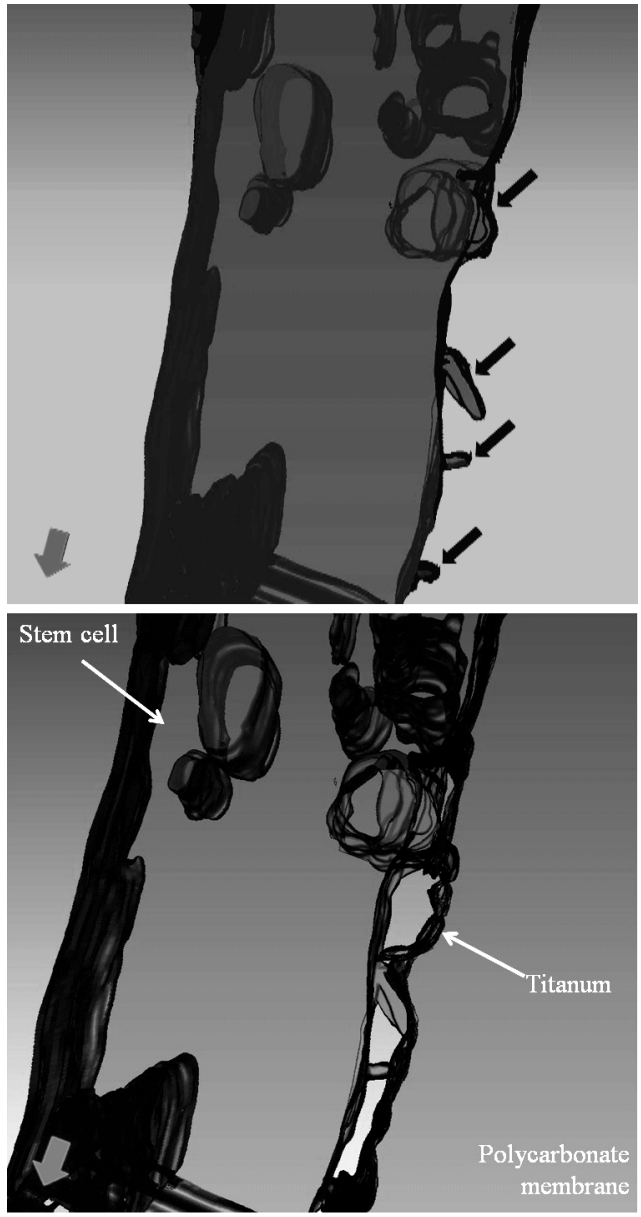

Figure 127: 3D tomogram with (bottom) and without (top) the titanium layer. The focal contact points are clearly visible between the stem cell and the nanopore membrane. The internal structures of the stem cell are partly represented. This tomogram corresponds to a 170 nm thick section of the stem cell - nanopore membrane system.

show that the stem cell is not in direct contact with the nanopore membrane except for the focal contact and at a small area at the top of the picture (grey area between the stem cell and the membrane) which suggests that a nanopore is in the vicinity. The focal contact is displayed at a higher magnification in Figure 126. All SEM images show that the nanopore membrane is corrugated, with the size of the corrugations exceeding the nanopore size. However, a study concerning stem cell differentiation via 30 nm pores on a flat titanium substrate (by Schürmann, not yet published) found that these corrugations do not influence the differentiation. 17 slices were used to reconstruct stem cell - nanopore interaction in 3D using the program Avizo. The tomogram with and without the titanium layer, given in Figure 127, shows the focal contacts between the stem cell and the nanopore substrate which are marked by black arrows. The tomogram shows an increased amount of focal contacts in the vicinity of nanopores, which was also found in the SEM images.

In addition to the electron microscopy, confocal laser scanning microscopy of the cells after 24 h, given in Figure 123, show that the F-actin (part of the cytoskeleton) rearranges and is highly ordered in comparison to cells on an unstructured titanium layer. The highly ordered actin fibers are marked by the black arrows.

Discussion

In all cases non-aptotic cells were obtained showing the biocompatibility of the samples. The electron microscopy evaluation of the stem cells on the different nanopore membranes shows that the stem cells not only possess a different shape but that they also interact differently with the substrate for the different nanopore sizes. The stem cells are roundish shaped on the 100 nm pores for which a pore specific interaction via tethers could not be observed. Electron microscopy measurements show a direct interact of the stem cells with the 30 nm nanopores via focal contacts. In addition a rearrangement of the F-actin was observed in confocal laser scanning microscopy measurements. Several studies (von Kossa and Alizarin Red S staining, ALP activity, qRT-PCR) verified that stem cell differentiation into an osteogenic lineage occurs on the the 30 nm pores and that osteogenesis-related transcripts are up-regulated

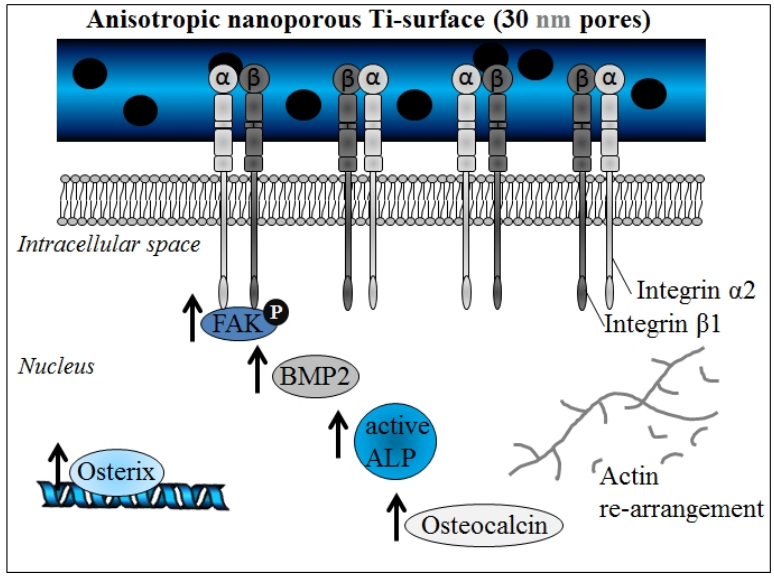

Figure 128: Illustration of the qRT-PCR measurement results: osteogenesis-related transcripts such as the integrin subunits β_1 and α_1, osteocalcin, osterix and BMP are up-regulated which is indicated by the black arrow. The BMP2 induces the expression of osterix which increases the expression of osteocalcin. The increased phoshorylation of FAK at Y397 is displayed by the black sphere with the label P. This increase is liked to the rearrangement of the actin within the cell. This illustration was drawn in analogy to Schürmann's work [231].

for the smaller pore size.

A possible signalling mechanism, which up-regulates the osteogenesis-related transcripts and induces the differentiation into an osteogenic lineage, is displayed in Figure 128. In this mechanism, which is based on the integrin clustering (due to the stem cell nanopore interaction), BMP2 is able to induce the expression of the osteogenic transcript osterix which in turn could elevate the expression of osteocalcin which then stimulates the generation of calcium deposits.

Summary

The measurements show that differentiation of human neural crest-derived inferior turbinate stem cells into an osteogenic lineage can be induced by using 30 nm pores in a titanium layer, on which the stem cells are cultivated. Electron microscopy measurements revealed that the stem cells directly interact with the nanopores via focal contacts. A possible signaling mechanism was found which is based on integrin clustering in the membrane (due to the interaction mechanism of the stem cell with the nanopores) that up-regulates

osteogenesis-related transcripts and induces the differentiation into an osteogenic lineage.

To determine possible influences such as nanopore distribution and arrangement on the differentiation, a well defined array of nanopores with tuneable densities is required. However, such a substrate is commercially not available at present. Therefore a technique which allows the fabrication of the desired arrays needs to be developed for future experiments.

FIB prepared samples

The biological investigation verified that the 30 nm nanopores induce osteogenic differentiation (spezialization into osteoblasts, (bone)) and thus that the limitation of the biochemical cues can be overcome. The SEM measurements (Figure 122) showed that the 30 nm pores ($D_{av,diameter} = 26\,\text{nm} \pm 7\,\text{nm}$) are irregularly distributed in the purchased membrane. The average inter-pore-distance was determined to $D_{av,distance} = 470\,\text{nm} \pm 269\,\text{nm}$ by evaluating 446 nanopores [82]. The asymmetric arrangement of the nanopores in the membrane provides unreliable and non-reproducable nanopore densities. The global average nanopore density of the membranes was determined to be between 6 pores/μm^2 to 7 pores/μm^2.

[82] All size evaluations were performed using the program Scion in which the pore diameter of a statistically sufficient amount of nanopores was manually measured.

To study the effect of pore density and pore arrangement, substrates with 30 nm pores, arranged in a well defined way over a large area (1 mm × 1 mm) are necessary. The sample requirements are illustrated in Figure 129. In addition, the pore density and pore arrangement need to be tunable. Structuring nanosized pores over

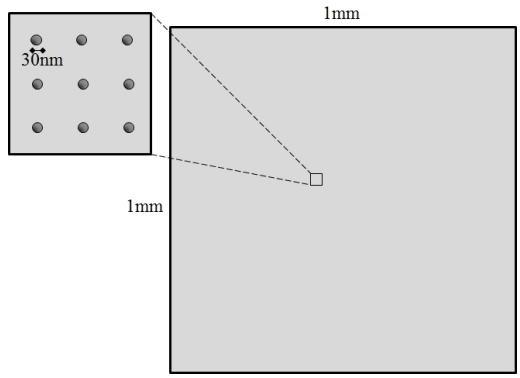

Figure 129: Sample requirements for the nanostructured array. 30 nm sized pores need to be structured on a 1 mm × 1 mm sized array.

a mm sized array with a high pore density represents a challenge for all light based structuring techniques. Electron beam lithography (e-beam lithography) as well as focused ion beam techniques, however, have the potential to fullfill the requirements. E-beam lithography is a structuring technique which allows for the preparation of structure sizes down to 10 nm[83]. To achieve short structuring times with this technique, a photoresist is spin coated onto a substrate (which is coated with titanium). The desired structures are exposed using a SEM and are removed in the next processing step. A 5 nm titanium layer is sputtered onto the sample afterwards. This process, in which the photoresist is part of the functional structure of the sample, is illustrated in Figure 130. The process requires multiple steps for the sample preparation which cannot be automated and is therefore time consuming. A possible drawback of this technique is represented by the remaining resist on the sample. The influence of the photoresist on stem cells is still unknown and could potentially create problems.

[83] The resolution depends on the resist and the structuring method.

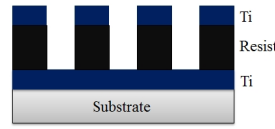

Figure 130: Illustration of a nanoporous titanium sample prepared by e-beam lithography. A thin titanium layer acts as a glue for the resist which is strucured using an electron beam. Part of the resist (which was not exposed by the electron beam) remains in the sample. A 5 nm titanium layer covers the sample.

Focused ion beam techniques allow to structure nanoporous arrays with nanopore diameters down to 10 nm [48]. In this technique a focussed ion beam is used to structure pre-defined patterns in a milling process. This technique has the advantage that the sample can be directly modified without the need of a photoresist and subsequent treatment and thus requires a less complex sample preparation. The possibility of scripting the desired structure allows a fully automated sample structuring. Large arrays of small structures represent a challenge due to the required process time and therefore only represents a viable option if short processing times can be achieved[84].

[84] A large amount of samples are required for biological investigations, thus a reasonably short structuring time ($\ll$ 24 h per sample) is important.

In this work, the focused ion beam technique, employing the DualBeam device, was chosen over electron lithography due to the unknown influence of the photoresist and the option of going down to 10 nm sized pores in future experiments. In addition, the scripting possibility allows an operator free method and does not require several intermediate steps. The DualBeam device can also be used to control the structured nanopores directly after the structuring process. A voltage of 20 kV and a current of 86 pA were used in all SEM evaluations. The secondary electron mode was chosen to study the structured arrays directly after the structuring process.

Table 13: Milling rates for different materials for the FEI DualBeam device.

Material	Rate / $\mu m^3 \cdot s^{-1}$
Si	4×10^{-3}
Au	4×10^{-2}

Choice of material and sample preparation

The choice of structuring material is essential if a larger nanopore array with small nanopore sizes is to be structured within a reasonable time frame. Therefore a sample setup needs to be developed in accordance with the experimental requirements: in this case, it needs to be biocompatible as well as a soft ion beam material (for a fast structuring process). In this work, gold was used as a structuring layer onto which a coating layer of titanium was sputtered after the structuring process. Gold, a biocompatible material, has a 10 times higher ion milling rate than a silicon, which represents a harder material for ion beam milling[85] (see Table 13). Titanium is a hard ion beam material and thus an ion milling rate closer to silicon is expected. To produce a sample within a reasonable time frame the structuring time needs to be minimized. Structuring gold instead of titanium and then sputtering a 5 nm titanium layer onto the structured sample represents a method that is faster by a factor of 10.

[85] The hardness for ion beam milling is caused by oxide layers that form on the material.

Microscope slides[86] were chosen as the sample substrate. The microscope slides were washed using dish washing liquid and distilled water for 10 min before they were sonicated in acetone for 5 min and in ethanol for 3 min afterwards to obtain a clean substrate. 5 nm tantalum[87] and 250 nm gold were sputtered onto the cleaned microscope slide using the "HBSD" (see Device chapter). The sample is then structured using the DualBeam device and a 5 nm titanium layer is sputtered onto the structured sample using the Leybold L560 afterwards. The sample setup is displayed in Figure 132.

[86] Microscope slides, superior laboratory glassware were purchased from Paul Marienfeld GmbH.

[87] Tantalum acts like a glue between the glas substrate and the gold.

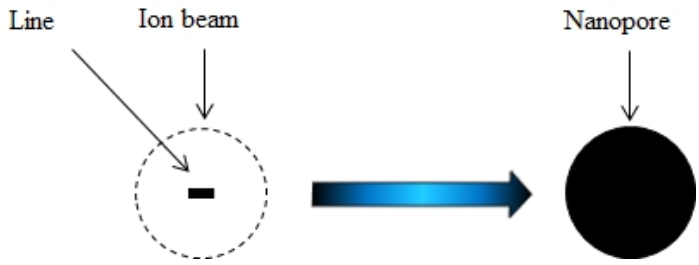

Figure 131: Illustration of the simplified nanopore structuring process: instead of milling a circle (regular polygon) a simpler geometric structure , a line, is structured with a diameter below the nominal ion beam diameter. The resulting nanopore is displayed in black.

Development of a new structuring method

Previous studies by Akemeier [48] showed that structuring a nanoporous array represents a challenge using the DualBeam device. In his work a 1.5 mm^2 sized array with around 22500 nanopores with a pore diameter of 100 nm was constructed. The automation technique employed in his work mills circles in specific spots within the array. Automation allows for structuring of large arrays, which takes several hours, without an operator at site. In such approaches, a scripting routine is used to give the neccessary commands to the device. In Akemeier's script a stitching routine moves the stage in a spiral-like fashion between the structuring processes to create the large array. This method, however, was deemed unsuitable in this work. 22500 nanopores already represent an upper limit for Akemeier's script due to the required process time. In his process, an increased amount of nanopores would lead to an increased amount of sleep times[88] (to avoid a system crash) in which the pattern is loaded and milled, which would result in excessive structuring times ($\gg$200 h). In addition, creating 30 nm pores represents a challenge using the circle pattern since a much lower beam current (which would additionally lead to a significant increase in processing times and possible system instabilities) with a nominal beam diameter of less than 6 nm would be required[89]. In this work, 10000 to 4×10^6 nanopores (depending on the pore density) need to be constructed with a smaller diameter in comparison to Akemeier's structures. Therfore, a new method needs to be developed which can structure such a nanopore array within a reasonable time frame without leading to system instabilities.

For a succsesful automation approach, a less complex automation procedure needs to be developed to reduce the computing time and to structure the smaller nanopores. Circles are regular polygons and thus represent a complex pattern for the DualBeam. The simplest geometry that can be milled (or deposited) with the device is a line. Milling a line which is shorter than the nominal beam diameter for each current should, for a well adjusted beam, lead to a nanopore instead of a line. This is illustrated in Figure 131. The positive result for a line with a length of 10 nm is displayed in Figure 139. This length is used for all nanopore structuring processes in this work.

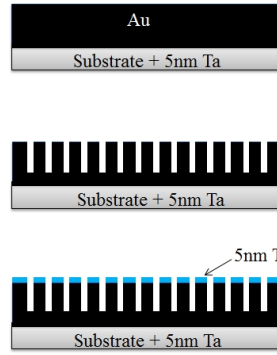

Figure 132: Sample setup: A cleaned microscope slide is used as a substrate. 5 nm tantalum and 250 nm gold are sputtered onto the substrate. Middle: The gold layer is structured using the DualBeam device. Bottom: In a final step an 5 nm titanium layer is sputtered onto the structured sample.

[88] Sleep times are a set amount of times in which the script execution is halted to finish the previous scripting commands.

[89] The nominal beam diameter in Akemeier's approach was 5× smaller than the pore size. 100 nm pores were constructed in his work using a beam with a nominal beam diameter of 17 nm.

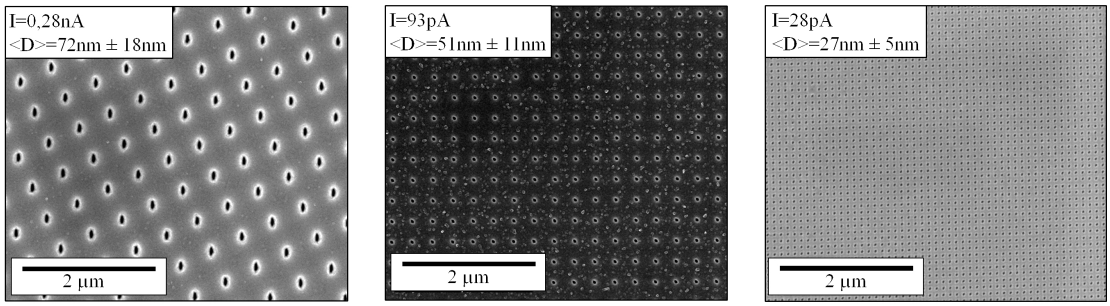

Figure 133: SEM images: Pore diameter depending on the ion beam current. The beam currents and the corresponding average pore diameter are given in the images. Smaller nanopores can be structured by using lower beam currents. The effect of astigmatism can be seen in the elliptical shape of the nanopores for the 0.28 nA current. 449 nanopores were used in the statistical evaluation of the pore diameter for the 0.28 nA current, 488 nanopores were evaluated for the 93 pA current and 503 nanopores for the 28 pA current.

Structuring 30 nm pores

To obtain 30 nm pores, several beam parameters and other influencing factors need to be determined. Since the nanopores are created directly by the beam shape instead of a predefined pattern, the only influencing factors for a well aligned ion beam are the beam current, the dwelltime, and the magnification. Circular nanopores can only be obtained for a well aligned ion beam. Astigmatism results in a non-symmetrical beam and therefore elliptic pores. This effect is discussed in more detail in Akemeier's work [48]. The influence of the above mentioned factors is discussed in this part of the chapter. All SEM images and evaluations were carried out prior to sputtering the titanium layer onto the sample.

Influence of the beam current on the nanopore size

[90] The beam current is set by different apertures in the device. The beam current notation, however, is used in this work since apertures differ between devices. The beam current therefore represents a more universal notation.

The focused ion beam diameter depends on the used beam current[90]. Different currents were tested and the effect on the pore size studied. A lower current has a smaller nominal beam diameter, leading to smaller pores. However, a reduced current requires a longer milling time for a structure in comparison to a higher current. The highest possible current should therefore be chosen for the structuring process. SEM images of the nanopores for different beam currents are displayed in Figure 133. The average pore diameters were determined statistically from the SEM images. The different currents, nominal beam diameters, and resulting pore sizes

are given in Table 14. The results show that 30 nm pores can be structured using a 28 pA current.

Table 14: Beam currents (Current) with the corresponding nominal beam diameters (Beam) as well as the resulting pore diameter (Pore).

Current pA	Beam nm	Pore nm
280	31	72 ± 18
93	24	51 ± 11
28	17	27 ± 5

Influence of the magnification on the nanopore size

Studies of the pore size and shape in relation to the magnification used in the structuring process showed large differences in pore quality. The effect of the magnification on the pore size and shape is displayed in the SEM images in Figure 134. An insufficient chosen magnification[91], which would mill a large array of nanopores, results in smeared out pores with an increased diameter which is undesirable. A higher magnification (5000× magnification) is required to obtain well definded 30 nm sized pores in the structuring process which leads to a smaller area that can be structured. A maximal area of $10\,\mu m \times 10\,\mu m$ can therefore be structured in a single processing step. This is illustrated in Figure 136.

A stitching move, in which the stage is moved between the milling processes, allows for a large array to be structured, and represents a work around for the encountered problem. The employed stitching move, in which the stage is moved in a meander-like fashion, is illustrated in Figure 136.

[91] The DualBeam scans a fixed amount of pixels. A smaller zoom therefore leads to a higher inaccuracy which results in smeared out pores.

Optimizing the milling parameters

The depth of the nanopore is directly linked to the dwelltime[92] of the beam. The dwelltime represents the time that the ion beam stays in a certain position of the sample. An increased dwelltime leads to longer milling and therefore increased structure depth. To obtain an optimal processing time, the depth of the nanopores in dependence of the ion beam dwelltime was studied and adjusted to a pore depth of 100 nm. Since up to 4×10^6 nanopores are to be milled, a fraction of a second less in dwelltime for each nanopore leads to a significant overall time difference for the nanoporous array.

To study the pore depth, a local sectioning of the array was performed. A cross section was removed in front of a row of nanopores to allow for a better visualization of the sectioning process. In this process the front face of the sample was milled using the ion beam[93] and the underlying front face imaged using the

[92] The dwelltimes × cycles represent the ion beam dose. In this work, one cycle was used for all structuring processes, thereby avoiding nanopore broadening caused by milling the nanopore numerous times for a shorter period of time (more cycles).

[93] A cleaning cross section was milled using the 28 pA current setting at 30 kV for the ion beam.

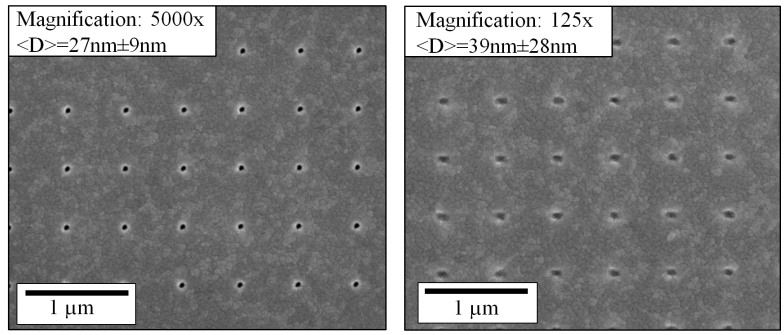

Figure 134: SEM images: Pores depending on the magnification. Nanopores with a higher magnification (left) yield well defined nanopores. A lower process magnification (right) leads to smeared out nanopores with an increased diameter. 253 nanopores were used to determine the average pore diameter for the higher magnification, while 227 nanopores were evaluated for the lower magnification.

electron beam[94] in analogy to the 3D tomography. The stepsize for the sectioning process was set to 4 nm to allow several sections within the nanopore. The illustrated process and SEM images are given in Figure 135. The pore depths were measured using the tilt correction since the sectioning was done with the stage tilted to 52°. The pore depths with respect to the dwelltimes are given in Table 15. The optimal dwelltime was determined to be 0.006 s.
A longer dwelltime (1 s) leads to an unneccessary pore depth and therefore represents an unefficient increase in overall structuring size. A shorter dwelltime (0.003 s) leads to an insufficient pore depth which can hardly be identified between the gold crystallites (see Figure 135 (right)). The process of milling 4×10^6 nanopores can be extrapolated from those times and should take about 7 h. The overall processing time, however, will be increased due to moving the beam from pore spot to pore spot within the 10 µm × 10 µm sized array and by the stage moves in the stitching process.

[94] The voltage and the current were chosen to 20 kV and 86 pA for the electron beam.

Table 15: Pore depth in dependence of the ion beam dwelltime used for the milling process.

Pore depth *nm*	Dwelltime *s*
274	1
156	0.006
≈ 45	0.003

Overview: Optimal structuring parameters

The optimal beam parameters were obtained by studying the influence of the beam current, the dwelltime and the magnification on the nanopore quality. The optimal parameters for this structuring process were determined to: I=28 pA; τ_D=0.006 s for a magnification ≫ 5000x with I as the ion beam current and τ_D as the dwelltime (the application material needs to be set to Si).

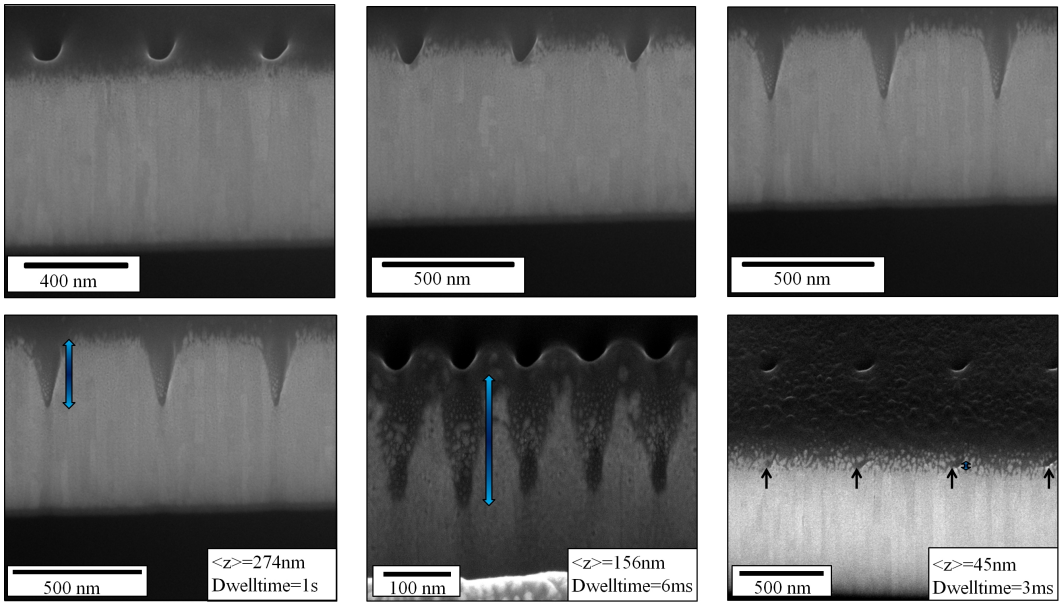

Figure 135: Top: Schematic of the sectioning process which was employed to study the depth of the nanopores. Sections of the nanopores are removed using the ion beam and the front face is then imaged by the electron beam. The pore depth can be measured in the SEM image. Bottom: SEM images of the nanopore cross section for different dwelltimes from which the nanopore depth was determined. All nanopores were milled using a 28 pA current.

Scripting

This section discusses the automation approach using *AutoScript xT* which was used to structure the 1 mm^2 sized array of 30 nm pores. The full script which was developed for the automation approach consists of two parts. The first part of the script defines the nanoporous array in a 10 µm × 10 µm area which is loaded once at the beginning of the script. Here, the 10 nm lines are set to specific coordinates through a programming loop. The second part of the script moves the stage in a meander-like fashion and mills the pre-defined pattern. The single parts of the script for a 5 µm inter-pore distance are given in Figure 137 and Figure 138. Instead of describing the function of every line in the script, the general idea is presented and the commands are elaborated on in the Appendix G since the script is commentated.

A more general type of scripting was chosen for greater flexibility which allows for changes in pattern, nanopore size, density, and array size. All scripts were run using the program *runscript*.

Defining a nanoporous array: To obtain the nanopore pattern a

10 µm × 10 µm sized array of lines needs to be defined. First, all previously defined patterns (if they exist) are removed and the milling parameters set according to the previously found optimal values. 10 nm long lines, used as a pattern for the nanopores, are set to specific coordinates in the μm^2-sized array using two loops: an inner loop (loop1) in which the positions of the lines within a single row (in x-direction)[95] are set, and an outer loop (loop2) which sets the amount of rows within the area (y-direction). The loops are repeated until all lines/nanopores are defined within the 10 µm × 10 µm array. Script excecution is halted for 10 seconds after the pattern is created to allow enough computational time to load the pattern prior to the first stage move.

[95] The amount of lines within a single row (in x-direction) is determined by the variable *millnmax* which needs to be determined for each inter-pore distance separately.

Stitching move: The stage is moved in a meander-like fashion by the stitching routine. For this routine, two inner and one outer loop were programmed which move the stage to the right, and at the end of the line, one step downwards (inner loop1), to the left until the end of the line and one step downwards (inner loop2). This pattern is repeated in the outer loop for a given number of times. After each stage move, the nanopattern is milled followed by a 2 s pause in which the progam excecution stops to allow enough time for the pattern processing[96].

Once the 1 mm × 1 mm array is milled, the *clear* command at the end of the script removes all defined patterns and the script is ended.

[96] Without the *sleep* commands which pause the script execution for a desired time, the processes cannot be excecuted in time leading to a process error.

A more detailed description can be found in Appendix G or the FEI AutoScript xT Technical Note [235].

A secured trial run of the script was performed using a 4 × 4 structuring array. The DualBeam device does not possess an internal failsafe mechanism for scripting, thus it is neccessary to make sure that the script is executed successfully. The commands

dialog 0,"New stagepos x",xnew,ynew
if (dresult=2) goto end

offer a secure way to test the script. Once the command *dialog 0,"New stagepos x",xnew,ynew* is reached in the script, the script execution stops and demands a manual confirmation from the operator

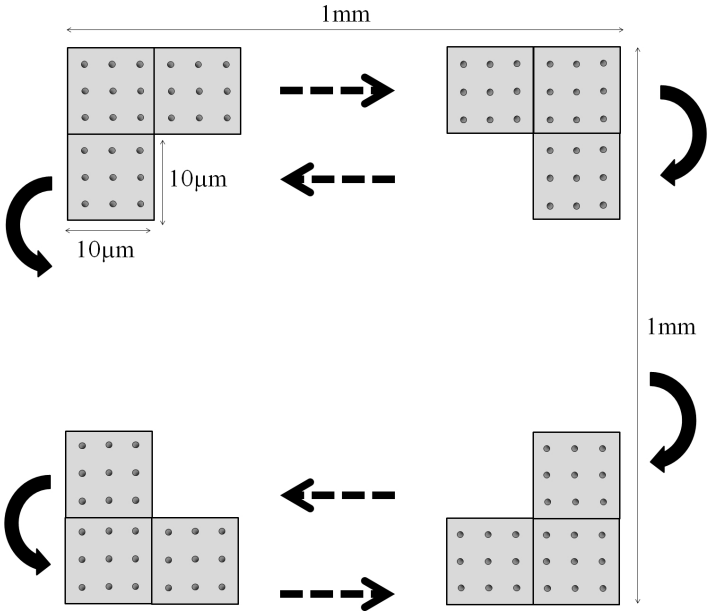

Figure 136: Workaround for the problem encountered with the influence of the magnification on the nanopore quality: In a stiching move smaller areas are structured and the stage moved between the structuring processes. This way a large array can be obtained.

before script execution is continued. The value 0 in the command sets the buttons in the dialog box (which is titled "New stagepos x") to "ok" and "cancel". "Ok" sets the dresult to 1 while "cancel" sets the dresult to 2. The next line *if (dresult=2) goto end* ends the script if the dresult was set to 2 by the cancel button. This way, each step in the script can be tested and the script aborted if necessary, without a crash of the *runscript* program. The two commands are removed from the script after a successful test.

Figure 139 shows part of a sample which was prototyped with the script. The 30 nm pores, displayed in a higher magnified SEM image in the inset of the Figure 139, have an inter-pore distance of 5 µm. The required total processing time for the 1 mm × 1 mm sized nanoporous array was 9 h, which represents an economically viable solution.

The final structure is marked by milling optically visual rectangles (≈ 60 µm × 15 µm) at the corners of the array, using a high current (21 nA) for the ion beam.

Figure 137: First part of the script in which the pattern is created. The # is followed by a comment in the script which is not processed in the script execution. Since a well aligned beam is essential to mill 30 nm pores, the beam parameters and magnification are set and adjusted manually. After clearing all possible defined patterns in the *clear previous milling pattern* section, the neccessary parameters such as the milling depth, material and nanopore pattern parameters (amount of pores, interpore distance) are set in the *set materials* and *define milling pattern loop variables* sections. The nanopore pattern is defined afterwards using two loops in the *create milling pattern* section. The nanopores are obtained by milling lines (easiest geometry that the DualBeam can structure) with a length below the nominal beam diameter (in this case 10 nm long lines.

```
# ----------------------------------------
# Beam Parameters
# ----------------------------------------
#beam parameters are set manually for a better result


# ----------------------------------------
# clear previous milling pattern
#----------------------------------------
clear

#----------------------------------------
# set material
#----------------------------------------
setpatinfo 0.09, si

#----------------------------------------
# define milling pattern loop variables
#----------------------------------------
xdist=5
ydist=5

m=0
millmmax=3
millnmax=3

#patterning distance is in microns
#needs to be adjusted depending on the pitch
#calculate how many pores go into 10 microns with the desired pitch

#----------------------------------------
# create milling pattern
#----------------------------------------
loop2:
n=0
loop1:
line (n*xdist), (m*ydist), ((n*xdist)+0.01), (m*ydist)
n=n+1
if (n<millnmax) goto loop1
m=m+1
if (m<millmmax) goto loop2
sleep 10000
```

```
#-----------------------------------------
# Pattern is created, move stage and mill
#-----------------------------------------

mill

#-----------------------------------------
# Position Parameters

getstagepos

xnew=x
ynew=y

nmax=66
stageshift=0.015
# stage move distances in mm


# -----------------------------------------
# Outer loop for y-direction move
nyc=0
loopYmove:

# -----------------------------------------
# Inner loop 1: Move stage to the right
nxc=0
loopRight:

xnew=xnew+stageshift

stagemove x, xnew
mill
sleep 2000

nxc=nxc+1
if (nxc<nmax) goto loopRight

# -----------------------------------------
# Move stage down

ynew=ynew-stageshift
stagemove y, ynew
mill
sleep 2000

nyc=nyc+1
```

```
# -----------------------------------------
# Inner loop 2: Move stage to the left
nxc=0
loopLeft:

xnew=xnew-stageshift
stagemove x, xnew
mill
sleep 2000

nxc=nxc+1

if (nxc<nmax) goto loopLeft

# -----------------------------------------
# Move stage down

ynew=ynew-stageshift
stagemove y, ynew
mill
sleep 2000

nyc=nyc+1

#-----------------------------------------
# outer loop repeat

if (nyc<nmax) goto loopYmove


# -----------------------------------------
# Clean up at end from script
# -----------------------------------------

endScript:

clear
```

Figure 138: Second part of the script in which a stitching process is used to create the nanoporous pattern over a large area. The amount of rectangles that need to be milled as well as the required shift between the rectangles (taking the inter-pore distance into account) is given in the *Position Parameters* subsection after the current stage position is read out. The stage is moved in a meander-like fashion (right, down, left) using two inner and one outer loop. After each stage movement, the predefined nanopore pattern is milled. This is repeated until the required amount of rectangles is milled. The stagemove distances need to be be given in mm (and not in μm as for the structuring distances) in *Autoscript xT*. All patterns that are loaded at the beginning of the script excecution are removed once the complete array is structured.

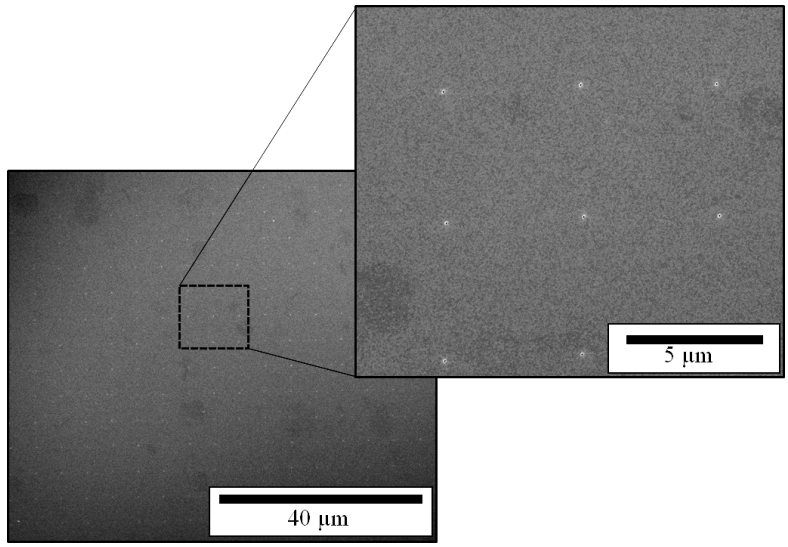

Figure 139: SEM images showing a part of a sample, created with the script. The 30 nm pores have an inter-pore distance of 5 µm. The inset shows an enlarged area where the 30 nm pores are clearly visible.

Changing the pore density

To study the effect of the pore density on stem cell differentiation, nanoporous arrays with different nanopore densities were structured with the automation approach described in the previous chapter. The different nanopore densities were achieved by different inter-pore distances between the 30 nm pores. The distances are given in Table 16 with the approximate corresponding structuring times. The structuring results are given in Figure 140.

The array with a 2 µm inter-pore distance was structured in four equivalent steps instead of a single process to avoid a system crash. The DualBeam program structure by FEI leads to a memory leak for larger processing scripts (more structures) which can result in system instability and a system crash without prior warning or error messages.

Table 16: Inter-pore distances and the approximate required processing time for a 1 mm × 1 mm nanoporous array.

Pore distance *µm*	Time *h*
2	12
5	9
10	4

High pore densities

Shorter inter-pore distances of around 500 nm are of great interest since they represent a comparable array to the purchased membranes

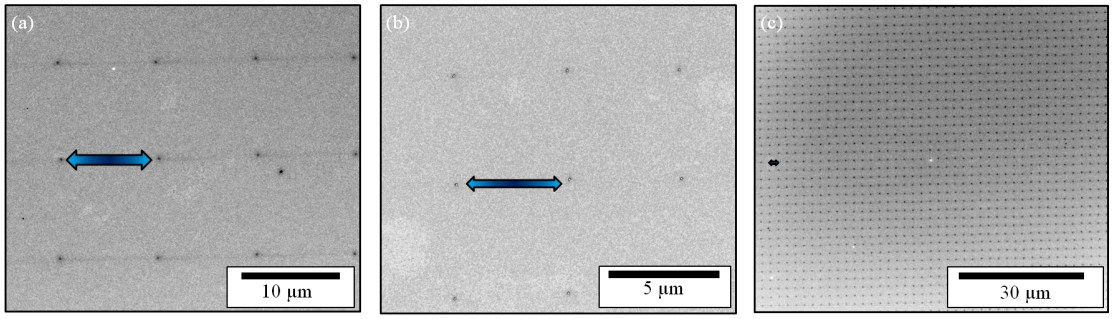

Figure 140: SEM images showing the nanopore array for different inter-pore distances: (a) 10 µm, (b) 5 µm, (c) 2 µm. Intensity inverted SEM images are given for better visibility of the nanopores.

(which were used in the biological investigation) and therefore allow a direct comparison between an ordered and a disordered nanoporous array. Structuring high pore density arrays represents a challenge due to the required processing time of the script and the incident memory leak. Evaluation of the scripting processing times show that a great part of the time is used to load the predefined patterns as well as for additional sleeping times to prevent system instabilities. Milling a 1 mm × 1 mm with an inter-pore distance of 500 nm array using the prototyping approach would take more than 80 h, due to the increased computing time of the pattern and neccessary increased sleep times, which is unviable.

An alternative method needs to be employed to define and mill an array with the small inter-pore distances while the stage is moved using the scripting routine. A possible solution to the problem represents the *pitch* option for milling a rectangle. In this advanced option the distance between the milled points for a rectangular pattern can be set. In a conventional process the ion beam is moved over the area in such a way that a beam overlap between the points occurs to ensure a smooth milling (see Figure 141). For a negative beam overlap, or larger pitch, a nanoporous array is milled instead of a rectangle. This is illustrated in Figure 142. A 1 mm × 1 mm nanoporous array with an inter-pore distance of 500 nm can be milled within 16 h in this manual approach. The reason that this faster structuring method was not employed in the prototyping is that the advanced options in which the pitch is set cannot be programmed since *Autoscript xT* does not offer commands to set the advanced options. This method therefore only represents a

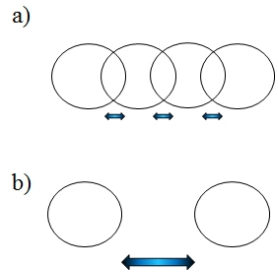

Figure 141: Milling process of a rectangle with different beam overlaps (pitches): (a) Conventional milling process in which the beam is scanned over the area. A beam overlap between the scanned/milled points ensures a smooth milling. The arrows mark the beam overlap. (b) A negative beam overlap (pitch) leads to a nanoporous pattern instead of a smooth rectangle. The arrow marks the negative beam overlap (pitch) between the two beam positions.

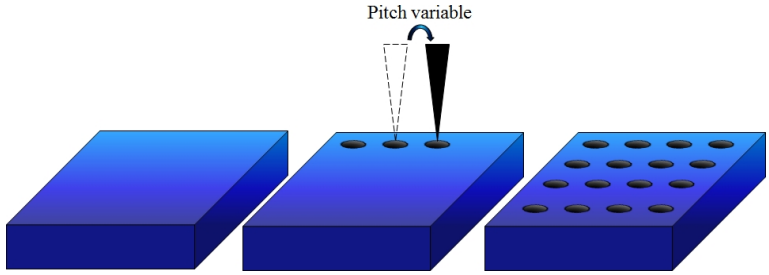

Figure 142: Structuring method employing a rectangle and a pitch. A pitch between the ion beam positions is set for a rectangular milling pattern, leading to a nanoporous array instead of a rectangle.

semi automatic approach in which the stage is moved with the second part of the script while the pattern (which would require an increased computational time using the script) is milled manually for each step. The mill command as well as the complete first part of the script which defines the nanoporous array is removed and the sleep time is increased to 5 s between the stage moves to allow manual milling. Figure 143 shows part of the nanoporous array. The alignment of the 10 μm^2 arrays is not as well defined as with the fully automated approach. This misalignment is caused by starting the milling process manually within a fraction of a second after the stage was move was performed by the program. Small deviations in patterning start time lead to this misalignment. However, these misalignments are most likely negligible since they are sufficiently small. The drawback of this method is that it requires an operator at all times. A software update in which the advanved options of the milling patterns can be scripted would solve the problem [236].

Discussion

The scripting process which was developed within the framework of this thesis can be used to structure large arrays of 30 nm pores with a tuneable inter-pore distance (and therefore pore density) within a reasonable time without requiring an operator at site. A large amount of the nanopore arrays are currently being produced for further experiments in which the influence of the nanopore density on stem cell differentiation is to be determined. In addition, the script can be easily modified in terms of nanopore arrangement, size, or structure geometry for future experiments[97] (for example milling 30 nm lines instead of pores) as well as for other applications (such as nano apertures).

[97] The script is designed in such a way that any pore size can be structured. Different pore sizes can be milled by changing the beam current. For each beam current, the optimal dwelltime and processing time should be determined prior to scripting for optimal results. The pore arrangement and inter-pore distance can easily be adjusted in the first part of the scipt.

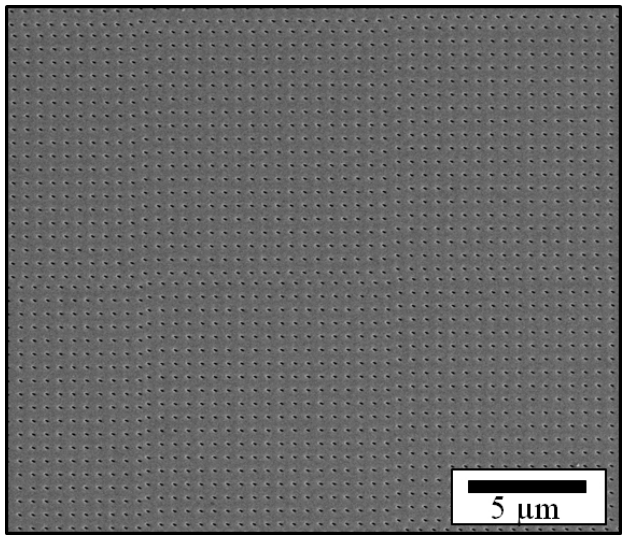

Figure 143: SEM image of a nanoporous array with a 500 nm inter-pore distance which was structured in the semi-manual approach.

Conclusion

Stem cell differentiation via physical cues was studied in this work. The results show that differentiation of human inferior turbinate stem cells into an osteogenic lineage can be induced by a nanostructured titanium layer with 30 nm pores and that the limitation of biochemical cues, currently used, can thus be overcome. The stem cells interact directly with the nanoporous substrate via nanoscaled filopodia protrusions and tethers resulting in a signaling mechanism within the cell that up-regulates the osteogenic related transcripts required for differentiation.

To allow a further study of the influence of such nanoporous arrays on stem cell differentiation, a DualBeam automation technique was succsessfully developed in which a large array of 30 nm pores with variable inter-pore distances was structured. In this approach, small lines, representing the simplest geometries that can be milled using the ion beam device, with a nominal length below the beam diameter are used to structure nanopores. A scripting routine, which defines an array of nanopores and moves the stage in a meander-like fashion to structure a $1\,mm^2$ sized sample, represents a fully automated approach which does not require an operator during the structuring process. High pore densities (4×10^6 nanopores$/mm^2$) represent a challenge for this approach due to required computing time and occuring memory leak. A semi-automatic approach in which the nanoporous array is stuctured by milling rectangles with a negative beam overlap (pitch between the milled points) while the script moves the stage represents a work-around to the problem. A FEI software update, in which the advanced milling options can be scripted, would not only allow for a fully automated approach and thus permit to structure higher pore densities, but would also most

likely decrease the structuring times for all other pore densities.

The advantage of this approach over Akemeier's script [48] becomes clear by comparing the processing times and the possible amount of structured nanopores of both scripts. With this script, a higher beam current ($\gg$0.28 nA) can be chosen to mill 100 nm pores, resulting in a faster process. In addition, the less complex geometry of the milled patterns allows for an increased amount of nanopores.

The focussed ion beam approach allows a fully automated structuring process and simple sample preparation for lower nanopore densities in comparison to e-beam lithography in which several additional steps, such as spin coating of the resist as well as removal of the resist, are necessary. In addition only biocompatible materials can be used in the focused ion beam approach. E-beam lithography currently represents a better option for high pore densities[98]. However, a FEI software update would negate this current advantage.

[98] It only represents a better option under the assumption of a non-toxicity of the resist.

Outlook

Experiments in which the titanium layer is replaced by gold, tantalum, niobium and zirconium to study the effect of different materials on stem cell differentiation are also of great interest and are planned.

Further studies in which the script versatility will show include different nanopore arrangements that can easily be achieved with only minor changes in a subpart of the scripting routine. In addition, the script can be used for different pore sizes by using different currents and also can potentially be used to structure nanoporous arrays with nanopore sizes down to 10 nm. Different nanopore shapes can be realized by using the effect of astigmatism on the beam shape. Astigmatism leads to an elliptical beam shape and this could be used to structure non-circular pores. Further experiments using different geometries such as 30 nm thick lines with variable inter-line distances can be created by milling rectangles with a high beam current[99]. For such a structure, only small changes in the script need to be made in which the line command is replaced by a rectangle command, the dwelltime is replaced by the optimal value for the rectangular structure and beam current, and where the amount of rectangles and their distances are altered to fit into the $10\,\mu m^2$ array. The idea of this script could easily be applied to other focused ion beam devices, if necessary.

[99] The optimal beam current and dwelltime would need to be determined for this approach.

Bibliography

[1] http://www.pa.msu.edu/~yang/rfeynmanplentyspace.pdf, 31.12.2013.

[2] http://www.nobelprize.org/, 01.12.2013.

[3] P.A. Midgley, E.P.W. Ward, A.B. Hungria, and J.M. Thomas. Nanotomography in the chemical, biological and materials sciences. *Chem. Soc. Rev.*, 36:1477–1494, 2007.

[4] Ch. Kittel. *Einführung in die Festkörperphysik*, volume 14th Ed. Oldenbourg, 2006.

[5] A.Zabet-Khoscousi and A.Dhirani. Charge transport in nanoparticle assemblies. *Chem. Rev.*, 108, 2008.

[6] L.Y. Gorelik, A. Isacsson, M.V.Voinova, B.Kasemo, R.I.Shekhter, and M. Jonson. Shuttle mechanism for charge transfer in coulomb blockade nanostructures. *Physical Review Letters*, 80, 1998.

[7] A. Akbarzadeh, M. Samiei, and S. Davaran. Magnetic nanoparticles: preparation, physical properties and applications in biomedicine. *Nanoscale Research Letters*, 7, 2012.

[8] C.Thelander, M.H.Magnusson, K.Deppert, and L.Samuelson. Gold nanoparticle single-electron transistor with carbon nanotube leads. *Applied Physics Letters*, 79, 2001.

[9] A. Lisfi, C.M. Williams, L.T. Nguyen, J.C. Lodder, A. Coleman, H. Corcoran, A. Johnson, P. Chang, A. Kumar, and W. Morgan. Reorientation of magnetic anisotropy in epitaxial cobalt ferrite thin films. *Phys. Rev. B*, 76, 2007.

[10] S.A. Majetich, J.H. Scott, E.M. Kirkpatrick, K. Chowdary, K. Gallagher, and M.E. McHenry. Magnetic nanoparticles and magnetocrystalline anisotropy. *Nanostructured Materials*, 9:291–300, 1997.

[11] Z. Ibusuki, S. Kojima, O. Kitakami, and Y. Shimada. Magnetic anisotropy and behaviors of fe nanoparticles. *IEEE Trans, Mag.*, 37, 2001.

[12] S.H. Gee, Y.K. Hong, D.W. Erickson, M.H. Park, and J.C. Sur. Synthesis and aging effect of spherical magnetite (Fe_3O_4) nanoparticles for biosensor applications. *J. Appl. Phys.*, 93:7560–7562, 2003.

[13] I. Koh and L. Josephson. Magnetic nanoparticle sensors. *Sensors*, 9:8130–8145, 2009.

[14] L.L. Vatta, R.D. Sanderson, and K.R. Koch. Magnetic nanoparticles: Properties and potential applications. *Pure Appl. Chem.*, 78:1793–1801, 2006.

[15] G. Schmid. *Nanoparticles: From Theory to Application*. John Wiley and Sons, 2010.

[16] D. Vollath. *Nanomaterials*. Wiley, 2008.

[17] M.P. Pileni. *Nanocrystals forming mesoscopic structures*. Wiley, 2005.

[18] A. Hütten, D. Sudfeld, I. Ennen, G. Reiss, W. Hachmann, U. Heinzmann, K. Wojczykowski, P. Jutzi, W. Saikaly, and G. Thomas. New magnetic nanoparticles for biotechnology. *J. of Biotechnology*, 112:47–63, 2004.

[19] R.H. Kodama. Magnetic nanoparticles. *J. of Magnetism and Magnetic Materials*, 200:359–372, 1999.

[20] S.P. Gubin, Y.A. Koksharov, G.B.Khomutov, and G.Y. Yurkov. Magnetic nanoparticles: preparation, structure and properties. *Russian Chemical Reviews*, 74:489–520, 2005.

[21] D. Horn and J. Rieger. Organische nanopartikel in wässriger phase. *Angew. Chem.*, 113:4460–4492, 2001.

[22] J.W.M. Bulte. Magnetic nanoparticles as markers for cellular mr imaging. *Magn. Magn. Mat.*, 289, 2005.

[23] Q.A. Pankhurst, J. Conolly, S. Jones, and J. Dobson. Applications of magnetic nanoparticles in biomedicine. *J. Phys. D: Appl. Phys.*, 36, 2003.

[24] W.S. Seo, J.H. Lee, X. Sun, Y. Suzuki, D. Mann, Z. Liu, M. Terashima, and D.G. Nishimura H. Dai P.C. Yang, M.C. McConnell. Feco/graphitic-shell nanocrystals as advanced magnetic-resonance-imaging and near-infrared agents. *Nat. Mater.*, 5, 2006.

[25] D.H. Kim, S.H. Lee, K.N. Kim, K.M. Kim, I.B. Shim, and Y.K. Lee. Temperature change of various ferrite particles with alterning magnetic field for hyperthermic application. *J. Magn. Magn. Mater.*, 293, 2005.

[26] S. Mornet, S.Vasseur, F. Grasset, and E.Duguet. Magnetic nanoparticle design for medical diagnosis and therapy. *J. Mater. Chem.*, 14, 2004.

[27] J.M. De Teresa, C. Marquina, and D. Serrate. From magnetoelectronic to biomedical applications based on the nanoscale properties of advanced magnetic materials. *Int. J. Nanotechnology*, 2, 2005.

[28] G. Baldi, D. Bonacchi, M.C. Franchini, D. Gentili, G. Lorenzi, A. Ricci, and C. Ravagli. Synthesis and coating of cobalt ferrite nanoparticles: A first step toward the obtainment of new magnetic nanocarriers. *Langmuir*, 23:4026–4028, 2007.

[29] A. Jordan, P. Wust, R. Scholz, B. Tesche, H. Fahling, T. Mitrovics, T. Vogl, J. Cervos-Navarro, and R. Felix. *Int. J. Hyperthermia*, 12, 1996.

[30] A. Jordan, R. Scholz, P. Wurst, H. Schirra, T. Schiestel, H. Schmidt, and R. Felix. Endocytosis of dextran and silan-coated magnetite nanoparticles and the effect of intracellular hypertermia on human mammary carcinoma cells. *J. Magn. Magn. Mater.*, 194, 1999.

[31] http://www.startrek.com/databasearticle/nanoprobes, 31.12.2013.

[32] K.H. Campbell, J. McWhir, W.A. Ritchie, and I. Wilmut. Sheep cloned by nuclear transfer from a cultured cell line. *Nature*, 380, 1996.

[33] A. Atala and R. Lanza. *Handbook of Stem Cells*, volume 1. Elsevier Academic Press, 2013.

[34] S. Lavenus, M. Berreur, V. Trichet, P. Pilet, G. Louarn, and P. Layrolle. Adhesion and osteogenic differentiation of human mesenchymal stem cells on titanium nanopores. *European Cell and Materials*, 22:84–96, 2011.

[35] T. Speck. Bionik, biomimetik, ein interdisziplinäres forschungsgebiet mit zukunftspotenzial. *Naturwissenschaftliche Rundschau*, 57 Jahrgang, Heft 4, 2004.

[36] Princeton Measurements Corporation. *Instruction manual MicroMag^{TM} 2900, 2002*.

[37] I. Ennen. *Magnetische Nanopartikel als Bausteine für granulare Systeme: Mikrostruktur, Magnetismus und Transporteigenschaften*. Universität Bielefeld, 2008.

[38] D.B. Williams and C.B. Carter. *Transmission Electron Microscopy - A Textbook for Materials Science*. Plenum Press, New York, 1996.

[39] *Philips, Manual CM200 Super Twin, 1995*.

[40] J. Bernardi, M. Stöger-Pollach, and P. Schattschneider. *PR Elektronenmikroskopie, Skriptum zur Lehrveranstaltung*. TU Wien.

[41] B. Fultz and J.M. Howe. *Transmission Electron Microscopy and Diffractometry of Materials*, volume Third Ed. Springer, 2008.

[42] R.F. Egerton. Electron energy-loss spectroscopy in the tem. *Rep. Prog. Phys.*, 72, 2009.

[43] R.K. Wild and P.E.J. Flewit. *Physical methods for material characterization*. Institute of Physics Publishing, 1994.

[44] P. Schattschneider, M. Stöger-Pollach, and W. Werner. *Electron Beam Techniques for Nanoanalysis, Skriptum zur Lehrveranstaltung*. TU Wien, 2011.

[45] N. Yao. *Focused Ion Beam Systems, Basics and Applications*. Cambridge University Press, 2007.

[46] F. Eggert. *Standardfreie Elektronenstrahl-Mikroanalyse*. Books on Demand GmbH, 2005.

[47] Nist,http://physics.nist.gov/cgi-bin/asd/ie.pl, 05.12.2013.

[48] D. Akemeier. *Nano-Prototyping and 3D Bioimaging with Dual Beam Microscopy*. Universität Bielefeld, 2013.

[49] D. Magde, W.W. Webb, and E. Elson. Thermodynamic fluctuations in a reacting system-measurements by fluorescence correlation spectroscopy. *Phys. Rev. Lett.*, 29, 1972.

[50] J.R. Lakowitz. *Principles of Fluorescence Spectroscopy*, volume 3rd Ed. Springer, 2006.

[51] FP Praktikum handout for FCS. *Quick data evaluation of diffusion measurements of free organic fluorophores*.

[52] M. Stührenberg. *Diffusionseigenschaften von Quantum Dots und ihre Anwendung, untersucht mittels Fluoreszenz-Korrelationsspektroskopie*. Universität Bielefeld, 2010.

[53] R. Rigler and E.S. Elson. *Fluorescence Correlation Spectroscopy, Theory and application*. Springer, 2001.

[54] G. Will. *The Rietveld Method and the Two-Stage Method*. Springer, 2006.

[55] A. Dippel. *Diffractometers for powder diffraction*. Rietveld workshop, 2011.

[56] L.Spiess, G. Teichert, R. Schwarzer, H. Behnken, and C. Genzel. *Moderne Roentgenbeugung*. Vieweg, Teubner, 2009.

[57] J. Rodriguez-Carvajal. *An Introduction to the program FullProf 2000*. Laboratoire Leon Brillouin, 2001.

[58] Haass. *Anmerkungen und Mitschriften zum Pulverdiffraktometriekurs*. TU Darmstadt, 2002.

[59] H. Krischner and B. Koppelhuber-Bitschnau. *Röntgenstrukturanalyse und Rietveldmethode*. Vieweg, 1994.

[60] R.A. Young. *The Rietveld Method*. Oxford University Press, 1995.

[61] R.Allmann. *Röntgenpulverdiffraktometrie*. Springer, 2003.

[62] H.D. Megaw and C.N.W. Darlington. Geometrical and structural relations in the rhombohedral perovskites. *Acta Cryst.*, A31, 1975.

[63] M. Meinert. *Ferrimagnetic Heusler compounds: from first principles to thin films*. Universität Bielefeld, 2011.

[64] Tobias Hempel. *GMR Layers for Interlayer Coupled and Pinned Trilayers and New Concepts for GMR-Sensors*. Universität Bielefeld, 2005.

[65] A. Komeili, Z. Li, D.K.Newman, and G.J.Jensen. Magnetosomes are cell membrane invaginations organized by the actin-like protein mamk. *Science*, 311, 2006.

[66] R.B.Frenkel and D.A.Bazylinski. How magnetotactic bacteria make magnetosomes queue up. *Trends in Microbiology*, 14, 2006.

[67] A. Dannenberg, M.E.Gruner, A. Hucht, and P.Entel. Surface energies of stoichiometric fept and copt alloys and their implications for nanoparticle morphologies. *Physical Review B*, 80, 2009.

[68] M. Riskin, B. Basnar, Y. Huang, and I. Willner. Magnetoswitchable charge transport and bioelectrocatalysis using maghemite-au core-shell nanoparticle7polyaniline composites. *Adv.Mater.*, 19, 2007.

[69] J.Q.You and L. Zhang and.K.Gosh. Electronic transport in nanostructures consisting of magnetic barriers. *Physical Review B*, 1995.

[70] I.V. Roslyakov, K.S. Napol'skii, A.A. Eliseev, A.V. Lukashin, D.Y. Chernyshow, and S.V. Grigor'ev. Preparing magnetic nanoparticles with controllable anisotropy of functional properties within a porous matrix of aluminia. *Nanotechnologies in Russia*, 4:176–181, 2009.

[71] D.A. Bazylinski, R.B. Frankel, B.R. Heywood, S. Mann, J.W. King, P.L. Donaghay, and A.K. Hanson. Controlled biomineralization of magnetite (Fe_3O_4) and greigite (Fe_3S_4) in a magnetotactic bacterium. *Applied and Enviromental Microbiology*, 61:3232–3239, 1995.

[72] J.L. Kirschvink, J.W. Hagadorn, and E. Bäuerlein (ed). *The Biomineralization of Nano- and Micro-Structures: A Grand Unified Theory of Biomineralization*. Wiley VCH Verlag GmbH, Weihneim, 2000.

[73] D. Bazylinski. Controlled biomineralization of magnetic minerals by magnetotactic bacteria. *Chemical Geology*, 132, 1996.

[74] A. Arakaki, H. Nakazawa, M Nemoto, T. Mori, and T. Matsunaga. Formation of magnetite by bacteria and its application. *J. Roy. Soc. Int.*, 6, 2008.

[75] R. Blakemore. Magnetotactic bacteria. *Annu. Rev. Microbiol*, 36:217–238, 1982.

[76] T. Hyeon, Y. Chung, J. Park, S. lee, Y. Kim, and B. Park. Synthesis of highly crystalline and monodisperse cobalt ferrite nanocrystals. *J. Phys. Chem B*, 106:6831–6833, 2002.

[77] A. Arakaki, J. Webb, and T. Matsunaga. A novel protein tightly bound to bacterial magnetic particles in magnetospirillum magneticum strain amb-1. *J. Biol. Chem.*, 278, 2003.

[78] D. Bazylinski and D. Schüler. Biomineralization and assembly of the bacterial magnetosome chain. *Microbe*, 4, 2009.

[79] C. Lang, D. Schüler, and D. Faivre. Synthesis of magnetite nanoparticles for bio- and nanotechnology: Genetic engineering and biomimetics of bacterial magnetosomes. *Macromolecular Bioscience*, 7, 2007.

[80] A. Scheffel, M. Gruska, D. Faivre, A. Linaroudis, J.M. Plitzko, and D. Schüler. An acidic protein aligns magnetosomes along a filamentous structure in magnetotactic bacteria. *Nature*, 440, 2006.

[81] A. Scheffel and D. Schüler. The acidic repetitive domain of the magnetospirillum gryphiswaldense mamj protein displays hypervariability but is not required for magnetosome chain assembly. *J. Bacteriology*, 189, 2007.

[82] A. Komeili, H. Vali, T.J. Beveridge, and D.K. Newman. Magnetosome vesicle are present before magnetite formation and mama is required for their activation. *PNAS*, 101, 2004.

[83] M. Tanaka, E. Mazuyama, A. Arakaki, and T. Matsunaga. Mms6 protein regulates crystal morphology during nano-sized magnetite biomineralization in vivo. *J. of Biological Chemistry*, 286, 2011.

[84] S. Mann. Molecular tectonics in biomineralization and biomimetic materials chemistry. *Nature*, 365, 1993.

[85] M. Sarikaya, C. Tamerler, A. Jen, K. Schulten, and F. Baneyx. Molecular biomimetics: nanotechnology through biology. *Nature Materials*, 2, 2003.

[86] S. Mann, D. Archibald, J. Didymus, T. Douglas, B. Heywood, F. Meldrum, and N. Reeves. Crystallization at inorganic-organic interfaces: Biominerals and biomimetic synthesis. *Science*, 261, 1993.

[87] D. Simberg, T. Duza, J. Park, M. Essler, J. Pilch, L. Zhang, A. Derfus, M. Yang, R. Hoffmann, S. Bhati, M. Sailor, and E. Ruoslahti. Biomimetic amplificatino of nanoparticle homing to tumors. *PNAS*, 104, 2007.

[88] T. Cedervall, I. Lynch, S. Lindman, T. Berggard, E. Thulin, H. Nilsson, K. Dawson, and S. Linse. Understanding the nanoparticle-protein corona using methods to quantify exchange rates and affinities of proteins for nanoparticles. *PNAS*, 104, 2007.

[89] S. Yu. Bio-inspired crystal growth by synthetic templates. *Top Curr Chem*, 271, 2007.

[90] A.M. Belcher and C. Mao. Biological routes to metal alloy ferromagnetic nanostructures. *NanoLetters*, 4:1127–1132, April 2004.

[91] A.M. Belcher, S. Lee, and D.S. Yun. Cobalt ion mediated self-assembly of genetically engineered bacteriophage for biomimetic co-pt hybrid material. *Biomacromolecules*, 7:14–17, November 2005.

[92] T. Matsunaga and H. Takeyama. Biomagnetic nanoparticle formation and application. *Supramolecular Science*, 5, 1998.

[93] E. Dujardin and S. Mann. Bio-inspired materials chemistry. *Advanced Materials*, 14, 2002.

[94] A.David. Bioinspired synthesis of magnetic nanoparticles. *Masterthesis*, 2009.

[95] A.M. Belcher, P.K. Hansma, G.D. Stucky, and D.E. Morse. First steps in harnessing the potential of biomineralization as a route to new high-performance composite materials. *Acta mater.*, 46:733–736, 1998.

[96] M. Epple. *Biomaterialien und Biomineralisation, Eine Einführung für Naturwissenschaftler, Mediziner und Ingenieure*. Teubner, 2003.

[97] S.Yu and H. Cölfen. Bio-inspired crystal morphogenesis by hydrophillic polymers. *J. Mater. Chem.*, 14, 2004.

[98] S. Mann. Biomineralisation: Ein neuer zweig der bioanorganischen chemie. *Chemie in unserer Zeit*, 3, 1986.

[99] D. Faivre. Von der bio-zur anorganischen mineralisation von magnetit. *Max-Planck-Gesellschaft*, http://mpg.de/print/388136, 2010.

[100] l. Sjen, N. Bao, P.E. Prevelige, and A. Gupta. Fabrication of ordered nanostructures of sulfide nanocrystal assemblies over self-assembled genetically engineered p22 coat protein. *JACS Communications*, 132, 2010.

[101] K. Liu and L. Jiang. Bio-inspired design of multiscale structures for function integration. *Nano Today*, 6:155–175, 2011.

[102] M.T. Klem, M. Young, and T. Douglas. Biomimetic magnetic nanoparticles. *Materials Today*, 8, 2005.

[103] S. Brown, M. Sarikaya, and E. Johnson. A genetic analysis of crystal growth. *J. Mol. Biol.*, 299, 2000.

[104] R.Olivares-Navarrete, S. Hyzy, D. Hutton, C. Erdman, M. Wieland, B.D. Boyan, and Z. Schwartz. Direct and indirect effects of microstructured titanium substrates on the induction of mesenchymal stem cell differentiation towards the osteoblast lineage. *Biomaterials*, 31, 2010.

[105] S. Mann. Biomineralisation: Ein neuer zweig der bioanorganischen chemie. *Chemie in unserer Zeit*, 20. Jahrg. Nr. 3, 1986.

[106] J.M. Slocik and R.R. Naik. Probing peptide-nanomaterial interactions. *Chem. Soc. Rev.*, 39:3454–3463, 2010.

[107] T. Prozorov, P. Palo, L. Wang, M. Nilsen-Hamilton, D. Jones, D. Orr, S. Mallapragada, B. Narasimhan, P. Canfield, and R. Prozorov. Cobalt ferrite nanocrystals: Out-performing magnetotactic bacteria. *ACSNano*, 1, 2007.

[108] X. Cao and L. Gu. Spindly cobalt ferrite nanocrystals: preparation, characterization and magnetic properties. *Nanotechnology*, 16:180–185, 2005.

[109] Y.H. Hou, Y.J. Zhao, Z.W. Liu, H.Y. Yu, X.C. Zhong, and W.Q. Qiu. Structural, electronic and magnetic properties of partially inverse spinel $cofe_2o_4$. *J. Phys. D: Applied Physics*, 43, 2010.

[110] C.N. Chinnasamy, M. Senoue, B. Jeyadevan, O. Perales-Perez, K. Shinoda, and K. Tohiji. Synthesis of size-controlled cobalt ferrite particles with high coercivity and squareness ratio. *J. Colloid and Interface Science*, 263:80–83, 2003.

[111] V. Pillai and D. Shah. Synthesis of high-coercivity cobalt ferrite particles using water-in-oil microemulsions. *J. Magn. Magn. Mater.*, 163:243–248, 1996.

[112] A. Wolff. *Novel approach to synthesize magnetic nanoparticles*. Universität Bielefeld, 2010.

[113] R. Eden. The decades of the newe worlde or west india (reprinted 1885). page 264, 1555.

[114] R. Hakluyt. The principall navigations, vojages and discoueries of the english nation (reprinted 1598-1600). page 264, 1589.

[115] A. Walsh, S.H. Wei, Y. Yan, M. Al-Jassim, J.A. Turner, M. Woodhouse, and B.A. Parkinson. Structural, magnetic and electronic properties of the co-fe-al oxide spinel system: Denisty-functional theory calculations. *Physical Review B*, 76, 2007.

[116] Y.H. Hou, Y.J. Zhao, Z.W. Liu, H.Y. Yu, X.C. Zhong, W.Q. Qiu, D.C. Zheng, and L.S. Wen. Structural, electronic and magnetic properties of partially inverse spinel $cofe_2o_4$: a first-principles study. *J. Phys. D: Appl. Phys.*, 43, 2010.

[117] T.R. Paudel, A. Zakutayev, S. Lany, M. d'Avezac, and A. Zunger. Doping rules and doping prototypes in a_2bo_4 spinel oxides. *Adv. Funct. Mater.*, 21:4493–4501, 2011.

[118] R.D. Desautels, J.M. Cadogan, and J. van Lierop. Spin dynamics in $cofe_2o_4$ nanoparticles. *J. Appl. Phys*, 105, 2009.

[119] M. Rajendran, R.C. Pullar, A.K. Bhattacharya, D. Das, S.N. Chintalapudi, and C.K. Majumdar. Magnetic properties of nanocrystalline $cofe_2o_4$ powders prepared at room temperature: variatino with crystallite size. *J. Magn. and Magnetic Materials*, 2000.

[120] Z. Szotek, W.M. Temmerman, D. Ködderitzsch, A. Svane, and H. Winter L. Petit. Electronic structures of normal and inverse spinel ferrites from first principles. *Phys. Rev. B*, 74, 2006.

[121] T.L. Templeton, A.S. Arrott, A.E. Curzon, M.A. Gee, X.Z. Li, and Y. Yoshida. Magnetic properties of coxfe3-xo4 during

conversion from normal to inverse spinel particles. *J. Appl. Phys.*, 73:6728–6730, 1993.

[122] J.C. Slonczewshi. Origin of magnetic anisotropy in coxfe3-xo4. *J. Appl. Phys.*, 29:448–449, 1958.

[123] M. Tachiki. Origin of the magnetic anisotropy energy of cobalt ferrite. *Progress of Theoretical Physics*, 23, 1960.

[124] C.N. Chinnasamy, B. Jeyadevan, K-Shinoda, K. Tohji, D.J. Djayaprawira, M. Takahashi, R. Justin Joseyphus, and A. Narayanasamy. Unusually high coercivity and critical single-domain size of nearly monodospersed $cofe_2o_4$ nanoparticles. *Applied Physics Letters*, 83, 2003.

[125] J.S. Jung, J.H. Lim, K.H. Choi, S.L. Oh, Y.R. Kim, S.J. Lee, D.A. Smith, K.L. Stokes adn L.Malkinski, and C.J. O'Connor. $Cofe_2o_4$ nanostructures with high coercivity. *J. of Applied Physics*, 97, 2005.

[126] N.Ch. Pramanik, T. Fujii, M. Nakanishi, and J. Takada. Effect of co^{2+} ion on the magnetic properties of sol-gel cobalt ferrite thin films. *J. of Materials Chemistry*, 14:3328–3332, 2004.

[127] G.H. Jonker. Analysis of the semiconducting properties of cobalt ferrite. *J.Phys.Chem.Solids*, 9:165–175, 1959.

[128] V. Blaskov, V. Petkov, V. Rusanov, L.M. Martinez, B. Martinez, J.S. Munoz, and M. Mikhov. Magnetic properties of nanophase $cofe_2o_4$ particles. *J. of Magnetism and Magnetic Materials*, 162:331–337, 1996.

[129] Q. Song and Z. Zhang. Shape control and associated magnetic properties of spinel cobalt ferrite nanocrystals. *J. Am. Chem. Soc.*, 126:6164–6168, 2004.

[130] E. Manova, B. Kunev, D. Paneva, I. Mitov, L. Petrov, C. Estournes, C. D'Orleans, J. Rehspringer, and M. Kurmoo. Mechano-synthesis, characterization and magnetic properties of nanoparticles of cobalt ferrite, $cofe_2o_4$. *Chem. Mater.*, 16:5689–5696, 2004.

[131] N. Moumen, P. Veilllet, and M. Pileni. Controlled preparation of nanosize cobalt ferrite magnetic particles. *J. Magn. Magn. Mater.*, 149:61–71, 1995.

[132] Z. Liu, X. Li, Y. Leng, J. Lian, S. Liu, Z. Xiu, D. Huo, J. Li, and X. Sun. Homogeneous precipitation synthesis and magnetic properties of cobalt ferrite nanoparticles. *J. of Nanomaterials*, 2008.

[133] Inorganic crystal structure database, http://www.fiz-karlsruhe.de/icsd.html, 2013.

[134] A. Wolff, K. Frese, M. Wissbrock, K. Eckstädt, I. Ennen, W. Hetaba, S. Löffler, A. Regtmeier, P. Thomas, N. Sewald, P. Schattschneider, and A. Hütten. Influence of the synthetic polypeptide c25-mms6 on cobalt ferrite nanoparticle formation. *J. Nanopart. Res.*, 14, 2012.

[135] M. Sugimoto. The past, present, and future of ferrites. *J. Am. Ceram. Soc.*, 82:269–280, 1999.

[136] K.E. Sickafus and J.M. Wills. Structure of spinel. *J. Am. Ceram. Soc.*, 82:3279–3292, 1999.

[137] S. Krupicka. *Physik der Ferrite und der verwandten magnetischen Oxide*. Vieweg, 1973.

[138] J. Smit and P.H. Wijn. *Ferrite*. Philips Technische Bibliothek, 1962.

[139] G. Dhanaraj, K. Byrappa, V. Prasad, and M. Dudley. *Handbook of Crystal Growth*. Springer, 2010.

[140] H. Cölfen and S. Mann. Organization of nanostructures, higher-order organization by mesoscale self-assembly and transformation of hybrid nanostructures. *Angewandte Chemie*, 42, 2003.

[141] Q. Zhang, S. Liu, and S. Yu. Recent advances in oriented attachment growth and synthesis of funtional materials: concept, evidence, mechanism and future. *J. Mater. Chem*, 19:191–207, 2009.

[142] Y. Oaki, A. Kotachi, T. Miura, and H. Imai. *Adv. Funct. Mater*, 16:1633–1639, 2006.

[143] M. Niederberger and H. Cölfen. *Phys. Chem. Chem. Phys.*, 8:3271–3287, 2006.

[144] H. Cölfen and M. Antonietti. *Mesocrystals and Nonclassical Crystallization*. John Wiley and Sons, Ltd, Chichester, U.K., 2008.

[145] A. Dreyer. *Nanoskopische Metalltropfen als Vorstufen in der morphologiekontrollierten Synthese kristalliner Partikel aus Zinn, Germanium und Cobalt*. Universität Bielefeld, 2011.

[146] P.R. ten Wolde and D. Frenkel. Enhancement of protein crystal nucleation by critical density fluctuations. *Sciene*, 277, 1997.

[147] J.V.I Timonen, E.T. Seppälä, I. Ikkala, and R.H.A. Ras. From hot-injection synthesis to heating-up synthesis of cobalt nanoparticles: Observation of kinetically controllable nucleation. *Angew. Chem.*, 123, 2011.

[148] S.T. Yau and P.G. Venkilov. Quasi-planaer nucleus structure in apoferritin crystallization. *Nature*, 406, 2000.

[149] J. Baumgartner, A. Dey, P.H.H. Bomans, C. Le Coadou, P. Fratzl, N.A.J.M. Sommerdijk, and D. Faivre. Nucleation and growth of magnetite from solution. *Nature Materials*, 12:310–314, 2013.

[150] A. Weddemann, I. Ennen, A. Regtmeier, C. Albon, A. Wolff, K. Eckstädt, N. Mill, M.K. Peter, J. Mattay, C. Plattner, N. Sewald, and A. Hütten. Review and outlook: from single nanoparticles to self-assembled monolayers and granular gmr sensors. *Beilstein J. Nanotechnol.*, 1:75–93, 2010.

[151] M. Muthukumar. Theory of competitive adsorption-nucleation in polypeptide-mediated biomineralization. *J. Chem. Phys.*, 130, 2009.

[152] J. Zhang, F. Huang, and Z. Lin. Progress of nanocrystalline growth kinetics based on oriented attachment. *Nanoscale*, 2:18–34, 2010.

[153] R.L. Penn and J.F. Banfield. Morphology development and crystal growth in nanocrystalline aggregates under hydrothermal conditions: Insights from titania. *Geochimica et Cosmochimica Acta*, 63:1549–1557, 1999.

[154] R.L. Penn and J.F. Banfield. Oriented attachment and growth, twinning, polypeptism and formation of metastable phases: Insights from nanocrystalline tio$_2$. *American Mineralogist*, 83:1077–1082, 1998.

[155] R.L. Penn and J.F. Banfield. Imperfect oriented attachment: Dislocation generation in defect-free nanocrystals. *Science*, 281:969–971, 1998.

[156] R.D. Gunning, C. O'Sullivan, and K.M. Ryan. A multi-rate kinetic model for spontaneous oriented attachment of cds nanorods. *Phys. Chem. Chem. Phys.*, 12:12430–12435, 2010.

[157] S.H. Yu and S. Chen. Biomineralization: Self-assembly processes. *Encyclopedia of Inorganic and Bioinorganic Chemistry, Online*, 2011.

[158] H. Cölfen and M. Antonietti. *Angew. Chem. Int. Ed.*, 44:5576–5591, 2005.

[159] R.Q. Song and H. Cölfen. *Advanced Materials*, 22:1301–1330, 2010.

[160] V.M. Yuwono, N.D. Burrows, J.A. Soltis, and R.L. Penn. Oriented aggregation: Formation and transformation of mesocrystal intermediates revealed. *J. Am. Chem. Soc*, 132, 2010.

[161] B. Gilbert, H. Zhang, F. Huang, M.P. Finnegan, G.A. Waychunas, and J.F. Banfield. Special phase transformation and crystal growth pathways observed in nanoparticles. *Geochem. Trans.*, 4:20–27, 2003.

[162] H. Cölfen. Kinetik der festkörper-phasenumwandlung. *Max-Planck-Institut für Metallforschung*, http://www.mpg.de/print/362713, 2006.

[163] H. Cölfen. Nichtklassische kristallisation. *Max-Planck-Institut für Metallforschung,Tätigkeitsbericht*, 2004.

[164] G.H. Nancollas and W. Wu. Biomineralization mechanisms: a kinetics and interfacial energy approach. *J. Crytal Growth*, 211:137–142, 2000.

[165] M. Perez, M. Dumont, and D. Acevedo-Reyes. Implementation of classical nucleation and growth theories for precipitation. *Acta Materialia*, 56:2119–2132, 2008.

[166] T.H. Zhang and X.y. Liu. Nucleation: What happens at the initial stage? *Angew, Chem.*, 121:1334–1338, 2009.

[167] V.J. Anderson and H.N. Lekkerkerker. Insights into phase transition kinetics from colloid science. *Nature*, 416:811–816, 2002.

[168] H. Cölfen. A crystal-clear view. *Nature Materials*, 9:960–961, 2010.

[169] B. Mutaftschiev. *The Atomistic Nature of Crystal Growth*. Springer, 2001.

[170] J. Anwar and D. Zahn. Atomistisches verständnis der keimbildung und des kristallwachstums durch molekulare substanzen. *Angew. Chem.*, 123:2042–2061, 2011.

[171] H. Cölfen. *Nichtklassische Kristallisation*. Max-Planck-Gesellschaft, volume=Tätigkeitsbericht, year=2004,.

[172] A. Dreyer, I. Ennen, T. Koop, A. Hütten, and P. Jutzi. From nanoscale liquid spheres to anisotropic crystalline particles of tin: Decomposition of decamethylstannocence in organic solvents. *Small*, 7:3075–3086, 2011.

[173] D.A. Bazylinski, R.B. Frankel, and K.O. Konhauser. Modes of biomineralization of magnetite by microbes. *Geomicrobiology J.*, 24:465–475, 2006.

[174] D. Schüler. Genetics and cell biology of magnetosome formation in magnetotactic bacteria. *FEMS Microbiol. Rev.*, 32:654–672, 2008.

[175] T. Matsunaga and Y. Okamura. Genes and proteins involved in bacterial magnetic particle formation. *Trends in Microbiology*, 11, 2003.

[176] R. Prozorov, T. Prozorov, S. Mallapragada, B. Narasimhan, T. Williams, and D. Bazylinski. Magnetic irreversibility and verwey transition in nano-crystalline bacterial magnetite. *Phys. Rev. B*, 76, 2007.

[177] K. Grünberg, E.C. Müller, A. Otto, R. Reska, D. Linder, M. Kube, R. Reinhard, and D. Schüler. Biochemical and proteomic analysis of the magnetosome membrane in magnetospirillum gryphiswaldense. *Applied and Enviromental Microbiology*, 70, 2004.

[178] D.A.Bazylinski and R.B.Frankel. Magnetosome formation in prokaryotes. *Nature Reviews*, 2, 2004.

[179] A. Komeili. Molecular mechanism of magnetosome formation. *Annu. Rev. Biochem.*, 76, 2007.

[180] D. Schultheiss, R. Handrick, D. Jendrossek, M. Hanzlik, and D. Schüler. The presumptive magnetosome protein mms16 is a poly(3-hydroxybutyrate) granule-bound protein (phasin) in magnetospirillum gryphiswaldense. *J. Bacteriology*, 187:2416–2425, 2005.

[181] M. Charilaou, K.K. Sahi, D. Faivre, A. Fischer, and I. Garcia-Rubio. Evolution of magnetic anisotropy and thermal stability during nanocrystalchain growth. *Appl. Phys. Lett.*, 99, 2011.

[182] M. Tanaka, A. Arakaki, and T. Matsunaga. Identification and functional characterization of liposome tubulation protein from magnetotactic bacteria. *Molecular Microbiology*, 76:480–488, 2010.

[183] D. Schüler. Molecular analysis of a subcellular compartment: the magnetosome membrane in magnetospirillum gryphiswaldense. *Arch. Microbiol.*, 181:1–7, 2004.

[184] D. Faivre and D. Schüler. Magnetotactic bacteria and magnetosomes. *Chem Rev.*, 108:4875–4898, 2008.

[185] C. Nakamura, J.G. Burgess, K. Sode, and T. Matsunaga. An iron-regulated gene, maga, encoding an iron transport protein of magnetospirillum sp. strain amb-1. *J. of Biological Chemistry*, 270:28392–28396, 1995.

[186] A. Komeili, Z. Li, D.K. Newman, and G.J. Jensen. Magnetosomes are cell membrane invaginations organized by the actine-like protein mamk. *Science*, 311:242–245, 2006.

[187] D. Faivre and D. Schüler. Magnetotactic bacteria and magnetosomes. *Chem. Rev.*, 108:4875–4898, 2008.

[188] A. Komeili. Molecular mechanism of magnetosome formation. *Annu. Rev. Biochem.*, 76:351–366, 2007.

[189] A. Spakowitz and Z. Wang. End-to-end vector distribution with fixed end orientations for the wormlike chain model. *Physical Review*, 72, 2005.

[190] W. Hoppe, W. Lohmann, H. Markl, and H. Ziegler. *Biophysik*. Springer, 1977.

[191] A. Fersht. *Structure and Mechanism in Protein Science: A Guide to Enzyme Catalysis and Protein Folding*. W.H. Freeman, First Ed., 1998.

[192] A.M. Lesk. *Introduction to Protein Science: Architecture, Function, and Genomics*. Oxford University Press, 2010.

[193] http://ghr.nlm.nih.gov/handbook/howgeneswork/protein, 2013.

[194] R. Pearce and W.R. Patterson. *Catalysis and chemical processes*. Wiley, 1981.

[195] E.V. Dehmlow and S.S. Dehmlow. *Phase Transfer Catalysis*. VCH, 1993.

[196] D. Astruc. *Nanoparticles and Catalysis*. Wiley, 2008.

[197] K.A. Jackson. *Kinetic Processes*. Wiley-VCH, 2004.

[198] M.A. Vannice. *Kinetics of Catalytic Reactions*. Springer, 2005.

[199] R.J.D. Tilley. *Understanding solids*. Wiley, 2013.

[200] B.D. Cullity and C.D. Graham. *Introduction to Magnetic Materials*. Wiley, 2009.

[201] B. Aktas and F. Mikailov. *Advances in Nanoscale Magnetism*. Springer, 2009.

[202] E. Polizzi and N. B. Abdallah. Subband decomposition approach for the simulation of quantum electron transport in nanostructures. *J. of Computational Physics*, 202, 2005.

[203] C. Chen and N.L. Rosi. Peptide-based methods for the preparation of nanostructured inorganic materials. *Angew. Chem. Int. Ed.*, 49:1924–1942, 2010.

[204] http://www.innovagen.sc, 2013.

[205] M. Hoefling, S. Monti, S. Corni, and K.E. Gottschalk. Interaction of β-sheet folds with a gold surface. *PLoS ONE*, 6, 2011.

[206] M.T.J. Oliveira, S. Botti, and M.A.L. Marques. Modeling van der waals interactions between proteins and inorganic surfaces from time-dependent density functional theory calculations. *Phys. Chem. Phys.*, 13:15055–15061, 2011.

[207] R.W. Friddle, M.L. Weaver, S.R. Qiu, A. Wierzbicki, W.H. Casey, and J.J. De Yoreo. Subnanometer atomic force microscopy of peptide-mineral interaction links clustering and competition to acceleration and catastroph. *PNAS*, 107:11–15, 2010.

[208] M.L. Labanov et al. Radius of gyration as an indicator of protein structure compactness. *Molecular biology*, 42:623–625, 2008.

[209] K. Shiraki, K. Nishikawa, and Y. Goto. Trifluoroethanol-induced stabilization of the α-helical structure of β-lactoglobulin: Implication for non-hierarchical protein folding. *J. Mol. Biol.*, 245:180–194, 1995.

[210] O. Lagerstedt and B. Monemar. Variation of lattice parameters in gan wotj stpochiometry and doping. *Phys. Rev. B*, 19:3064–3070, 1979.

[211] J. Zhang, F. Huang, and Z. Lin. Process of nanocrystalline growth kinetics based on oriented attachment. *Nanoscale*, 2:18–34, 2010.

[212] R.L. Penn. Kinetics of oriented aggregation. *J. Phys. Chem. B*, 108:12707–12712, 2004.

[213] K. Maaz, Ar. Mimtaz, S.K. Hasanain, and Ab. Ceylan. Synthesis and magnetic properties of cobalt ferrite (cofe2o4) nanoparticles prepared by wet chemical route. *J. Magn. Magn. Mater.*, 308:289–295, 2007.

[214] C. Haas. Phase transitions in crystals with the spinel structure. *J. Phys, Chem. Solids*, 26:1225–1232, 1965.

[215] P. Mayer and W.W. Smeltzer. The kinetics and morphological development of oxide scales on cobalt-iron alloys (0-70 wt% fe)at 1200°C. *Oxidation of Metals*, 10:329–339, 1976.

[216] P. Schmidt. How to get ternary solid solutions $fe_{1-x}m'_xo$ (m=co, ni)? a thermodynamic concept. *Eur. J. Inorg. Chem*, pages 2847–2855, 2008.

[217] https://www.materialsproject.org/, 2013.

[218] S. Prakash and D. Shum-Tim. *Stem Cell Bioengineering and Tissue Engineering Microenviroment*. World Scientific, 2011.

[219] S. Li, N. L'Heureux, and J. Elisseeff. *Stem Cell and Tissue Engineering*. World Scientific, 2011.

[220] R. Lanza, J. Gearhart, B. Hogan, D. Melton, R. Pedersen, E. D. Thomas, J. Thomas, and M. West. *Essentials of Stem Cell Biology*. Elsevier Academic Press, 2006.

[221] B. Alberts. *Essential Cell Biology*. Taylor and Francis, 2009.

[222] K. Munk. *Taschenlehrbuch Biologie Biochemie Zellbiologie*. Thieme, 2008.

[223] H.K. Väänänen. Mesenchymal stem cells. *Anals of Medicine*, 2005.

[224] http://www.cell.com/cell_picture_show-cellmotility, 2013.

[225] http://web.biologie.uni-bielefeld.de/cellbiology/index.php/research/neural-crest-derived-stem-cells, 05.12.2013.

[226] D. Widera, W.D. Grimm, J.M. Moebius, I. Mikenberg, C. Piechaczek, G. Gassmann, N.A. Wolff, F. Thevenod, C. Kaltschmidt, and B. Kaltschmidt. Highly efficient neural differentiation of human somic stem cells, isolated by minimally invasive periodontal surgery. *Stem Cells Dev*, 16:447–460, 2007.

[227] D. Widera, C. Zander, M. Heidbreder, Y. Kasperek, T. Noll, O. Seitz, B. Saldamli, H. Sudhoff, R. Sader, C. Kaltschmidt, and B. Kaltschmidt. Adult palatum as a novel source of neural crest-related stem cells. *Stem Cells*, 27:1899–1910, 2009.

[228] D. Widera, P. Heimann, C. Zander, Y. Imielski, M. Heidbreder, M. Heilemann, C. Kaltschmidt, and B. Kaltschmidt. Schwann cells can be reprogrammed to multipotency by culture. *Stem Cells Dev*, 20, 2011.

[229] S. Hauser, D. Widera, F. Qunneis, J. Müller, C. Zander, J. Greiner, C. Strauss, P. Lüningschrör, P. Heimann, H. Schwarze, J. Ebmeyer, H. Sudhoff, M.J. Araúzo-Bravo, B. Greber, H. Zaehres, H. Schöler, C. Kaltschmidt, and B. Kaltschmidt. Isolation of novel multipotent neural crest-derived stem cells from adult human inferior turbinate. *Stem Cels Dev*, 21:742–756, 2012.

[230] J.F. Greiner, S. Hauser, D. Widera, J. Müller, F. Qunneis, C. Zander, I. Martin, J. Mallah, D. Schuetzmann, C. Prante, H. Schwarze, W. Prohaska, A. Beyer, K. Rott, A. Hütten, A. Gölzhäuser, H. Sudhoff, C. Kaltschmidt, and B. Kaltschmidt. Efficient animal-serum free 3d cultivation method for adult human neural crest-derived stem cell therapeutics. *Eur. Cell. Mater.*, 22:403–419, 2011.

[231] M. Schürmann, A. Wolff, D. Widera, S. Hauser, P. Heimann, A. Hütten, C. Kaltschmidt, and B. Kaltschmidt. Interaction of adult himan neural crest-derived stem cells with nanoporous titanium surface is sufficient to induce their osteogenic differentiation. *Stem Cell Therapy (submitted)*, 2013.

[232] L.Y. Roussel, D. Stokes, I. Gestman, M. Darus, and R. Young. Extreme high resolution scanning electron microscopy and beyond. *Scanning Microscope*, 7378:73780W–73780W–9, 2009.

[233] T.M. Svitkina, E.A. Bulanova, O.Y. Chaga, D.M. Vignjevic, S.i. Kojima, J.M. Vasiliev, and G.G. Borisy. Mechanism of filopodia initiation by reorganization of a dendritic network. *JCB*, 160, 2003.

[234] J.W. Lee, K.B. Lee, H.S. Jeon, and H.K. Park. Effects of surface nano-topography on human osteoblast filopodia. *Analytical Sciences*, 27, 2011.

[235] FEI Company. *AutoScript xT Technical Note*.

[236] Telefone conversation between a. wolff and fei., 2013.

[237] http://www.cryst.bbk.ac.uk/education/aminoacid/overview.html, 2013.

Appendix

Appendix A

Amino acid	Code
alanine	A
arginine	R
asparagine	N
aspartic acid	D
cysteine	C
glutamine	Q
glutamic acid	E
glycine	G
histidine	H
isoleucine	I
leucine	L
lysine	K
methionine	M
phenylalanine	F
proline	P
serine	S
threonine	T
tryptophan	W
tyrosine	Y
valine	V

Table 17: List of amino acids (Amino acid) and their one letter code (Code), taken from the Birkbeck Crystallography Homepage [237].

Appendix B

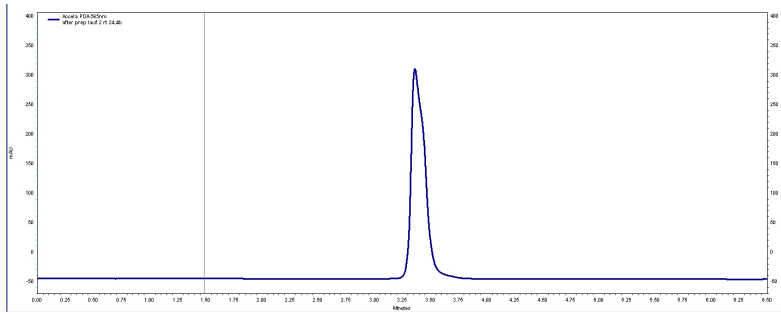

Figure 144: HPLC measurement of the RhondamineB labelled polypeptide c25-mms6.

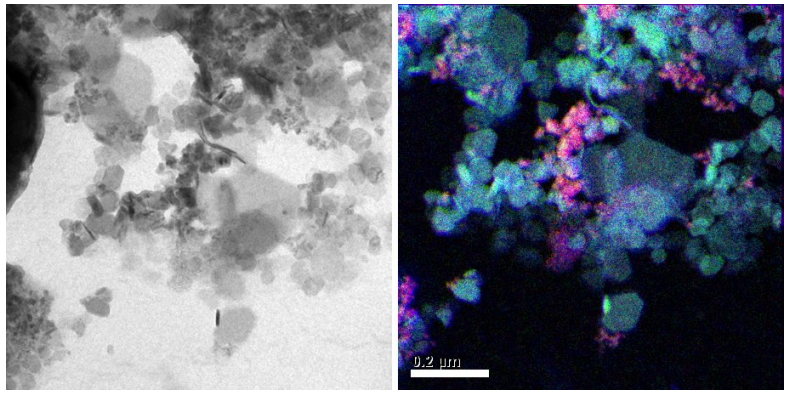

Figure 145: STEM (left) and EFTEM measurement (right) of the biosynthesized particles after 28 days. This measurment shows the phase separation between the discs (cobalt-rich) and the spheres (iron-rich). The same behavior was also found for the control experiment particles.

Appendix C

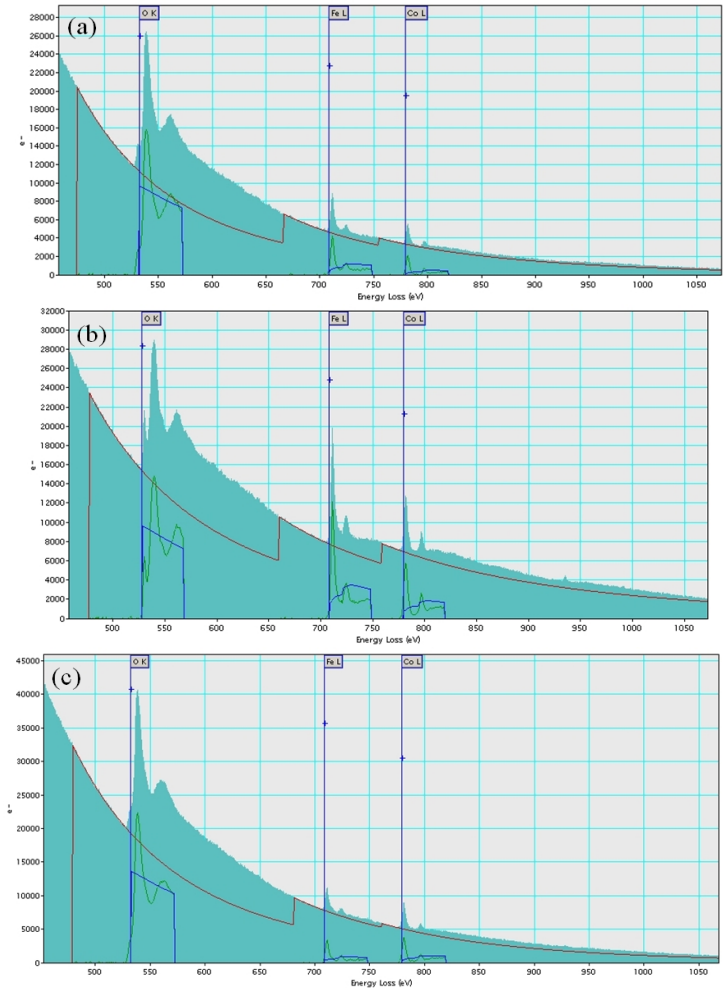

Figure 146: EELS spectra of the biosynthesized nanoparticles at different stages of the growth process: (a) after 5 min, (b) after 1 d, (c) after 2 d.

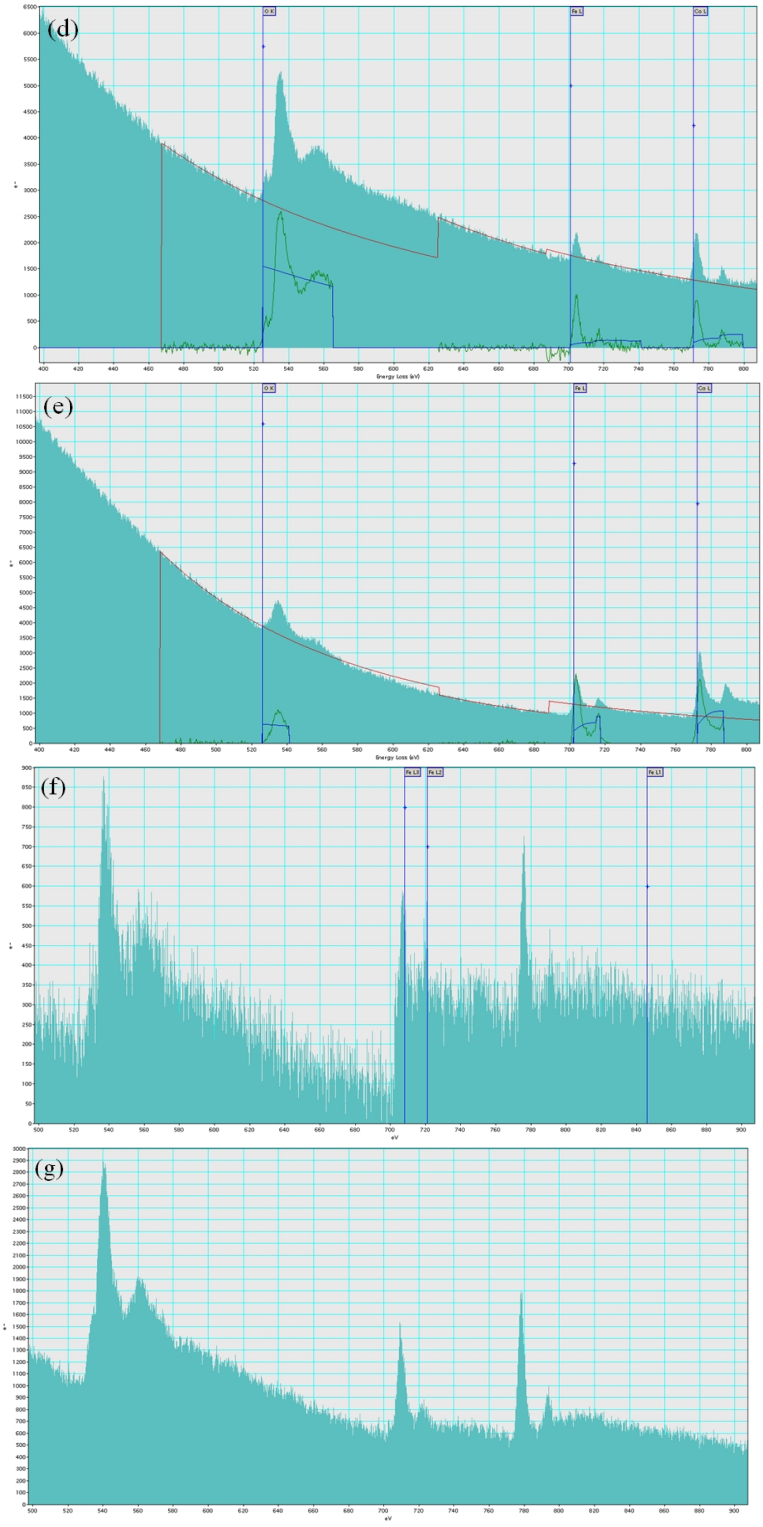

Figure 147: EELS spectra of the incomplete biosynthesized nanoparticles: (d) unfinished hexagon, (e) incomplete irregular disc, (f) position 1 in the incomplete diamond-shaped nanoparticle, (g) position 2 in the incomplete diamond-shaped nanoparticle

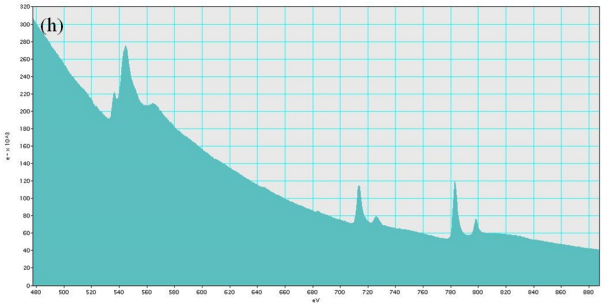

Figure 148: EELS spectrum of a stoichiometric, biosynthesized, final nanoparticle after 28 d.

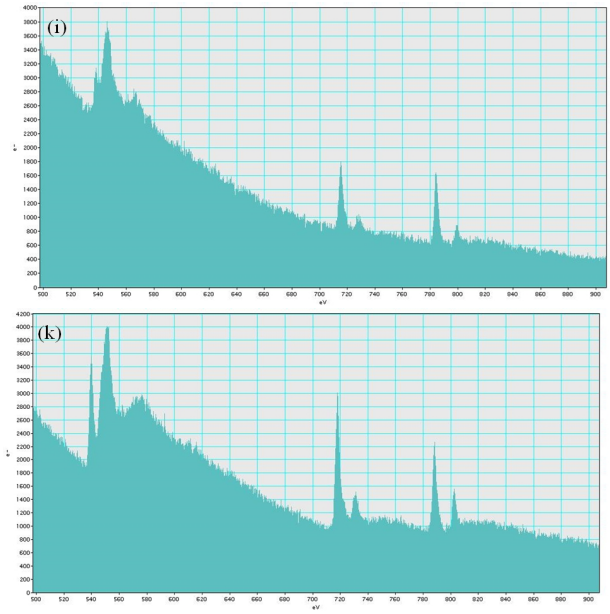

Figure 149: EELS spectra of the final nanoparticles synthesized without c25-mms6 corresponding to the different positions in Figure 80: (i) corresponds to position 1, (k) corresponds to position 2.

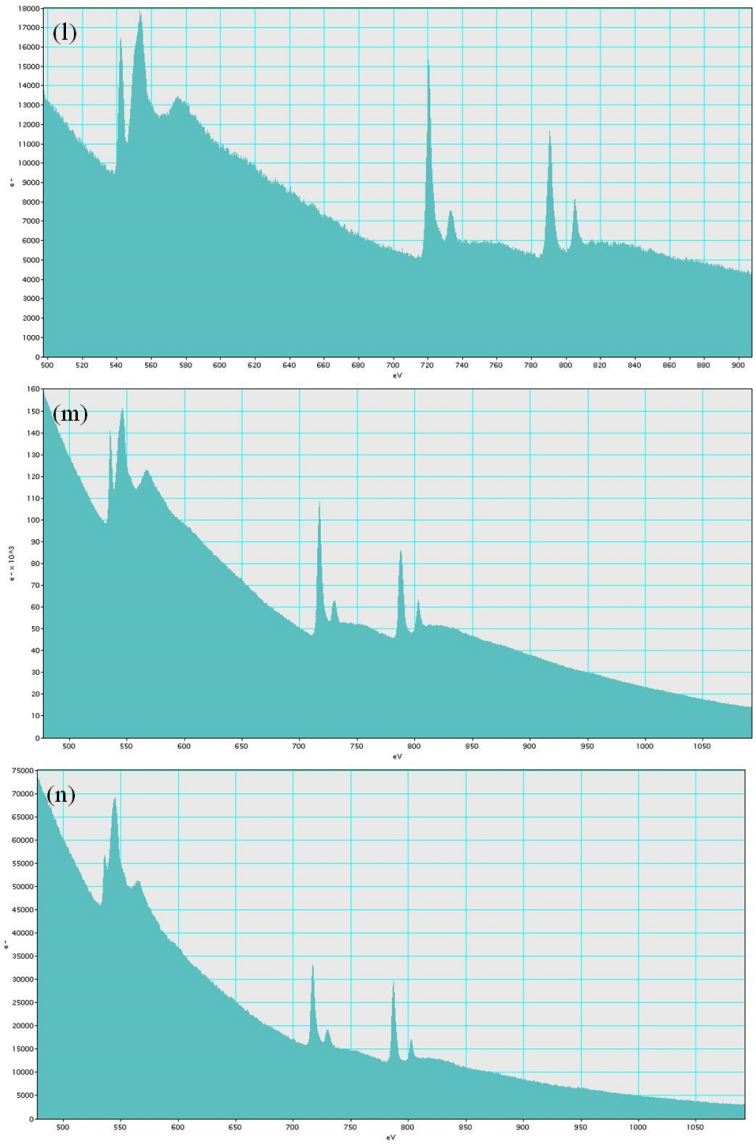

Figure 150: EELS spectra of the final nanoparticles synthesized without c25-mms6 corresponding to the different positions in Figure 80:(l) corresponds to position 3, (m) corresponds to position 4, (n) corresponds to position 5.

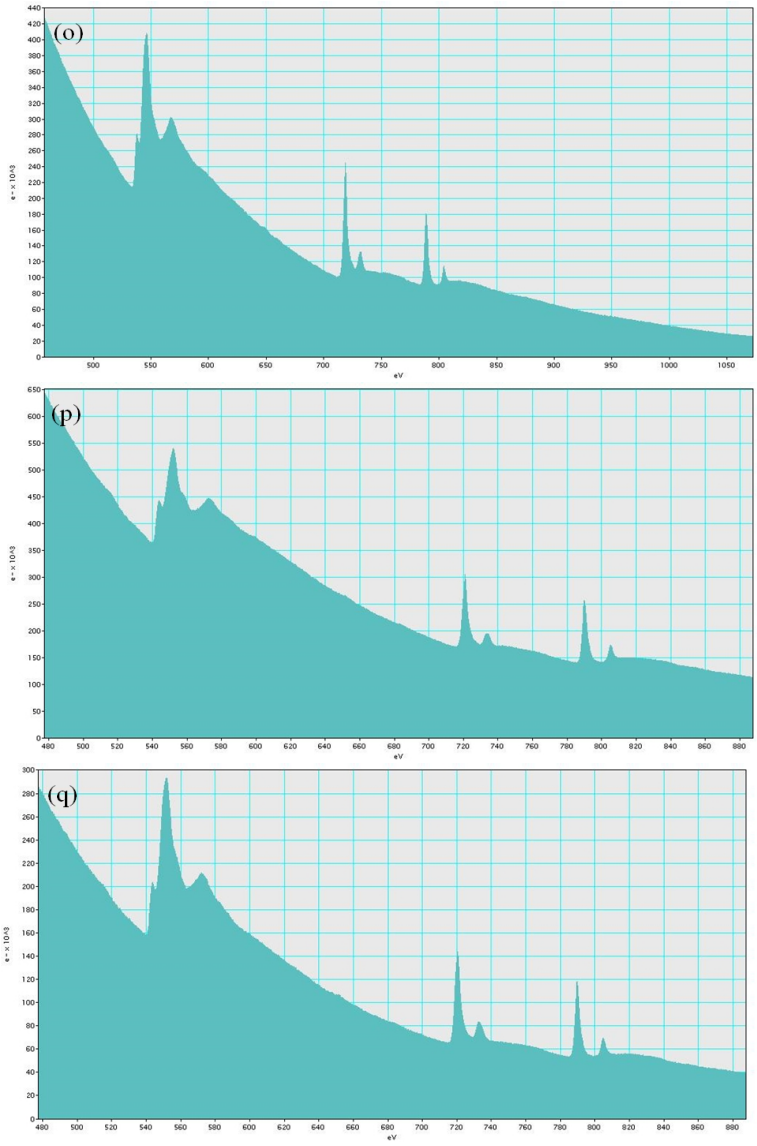

Figure 151: EELS spectra of the final nanoparticles synthesized without c25-mms6 corresponding to the different positions in Figure 80:(o) corresponds to position 7, (p) corresponds to position 8, (q) corresponds to position 9.

Appendix D

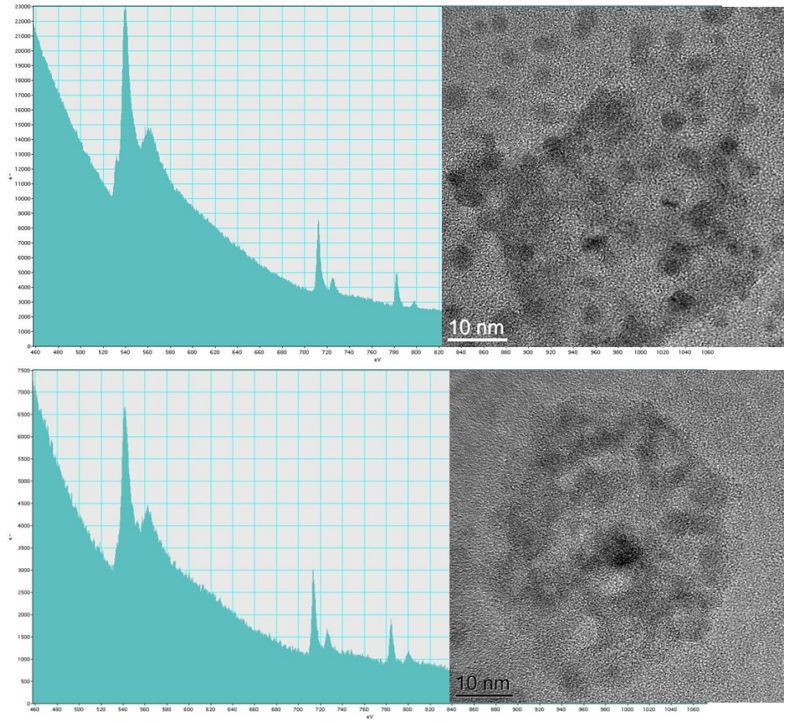

Figure 152: Top: EELS measurement of the biosynthesized nanoparticle after 5 minutes. Bottom: EELS measurement of a control experiment nanoparticle after 5 minutes. A comparison of the oxygen edge in the spectrum shows that the oxygen edge has an additional peak to the left of the main peak for the biosynthesized nanoparticle. Whether this feature can be linked to the particle stability needs to be determined.

Appendix E

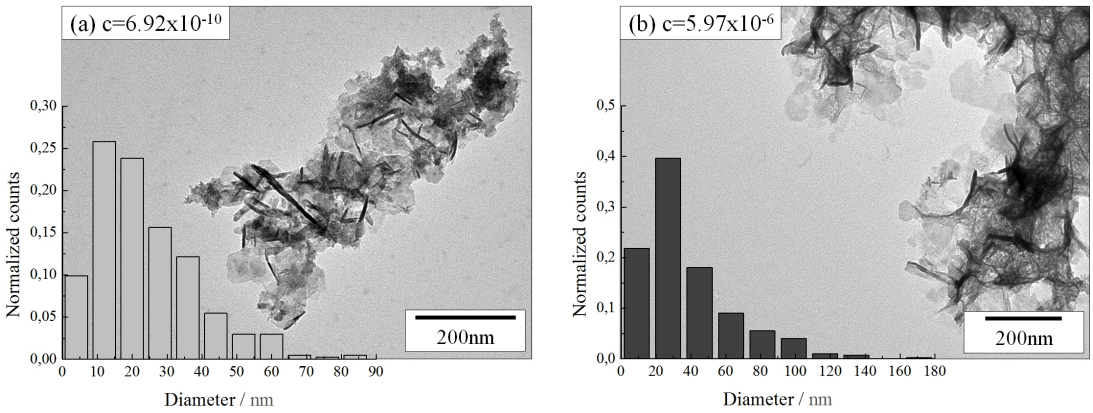

Figure 153: TEM images of the particles obtained for the different c25-mms6 concentrations. The size distributions were normalized with respect to 403 particles for the lower concentration and 399 particles evaluated for the higher peptide concentration.

c25-mms6 concentration $[M]$	Diameter $[nm]$	Hexagonal shape [%]
0	35 ± 17	23
6.92×10^{-10}	24 ± 14	45
6.92×10^{-9}	43 ± 18	55
5.97×10^{-6}	37 ± 26	58

Table 18: Comparison of the microstructure and morphology for the particles synthesized with different c25-mms6 concentrations after 15 days.

Appendix F

The following sample preparation was performed for the 3D tomography of the stem cells: Cells were washed briefly with phosphate buffer, fixed in 4 % (v/v) glutaraldehyde and 2 % (v/v) paraformaldehyde in 0.1 M phosphate buffer for 1 h at 4 °C. After washing three times for 1 min at room temperature cells were post-fixed in the dark in 2 % osmiumtetroxide, 1.5 % potassium hexacyanoferrate in 100 mM phosphate buffer, pH 7.2. Samples were dehydrated in an ascending acetone series and by subsequent critical point-drying with water-free CO2. Some chemically fixed specimens were ultra-fast shock frozen in liquid propane at −190° and subsequently became freeze-dried in a Balzers high-vacuum apparatus. The samples were embedded in resin for the tomography. A small tomography block on top of the sample, containing a single stem cell on the 30 nm pores was pre-cut using an ultramicrotome. The sample preparation was carried out by Peter Heimann, Faculty of Biology, Bielefeld University.

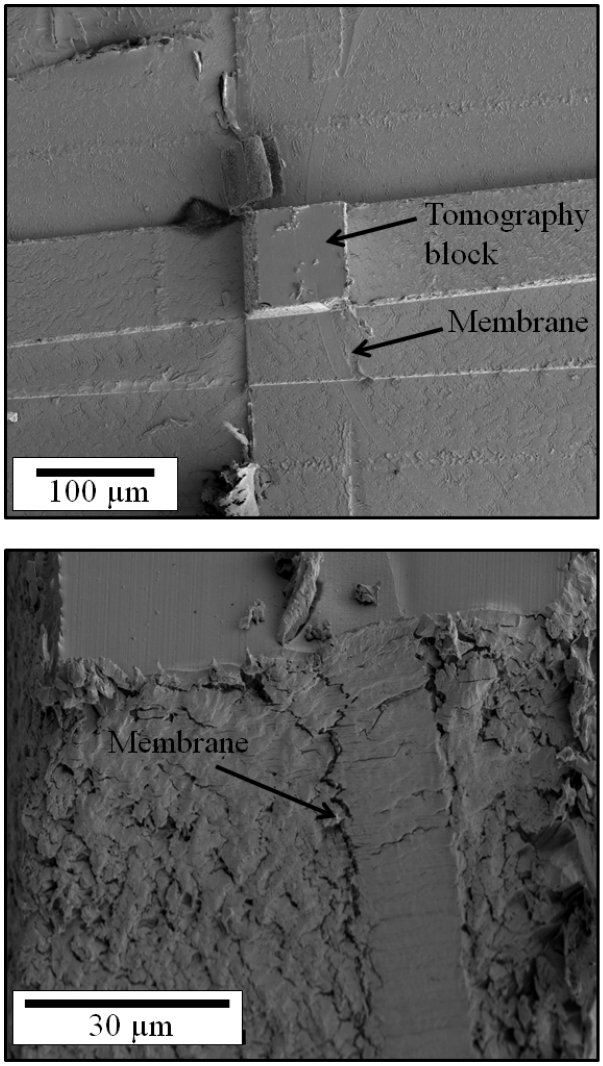

Figure 154: Top: SEM image of the 3D tomography sample. The tomography block as well as the membrane are labelled. Bottom: Front layer of the raw sample. A voltage of 3 kV and a current of 0.34 nA were used for all imaging processes. The stage is tilted to 52° to visualize the front face of the tomography block.

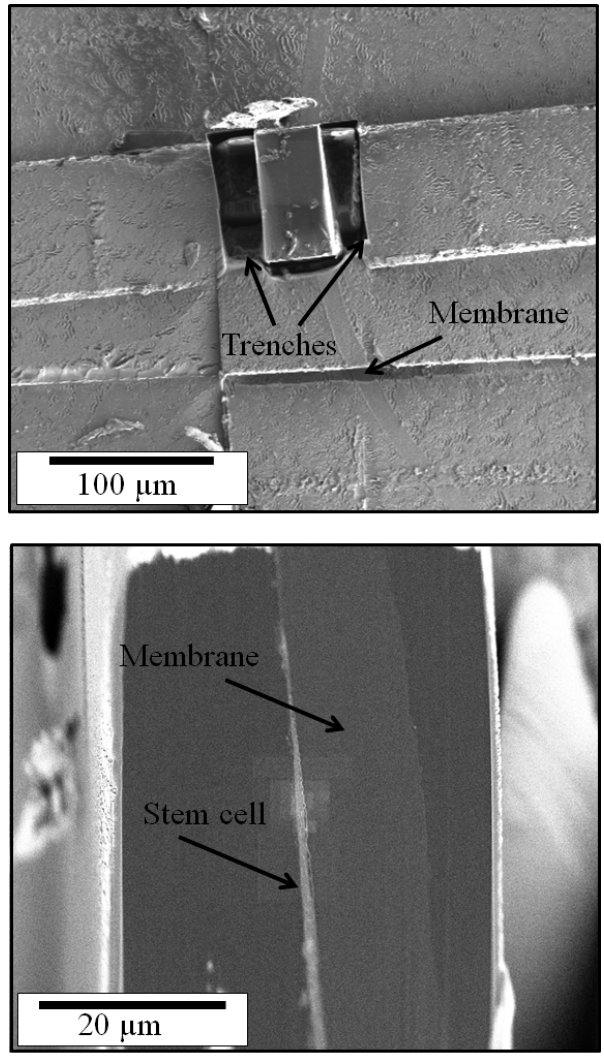

Figure 155: Top: Ion beam image of the sample. The outer edges of the block were removed using the ion beam (30 kV,21 nA). The removed areas are labelled as trenches. A voltage of 30 kV and a current of 2.8 nA were used for the imaging. Bottom: Front face after two polishing steps. The first polishing step was conducted using a voltage of 30 kV and a current of 9.3 nA. The final polishing step was performed using a voltage of 30 kV and a current of 2.8 nA.

Appendix G

clear: Removes all patterns that are defined.

setpatinfo 0.09, si: The milling depth is set to 90 nm for the material silicon[100]. The depth corresponds to a dwelltime of 0.006 s for silicon (see Section III) which was found to be the optimal dwelltime.

[100] Choosing another material leads to different material optimized dwelltimes. The dwelltime however was optimized in the previous experiments for silicon. Therefore silicon is set here as a material.

variables xdist, ydist: Define the inter-pore distances in x- and y-direction. Their values are given in μm.

variables m,n: Represent the loop counters for the inner loop (loop1,n) and the outer loop (loop2,m) for the pattern creation.

variables millmmax, millnmax: Determine how many lines are to be milled per row in x- and y-direction within the 10 µm × 10 µm area. With a 5 µm inter-pore distance 9 nanopores can be fit into the 10 µm × 10 µm array.

labels loop1, loop2, loopRight, loopLeft, loopYmove: Used for the *if () goto* command to create the loops.

*line (n*xdist), (m*ydist), ((n*xdist)+0.01), (m*ydist):* The lines are defined in a general way with (n*xdist), (m*ydist) as the x- and y- coordinate of the lines origin and ((n*xdist)+0.01), (m*ydist) as the x- and y- coordinate of the line end. The length of the line is determined by the shift in the x-coordinate of the line end ((n*xdist)**+0.01**) in comparison to the x-coordinate of the line origin (n*xdist)[101].

[101] A line of 0.01 µm is used in this script which is below the nominal ion beam diameter.

if (n≤millnmax) goto loop1: If the argument is true, the script execution will go to the line which starts with the label (loop1:) after the goto.

sleep: Pauses the script execution for a given amount of time (in ms).

mill: Mills all patterns that are defined

getstagepos: Reads the current stage positions x,y,z,r,t

variables xnew, ynew, stageshift: Variables which are used to set a new stage position. The new stage position is defined by adding the stageshift variable (set to 0.015 (in mm)) to the current stage-position. The stageshift variable is used to move the stage in

the stagemove command and corresponds the the shift of 10 μm (rectangle size) and an additional 5 μm which takes the inter-pore distance into account.

variable nmax: Defines the maximal amount of 10 μm × 10 μm areas in x- and y-direction.

stagemove x,xnew / y,new: Moves the stage in x/y direction to the new stage position xnew/ynew.

variables nyc, nxc: Represent the loop counter for the inner and outer loops which move the stage in the stitching process.

Publications

The papers and conference contributions, listed in chronological order, represent parts of this work.

Papers

1. A. Weddemann, I. Ennen, A. Regtmeier, C. Albon, A. Wolff, K. Eckstädt, N. Mill, M.K. Peter, J. Mattay, C. Plattner, N. Sewald, A. Hütten, (2010) Review and outlook: from single nanoparticles to self-assembled monolayers and granular GMR sensors. Beilstein J. Nanotechnol. 1:75-93

2. A. Wolff, K. Frese, M. Wißbrock, K. Eckstädt, I. Ennen, W. Hetaba, S. Löffler, A. Regtmeier, P. Thomas, N. Sewald, P. Schattschneider, A. Hütten, (2012) Influence of the Synthetic Polypeptide c25-mms6 on Cobalt Ferrite Nanoparticle Formation. J. Nanopart. Res. 14:

3. A. Wolff, W. Hetaba, M. Wißbrock, S. Löffler, N. Mill, K. Eckstädt, A. Dreyer, N. Sewald, P. Schattschneider, A. Hütten, (2013) Oriented attachment explains Cobalt Ferrite Nanoparticle growth in bioinspired syntheses, Beilstein J. Nanotechnol. (accepted)

4. M. Schürmann, A. Wolff, D. Widera, S. Hauser, P. Heimann, A. Hütten, C. Kaltschmidt, B. Kaltschmidt, Interaction of human neural-crest derived stem cells with nanoporous titanium surface is sufficient to induce their osteogenic differentiation, Stem Cell Therapy (submitted)

Conferences

1. A. Wolff, K. Frese, M. Wißbrock, K. Eckstädt, I. Ennen, W. Hetaba, S. Löffler, A. Regtmeier, P. Thomas, N. Sewald, P. Schattschneider, A. Hütten, (2012) Influence of the synthetic polypeptide c25-mms6 on nanoparticle growth, DPG Spring Meeting 2012, Berlin, Talk

2. A. Wolff, K. Eckstädt, W. Hetaba, M. Wißbrock, N. Mill, S. Löffler, N. Sewald, P. Schattschneider, A. Hütten, (2012) Synthetic Polypeptide c25-mms6 alters Cobalt Ferrite Nanoparticle Growth, DPG Physikerinnentagung 2012, Freiburg, Talk

3. A. Wolff, I. Yahiatenne, W. Hetaba, N. Mill, M. Wißbrock, S. Löffler, K. Eckstädt, P. Schattschneider, N. Sewald, A. Huetten, (2013) Understanding the protein-inorganic crystal interaction in bioinspired syntheses, DPG Spring Meeting 2013, Regensburg, Poster

4. A. Wolff, W. Hetaba, N. Mill, M. Wißbrock, S. Löffler, P. Schattschneider, N. Sewald, A. Huetten, (2013) Biomimetics: A promising route to obtain magnetically anisotropic nanoparticles, Fifth Seeheim Conference on Magnetism, Frankfurt, Poster

5. A. Wolff, M. Schürmann, P. Heimann, B. Kaltschmidt, C. Kaltschmidt, A. Hütten, (2013) Controlling stem cell differentiation through nanopores, DPG Physikerinnentagung 2013, Heidelberg, Talk

6. A. Wolff, W. Hetaba, N. Mill, M. Wißbrock, S. Löffler, I. Yahiatenne, K. Eckstädt, P. Schattschneider, N. Sewald, A. Hütten, (2014) Biomimetics: A promising route to obtain magnetic nanoparticles, 1st International Symposium on Nanoparticles/Nanomaterials and Applications 2014, Lisbon, Poster

Acknowledgements

I would like to thank *Prof. Andreas Hütten* for giving me the opportunity to do my PhD thesis as well as for helpful discussions and support throughout the past three years. I would also like to thank *Prof. Huser* for assessing this thesis as a co assessor. I would like to thank *Prof. Akemann* and *Prof. Anselmetti* for being the further members in the comitee.

I would like to thank all the cooperation partners for their continious support, many helpful discussions and hard work: *Nadine Mill* (Faculty of Physics, Bielefeld University) for numerous nanoparticle syntheses, many helpful discussion, her continuous support and help during the sample perparations in the chemical lab; *Prof. Sewald* (Faculty of Chemistry, Bielefeld University) for the continuous support since my diploma thesis concerning the peptide synthesis and for the many helpful discussions; *Marco Wissbrock* (Faculty of Chemistry, Bielefeld University) for the many polypeptide syntheses, the HPLC and the CD spectroscopy measurements; *Walid Hetaba* as well as *Stefan Löffler* and *Prof. Schattschneider* (TU Wien) for the HRTEM-, EELS-, electron diffraction measurements, many helpful discussions, corrections concerning the manuscripts and a wonderful working atmosphere and many laughs; *Idir Yahiatenne* (Faculty of Physics, Bielefeld University) for FCS measurements and discussions regarding the evaluation of the measurements; *Cemil Yigit* (Helmholtz Institute) for the peptide simulations; *Bastian Wedel* and *Frank Lüder* as well as and *Prof Hellweg* (Faculty of Chemistry, Bielefeld University) for DLS measurements, *Dr. Faivre* (Max Planck Institute of Colloids and Interfaces, Potsdam) for the magnetotactic bacteria; *Christoph Wigge* (Buchmann Institute for Molecular Life Science, Goethe University Frankfurt) and *Stefanie Höhn* (Faculty

of Biology, Bielefeld University) for the 3D tomography sample preparation of the magnetotactic bacteria; *Matthias Schürmann, Peter Heimann* as well as *Barbara and Christian Kaltschmidt* (Faculty of Biology, Bielefeld University) for the opportunity to work on an interdisciplinary science project, the biological investigations concerning the stem cell project, as well as many helpful discussions; *Inga Ennen* (Faculty of Physics, Bielefeld University) for the HRTEM and EELS measurements as well as for many useful discussions; *Katrin Eckstädt* (Faculty of Physics, Bielefeld University) for the first nanoparticle synthesis in my diplomathesis; *Katrin Frese* (Faculty of Chemistry, Bielefeld University) for the first peptide synthesis in my diplomathesis; *Anna Regtmeier* (Faculty of Physics, Bielefeld University) for helpful discussions concerning nanoparticles; *Patrick Thomas* and *Christian Sterwerf* (Faculty of Physics, Bielefeld University) for all the XRD measurements; *Prof Koop* and *Axel Dreyer* (Faculty of Chemistry, Bielefeld University) for the discussion concerning oriented attachment and *Prof. Gupta* from the University of Alabama for discussions concerning the cobalt ferrite nanoparticles and for taking interest in the work. I would like to thank *Marcel Müller* for the many helpful discussions regarding the nanopore script, *Daniela Wengler* and *Fabian Humpert* for the discussions regarding FCS. I would like to thank *Brendan Sanders* for reading the manuscript, making suggestions with respect to spelling, punctuation and the mechanics and fluidity of some sentences. I would also like to thank *Wiebke Hachmann* for the TEM lessons.

I would also like to thank all those people from the "Thin films and physics of nanostructures" research group that have introduced me to the various types of laboratory equipment: *Camelia Albon* (Coati); *Dieter Akemeier* and *Karsten Rott* (FIB, many helpful discussions and never ending patience); *Britta Vogel* (EDX,TEM,AGM); *Jan Rogge* (for introducing me to the Leybold L560) and *Markus Meinert* (for many helpful discussions regarding XRD spectra).

I would like to thank my office collegues *Bernhard Eickenberg, Dieter Akemeier, Daniel Kappe* and *Fabian Schmidt-Michels* for a wonderful time during the past years, the many helpful discussions, corrections of the manuscripts, many laughs and never ending support. I would also like to thank the whole research group D2 for the nice atmosphere throughout the past years.

I would like to thank FOR 945 for the financial support in the framework of project 3 throughout the past three years.

I would like to thank my former teachers Herr Thöneböhn for getting me interested in physics and Mr. Martin for teaching me how to "think math" as well as Mr. Keegan who took the time to teach me how to write essays and papers.

I would like to thank my friends *Bernhard Eickenberg, Dieter Akemeier, Britta Vogel, Alex Hintzman, Naomi Forman, Marcel Müller, Jana Münchenberger, Andreas and Johanna Helmstedt, Caro Rademacher, Andi Markwirth, Julia Bader, Gisela and Detlef Korbanek, Sandra und Nicole Retzlaff, Tanja Ackgül, Maryanne Ryan* as well as *Tom and Jenn McEwan* who have supported me in every possible way. I am thankful for such wonderful friends.

I would like to thank my family *Christiane and Jochen Maydorn, Sarah Maydorn, Dieter Markmann, Tante Püppi, Nils Bohle, Andreas Maydorn, and Josef Mensing* as well as my late grandparents for their never ending support, for believing in me, for the wonderful childhood, the financial support during my studies, the physics library, the many small and big favors, the hockey games and the times their thoughts have been with me.

Last but not least I would especially like to thank my husband *Brendan Wolff* for the continuous support in every possible way and faith in me. I could not wish for a better husband.